Plasma Physics Reports, Vol. 26, No. 10, 2000, pp. 813–819. Translated from Fizika Plazmy, Vol. 26, No. 10, 2000, pp. 867–873.

TOKAMAKS

Study of Plasma Fluctuations in the Tuman-3M Tokamak Using Microwave Reflectometry with an Obliquely Incident Probing Beam

V. V. Bulanin*, S. V. Lebedev, L. S. Levin**, and V. S. Roytershteyn***

**St. Petersburg State Technical University, Politekhnicheskaya ul. 29, St. Petersburg, 195251 Russia*

***Ioffe Physicotechnical Institute, Russian Academy of Sciences, Politekhnicheskaya ul. 26, St. Petersburg, 194021 Russia*

Received December 9, 1999; in final form, March 10, 2000

Abstract—Plasma fluctuations in the Tuman-3M tokamak are studied experimentally by analyzing backscattered radiation for different angles of incidence of the probing beam from the normal to the cut-off surface. The poloidal rotation velocity of the plasma fluctuations is determined from the Doppler shift of the reflected radiation spectrum measured on the edge of the tokamak during the transition to the H-mode. It is shown that, before the transition to the H-mode, the rotation velocity can be estimated quantitatively from the spectral shift or from the rate at which the phase of the reflected signal grows. The experimental data obtained during the transition to the H-mode provide evidence for the onset of a sheared poloidal flow. The shear makes it difficult to correctly estimate the poloidal rotation velocity in the improved confinement regime. The main mechanisms responsible for the broadening of the backscattered radiation spectra are considered. The turbulent diffusion coefficients determined under the assumption that the spectral broadening is diffusive in character are found to be close to those determined from the charged-particle balance. *© 2000 MAIK "Nauka/Interperiodica".*

1. INTRODUCTION

Many experimental and theoretical studies of the transport barriers that arise in tokamaks during the transition to improved confinement indicate that sheared poloidal plasma flows play a key role in the suppression of anomalous transport in tokamak plasmas (see, e.g., [1]). In this connection, various techniques have been developed for measuring the rotation plasma velocity and radial electric field. In this paper, we analyze the possibility of determining the poloidal rotation velocity of plasma fluctuations in a tokamak by microwave backscattering during the oblique incidence of a probing beam. Our investigations are motivated by the circumstance that some phase measurements from reflectometry on tokamaks and stellarators at a high level of plasma fluctuations have revealed an anomalously rapid growth of the phase of the backscattered signal—the so-called phenomenon of phase "runaway" (PR), which cannot be attributed to the displacement of the cut-off surface [2, 3]. The PR effect can be explained by the Doppler frequency shift $\Delta\omega = V_\theta k_\theta$ (where k_θ is the poloidal component of the wave vector of the incident wave) of the reflected signal due to the poloidal rotation of plasma fluctuations, provided that the probing beam is incident obliquely on the cut-off surface, when, e.g., reflectometry measurements are carried out with an inclined antenna or with two antennas. When the incidence angle and, accordingly, k_θ are specified, the poloidal rotation velocity V_θ may be determined from the shift of the backscattered radiation spectrum. In the published literature on the reflectometry measurements in which the spectra of the reflected signals were observed to shift, the angle of incidence of the probing beam with respect to the magnetic surface was specified at fixed positions of both the emitting and receiving antennas [2, 4, 5]. In those experiments, the displacement of the cut-off surface due to the change in the electron density caused only slight time variations of the angle of incidence of the probing beam to the cut-off surface. Here, we examine a broad range of incidence angles, which can be changed by turning the antenna of a reflectometer. This experimental scheme allows us to compare the data obtained at different incidence angles for similar discharges in tokamak experiments. The spectra of the backscattered radiation were studied in the Tuman-3M tokamak during transitions to the Ohmic H-mode that were triggered in different ways.

2. TECHNIQUE FOR MEASURING BACKSCATTERED RADIATION

The diagnostic technique for measuring backscattered radiation in the Tuman-3M tokamak (a = 0.22 m, R = 0.53 m, $B_t \le 1.2$ T) is based on a single-antenna reflectometry system, which makes it possible to probe plasmas by either O- or X-mode microwave radiation over the frequency band F = 17–25 GHz. For this frequency band, the cut-off surface is located at the plasma edge, where the transport barrier appears during

1063-780X/00/2610-0813$20.00

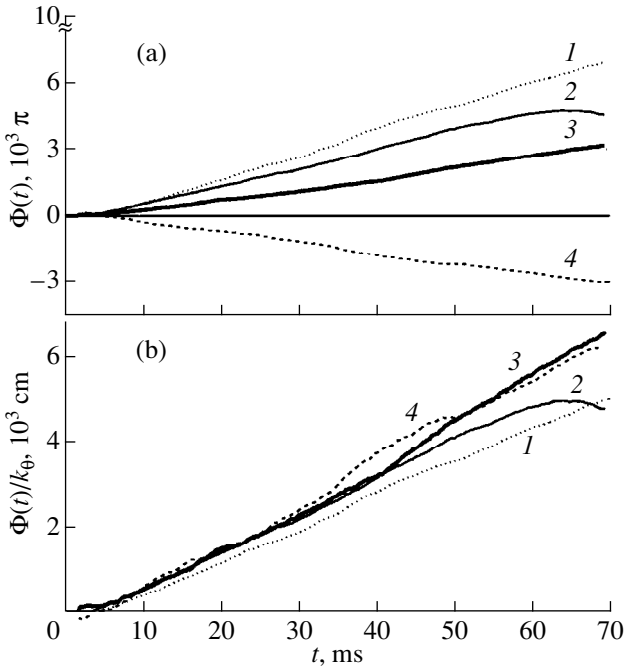

Fig. 1. Time evolutions of (a) the phase $\Phi(t)$ and (b) the normalized phase $\Phi(t)/k_\theta$ in discharges with a transition to the Ohmic H-mode (a discharge started at t = 5 ms, and the transition to the H-mode occurred at t = 34 ms) for different incidence angles of the X-mode incident beam (F = 22 GHz): φ = (*1*) +30°, (*2*) +20°, (*3*) +10°, and (*4*) –20°. Positive incidence angles refer to the antenna pattern directed toward the lower part of the torus.

the transition to the Ohmic H-mode. The probing radiation was launched from the side of the low magnetic field by means of a conical antenna with a diameter of 4 cm and a length of 8 cm. A specially designed scheme allowed us to change the angle φ between the axis of the probing microwave beam and the normal to the cut-off surface. For this purpose, between the shots, both the antenna and microwave scheme were rotated as a whole in the plane of the minor cross section of the torus. The measurements were performed at the following fixed incidence angles: $\varphi = 0°, \pm5°, \pm10°$, and $\pm20°$ (the angle φ refers to the cut-off surface that coincides with the last closed flux surface). The zero incidence angle corresponded to the antenna positioned in the equatorial plane of the torus. The technique used to record the backscattered radiation by a quadrature homodyne detector operating in the microwave band is described in detail in [6]. This technique allowed us to estimate the spectrum shapes in the blue and red spectral regions from the Fourier transformed complex signal $\dot{U}(t) = U_{\cos}(t) + iU_{\sin}(t)$, where the reference signals from the two channels of the homodyne system, $U_{\cos}(t)$ and $U_{\sin}(t)$, are shifted by $\pi/2$. Depending on the sampling rate of the analog-to-digital converter (ADC) used to record the signals, the frequency band under analysis varied from ±0.5 to ±2 MHz. Additionally, in the course of a discharge, we calculated the phase $\Phi(t)$ of the complex signal $\dot{U}(t)$ from the reflectometer.

3. FREQUENCY SHIFTS OF THE SPECTRA OF BACKSCATTERED RADIATION

The experiments on microwave backscattering in the Tuman-3M tokamak were carried out after boronization of the chamber at fairly high discharge currents $I_p > 160$ kA. The transition to the H-mode was triggered either by a pulsed gas puffing [7] or by a microwave pulse at the ion-cyclotron resonance (ICR) frequency. The formation of the edge transport barrier was determined from the growth of the averaged electron density and the drop in the intensity of the D_α line.

As expected, inclining the antenna resulted in a shift in the backscattered radiation spectra; for all incidence angles, the shift was smaller than the spectral width. The fact that the spectra were displaced as a whole likely provides evidence that, in the entire region where microwaves are backscattered, the plasma fluctuations rotate in the same direction. Note that, in the range of nearly zero frequencies, no pronounced peak was observed in the spectra; i.e., there was no signal at the probing frequency. As a function of time, the average frequency shift was calculated in the form

$$\Delta\omega(t) = \int \omega S(\omega) d\omega / \int S(\omega) d\omega, \qquad (1)$$

where $S(\omega)$ is the averaged estimate of the power spectrum of the backscattered signal and the time t corresponds to the beginning of the time interval over which the spectrum was estimated. The resulting shift was integrated over time to obtain the phase $\Phi_S(t) = \int_0^t \Delta\omega(t)dt$, which was then compared with the phase $\Phi(t)$ determined from the complex reflectometry signal. For both of the obtained phases, the PR effect was observed to manifest itself in the same manner. Figure 1 shows that the larger the incidence angle φ, the larger the frequency shift and, accordingly, the higher the rate at which the phase grows. For the probing beams that were symmetric about the equatorial plane of the torus (i.e., for the incidence angles $\pm\varphi$]), the frequency shifts that were obtained before the transition to the H-mode in the Ohmic stage of a discharge are equal in absolute value but differ in sign. If the frequency shift is governed by the Doppler shift, then the normalized (to k_θ) frequency shift and the rate at which the phase grows should determine the projection of the rotation velocity onto the direction perpendicular to the magnetic field. Without neutral beam injection, when the toroidal plasma rotation velocity in the Tuman-3M tokamak is lower than the poloidal rotation velocity, the main contribution to the Doppler shift comes from the poloidal plasma rotation: $\Delta\omega = V_\theta k_\theta$. Figure 1 shows time evolutions of the normalized phase $\Phi(t)/k_\theta$, where k_θ is approximately equal to $2k\sin\varphi$ (with k the wavenumber

in vacuum) when the cut-off surface nearly coincides with the last closed flux surface. We can see that, during Ohmic discharges (up to the time $t = 34$ ms), the slope angle of the time evolutions remains approximately the same for different incidence angles φ and yields the estimate 8×10^4 cm/s for the poloidal rotation velocity of plasma fluctuations. This estimate is close to the neoclassical predictions for V_θ in the Ohmic stage of a discharge.

After the transition to the H-mode, both the spectral shift and, accordingly, the rate at which the phase grows become strongly dependent on the frequency F of the probing radiation. As an example, Fig. 2 shows time evolutions of the normalized phase $\Phi(t)/k_\theta$ for two frequencies F of the O-mode incident radiation. Also shown are the radii $r_c(t)$ of the cut-off surfaces calculated from the plasma density profile corresponding to the Ohmic stage of the discharge. In actuality, the distance between the cut-off surfaces is smaller than that in Fig. 2 because of steeper edge density profiles in the H-mode. In any case, it can be expected that, when the probing frequency is shifted by 1.5 GHz, this distance will be much smaller than the half-width of the first maximum of the Airy function, which characterizes the spatial resolution of the reflectometry measurements. Figure 2 clearly demonstrates that, throughout the Ohmic stage of the discharge and at $t > 40$ ms, the rate at which the phase grows is essentially the same for different frequencies of the incident radiation and that the sign of the phase $\Phi(t)$ corresponds to the rotation in the direction of the diamagnetic ion drift, i.e., the positive direction of the radial electric field. However, over the time interval $28 < t < 40$ ms, the phase grows at very different rates, which likely provides evidence for the onset of a significant sheared poloidal flow. That the phase behaves very differently at different frequencies F was already observed in the case of probing radiation incident at large angles [2]. Note that the appearance of the rotation velocity field that is radially inhomogeneous on scales shorter than the spatial resolution available with our reflectometry techniques may lead to an uncertainty in the determination of the poloidal velocity shear. This uncertainty stems from the fact that the frequency shift $\Delta\omega$ [see (1)] averaged over the volume of the scattering region depends on the shape of the radial profiles of both the fluctuation amplitudes and poloidal velocities.

Experiments with obliquely incident probing beams showed that there is yet another difficulty in estimating the poloidal rotation velocity V_θ from the spectral shift. The reason for this is that the symmetry in the phase for symmetric probing beams with the incidence angles $\pm\varphi$ in the Ohmic stage of the discharge was observed to disappear during the transition to the H-mode. Figure 3 presents time evolutions of the phase for the symmetric incidence angles $\varphi = \pm 10°$. These evolutions were obtained from two tokamak discharges with identical parameters measured by all the tokamak monitoring

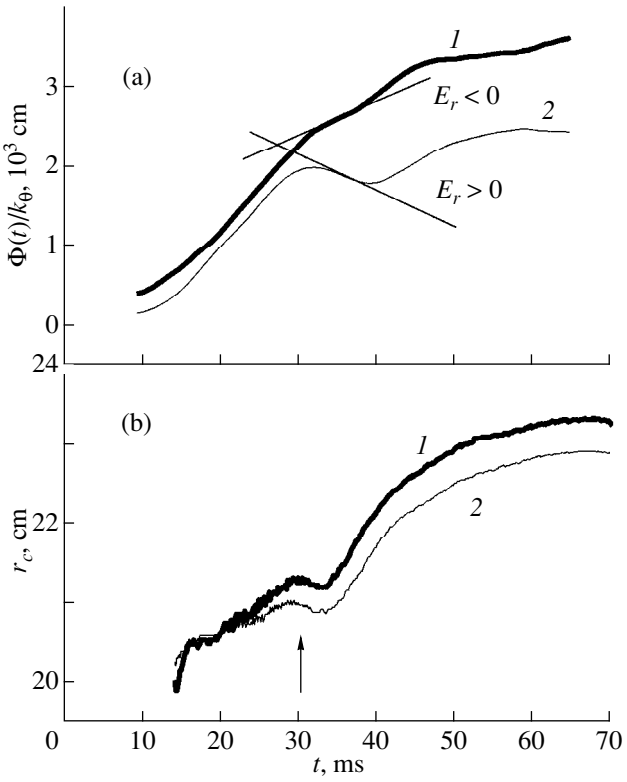

Fig. 2. Illustration of the difference in the rates at which the phase grows for different positions of the cut-off surface in the case of an O-mode incident beam: (a) the change in the normalized phase $\Phi(t)/k_\theta$ for two probing frequencies (*1*) 17.5 and (*2*) 19 GHz (the tangents to the curves indicate that the sign of the phase increment corresponds to the sign of the radial electric field E_r) and (b) the calculated radii $r_c(t)$ of the cut-off surfaces (the vertical arrow marks the instant at which the discharge passes over to the H-mode).

diagnostics. We can clearly see that, at the times after $t \geq 30$ ms and after $t \geq 41$ ms, the rates at which the phase grows are very different. In experiments in which such symmetry was absent, the growth of the phase was found to be anomalous even in the case of normally incident probing beams ($\varphi = 0°$). The effect of phase asymmetry, which was discovered due to the possibility of carrying out measurements with symmetric probing beams with the incidence angles $\pm\varphi$, may be interpreted as follows. It is well known that, at a low fluctuation level such that the fluctuations can be described in the Born approximation, the incident wave and the wave reflected from the cut-off surface are equally backscattered. In this case, the Doppler shift should be symmetric for symmetric incidence angles, regardless of the profile of the scattering fluctuations. Under our experimental conditions, the level of radiation backscattered from the cut-off surface at the probing frequency was low; consequently, we can anticipate that the detected signal was mainly governed by the backscattered incident wave rather than the reflected wave. If there are anisotropic fluctuations skewed with

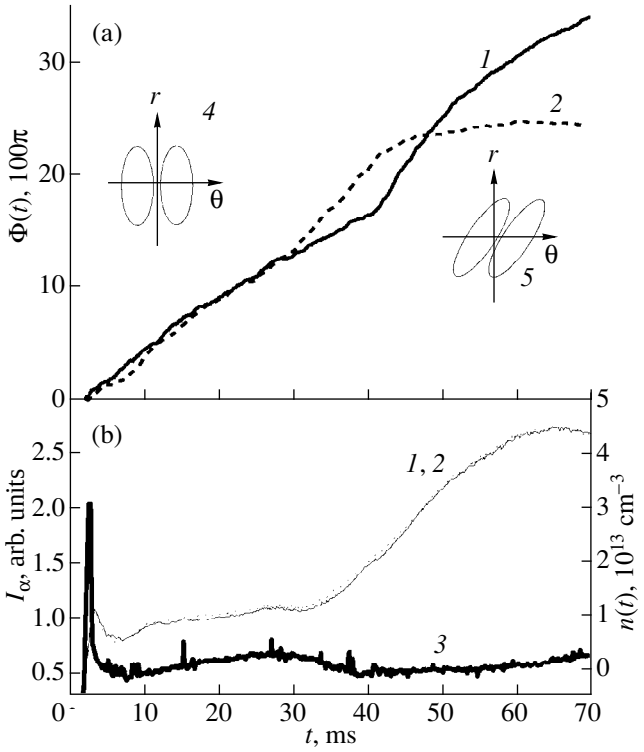

Fig. 3. Asymmetry in the rates at which the phase grows for symmetrically incident probing beams according to the experimental observations of two discharges with identical measured parameters in the case of an X-mode incident beam at the frequency F = 22.08 GHz: (a) time evolutions of the phase for φ = (*1*) +10° and (*2*) –10° and a schematic picture of the scattering fluctuations (*4*) before and (*5*) after the transition to the H-mode and (b) the electron density for incidence angles *1* and *2* and (*3*) the radiation intensity at the D_α line.

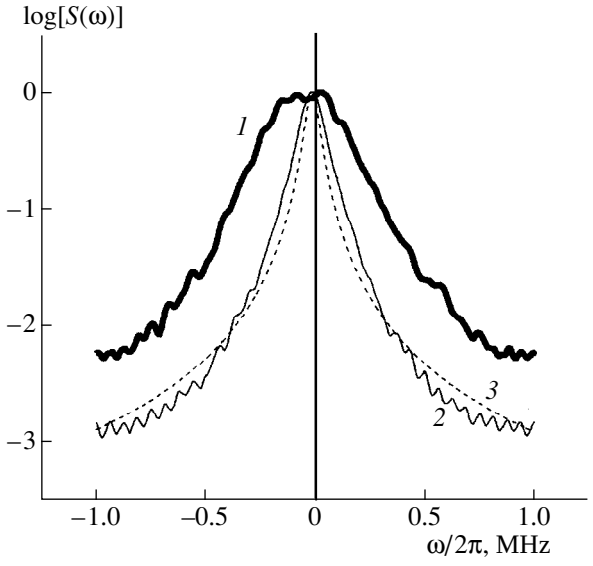

Fig. 4. Comparison between the spectra of the backscattered radiation that were recorded (*1*) before and (*2*) after the transition to improved confinement for φ = 5° in the case of an O-mode incident beam at the frequency F = 18 GHz. The dashed curve *3* is the Lorentzian approximation of spectrum *2*.

respect to the magnetic surface in the minor cross section of the torus (as is shown in Fig. 3), then we might expect that the spectra will be asymmetric at symmetric incidence angles. This is attributed to the fact that the k_θ-spectra of the skewed fluctuations are asymmetric. The occurrence of such fluctuations during the formation of the sheared poloidal plasma flow is predicted by the theory of the transition to the H-mode (see, e.g., [1]). Hence, when the turbulence level is high, the PR effect, which was discovered in the course of phase measurements from reflectometry in Tuman-3M, can be explained by the onset of the poloidal sheared flow.

4. WIDTH AND SHAPE OF THE BACKSCATTERED RADIATION SPECTRA

The experiments with oblique probing beams revealed the phenomenon of the strong suppression of high-frequency spectral components of the backscattered radiation during the transition to the Ohmic H-mode. This phenomenon was previously observed in the Tuman-3 tokamak [6]. The characteristic fall time of the high-frequency components depended on the way in which the transition to the H-mode was initiated and was found to be the shortest for transitions driven by a microwave pulse at the ICR frequency. The observed suppression of high-frequency spectral components is equivalent to a significant narrowing of the spectra. In order to illustrate the considerable difference in the spectral widths, Fig. 4 displays two averaged spectra of the signal power $U(t)$ that were measured before and after the transition to the H-mode. Figure 5 shows time evolutions of the spectral width $\delta\omega(t)$ for different incidence angles φ. For each of the incidence angles, the probing frequency F was adjusted so that the radiation incident at different angles was reflected from the cut-off surfaces that were close to each other. Before the transition to the H-mode, the spectral width was observed to depend weakly on the incidence angle. However, just after the transition, the spectrum of the normally incident microwave beam was found to narrow substantially. For microwave beams incident at large angles such that $\varphi > 10°$, the spectra started to narrow significantly later.

The distinguishing feature of the obtained spectra is their shape, which is closely related to the mechanism for spectral broadening. In various regimes of the discharges, the spectra were observed to be nearly Lorentzian in shape and to differ strongly from Gaussian spectra (Fig. 4). We can mention several factors that govern the shape and width of the spectrum of the backscattered signal. The experimentally obtained spectral widths cannot be explained in terms of the conventional Doppler broadening $\delta\omega \approx \delta k_\theta V_\theta$, which is associated with the antenna directional pattern. The reason for this is that, for $\delta k_\theta < k_\theta$, the spectral shift remained smaller than the spectral width. (The measured profile of the antenna directional pattern as a function of the wave-

number k_θ is presented in Fig. 6b.) The spectral width $\delta\omega \approx k_\theta \Delta V_\theta$ also cannot be explained in terms of the shear of the poloidal plasma flow, i.e., in terms of a finite interval of the poloidal velocities ΔV_θ in the spatial region where the incident beam is backscattered. Our estimates show that, in order to explain the recorded spectra, the shear velocities should be about 5×10^6 s^{-1}, which is obviously far above their theoretical predictions. Moreover, according to the accepted views, the shear of the poloidal plasma flow should increase during the transition to the H-mode, in which case the spectrum should broaden accordingly. However, in our experiments, the spectrum behaved in the opposite manner (Figs. 4, 5). For discharges with strong edge turbulence, we must take into account the possible effect of multiple scattering on the spectral broadening. However, that the spectra for different incidence angles φ evolve in different ways can hardly be explained only in terms of the broadening due to multiple scattering. In fact, if the suppression of high-frequency spectral components during the transition to the H-mode in the case of nearly normal incidence is associated with a reduction in the fluctuation level and, accordingly, with the progressively smaller role of multiple scattering, then it remains unclear why this is not so in the case of oblique incidence (Fig. 5). Note also that the familiar model of a phase screen, which was developed by Nazikian and Mazzucato [8] in order to explain the spectral broadening under the conditions of strong fluctuations, predicts that the spectra should be Gaussian in shape, unlike the experimentally recorded Lorentzian spectra (Fig. 4).

Gresillon *et al.* [9] predicted Lorentzian shapes of the spectra in the case of laser scattering, when the spectra broaden diffusively, i.e., when the characteristic spatial scale of the scattering fluctuations is longer than the correlation length of turbulent motions. In this case, we can write

$$S(\omega) = \frac{2(k^2 D_\perp)}{(\omega - \mathbf{k}\cdot\mathbf{V})^2 + (k^2 D_\perp)^2}, \qquad (2)$$

where $D_\perp$ is the turbulent diffusion coefficient and $\mathbf{V}$ is the mean plasma velocity. According to (2), the width of the frequency spectrum is directly related to the transverse turbulent diffusion coefficient $D_\perp$. If we assume that the diffusion mechanism for spectral broadening dominates in our experiments, then we find that the spectral narrowing observed experimentally during the transition to the H-mode agrees qualitatively with the familiar theoretical results and experimental data on the suppression of anomalous edge transport in the H-mode, in which case, however, the transverse diffusion coefficient $D_\perp$ is difficult to estimate because of the uncertainty in the wavenumber k of the scattering fluctuations. We can, however, turn to the fact that, in the Ohmic phase of the discharge, the spectral width was weakly sensitive to the incidence angle. Formula

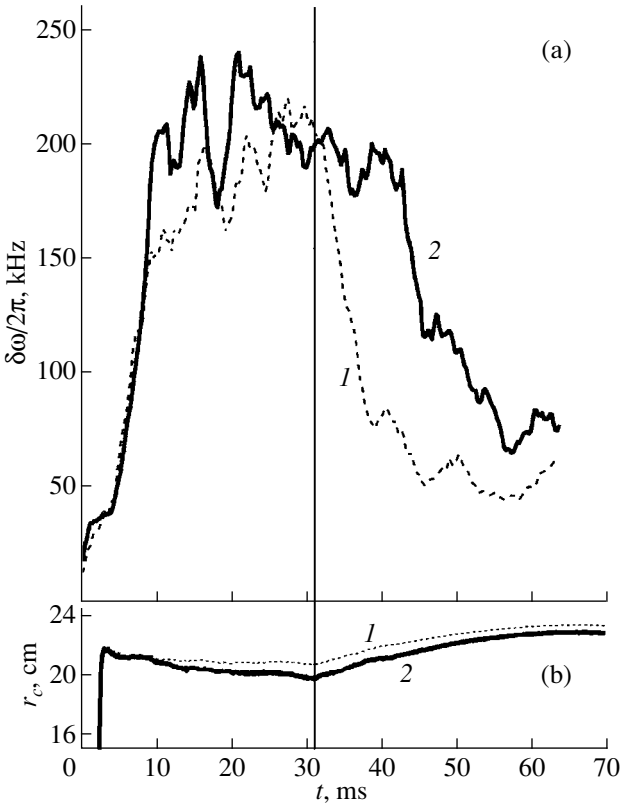

Fig. 5. Comparison between the spectral widths of the backscattered signals for two incidence angles φ = (*1*) –5° and (*2*) –20° in the case of an O-mode incident beam: (a) the time evolution of the spectral width δω(*t*) and (b) the calculated radii $r_c(t)$ of the cut-off surfaces.

(2) implies that such a weak dependence on $k_\theta = 2\sin\varphi$ can be observed only in the case of scattering by fluctuations with a certain absolute value $|\mathbf{k}|$ of the wavenumber. To verify this conclusion, we carried out two-dimensional modeling of the backscattered power spectrum as a function of k_θ (i.e., of the k_θ-spectrum) in the Born approximation in rectangular geometry (the method of calculation is described, e.g., in [10]). In simulations, we assumed that fluctuations with a fixed $|\mathbf{k}|$ develop in a layer with a Gaussian density profile and that the k_θ-spectrum of the antenna is also Gaussian in shape. In Fig. 6, we compare this spectrum with the antenna spectrum measured in the near wave zone. In modeling, the absolute value $|\mathbf{k}|$, the layer thickness, and the coordinate of the layer with respect to the cut-off surface served as free parameters. In Fig. 6, the spectrum $S(k_\theta)$ computed at $k = 4$ cm^{-1} is compared with the experimental spectrum obtained from four tokamak discharges with nearly the same parameters. Even a comparison with the results of such a simplified model shows that the appearance of fluctuations in a narrow interval of k values can in principle agree with the experimentally obtained k_θ-spectra. With the value

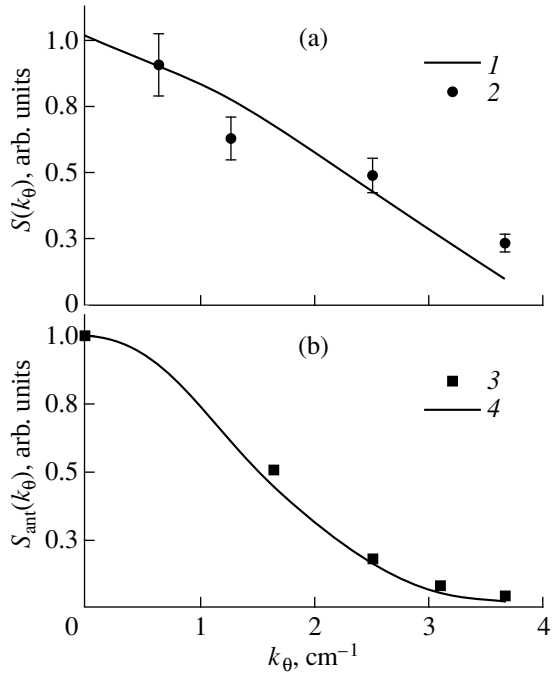

Fig. 6. Results from modeling the k_θ-spectra in the case of an O-mode incident beam at the frequency F = 17.5 GHz. (a) The power of the backscattered radiation vs. $k_\theta = 2k\sin\varphi$. Curve *1* is for the calculated spectrum, and curve *2* is for the experimental k_θ-spectrum. The vertical error bars reflect errors that were estimated without taking into account the slight difference between the tokamak discharges in which the measurements were carried out. (b) The k_θ-spectrum of the antenna: (*3*) the recorded angular antenna spectrum as a function of k_θ and (*4*) the antenna spectrum used in the model.

k = 4 cm^{-1} chosen above and the experimental data on the spectral width, formula (2) yields the following values of the transverse turbulent diffusion coefficient: 8 m^2/s for the Ohmic stage of discharge and 2 m^2/s for the H-mode. These values are close to the $D_\perp$ values characteristic of the edge plasma in Tuman-3M [11].

Bulanin *et al.* [12] pointed out that, in the case of oblique probing of discharge plasmas with a highly sheared poloidal flow, the shape of the spectrum that broadens due to stochastic fluctuations should differ significantly from the shape described by expression (1). Estimates showed that the spectral width should increase in proportion to $(dV_\theta/dr)^{2/3}$. Presumably, it is the onset of a highly sheared poloidal plasma flow that is capable of explaining the marked difference observed in the spectral widths during the transition to the H-mode in discharge plasmas probed by microwave beams at small and large incidence angles (Fig. 5).

5. CONCLUSION

Our experiments have demonstrated that, at a high fluctuation level, the inclination of the antenna of a reflectometer leads to shifts in the spectra of the backscattered radiation and to growth in the phase of the signal from a reflectometer (the latter effect is known as the phase runaway). We have shown that experimental data on discharges without a transition to the H-mode can serve to estimate the poloidal rotation velocity of fluctuations if the spectral shifts are treated as Doppler shifts. Experimental data also provide clear evidence for the onset of a sheared poloidal plasma flow during the transition to the H-mode. The onset of a sheared flow is also evidenced, first, by a pronounced difference in the shifts of the spectra of the backscattered signal at different frequencies of the probing radiation and, second, by the asymmetry in the rates at which the phase grows in the case of symmetrically incident probing microwave beams. However, under the conditions of our experiments, it is the onset of a sheared poloidal flow that makes the poloidal velocities in the improved confinement modes more difficult to estimate correctly. The fact that the experimentally recorded spectra of the backscattered radiation were Lorentzian in shape and became narrower during the transition to the H-mode allows us to assume that the spectral broadening can be explained in terms of the diffusion mechanism. The turbulent transport conditions estimated on the basis of this assumption were found to be close to those determined previously from the balance equations. If this assumption is confirmed for other spatial regions of tokamak discharges, then we may hope that the method of backscattered microwave radiation can be applied to estimate turbulent transport rates directly from the backscattered radiation spectra.

ACKNOWLEDGMENTS

We are grateful to E.Z. Gusakov for fruitful discussions and to A.M. Kalugin for his help in the development and design of a reflectometer with a tilting directional pattern of the antenna. This work was supported in part by the Russian Foundation for Basic Research (project no. 97-02-18119) and INTAS (grant no. 97-11018).

REFERENCES

1. K. L. Burrell, Phys. Plasmas **4**, 1499 (1998).
2. V. V. Bulanin, V. V. Dreval, and D. O. Korneev, in *Proceedings of the 20th European Conference on Controlled Fusion and Plasma Physics, Lisboa, 1993*, Vol. 17C, Part. IV, p. 1517.
3. J. Sánchez, T. Estrada, and H. J. Hartfuss, in *Proceedings of the IAEA Technical Meeting on Microwave Reflectometry for Fusion Plasma Diagnostics, JET, 1992*, p. 133.
4. C. Christou, J. Baldzuhn, M. Hirsch, *et al.*, in *Proceedings of the 1998 ICPP and 25th European Conference on Controlled Fusion and Plasma Physics, Prague, 1998*, Vol. 22C, p. 1466.

5. X. L. Zou, T. F. Seak, M. Paume, *et al.*, in *Proceedings of the 26th European Conference on Controlled Fusion and Plasma Physics, Maastricht, 1999*, Vol. 23J, p. 1041.
6. V. V. Bulanin and D. O. Korneev, Fiz. Plazmy **20**, 20 (1994) [Plasma Phys. Rep. **20**, 14 (1994)].
7. M. V. Andrejko, L. G. Askinazi, V. E. Golant, *et al.*, in *Proceedings of the 24th European Conference on Controlled Fusion and Plasma Physics, Berchtesgaden, 1997*, Vol. 21A, Part II, p. 693.
8. R. Nazikian and E. Mazzucato, Rev. Sci. Instrum. **66**, 392 (1995).
9. D. Gresillon, B. Cabrit, J. P. Villain, *et al.*, Plasma Phys. Controlled Fusion **34**, 1985 (1992).
10. X. L. Zou, L. Laurent, and J. M. Rax, Plasma Phys. Controlled Fusion **33**, 903 (1991).
11. S. V. Lebedev, S. V. Andrejko, L. G. Askinazi, *et al.*, Plasma Phys. Controlled Fusion **36**, B289 (1994).
12. V. V. Bulanin, D. O. Korneev, V. A. Rozhansky, and M. Tendler, in *Proceedings of the 22nd European Conference on Controlled Fusion and Plasma Physics, Bournemouth, 1995*, Vol. 19C, Part II, p. 089.

Translated by G.V. Shepekina

Plasma Physics Reports, Vol. 26, No. 10, 2000, pp. 820–830. Translated from Fizika Plazmy, Vol. 26, No. 10, 2000, pp. 874–884.

PLASMA OSCILLATIONS AND WAVES

Passage of Electromagnetic Waves through the Critical Surface

A. V. Timofeev

Russian Research Centre Kurchatov Institute, pl. Kurchatova 1, Moscow, 123182 Russia

Received February 17, 2000

Abstract—A study is made of the passage of electromagnetic waves through the critical surface at small angles between the plasma density gradient and the magnetic field. Expressions are derived for the transmission and reflection coefficients of electromagnetic oscillations that are periodic in the direction transverse to the density gradient. The penetration of wave beams is also analyzed. In the case of a wide beam, the incident and transmitted ray trajectories are shown to be mirror-image about the resonance surface. Behind the resonance surface, a narrow incident wave beam generates a beam propagating along the magnetic field. © *2000 MAIK "Nauka/Interperiodica".*

1. INTRODUCTION

It is well known that electromagnetic waves cannot penetrate into an unmagnetized plasma with a density above the critical value defined by the condition $\omega_{pe} = \omega$, where ω_{pe} is the electron Langmuir frequency and ω is the wave frequency. Applying a magnetic field permits radiation to pass through this barrier. However, strictly speaking, electromagnetic waves cannot penetrate completely through the critical surface, because it reflects part of the radiation. On the other hand, in the vicinity of the critical surface, the waves are partially transformed so that the wave polarization and other wave parameters change.

The problem of the penetration of electromagnetic waves through the critical surface arises from investigations of the propagation of radio waves in the Earth's ionosphere. Theoretical models usually deal with a planar plasma slab and assume that electromagnetic waves propagate along the density gradient, i.e., that $\theta = \chi$, where θ is the angle between the wave vector and the magnetic field and χ is the angle between the density gradient and the magnetic field. Different approximate methods developed for analyzing the wave equation made it possible to cover the entire parameter range for the propagation problem (see, e.g., [1]). Expressions derived for the transmission and reflection coefficients imply that, at $\theta = \chi$, the wave penetrates through the critical surface almost completely only if the angle χ is sufficiently small. On the other hand, it was noted that, regardless of the value of χ, the wave penetration would be complete if the wave vector at the critical surface were parallel to the magnetic field ($\theta = 0$). Complete penetration can be achieved by launching the wave from a vacuum at a certain angle to the magnetic field.

Interest in the penetration problem increased considerably after the publication of paper [2] by Preinhalter and Kopecky, who pointed out that the waves that crossed the critical surface and continued to propagate in a plasma could transform into so-called Bernstein modes (the transformation phenomenon itself was described in reviews [3, 4]). The fact that Bernstein modes interact strongly with electrons opens the possibility of heating dense plasmas in closed magnetic confinement systems in which the magnetic field lines make small angles with the chamber wall and, accordingly, the plasma density gradient is nearly perpendicular to the magnetic field ($\chi \approx \pi/2$). This problem was studied theoretically in [5–7], and experiments on plasma heating via Bernstein modes were carried out in the W7-AS stellarator [8].

In this paper, we consider the penetration of electromagnetic waves through the critical surface, assuming that the angle χ between the density gradient and the magnetic field is small. In such configurations, which are characteristic of open magnetic devices, the efficiency of the ECR heating of low-density ($\omega_{pe} < \omega$) plasmas by microwaves launched through the magnetic mirror into an open confinement system at a small angle to the magnetic field was found to be fairly high [9]. To analyze whether this version of the ECR heating of a dense ($\omega_{pe} > \omega$) plasma might be implemented in practice requires detailed investigations of the propagation of electromagnetic waves through the critical surface at small angles χ. This limiting case is also the most interesting from a theoretical standpoint, because, for $\chi \ll 1$, the plasma resonance surface is close to the critical surface, in which case the wave incident on the critical surface is perturbed so strongly that we can reveal all of the possible channels of energy losses.

Here, we derive general expressions for the transmission, reflection, and transformation coefficients for the wave incident on the critical surface, assuming that $\theta, \chi \ll 1$. We trace the ray trajectories in the vicinity of the critical surface, which, generally speaking, is not transparent to electromagnetic radiation. For the limiting cases of wide and narrow wave beams, we determine the conjugation rules for the beams on both sides of the opaque region.

1063-780X/00/2610-0820$20.00 © 2000 MAIK "Nauka/Interperiodica"

2. PLASMA OSCILLATIONS NEAR THE CRITICAL SURFACE

For a homogeneous plasma, the Maxwell equations reduce to the vector algebraic equation

$$\mathbf{N} \times [\mathbf{N} \times \mathbf{E}] + \mathbf{D} = 0, \quad (1)$$

where $\mathbf{N} = \mathbf{k}c/\omega$ and $D_i = \varepsilon_{ij}E_j$. Here and below, all quantities with units of length are normalized to c/ω.

It is convenient to represent the transverse (with respect to the main magnetic field) electric fields of the wave as a superposition of two circularly polarized components $E_\pm$, one of which (left-polarized) rotates in the same direction as the ions and the other (right-polarized) in the same direction as the electrons. In Cartesian coordinates with the z-axis directed along the magnetic field, we have $E_\pm = (E_x \pm iE_y)/\sqrt{2}$, in which case the wave Eq. (1) becomes

$$\begin{pmatrix} N_\parallel^2 + N_+N_- - \varepsilon_+ & -N_-^2 & -N_\parallel N_+ \\ -N_+^2 & N_\parallel^2 + N_+N_- - \varepsilon_- & -N_\parallel N_- \\ -N_\parallel N_+ & -N_\parallel N_- & 2N_+N_- - \varepsilon_\parallel \end{pmatrix} \times \begin{pmatrix} E_+ \\ E_- \\ E_\parallel \end{pmatrix} = 0, \quad (2)$$

where $N_\pm = (N_x \pm iN_y)/\sqrt{2}$. The plasma is assumed to be cold ($\varepsilon_\pm = 1 - \dfrac{\omega_{pe}^2}{\omega(\omega \pm \omega_e)}$ and $\varepsilon_\parallel = 1 - \dfrac{\omega_{pe}^2}{\omega^2}$).

In the case of an inhomogeneous plasma, the wave equations (2) describe the propagation of a wave far from the critical surface, i.e., in the region in which the quasiclassical approximation is applicable.

It follows from further analysis (see also [1]) that the critical surface is essentially opaque to incident waves with $N_\perp \geq N_\parallel$. Since such waves are not of interest to us, we set $N_\parallel \gg N_\perp$, in which case the first two equations in (2) give

$$E_\pm \approx \frac{N_\parallel N_\pm}{N_\parallel^2 - \varepsilon_\pm} E_\parallel. \quad (3)$$

We substitute (3) into the third equation in (2) and perform simple manipulations to obtain

$$D(\mathbf{N})E_\parallel = 0, \quad (4)$$

where

$$D(\mathbf{N}) \approx (N_\parallel^2 - \varepsilon_+)(N_\parallel^2 - \varepsilon_-)\varepsilon_\parallel + \varepsilon_\perp N_\perp^2 (N_\parallel^2 - 1). \quad (5)$$

The dispersion relation $D(\mathbf{N}) = 0$ determines the parameters of the natural waves that can propagate in a plasma.

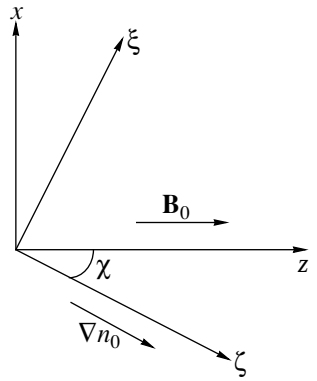

Fig. 1. Working coordinate system.

We analyze the waves in the vicinity of the critical surface using the plane plasma slab approximation [1, 2, 5–7], which seems to be suitable for our purposes because, on spatial scales of about the wavelength of incident radiation, the critical surface is usually curved only slightly.

We introduce Cartesian coordinates with the ζ-axis directed along the density gradient, the ξ-axis lying in the plane that passes through the point ∇n_0 and contains the vector $\mathbf{B}_0$, and the η-axis orthogonal to this plane (Fig. 1). To write Eq. (4) in these coordinates, we must make the replacement $N_\parallel = -\sin\chi N_\xi + \cos\chi N_\zeta$, $N_\perp^2 = (\cos\chi N_\xi + \sin\chi N_\zeta)^2 + N_\eta^2$, where χ is the angle between ∇n_0 and $\mathbf{B}_0$.

In order to obtain a rough picture of the processes in the vicinity of the critical surface, we analyze the dependence of the refractive index on the plasma density or, equivalently, on the ζ-coordinate. First, we consider one-dimensional waves ($N_\xi = N_\eta = 0$, $N = N_\zeta$). Under the additional assumptions $\nabla n_0 \| \mathbf{B}_0$ (i.e., $\chi = 0$) and $\omega_e > \omega$, we arrive at the profiles shown in Fig. 2a, in which the horizontal lines $N^2 = \varepsilon_+$ and $N^2 = \varepsilon_-$ refer to electromagnetic waves with left-hand and right-hand circular polarizations, respectively, and the vertical line corresponds to potential electron Langmuir waves localized at the plasma resonance surface, which coincides with the critical surface ($\varepsilon_\parallel = 1 - \omega_{pe}^2/\omega^2 = 0$). Waves of different types do not interact with each other because their electric fields are mutually orthogonal. As a result, electromagnetic waves freely cross the critical surface.

For $\chi \neq 0$, the plasma resonance surface does not coincide with the critical surface. In a plane-stratified plasma, electromagnetic waves can reach the plasma resonance surface ($N^2 = \infty$) only due to the change in N_ζ (because N_ξ, N_η = const). In this case, the waves propagate at a nonzero angle χ to the magnetic field; conse-

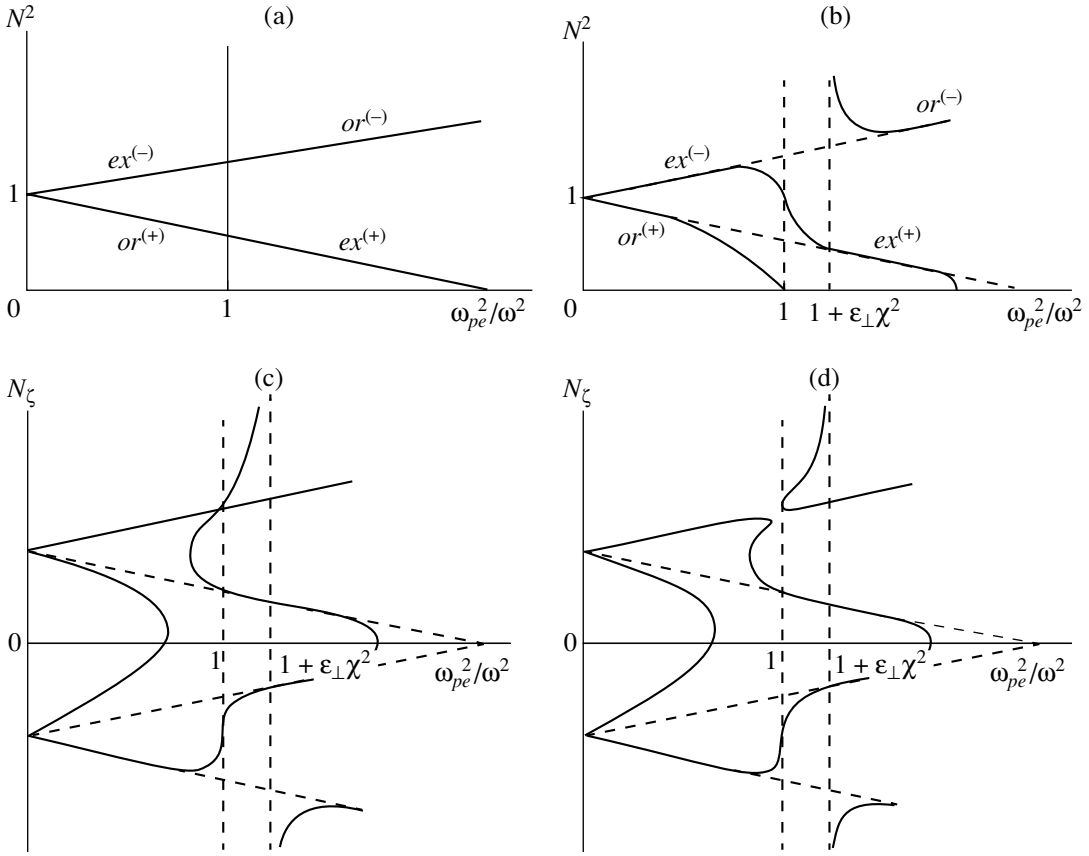

Fig. 2. Refractive index vs. the plasma density for (a) $\chi = \theta = 0$, (b) $\chi = \theta \neq 0$, (c) $\chi \neq 0$ and $N_\xi = \sqrt{\varepsilon_-}\sin\chi$, and (d) $\chi \neq 0$ and $N_\xi > \sqrt{\varepsilon_-}\sin\chi$.

quently, the location of the resonance surface is determined by the condition

$$\varepsilon_\perp \sin^2\chi + \varepsilon_\parallel \cos^2\chi = 0. \quad (6)$$

Since, for $\chi \neq 0$, the wave vector (and, accordingly, the electric field) of the potential wave is not parallel to $\mathbf{B}_0$, it should interact with electromagnetic waves. In the interaction region, the polarization of the electromagnetic waves changes: their electric field acquires a significant longitudinal component. On the other hand, far from the critical surface, the polarization of electromagnetic waves of interest to us (i.e., those propagating at a small angle to the magnetic field) is nearly circular and the refractive index can be approximated by $N^2 \approx \varepsilon_\pm$. To distinguish between the two types of oscillations, we call them the left-hand and right-hand polarized waves. Experiments on ECR plasma heating should naturally be carried out with right-hand polarized waves, whose electric vector rotates in the direction of the electron gyration. Figure 2b also implies that, when crossing the critical surface, the right-hand polarized waves transform into left-hand polarized waves.

However, since the refractive index changes sharply in the vicinity of the critical surface, the quasiclassical approximation (in which the refractive index can only be introduced) may fail to hold. In this case, the wave energy can be transmitted through the opaque region that separates the zones of propagation of the right-hand polarized waves.

In the case of non-one-dimensional waves ($N_\xi \neq 0$), the opaque region may become smaller. In a plane-stratified plasma, N_ξ remains unchanged during the wave propagation. For $N_\xi = \sqrt{\varepsilon_-}\sin\chi$, the wave vector at the critical surface is parallel to the magnetic field. Such waves freely traverse the critical surface (Fig. 2c). The case of small values of $N_\xi - \sqrt{\varepsilon_-}\sin\chi > 0$ is illustrated in Fig. 2d. The characteristic feature of the case $N_\xi - \sqrt{\varepsilon_-}\sin\chi < 0$ is that the opaque region is located to the right of the critical surface. The plots in Fig. 2 were obtained under the assumption $\omega_e > \omega$. In the opposite case $\omega_e < \omega$, the plots in the vicinity of the critical surface remain qualitatively the same.

Note that, for the same value of N_ξ, the absolute value of N depends on the propagation direction of a wave along the ζ-axis in a plane-stratified plasma. Consequently, the right-hand polarized waves that are incident from the side of higher density pass almost freely through the critical surface if $N_\xi \approx -\sqrt{\varepsilon_-}\sin\chi$. Analogously, for $N_\xi = \pm\sqrt{\varepsilon_+}\sin\chi$, the critical surface is opaque to the left-hand polarized waves that are incident from the side of lower (higher) density.

3. SOLUTION OF THE WAVE EQUATION

Qualitatively, the penetration of waves through the critical surface should be described by the wave equation, which can be obtained from the algebraic Eq. (4) through the substitution $N_\zeta \longrightarrow -i\partial/\partial\zeta$.

Since we are interested in the processes occurring in the vicinity of the critical surface, we set $\varepsilon_\pm$ = const and approximate the dependence $\varepsilon_\parallel(\zeta)$ by the linear function $\varepsilon_\parallel(\zeta) = -\zeta/L$.

Under these assumptions, the wave equation in the vicinity of the critical surface can be written as

$$\left\{\left(\frac{\partial^2}{\partial\zeta^2}+\varepsilon_+\right)\left(\frac{\partial^2}{\partial\zeta^2}+\varepsilon_-\right)\frac{\zeta}{L}\right.$$
$$\left.-\varepsilon_\perp\left(\left(\chi\frac{\partial}{\partial\zeta}-iN_\xi\right)^2-N_\eta^2\right)\left(\frac{\partial^2}{\partial\zeta^2}+1\right)\right\}E_\parallel = 0. \quad (7)$$

Here, we take into account the relationship $\varepsilon_\perp = \frac{1}{2}(\varepsilon_+ + \varepsilon_-) \approx \varepsilon_+\varepsilon_- \approx \frac{\omega_e^2}{\omega_e^2-\omega^2}$, resulting from $\varepsilon_\pm \approx \frac{\omega_e}{\omega_e\pm\omega}$, which is valid at $|\varepsilon_\parallel| \ll 1$. We assume that the quantity $|\omega_e - \omega|$ is of the same order of magnitude as ω, in which case the cyclotron resonance surface is far enough from the critical surface.

The wave equation (7) is a singular equation, because the coefficient in front of the highest (fourth) derivative vanishes at $\zeta = \varepsilon_\perp L\chi^2$. The singular point is a plasma resonance point (see above). To continue the solution through the resonance point, we use the Landau contour. This way of continuing the solution usually assumes wave energy absorption. The problem as formulated implies that dissipative processes inevitably come into play because the wave vector increases without bound when approaching the plasma resonance point.

We supplement the frequency in the expression for $\varepsilon_\parallel$ with the small positive imaginary part, $\varepsilon_\parallel = 1 - \frac{\omega_{pe}^2}{(\omega+i\nu)^2} \approx -\frac{\zeta}{L} + \frac{2i\nu}{\omega}$, in order to displace the singular point from the real axis into the upper half-plane. Consequently, when the solution is continued through the singular point, it should be bypassed along the Landau contour lying in the lower half-plane of the complex variable ζ.

The wave Eq. (7) is linear in ζ. It is convenient to solve such equations by the method of integral transformations, setting

$$E_\parallel(\zeta) = \int_C dp e^{p\zeta}F(p), \quad (8)$$

where C is the integration contour in the plane of the complex variable p. The integration contour can be either closed or such that the integrand vanishes at both ends. Below, we will use contours of the second type.

Substituting Eq. (8) into Eq. (7), we find that the function $F(p)$ should satisfy the equation

$$\left\{(p^2+\varepsilon_+)(p^2+\varepsilon_-)\frac{d}{dp}\right.$$
$$\left.+\varepsilon_\perp L[(\chi p - iN_\xi)^2 - N_\eta^2](p^2+1)\right\}F(p) = 0, \quad (9)$$

which has the solution

$$F(p) = (p-p_+)^{iA_{+,1}}(p-p_-)^{iA_{-,1}}(p+p_+)^{-iA_{+,2}}$$
$$\times(p+p_-)^{-iA_{-,2}}\exp(-L\varepsilon_\perp\chi^2 p),$$

where $p_\pm = i\sqrt{\varepsilon_\pm}$, $A_{\pm,1} = \frac{L\sqrt{\varepsilon_\pm}}{4}((\chi\sqrt{\varepsilon_\pm}+N_\xi)^2 + N_\eta^2)$, and $A_{\pm,2} = \frac{L\sqrt{\varepsilon_\pm}}{4}((\chi\sqrt{\varepsilon_\pm}-N_\xi)^2 + N_\eta^2)$.

4. TRANSMISSION AND REFLECTION COEFFICIENTS FOR WAVES CROSSING THE CRITICAL SURFACE

We begin by considering the waves that are incident on the critical surface from the side of higher density ($\zeta > 0$). Below, we will show that, in this case, the waves are not reflected from the critical surface (see also [1]). Consequently, the right-hand and left-hand polarized waves are described by the integrals over contours C_1 and C_2 in Fig. 3, respectively. The asymptotic expression for the amplitude of the right-hand polarized wave at $\zeta \gg 1$ is

$$E_\parallel^{(1)}(\zeta) \approx \frac{2\pi i}{\Gamma(iA_{-,1})}\zeta^{-iA_{-,1}-1}e^{-p_-\zeta}\Phi^{(1)}, \quad (10)$$

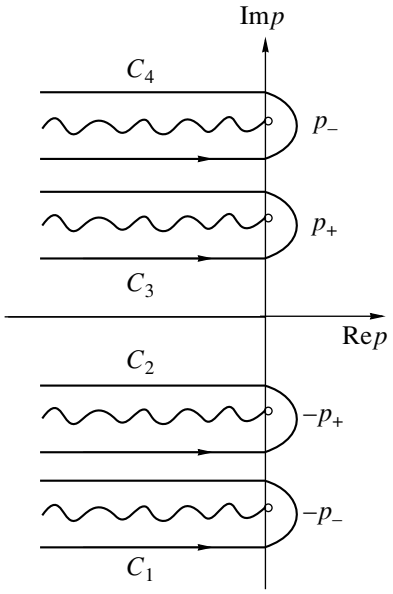

Fig. 3. Integration contours for the integral in (8) that correspond to linearly independent solutions to Eq. (7) at $\zeta > 0$.

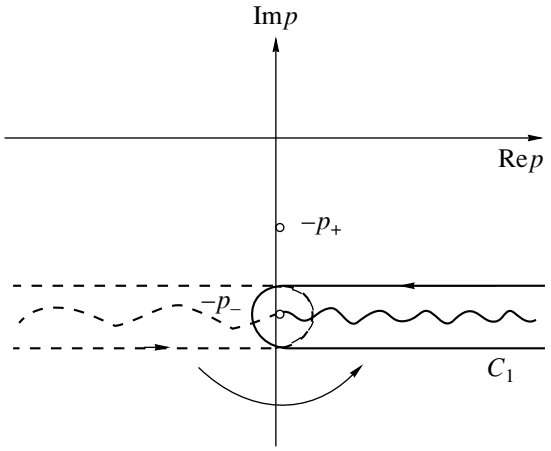

Fig. 4. How the contour C_1 should be turned in order to continue the solution through the critical surface according to Landau's rule.

where $\Phi^{(1)} = \exp\left(\frac{\pi}{2}(-A_{+,1} + A_{+,2} + A_{-,2})\right)|p_+ - p_-|^{iA_{+,1}}|2p_-|^{-iA_{+,2}}|p_+ + p_-|^{-iA_{-,2}}$. Here and below, we displace the origin of the ζ-coordinate by the distance $L\chi^2\varepsilon_\perp$ from the critical surface to the resonance surface.

We continue the solution to the negative real semiaxis with the help of the Landau contour (see above), in which case the analytic continuation should be carried out through the lower half-plane of the complex variable ζ. For the integral in Eq. (8) to converge, the integration contour C_1 should be turned as indicated in Fig. 4. This keeps the structure of expression (10) unchanged; however, the absolute value of the amplitude of the right-hand polarized wave decreases by a factor of $e^{\pi A_{-,1}}$ because $\arg\zeta$ changes.

Hence, the transmission coefficient for the right-hand polarized wave incident on the critical surface from the side of higher density is equal to

$$T_{--}^{\downarrow} = e^{-2\pi A_{-,1}}. \tag{11}$$

Here, the first and second subscripts correspond to the energy gain and loss, respectively, and the arrows directed upward and downward indicate the propagation direction of waves (toward higher and lower densities).

Since, in the case at hand, there are no reflected waves, a right-hand polarized wave loses energy when crossing the critical surface. This effect can be explained by the energy outflow toward the plasma resonance region.

Note that, although the refractive index changes sharply in the vicinity of the critical surface, the waves that are incident from the side of higher density are not reflected from the critical surface. This is also true for the left-hand polarized waves. To analyze them, we take the integral in Eq. (8) along contour C_2 in Fig. 3. For $\zeta > 0$, we obtain

$$E_\parallel^{(2)}(\zeta) = \frac{2\pi i}{\Gamma(iA_{+,1})}\zeta^{-iA_{+,1}-1}e^{-p_+\zeta}\Phi^{(2)}, \tag{12}$$

where $\Phi^{(2)} = \exp\left(\frac{\pi}{2}(A_{-,1} + A_{+,2} + A_{-,2})\right)|p_+ - p_-|^{-iA_{-,1}}|2p_+|^{-iA_{+,2}}|p_+ + p_-|^{-iA_{-,2}}$.

For negative real values of ζ, the integration contour should be turned in the lower half-plane (as is the case with right-hand polarized waves) so that it should always pass around the branch point $\zeta = p_-$ (Fig. 5). As a result, the asymptotic expression will contain an additional term describing the right-hand polarized wave:

$$E_\parallel^{(2)}(\zeta) \approx \frac{2\pi i}{\Gamma(iA_{+,1})}\zeta^{-iA_{+,1}-1}e^{-p_+\zeta}\Phi^{(2)} + \frac{2\pi i}{\Gamma(iA_{-,1})}\zeta^{-iA_{-,1}-1}e^{-p_-\zeta}\Phi^{(1)}(1 - e^{2\pi A_{+,1}}). \tag{13}$$

Comparing (13) with (12), we find the transmission coefficient for the left-hand polarized wave propagating from the side of higher density:

$$T_{++}^{\downarrow} = e^{-2\pi A_{+,1}}. \tag{14}$$

To obtain the transmission coefficient for the left-hand polarized wave that transforms into a right-hand polarized wave when traversing the critical surface, we need to consider the expression for the energy flux. Far from the critical surface (in the region where the wave

polarization is nearly circular), the energy flux density has the form

$$S_+ \approx \frac{cN_\parallel}{8\pi}|E_+|^2,$$

where E_+ can be taken from expression (3), in which, in accordance with (12), we must set $N_\parallel \approx \sqrt{\varepsilon_+} + A_{+,1}/\zeta$. Since $A_{+,1} = \frac{L}{4}\sqrt{\varepsilon_+}N_\perp^2$, the energy flux density becomes

$$S_+ \approx \frac{\zeta^2}{\varepsilon_+^{1/2}N_\perp^2}|E_\parallel|^2. \quad (15)$$

This quantity is independent of the ζ-coordinate by virtue of the relationship $|E_\parallel| \propto 1/|\zeta|$ (see above).

Taking into account the relationship [10]

$$|\Gamma(iA)|^2 = \frac{\pi}{A\sinh(\pi A)},$$

we arrive at the transmission coefficient for the left-hand polarized wave that transforms into a right-hand polarized wave when passing through the critical surface:

$$T_{+-}^{\downarrow} = (1-e^{-2\pi A_{+,1}})(1-e^{-2\pi A_{-,1}}). \quad (16)$$

The sum of the transmission coefficients (14) and (16) is smaller than unity, because, when the left-hand and right-hand polarized waves propagating from the side of higher density cross the critical surface, they are both partially converted into short-wavelength quasi-potential waves that carry energy toward the plasma resonance region.

In the region $\zeta > 0$, the solution $E_\parallel^{(3)}$ describing the left-hand polarized wave that is incident from the side of lower density can be obtained by taking the integral in Eq. (8) along contour C_3 in Fig. 3: $E_\parallel^{(3)} \propto e^{p_+\zeta}$. The solution describing the right-hand polarized wave propagating in the same direction is more complicated. In order for the solution in the region $\zeta < 0$ not to contain the exponential function $\propto e^{p_+\zeta}$, which corresponds to the left-hand polarized wave propagating in the same direction, the solution in the region $\zeta > 0$ should be taken in the form

$$\tilde{E}_\parallel^{(4)} = E_\parallel^{(4)} - E_\parallel^{(3)}(1-e^{-2\pi A_{+,2}}),$$

where $E_\parallel^{(4)}$ can be obtained by evaluating the integral in Eq. (8) along contour C_4 in Fig. 3: $E_\parallel^{(4)} \propto e^{p_-\zeta}$. A similar analysis of the expressions for $E_\parallel^{(3)}$ and $\tilde{E}_\parallel^{(4)}$ in the opposite half-plane of the complex variable ζ yields

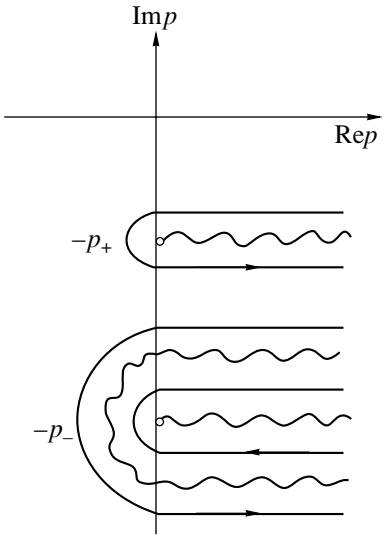

Fig. 5. Integration contour C_2 at $\zeta < 0$.

the following expressions for the transmission and reflection coefficients:

$$T_{++}^{\uparrow} = e^{-2\pi A_{+,2}}, \quad (17)$$

$$T_{+-}^{\uparrow} = 0, \quad (18)$$

$$R_{++}^{\uparrow} = (1-e^{-2\pi A_{+,1}})(1-e^{-2\pi A_{+,2}}), \quad (19)$$

$$R_{+-}^{\uparrow} = e^{-2\pi A_{+,1}}(1-e^{-2\pi A_{+,2}})(1-e^{-2\pi A_{-,1}}), \quad (20)$$

$$T_{--}^{\uparrow} = e^{-2\pi A_{-,2}}, \quad (21)$$

$$T_{-+}^{\uparrow} = (1-e^{-2\pi A_{+,2}})(1-e^{-2\pi A_{-,2}}), \quad (22)$$

$$R_{--}^{\uparrow} = e^{-2\pi(A_{+,1}+A_{+,2})}(1-e^{-2\pi A_{-,1}})(1-e^{-2\pi A_{-,2}}), \quad (23)$$

$$R_{-+}^{\uparrow} = e^{-2\pi A_{+,2}}(1-e^{-2\pi A_{+,1}})(1-e^{-2\pi A_{-,2}}). \quad (24)$$

The expressions obtained generalize Ginzburg's results [1] to the case of waves propagating obliquely to the plasma density gradient and also to arbitrary values of the dimensionless parameter L, which characterizes the density gradient.

To conclude this section, we determine the conditions under which the above analysis is valid. In calculating the asymptotics of the integral in Eq. (8), we took into account the variations of only one term in the expression for $F(p)$, while the remaining terms were assumed constant. This calculation method is valid if $|\zeta| \gg \max(1, LN_\perp^2, LN_\perp\chi)$. (Note that the quantities $LN_\perp^2$ and $2\pi A_{\alpha,i}$, where $i = 1, 2$ and $\alpha = \pm$, are comparable in magnitude.) In fact, this condition on $|\zeta|$ implies that, in the region under consideration, both types of electromagnetic oscillations are circularly

polarized waves that propagate independently of one another.

On the other hand, the basic equation (4) is valid under the condition $LN_\perp \gg |\zeta|$. In the opposite case, the coefficients of the differential equation cannot be approximated by the linear functions of ζ. These two conditions are compatible if $\theta, \chi \ll 1$.

For small angles χ, the critical surface is close to the resonance surface at which the wave equation has a singular point. As was noted in the Introduction, the incident wave near the resonance surface is perturbed so strongly that all possible channels of the wave energy losses may come into play.

Plasma configurations with large values $\chi \approx 1$ are characteristic of tokamaks and stellarators. The propagation of electromagnetic waves through the critical surface in such configurations was studied in [3–5]. It was shown that, the larger the angle χ, the farther the plasma resonance surface is from the critical surface. For $\chi \approx 1$, the resonance surface lies at a distance of about L from the critical surface. As a result, the coupling between different types of waves decreases and the properties of each wave are determined by its dispersion relation. For this reason, the two independent dispersion relations (into which the general dispersion relation splits) should incorporate the variations of both $\varepsilon_\parallel$ and $\varepsilon_\pm$, so that using the method of integral transformations, which underlies our analysis, is inconvenient, because the coefficients of the wave equations are nonlinear functions of ζ.

5. RAY TRAJECTORIES NEAR THE CRITICAL SURFACE

In the vicinity of the critical surface, the quantity N_ζ experiences abrupt variations (Fig. 2). The function $N_\zeta(\zeta, N_\xi)$ satisfies the dispersion relation $D(\mathbf{N}, \zeta) = 0$, which yields the expression $\frac{\partial N_\zeta}{\partial \zeta} = -\frac{\partial D/\partial \zeta}{\partial D/\partial N_\zeta}$. In the case under discussion, the quantity $|\partial N_\zeta/\partial\zeta|$ increases because of the decrease in the quantity $|\partial D/\partial N_\zeta|$, which also enters the expression for the group velocity, $\mathbf{V} = -\frac{\mathbf{\nabla}_\mathbf{N} D}{\partial D/\partial\omega}$. This expression implies that, in the vicinity of the critical surface, the velocities at which the wave packets move along the density gradient become lower. Since, in this region, the ξ-component remains essentially unchanged, the ray trajectories should be stretched preferentially along the critical surface.

More detailed information about the ray trajectories is contained in solutions to the wave equations. From expressions (10), (12), and (13) and similar expressions that can be obtained for $E_\parallel^{(3)}$ and $E_\parallel^{(4)}$, we can see that, at $|\zeta| \gg 1$, the asymptotic solution to the wave equation splits into two solutions:

$$E_\parallel(\zeta) \approx C(\zeta)\exp(i(a_\alpha\zeta + b_\alpha(N_\xi))\ln\zeta), \qquad (25)$$

where $a_\alpha = s_1\sqrt{\varepsilon_\alpha}$ and $b_\alpha = s_2 A_{\alpha,i}$ with $s_{1,2} = \pm 1$. The factor in front of the exponential function is $C(\zeta) \propto 1/\zeta$.

Each of these two solutions describes a quasiclassical wave with the wavenumber

$$N_\zeta(\zeta, N_\xi) \approx a_\alpha + b_\alpha(N_\xi)/\zeta. \qquad (26)$$

Of course, this expression for N_ζ can also be derived from the dispersion relation (5) treated in the vicinity of the critical surface. Accordingly, Eq. (26) can be regarded as an approximate dispersion relation written in the form

$$D(\mathbf{N}, \zeta) \approx a_\alpha + \frac{b_\alpha(N_\xi)}{\zeta} - N_\zeta. \qquad (27)$$

We trace the ray trajectories near the critical surface with the help of Eq. (26). The ray trajectories are described by the equations

$$\begin{aligned} \frac{d\mathbf{r}}{dt} &= \frac{\partial D}{\partial \mathbf{N}}\Big/\frac{\partial D}{\partial\omega}, \\ \frac{d\mathbf{N}}{\partial t} &= -\frac{\partial D}{\partial \mathbf{r}}\Big/\frac{\partial D}{\partial\omega}. \end{aligned} \qquad (28)$$

In the steady state (when we are interested only in the shape of ray trajectories), it is convenient to introduce the time-dependent parameter τ, $\frac{d\tau}{dt} = \left(\frac{\partial D(\mathbf{r}(t), \mathbf{N}(t))}{\partial\omega}\right)^{-1}$, in terms of which Eqs. (28) have the form

$$\begin{aligned} \frac{d\mathbf{r}}{d\tau} &= \frac{\partial D}{\partial \mathbf{N}}, \\ \frac{d\mathbf{N}}{d\tau} &= -\frac{\partial D}{\partial \mathbf{r}}. \end{aligned} \qquad (29)$$

Using expression (27) for D, we obtain from Eqs. (29)

$$\begin{aligned} \dot\zeta &= -1, \\ \dot\xi &= b'_{\alpha, N_\xi}/\zeta, \\ \dot N_\xi &= 0. \end{aligned} \qquad (30)$$

Equations (30) have the integral that describes the shape of the ray trajectories:

$$\zeta = \zeta_0\exp\left(\frac{\xi_0 - \xi}{b'_{\alpha, N_\xi}}\right).$$

The family of ray trajectories is symmetric about the resonance surface illustrated by the line $\zeta = 0$ in Fig. 6. The second equation in Eqs. (30) implies that, for the

same value of N_ξ, the derivative $\dot{\xi}$ has different signs for ray trajectories on different sides of the critical surface. Consequently, we can expect that fairly large displacements (in the ξ-direction) of the ray trajectories of the incident and transmitted waves will cancel each other to a great extent.

6. WAVE BEAMS IN THE VICINITY OF THE CRITICAL SURFACE

A steady wave beam arises from the propagation of perturbations along the ray trajectories. Hence, having established the coupling between the incident and transmitted wave beams, we can, in particular, derive the rules for conjugating the ray trajectories on both sides of this surface.

Above, we have examined the perturbations that are periodic in ξ. Taking into account expressions (25) and (26), we represent such a perturbation in the form

$$E_\parallel(\mathbf{r}, N_\xi) \approx C(\zeta)\exp\left(iN_\xi(\xi-\xi_0) + i\int_{\zeta_0}^{\zeta} d\zeta' N_\zeta(\zeta', N_\xi)\right). \quad (31)$$

The wave beam composed of perturbations (31) can be described as

$$E_\parallel(\mathbf{r}) = \int dN_\xi E_\parallel(\mathbf{r}, N_\xi)F(N_\xi). \quad (32)$$

In the simplest case of a Gaussian beam,

$$F(N_\xi) = \exp(-(N_\xi - N_{\xi 0})^2\Delta L^2),$$

we have

$$E_\parallel(\mathbf{r}) \approx \frac{\sqrt{\pi}}{\Delta L_0}\exp\left(iN_{\xi 0}(\xi-\xi_0) + i\int_{\zeta_0}^{\zeta} d\zeta' N_\zeta(\zeta', N_{\xi 0}) - \frac{1}{4(\Delta L_0)^2}\left(\xi-\xi_0 + \int_{\zeta_0}^{\zeta} d\zeta' \frac{\partial N_\zeta(\zeta', N_{\xi 0})}{\partial N_{\xi 0}}\right)^2\right), \quad (33)$$

where $(\Delta L_0)^2 = (\Delta L)^2 - \frac{i}{2}\int_{\zeta_0}^{\zeta} d\zeta' \frac{\partial^2 N_\zeta}{\partial N_{\xi 0}^2}$. The second term in the expression for $(\Delta L_0)^2$ accounts for the diffractive spreading of the beam.

According to (33), the wave beam is narrowest in the direction perpendicular to the group velocity: $l = \frac{V_{g\zeta}}{V_g}\frac{|\Delta L_0|^2}{\Delta L}$, where $V_{g\zeta}$ is the projection of the group velocity V_g onto the ζ-axis. Since $V_{g\zeta} \longrightarrow 0$ when approaching the critical surface, the wave beam contracts in the ζ-direction and expands in the $-\xi$-direction.

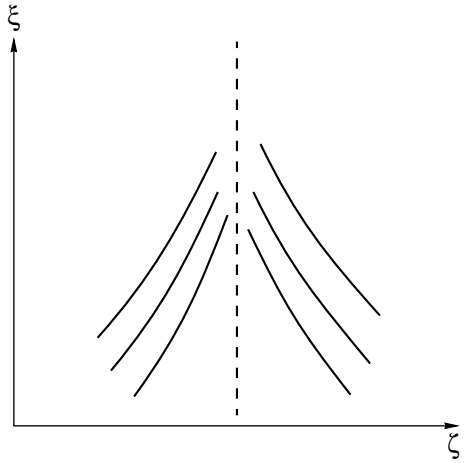

Fig. 6. General picture of ray trajectories in the vicinity of the critical surface.

Expression (15) for the ζ-component of the energy flux density allows us to represent the total energy flux in the beam as

$$P_\alpha = \frac{\zeta^2}{\varepsilon_\alpha^{1/2} N_\perp^2} J,$$

where $J = \int d\xi\, |E_\parallel(\mathbf{r})|^2$. We can readily take the integral J to obtain

$$P_\alpha = \frac{2^{1/2}\pi^{3/2}}{\varepsilon_\alpha^{1/2} N_\perp^2 \Delta L}. \quad (34)$$

Applying the Landau circumvention rule to solve the wave equation, we can find a solution describing the waves whose polarization does not change as they traverse the critical surface. We choose the Landau contour that lies below the singular point in the complex plane to obtain the following conjugation rule for the function $\ln\zeta$ in expression (25), e.g., when passing over from positive to negative values of the variable ζ:

$$\ln\zeta \longrightarrow \ln|\zeta| + i\pi.$$

Accordingly, the waves that have crossed the critical surface are described by the solution

$$E_\parallel(\mathbf{r}, N_\xi) \approx C(\zeta)\exp\left(-\pi b_\alpha(N_\xi) - 2ia\zeta_0 + iN_\xi(\xi-\xi_0) + i\int_{-\zeta_0}^{\zeta} d\zeta' N_\zeta(\zeta', N_\xi)\right). \quad (35)$$

The spatial structure of the transmitted beam is very sensitive to the beam width. For wide beams such that $\Delta L \gg L^{1/2}$, we obtain

$$E_\parallel(\mathbf{r}) \approx \frac{\sqrt{\pi}}{\Delta L_1}\exp\Bigg(-\pi b_\alpha(N_{\xi 0}) - 2ia\xi_0 + iN_{\xi 0}(\xi-\xi_0) + i\int\limits_{-\zeta_0}^{\zeta} d\zeta' N_\zeta(\zeta', N_{\xi 0}) - \frac{1}{4(\Delta L_1)^2}\left(\xi-\xi_0+\int\limits_{-\zeta_0}^{\zeta} d\zeta'\frac{\partial N_\zeta(\zeta', N_{\xi 0})}{\partial N_{\xi 0}}\right)^2\Bigg),$$

where $(\Delta L_1)^2 = (\Delta L)^2 - \frac{i}{2}\int_{-\zeta_0}^{\zeta} d\zeta' \frac{\partial^2 N_\zeta}{\partial N_{\xi 0}^2}$.

The ray trajectories are the trajectories of infinitely narrow wave beams. The propagation of a finite-width beam can naturally be described in terms of its central trajectory. In the case at hand, the central trajectory of the transmitted beam,

$$\xi - \xi_0 + \int\limits_{-\zeta_0}^{\zeta} d\zeta' \frac{\partial N_\zeta}{\partial N_{\xi 0}} = 0,$$

and the central trajectory of the incident beam are mirror-image about the resonance surface. Recall that the ζ-coordinate is measured from the resonance surface rather than from the critical surface. Therefore, we can conclude that the transmitted ray trajectories and incident ray trajectories are in a sense mirror images about the resonance surface.

If $\Delta L \ll L^{1/2}$, then, even for $b(N_{\xi 0}) \geq 1$, the Fourier spectrum of the beam extends to the values $N_{\xi,\alpha} \approx \chi\sqrt{\varepsilon_\alpha}$, which correspond to wave propagation along the magnetic field. In this case, the critical surface acts to filter out the waves with $N_\xi \approx N_{\xi,\alpha}$. As a result, the transmitted waves also give rise to a Gaussian beam propagating in the magnetic field direction:

$$E_\parallel(\mathbf{r}) \approx \frac{\sqrt{\pi}}{\Delta L_2}\exp\Big(-(\Delta L)^2(N_{\xi,\alpha}-N_{\xi 0})^2 - 2ia\xi_0 + iN_{\xi,\alpha}(\xi-\xi_0) + i\int\limits_{-\zeta_0}^{\zeta} d\zeta' N_\zeta(\zeta', N_{\xi,\alpha}) - \frac{1}{4(\Delta L_2)^2}\left(\xi-\xi_0+\int\limits_{-\zeta_0}^{\zeta} d\zeta'\frac{\partial N_\zeta(\zeta', N_{\xi,\alpha})}{\partial N_{\xi,\alpha}}\right)^2\Bigg),$$

where $(\Delta L_2)^2 = \frac{\pi}{4} L\sqrt{\varepsilon_\alpha} - \frac{i}{2}\int_{-\zeta_0}^{\zeta} d\zeta' \frac{\partial^2 N_\zeta}{\partial N_{\xi,\alpha}^2}$. It is natural to conclude that the beam spreads out in space as the Fourier spectrum narrows.

We can easily find the total energy flux in the transmitted beam for an arbitrary ratio between ΔL and $L^{1/2}$:

$$P_\alpha = \frac{2^{1/2}\pi^{3/2}F_\alpha^{1/2}}{\varepsilon_\alpha^{1/2} N_\perp^2 \Delta L}\exp(-2\pi b_\alpha(N_{\xi 0})F_\alpha), \qquad (36)$$

where $F_\alpha = \dfrac{(\Delta L)^2}{(\Delta L)^2 + \pi L\varepsilon_\alpha^{1/2}/4}$.

A comparison between (34) and (36) yields the following expression for the transmission coefficient of the wave beam whose polarization does not change as it crosses the critical surface:

$$T_{\alpha\alpha,0} = F_\alpha^{1/2}\exp(-2\pi b_\alpha(N_{\xi 0})F_\alpha).$$

The reflected waves and the transmitted waves whose polarization changes as they traverse the critical surface can be analyzed in a similar way. Omitting a detailed analysis, we only note that the "ray" trajectories of these waves (i.e., the central trajectories of the waves with $\Delta L \gg L^{1/2}$) are shifted along the ξ-axis from the ray trajectory of the incident waves. In fact, different types of electromagnetic waves are described by formulas with different factors $\Psi^{(i)}(N_\xi) = \Gamma^{-1}(iA_{\alpha,\beta})\Phi^{(i)}$ (see Section 3), which are responsible for the shift of the wave beam by $\Delta\xi^{(i)} = \dfrac{\partial}{\partial N_{\xi 0}}\arg\Psi^{(i)}$ along the ξ-axis and should be retained in expressions analogous to (34) and (31). If the type of incident wave (i) differs from the type of transmitted wave (j), then the corresponding ray trajectories will be shifted by $\Delta\xi^{(i)} - \Delta\xi^{(j)}$.

Note also that, in a real situation, the surfaces of equal density (and, accordingly, the critical surface) are curved. However, this circumstance can be neglected in evaluating the transmission coefficient for a wave beam if the radius of curvature is sufficiently large: $R \gg L^{1/2}\Delta L$.

7. NUMERICAL EXAMPLE

Our analysis shows that, in the region $LN_\perp \gg |\zeta| \gg \max(1, LN_\perp^2)$, the ray trajectories of the incident waves with $\Delta L \gg L^{1/2}$ and of the transmitted waves whose polarization does not change as they cross the critical surface are mirror images about the plasma resonance surface. The ξ-components of the refractive indices of the transmitted and incident waves coincide, while their ζ-components differ by $2b/\zeta$ (see Section 5).

The ray trajectories are known to be uniquely determined by the value of the refractive index at the initial point. As the initial point, we can choose an arbitrary

point where the ray trajectory of the incident waves is specularly reflected from the critical surface, in which case the initial value of the refractive index is determined by the rule outlined above. If the analysis performed in the previous section is consistent, then the ray trajectories of the transmitted waves that emerge from different initial points at the critical surface should approach each other.

In order to confirm this conclusion, we numerically traced the ray trajectories of the incident and transmitted waves with right-hand polarization in a plane plasma slab such that $\left(\frac{\omega_{pe}}{\omega}\right)^2 = 1 - \frac{x}{L_x} + \frac{z}{L_z}$. The results to be presented were computed for $L_x = 2 \times 10^3$ and $L_z = 10^2$ ($\chi = 0.05$). The magnetic field was assumed to be uniform and aligned with the z-axis. We also set $\omega_e = 2\omega$. The rays were assumed to come from the point ($x = 0$, $z = -30$) at the angles $\theta = \pm 0.0375$ to the z-axis. The crossing of the critical surface was modeled for three values of $\zeta = -2, -3$, and -5. Accordingly, for each of the incident rays, we traced three transmitted rays. In accordance with the above analysis, they should approach each other. In fact, the three rays that arise from the ray trajectory emerging at the angle $\theta = 0.0375$ essentially coincide (see Fig. 7). On the other hand, the transmitted rays that arise from the ray trajectory emerging at the angle $\theta = -0.0375$ slightly diverge. The discrepancy between these two cases stems from the asymmetry of the system around the horizontal axis ($L_x \neq \infty$). This asymmetry leads to slightly different coefficients of the transmission of waves through the critical surface for the upper ($T^{\uparrow}_{-,-} \approx 0.65$) and lower ($T^{\uparrow}_{-,-} \approx 0.55$) rays. The divergence of the rays in Fig. 7 seems to be quite natural because, in the above analytic treatment, we take into account only the first term in the asymptotic solution to the wave equation. Recall that the above analysis is valid under the condition $\sqrt{L} \gg |\zeta| \gg 1$. At larger values of L, the interval of the permissible values of $|\zeta|$ broadens, so that we are more justified in applying our model approach. In this case, we can expect that the divergence of rays will somewhat reduce. This expectation is supported by the results calculated for $L_z = 10^3$. The value $L_x = 6.7 \times 10^5$ was chosen from the condition for the transmission coefficient to coincide approximately with that obtained in the first numerical example. The ray trajectories were assumed to come from the point ($x = 0$, $z = -300$) at angles $\theta = \pm 0.0125$ to the magnetic field. The incident and transmitted trajectories were conjugated at $\zeta = -5, -10$, and -15. Our calculations show that, as expected, the larger the parameter L, the smaller the relative spread in the ray trajectories. Thus, in the first example ($L \approx 10^2$), the rays that come from the point with $z = 30$ and correspond to the lower incident ray trajectory diverge at most by $\Delta x \approx 0.3$, whereas, in the second example ($L \approx 10^3$), the divergence of the transmitted rays emerging from the point with $z = 300$ does not exceed $\Delta x \approx 1.5$. Our calculations also confirm that, as expected, the larger the angle θ, the larger the divergence of the ray trajectories. As a result, the coefficient $A_{-,i}$ increases and, accordingly, the transmission coefficient becomes smaller.

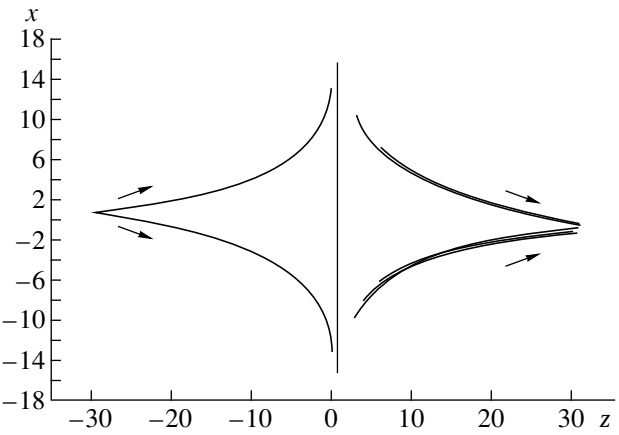

Fig. 7. Representative ray trajectories calculated from the exact dispersion relation and traced through the critical surface according to the conjugation rule outlined in the paper.

8. CONCLUSION

We have analyzed the propagation of electromagnetic waves through the critical surface in the case of small angles between the magnetic field and the plasma density gradient. We have considered unbounded waves that are periodic in the direction perpendicular to the density gradient and wave beams. We have found that the ray trajectory of a wide transmitted beam and the ray trajectory of an incident beam are mirror images about the resonance surface. A narrow wave beam that passes through the resonance surface generates a beam propagating along the magnetic field.

ACKNOWLEDGMENTS

I am grateful to V.A. Zhil'tsov, A.V. Zvonkov, A.Yu. Kuyanov, and A.A. Skovoroda for fruitful discussions.

REFERENCES

1. V. L. Ginzburg, *The Propagation of Electromagnetic Waves in Plasmas* (Nauka, Moscow, 1967; Pergamon, Oxford, 1970).
2. J. Preinhalter and V. Kopecky, J. Plasma Phys. **10**, 1 (1973).
3. V. E. Golant and A. D. Piliya, Usp. Fiz. Nauk **104**, 413 (1971) [Sov. Phys. Usp. **14**, 413 (1971)].

4. N. S. Erokhin and S. S. Moiseev, in *Reviews of Plasma Physics*, Ed. by M. A. Leontovich (Atomizdat, Moscow, 1973; Consultants Bureau, New York, 1979), Vol. 7.
5. A. A. Zharov, Fiz. Plazmy **10**, 1109 (1984) [Sov. J. Plasma Phys. **10**, 642 (1984)].
6. M. D. Tokman, Fiz. Plazmy **11**, 1205 (1985) [Sov. J. Plasma Phys. **11**, 689 (1985)].
7. J. Mjolhus, J. Plasma Phys. **31**, 7 (1984).
8. H. P. Laqua, W7-team, and ECRH-group, Plasma Phys. Controlled Fusion **41**, A273 (1999).
9. V. A. Zhil'tsov, A. A. Skovoroda, and A. G. Shcherbakov, Fiz. Plazmy **17**, 785 (1991) [Sov. J. Plasma Phys. **17**, 456 (1991)]; V. A. Zhil'tsov, A. A. Skovoroda, and A. V. Timofeev, Fiz. Plazmy **17**, 771 (1991) [Sov. J. Plasma Phys. **17**, 447 (1991)]; V. A. Zhil'tsov, A. Yu. Kuyanov, A. A. Skovoroda, and A. V. Timofeev, Fiz. Plazmy **20**, 267 (1994) [Plasma Phys. Rep. **20**, 242 (1994)].
10. *Handbook of Mathematical Functions*, Ed. by M. Abramowitz and I. A. Stegun (Dover, New York, 1971; Nauka, Moscow, 1979).

Translated by O.E. Khadin

Plasma Physics Reports, Vol. 26, No. 10, 2000, pp. 831–839. Translated from Fizika Plazmy, Vol. 26, No. 10, 2000, pp. 885–893.

PLASMA OSCILLATIONS AND WAVES

Effect of a Strong Monochromatic Electromagnetic Wave with Circular Polarization on One-Dimensional Wake Waves in Plasma

H. B. Nersisyan* and S. S. Elbakian**

**Institute of Radiophysics and Electronics, Academy of Sciences of Armenia, Ashtarak-2, 378410 Armenia*

***Yerevan Physical Institute, Yerevan, 375036 Armenia*

Received September 9, 1999; in final form, December 14, 1999

Abstract—A study is made of the excitation of wake waves by a one-dimensional bunch of charged particles in an electron plasma in the presence of an intense monochromatic pump wave with circular polarization. In the main state (in the absence of a bunch), the interaction between a pump wave and a plasma is described by the Maxwell equations and the nonlinear relativistic hydrodynamic equations for a cold plasma. The excitation of linear waves by a one-dimensional bunch is investigated against a cold plasma background. It is shown that, in a certain range of the parameter values of the bunch, pump wave, and plasma, the amplitude of the excited transverse waves grows as the energy of the bunch particles increases until the relativistic factor of the bunch reaches a certain threshold value above which the transverse wave amplitude becomes essentially independent of the bunch particle energy and grows as the intensity and frequency of the pump wave increase. The amplitude and wavelength of the longitudinal field, which is shown to depend weakly on the energy of the bunch particles, grows with increasing the pump wave intensity. © *2000 MAIK "Nauka/Interperiodica".*

1. INTRODUCTION

Plasma-based methods of charged particle acceleration, which have been actively developed over the past decade, occupy an important place among novel acceleration schemes (see, e.g., [1, 2] and the literature cited therein). The excitation of wake waves by charged-particle bunches is one of the ways of generating strong (up to $E \sim 1$ GeV/m) electromagnetic fields in plasmas. The induced wake fields can serve not only to accelerate charged particles but also to focus electron (positron) bunches [3] with the aim of generating high-density beams and ensuring high luminosity in the next generation of linear colliders.

Many papers have been devoted to the linear theory of one-dimensional wake waves [3–11]. The nonlinear theory of these waves was developed in [12–18]. An important consequence of the nonlinear theory is that the maximum strength of the induced wake field is equal to $E_{\max} = (mu\omega_p/e)[2(\gamma - 1)]^{1/2}$ and is achieved in the range $n_b/n_0 < 1/(2 + 1/\gamma)$, where ω_p is the electron plasma frequency; n_b and n_0 are the bunch and plasma densities, respectively; $\gamma = (1 - \beta^2)^{-1/2}$ is the relativistic factor of a bunch; $\beta = u/c$; and u is the bunch velocity.

In the nonrelativistic limit ($\gamma \approx 1$, $\beta \ll 1$) [17], the maximum electric field is equal to $E_{\max} \approx 2mu\omega_p/e$. In the linear approximation, when $n_b/n_0 \ll 1$, we have $E_{\max} \approx (2mu\omega_p/e)(n_b/n_0)$ for arbitrary γ.

In this paper, we study how the field of a circularly polarized electromagnetic wave of arbitrary intensity (including the case when the electron oscillatory velocity in the pump field is close to the speed of light) affects the excitation of electromagnetic wake waves by a one-dimensional relativistic electron bunch in a cold plasma. The pump field amplitude is described by the dimensionless parameter $A = eE_0/mc\omega_0$, where E_0 and ω_0 are the wave amplitude and frequency, respectively. One can obtain an exact solution to the Maxwell equations and the nonlinear hydrodynamic equations describing the interaction between a circularly polarized electromagnetic wave and a plasma [18, 19] and derive an exact dispersion relation for waves propagating in the same direction as the pump wave [19, 20]. The parametric instability of a plasma in the electromagnetic field of a circularly polarized wave was thoroughly investigated in earlier papers (see [19, 21, 22] and the literature cited therein). Max and Perkins [21] studied the low-frequency aperiodic instability of a plasma in the dipole approximation. When analyzing the plasma instability in the field of a strong electromagnetic wave, Kalmikov and Kotsarenko [19] showed that the relativistic character of the electron motion plays an important role in the parametric excitation of nonpotential plasma oscillations by a transverse electromagnetic wave at an arbitrary value of the pump field amplitude.

In this paper, we clarify the role played by a strong electromagnetic field with circular polarization in the excitation of one-dimensional linear wake fields in a plasma. We describe the pump-wave–plasma interaction in the absence of a bunch by the Maxwell equations and nonlinear hydrodynamic equations in the cold

1063-780X/00/2610-0831$20.00

plasma approximation. In this case, the plasma can be in a spatially homogeneous state [18, 19]. Then, assuming that a one-dimensional bunch propagating in the plasma distorts this state only slightly, we apply the perturbation theory to derive equations for the induced fields and for the electron plasma density and velocity.

2. BASIC EQUATIONS

Assuming that the oscillatory velocity of the plasma electrons in an external field is much higher than the electron thermal velocity and the pump frequency ω_0 is far above the electron–ion collision frequency, we start with the following basic set of equations, which includes the Maxwell equations and the relativistic hydrodynamic equations of motion for a cold electron plasma:

$$\nabla \times \mathbf{B} = \frac{1}{c}\frac{\partial \mathbf{E}}{\partial t} - \frac{4\pi e}{c} n\mathbf{v} - \frac{4\pi e}{c}\mathbf{u} n_b(\xi), \quad (1)$$

$$\nabla \times \mathbf{E} = -\frac{1}{c}\frac{\partial \mathbf{B}}{\partial t}, \quad \nabla \mathbf{B} = 0, \quad (2)$$

$$\nabla \mathbf{E} = -4\pi e(n - n_0) - 4\pi e n_b(\xi), \quad (3)$$

$$\frac{\partial \mathbf{v}}{\partial t} + (\mathbf{v}\nabla)\mathbf{v} = -\frac{e}{m}\sqrt{1 - \frac{\mathbf{v}^2}{c^2}}\left[\mathbf{E} + \frac{1}{c}\mathbf{v}\times\mathbf{B} - \frac{\mathbf{v}}{c^2}(\mathbf{v}\mathbf{E})\right], \quad (4)$$

$$\frac{\partial n}{\partial t} + \nabla(n\mathbf{v}) = 0, \quad (5)$$

where $\xi = z - ut$, n_0 is the unperturbed electron plasma density, and $n_b(\xi)$ is the density of a one-dimensional bunch propagating with the velocity $\mathbf{u}$ (such that $\mathbf{u} = u\mathbf{e}_z$, $|\mathbf{e}_z| = 1$) in a plasma. Since we are interested in relativistic bunches, we neglect oscillations of the bunch electrons in an electromagnetic pump wave.

In the field of a circularly polarized electromagnetic wave propagating along the z-axis, the plasma can be in a spatially homogeneous equilibrium state, in which the electromagnetic field and the electron velocity are given by the relationships [18, 19]

$$\mathbf{E}_0 = E_0(\mathbf{e}_x\cos\zeta + \mathbf{e}_y\sin\zeta), \quad E_{0z} = 0, \quad (6)$$

$$\mathbf{B}_0 = \frac{k_0 c}{\omega_0}E_0(-\mathbf{e}_x\sin\zeta + \mathbf{e}_y\cos\zeta), \quad B_{0z} = 0, \quad (7)$$

$$\mathbf{v}_e = c\beta_e(-\mathbf{e}_x\sin\zeta + \mathbf{e}_y\cos\zeta), \quad v_{ez} = 0, \quad (8)$$

where $\zeta = \omega_0 t - k_0 z$, $k_0 = (\omega_0/c)\sqrt{\varepsilon(\omega_0)}$, $\varepsilon(\omega) = 1 - \omega_L^2/\omega^2$, $\omega_L^2 = \omega_p^2\sqrt{1-\beta_e^2}$, $\beta_e = v_e/c$, $A = eE_0/mc\omega_0$,

$$v_e = c\frac{A}{\sqrt{1 + A^2}}, \quad (9)$$

$\omega_p^2 = 4\pi n_0 e^2/m$ is the plasma frequency, and c is the speed of light in a vacuum.

We consider small perturbations that are driven in the plasma by an electron beam with density n_b such that $n_b \ll n_0$. We represent all of the quantities in the form $f = f_0 + f'$, where f_0 stands for the unperturbed quantities in (6)–(9). Linearizing Eqs. (1)–(5) yields the following equations for the perturbed quantities f':

$$\nabla \times \mathbf{B}' = \frac{1}{c}\frac{\partial \mathbf{E}'}{\partial t} - \frac{4\pi e}{c}(n_0\mathbf{v}' + n'\mathbf{v}_e) - \frac{4\pi e}{c}\mathbf{u} n_b(\xi), \quad (10)$$

$$\nabla \times \mathbf{E}' = -\frac{1}{c}\frac{\partial \mathbf{B}'}{\partial t}, \quad \nabla \mathbf{B}' = 0, \quad (11)$$

$$\nabla \mathbf{E}' = -4\pi e n' - 4\pi e n_b(\xi), \quad (12)$$

$$\frac{\partial \mathbf{v}'}{\partial t} + (\mathbf{v}_e\nabla)\mathbf{v}' + (\mathbf{v}'\nabla)\mathbf{v}_e = -\frac{e}{m}\sqrt{1-\beta_e^2} \times\left[\mathbf{E}' + \frac{1}{c}\mathbf{v}_e\times\mathbf{B}' + \frac{1}{c}\mathbf{v}'\times\mathbf{B}_0 - \frac{\mathbf{v}_e}{c^2}(\mathbf{v}_e\mathbf{E}' + \mathbf{v}'\mathbf{E}_0)\right] + \frac{e(\mathbf{v}_e\mathbf{v}')}{mc^2\sqrt{1-\beta_e^2}}\left[\mathbf{E}_0 + \frac{1}{c}\mathbf{v}_e\times\mathbf{B}_0\right], \quad (13)$$

$$\frac{\partial n'}{\partial t} + n_0\nabla\mathbf{v}' + (\mathbf{v}_e\nabla)n' = 0. \quad (14)$$

These are partial differential equations with coefficients periodic in ζ.

We switch from the x- and y-components of the fields and electron plasma velocities to the new variables:

$$\begin{pmatrix} E^\pm \\ B^\pm \\ w^\pm \end{pmatrix} = \begin{pmatrix} E_x' \pm iE_y' \\ B_x' \pm iB_y' \\ v_x' \pm iv_y' \end{pmatrix} = \begin{pmatrix} \mathscr{E}^\pm \\ \mathscr{B}^\pm \\ \mathscr{V}^\pm \end{pmatrix}\exp(i\zeta). \quad (15)$$

In other words, we pass over to a rotating frame of reference associated with the pump wave. Transformation (15) converts Eqs. (10)–(14) to the following inhomogeneous ordinary differential equations with constant coefficients:

$$\frac{1}{\gamma^2}\frac{\partial^2\mathscr{E}^\pm}{\partial\xi^2} \mp 2i\left(k_0 - \beta\frac{\omega_0}{c}\right)\frac{\partial\mathscr{E}^\pm}{\partial\xi} - \left(k_0^2 - \frac{\omega_0^2}{c^2}\right)\mathscr{E}^\pm = \frac{4\pi e n_0}{c}\left(\beta\frac{\partial\mathscr{V}^\pm}{\partial\xi} \mp i\frac{\omega_0}{c}\mathscr{V}^\pm + \omega_0\beta_e\frac{n'}{n_0} \pm \frac{i\beta_e}{n_0}u\frac{\partial n'}{\partial\xi}\right), \quad (16)$$

$$\frac{1}{\gamma^2}\frac{\partial^2\mathcal{B}^\pm}{\partial\xi^2} \mp 2i\left(k_0 - \beta\frac{\omega_0}{c}\right)\frac{\partial\mathcal{B}^\pm}{\partial\xi} - \left(k_0^2 - \frac{\omega_0^2}{c^2}\right)\mathcal{B}^\pm = \pm\frac{4\pi e i n_0}{c}\left(\frac{\partial\mathcal{V}^\pm}{\partial\xi} \mp ik_0\mathcal{V}^\pm + k_0 v_e\frac{n'}{n_0} \pm \frac{iv_e}{n_0}\frac{\partial n'}{\partial\xi}\right), \quad (17)$$

$$\frac{\partial^2\mathcal{V}^\pm}{\partial\xi^2} + \frac{\omega_0^2}{u^2}\mathcal{V}^\pm = \frac{e}{mu}\sqrt{1-\beta_e^2} \times\left[\left(1-\frac{\beta_e^2}{2}\right)\left(\frac{\partial\mathscr{E}^\pm}{\partial\xi} \pm i\frac{\omega_0}{u}\mathscr{E}^\pm\right) + \frac{\beta_e^2}{2}\left(\frac{\partial\mathscr{E}^\mp}{\partial\xi} \mp i\frac{\omega_0}{u}\mathscr{E}^\mp\right)\right], \quad (18)$$

$$\frac{\partial E_z'}{\partial\xi} = -4\pi en' - 4\pi en_b(\xi), \quad B_z' = 0, \quad (19)$$

$$\frac{\partial n'}{\partial\xi} = \frac{n_0 e}{mu^2}\sqrt{1-\beta_e^2} \times\left[E_z' - \frac{\beta_e}{2}(\mathcal{B}^+ + \mathcal{B}^-) + \frac{k_0 E_0}{2\omega_0}(\mathcal{V}^+ + \mathcal{V}^-)\right], \quad (20)$$

$$v_z' = u\frac{n'(\xi)}{n_0}, \quad (21)$$

where $\beta = u/c$ and $\gamma^{-2} = 1 - \beta^2$. In deriving these equations, we assumed that all of the quantities depend solely on the variable $\xi = z - ut$. Equations (16)–(21) imply that, due to the presence of a pump wave in the plasma, the induced fields and the electron plasma velocities are parametrically coupled to each other. The right-hand side of Eq. (20) for the perturbed charge density contains not only the longitudinal component of the induced electric field but also the Lorentz force. The second term on the right-hand side of this equation stems from the interaction of plasma electrons moving at the unperturbed velocities with the perturbed magnetic field, and the third term accounts for the interaction of plasma electrons moving at the perturbed velocities with the unperturbed magnetic field of the pump wave. Equations (16)–(21) also imply that the coefficient β_e of the second term in square brackets in Eq. (20) approaches 1/2 and the coefficient of the third term increases as the pump wave becomes more intense. Below, we are going to examine solutions to Eqs. (16)–(21).

3. GREEN'S FUNCTION

To solve Eqs. (16)–(21), we need to derive equations for each of the quantities n', E_z', $\mathcal{V}^\pm$, $\mathcal{B}^\pm$, and $\mathscr{E}^\pm$. We solve Eqs. (16)–(21) by expanding the perturbed quantities in Fourier integrals over the variable ξ. After some manipulations, we obtain

$$\begin{pmatrix} E_z'(\xi) \\ \mathscr{E}^+(\xi) \end{pmatrix} = \int_{-\infty}^{+\infty} d\xi' n_b(\xi')\begin{pmatrix} G_z^{(e)}(\xi'-\xi) \\ G_\perp^{(e)}(\xi'-\xi) \end{pmatrix}. \quad (22)$$

Here, Green's functions $G_z^{(e)}$ and $G_\perp^{(e)}$ for the quantities E_z' and $\mathscr{E}^+$ have the form

$$G_z^{(e)}(s) = -2ie\int_{-\infty}^{+\infty}\frac{dk}{k}\frac{D_1(k,\omega)}{D(k,\omega)}\exp(iks), \quad (23)$$

$$G_\perp^{(e)}(s) = -\frac{2e\beta_e\omega_L^2}{c}\int_{-\infty}^{+\infty} dk(ku+\omega_0) \times\frac{R_{-1}(k,\omega)}{D(k,\omega)}\exp(iks), \quad (24)$$

where $\omega = ku$. According to Eqs. (11), the induced magnetic field is related to the transverse electric field as

$$\mathcal{B}^\pm(\xi) = \pm\frac{c}{u}\left\{i\mathscr{E}^\pm(\xi) + \left(\frac{\omega_0}{u} - k_0\right)\int_{-\infty}^{\xi} d\xi'\exp\left[i\frac{\omega_0}{u}(\xi'-\xi)\right]\mathscr{E}^\pm(\xi')\right\}, \quad (25)$$

where we introduce the notation

$$R_{\pm1}(k,\omega) = (k\pm k_0)^2 - \frac{(\omega\pm\omega_0)^2}{c^2}\varepsilon(\omega\pm\omega_0), \quad (26)$$

$$D_1(k,\omega) = \omega^2 R_1(k,\omega)R_{-1}(k,\omega) + \frac{\beta_e^2\omega_L^2}{2}\left(k^2 - \frac{\omega^2}{c^2}\right)[R_1(k,\omega) + R_{-1}(k,\omega)], \quad (27)$$

$$D(k,\omega) = \omega^2\varepsilon(\omega)R_1(k,\omega)R_{-1}(k,\omega) + \frac{\beta_e^2\omega_L^2}{2}\left(k^2 - \frac{\omega^2}{c^2}\varepsilon(\omega)\right)[R_1(k,\omega) + R_{-1}(k,\omega)]. \quad (28)$$

The transverse components of the induced electric and magnetic fields can be found from expressions (15) by taking either a real or an imaginary part of the complex quantities $\mathscr{E}^+$ and $\mathcal{B}^+$. As a result, we obtain

$$\begin{pmatrix} E_x'(z,t) \\ B_x'(z,t) \end{pmatrix} = \begin{pmatrix} E_r(\xi) \\ B_r(\xi) \end{pmatrix}\cos\zeta - \begin{pmatrix} E_i(\xi) \\ B_i(\xi) \end{pmatrix}\sin\zeta, \quad (29)$$

$$\begin{pmatrix} E_y'(z,t) \\ B_y'(z,t) \end{pmatrix} = \begin{pmatrix} E_r(\xi) \\ B_r(\xi) \end{pmatrix}\sin\zeta + \begin{pmatrix} E_i(\xi) \\ B_i(\xi) \end{pmatrix}\cos\zeta, \quad (30)$$

where

$$\begin{pmatrix} E_r(\xi) \\ B_r(\xi) \end{pmatrix} = \mathrm{Re}\begin{pmatrix} \mathscr{E}^+(\xi) \\ \mathscr{B}^+(\xi) \end{pmatrix},$$
$$\begin{pmatrix} E_i(\xi) \\ B_i(\xi) \end{pmatrix} = \mathrm{Im}\begin{pmatrix} \mathscr{E}^+(\xi) \\ \mathscr{B}^+(\xi) \end{pmatrix}. \quad (31)$$

Hence, expressions (29) and (30) for the transverse components of the induced fields describe modulational perturbations in the plasma. As an example, we represent the component E_y' in the form

$$E_y'(z,t) = E_{\perp 0}(\xi)\sin(\zeta + \psi_0(\xi)), \quad (32)$$

where $E_{\perp 0}(\xi) = \sqrt{E_r^2(\xi) + E_i^2(\xi)}$ is the amplitude of the perturbations and $\psi_0(\xi) = \arctan[E_i(\xi)/E_r(\xi)]$ is their phase shift. The expressions for the other perturbed quantities are analogous to (32). In the rest frame of the bunch, expression (32) describes a transverse harmonic wave. In an arbitrary frame of reference, expression (32) describes a modulated transverse wave whose profile is determined by the function $E_{\perp 0}(\xi)$. Note that, in the absence of a pump wave ($\beta_e = 0$), the transverse components of the perturbed quantities vanish and Eq. (19) and its solution [the first expression in (22) taken with expressions (27) and (28)] pass over to the familiar formulas for one-dimensional linear fields.

Now, we proceed to a calculation of Green's functions defined in (23) and (24). The poles of the integrals in (23) and (24) are the roots of the dispersion relation $D(k, \omega) = 0$. In the general case (i.e., when the Cherenkov resonance condition $\omega = ku$ is not imposed), this dispersion relation was investigated in detail by Kalmikov and Kotsarenko [19]. In the absence of a pump wave ($\beta_e = 0$), Eq. (28) passes over to the dispersion relations for ordinary plasma waves, $\omega = \omega_p$, and for transverse (electromagnetic) waves, $\omega^2 = \omega_p^2 + k^2c^2$. The presence of a pump wave ($\beta_e \neq 0$) gives rise to coupled waves in a plasma. If the pump wave is sufficiently weak ($\beta_e \ll 1$), then the growth rate of the coupled waves increases linearly with β_e. Consequently, the coupled waves are parametrically unstable down to $\beta_e = 0$. However, when the plasma density is not too high ($\omega_p < 10^{13}\ \mathrm{s}^{-1}$; i.e., $n_0 < 10^{17}\ \mathrm{cm}^{-3}$) and the pump frequency ω_0 is in the optical range ($\omega_0 \sim 10^{15}\ \mathrm{s}^{-1}$), the time interval over which a relativistic bunch interacts with a plasma is much shorter than the time scale on which the parametric instability develops [19], so that we can neglect the effect of the parametric instability on the excitation of wake waves.

Under the Cherenkov resonance condition $\omega = ku$, Eq. (28) gives the dispersion relation

$$\left(k^2 - \frac{\omega_L^2}{u^2}\right)\left[k^2 - 4\gamma^4\left(k_0 - \beta\frac{\omega_0}{c}\right)^2\right] + \frac{\beta_e^2\omega_L^2}{u^2}\left(k^2 + \gamma^2\frac{\omega_L^2}{c^2}\right) = 0. \quad (33)$$

We introduce the dimensionless wave vector λ, which is related to k by $k = (\omega_L/u)\lambda$, in order to represent the solutions to Eq. (33) in the form

$$\lambda_\pm^2 = \frac{1}{2a^4} + 2\beta^2\gamma^4F^2 \pm \sqrt{\left(\frac{1}{2a^4} + 2\beta^2\gamma^4F^2\right)^2 - \beta^2\gamma^2\left(\frac{a^4-1}{a^4} + 4\gamma^2F^2\right)}, \quad (34)$$

where

$$F = \sqrt{a^2\Delta^2 - 1} - \beta a\Delta, \quad (35)$$

$\Delta = \omega_0/\omega_p$, and $a^2 = \sqrt{1 + A^2}$. The character of the solutions to Eq. (33) (and, accordingly, the electron plasma velocity and the nature of the induced fields) is largely governed by the sign of the expression under the square root in formula (34). We denote the regions where this expression is positive and negative by I and III, respectively. The boundary between these regions is denoted by II. To determine this boundary, we equate the expression at hand to zero and obtain

$$\Delta = \frac{\gamma}{a}(\sqrt{1 + \gamma^2F_+^2} \pm \beta\gamma F_+) \quad \text{for} \quad a > 1, \quad (36)$$

$$\Delta = \frac{\gamma}{a}(\sqrt{1 + \gamma^2F_-^2} \pm \beta\gamma F_-) \quad \text{for} \quad 1 < a < a_0(\gamma), \quad (37)$$

where

$$F_\pm = \sqrt{\frac{2 - 1/a^4 \pm 2\gamma\sqrt{1 - 1/a^4}}{4\gamma^2(\gamma^2 - 1)}}, \quad (38)$$

$$a_0(\gamma) = \left\{\frac{\gamma + \sqrt{\gamma^2 - 1}}{2\sqrt{\gamma^2 - 1}}\right\}^{1/4}. \quad (39)$$

Formulas (36)–(39) were obtained under the assumption $\gamma > \gamma_1 \approx 1.45$, where γ_1 is the real positive root of the equation $2\gamma^2(\gamma^2 - 2) = \gamma - 1$, satisfying the condition $\gamma > 1$. For a small-amplitude pump wave ($a - 1 \ll 1$), the functions with the plus sign in (36) and (37) coincide. This is also true for the functions with the minus sign in

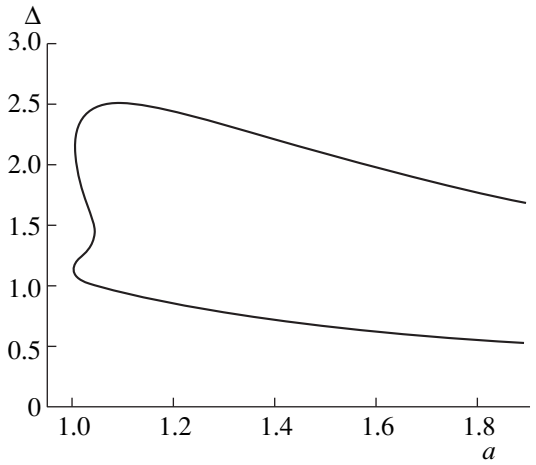

Fig. 1. The curve $\Delta = \Delta(a)$, on which the expression under the square root in (34) equals zero, for $\gamma = 1.5$. Boundary II corresponds to the curve $\Delta = \Delta(a)$, and regions I and III lie outside and inside the curve, respectively.

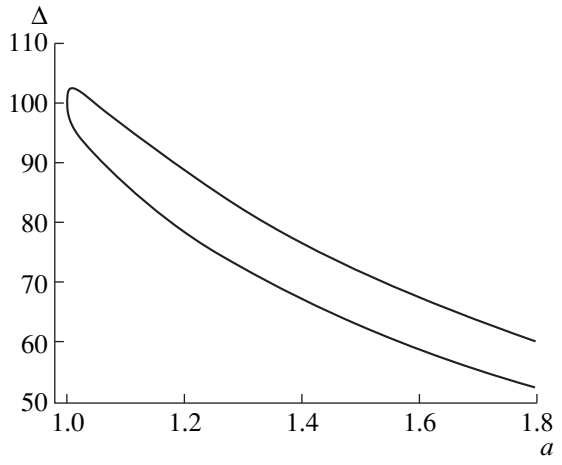

Fig. 2. Curve $\Delta = \Delta(a)$ for $\gamma = 100$.

(36) and (37). We denote these functions by $\Delta_{\pm}$, for which from (36) and (37) we obtain

$$\Delta_{\pm} = \gamma\sqrt{1 + \frac{1}{4(\gamma^2 - 1)}} \pm \frac{1}{2}. \tag{40}$$

Figures 1 and 2 show regions I and III for $\gamma = 1.5$ and 100, respectively. The boundaries II between these regions in the figures are represented by the curves which close upon themselves at infinity ($a \longrightarrow \infty$). For present-day laser intensities ($I_L < 10^{20}$ W/cm^2) and for pump frequencies of about $\omega_0 \approx 3 \times 10^{15}$ s^{-1}, the values of the parameter a are in the range $a < 3$. Consequently, Figs. 1 and 2 and formulas (36)–(40) imply that, for the parameter values $\omega_0 \approx 10^{15}$ s^{-1} and $n_0 < 10^{17}$ cm^{-3} ($\omega_p < 10^{13}$ s^{-1}), the solutions to Eq. (33) lie in region I over a broad range of γ-values (up to $\gamma < (\omega_0/\omega_p)a$ and even higher). In order for the solutions to Eq. (33) to lie in region III or at boundary II, the condition $\gamma \sim a\Delta = (\omega_0/\omega_p)a > 100$ should be satisfied; i.e., the bunch should be ultrarelativistic. In what follows, we restrict ourselves to treating region I and study induced fields for the relevant parameter values. For boundary II and region III, solutions (34) imply that the amplitude of the induced electric fields either increases (at boundary II) or falls off exponentially with distance from the bunch (in region III). Solutions at boundary II should be treated in the nonlinear approximation, and solutions in region III are totally uninteresting for the generation of high accelerating or focusing electric fields in plasmas.

Now, we evaluate Green's function for the parameters from region I. In this case, the roots of Eq. (33) are real and lie in the upper half-plane of the complex variable k. We integrate expressions (23) and (24) over k to obtain

$$G_z^{(e)}(s) = \frac{4\pi e\theta(s)}{\lambda_+^2 - \lambda_-^2}\left[\left(\lambda_+^2 + \frac{a^4 - 1}{a^4} - 4\beta^2\gamma^4F^2\right)\right. \tag{41}$$
$$\left.\times\cos\left(\frac{\lambda_+}{a}k_p s\right) - \left(\lambda_-^2 + \frac{a^4 - 1}{a^4} - 4\beta^2\gamma^4F^2\right)\cos\left(\frac{\lambda_-}{a}k_p s\right)\right],$$

$$G_\perp^{(e)}(s) = \pi ie\frac{\sqrt{a^4 - 1}}{a}\frac{\Delta F}{F^2 + (a^4 - 1)/4\gamma^2a^4}$$
$$\times[\theta(s) - \theta(-s)] + \frac{4\pi e\beta\gamma^2}{\lambda_+^2 - \lambda_-^2}\frac{\sqrt{a^4 - 1}}{a^2}\theta(s)$$
$$\times\left\{(a\Delta - 2\beta\gamma^2F)\left[\frac{1}{\lambda_+}\sin\left(\frac{\lambda_+}{a}k_p s\right) - \frac{1}{\lambda_-}\sin\left(\frac{\lambda_-}{a}k_p s\right)\right]\right. \tag{42}$$
$$+ i\left(1 - \frac{2\beta\gamma^2a\Delta F}{\lambda_-^2}\right)\cos\left(\frac{\lambda_-}{a}k_p s\right)$$
$$\left. - i\left(1 - \frac{2\beta\gamma^2a\Delta F}{\lambda_+^2}\right)\cos\left(\frac{\lambda_+}{a}k_p s\right)\right\},$$

where $k_p = \omega_p/u$, $F_0 = \sqrt{a^2\Delta^2 - 1}$, and $\theta(s)$ is the Heaviside step function. From (41) and (42), we can see that a bunch propagating in a plasma excites two types of waves: with frequencies $\omega_L\lambda_+$ and $\omega_L\lambda_-$. In the absence of a pump wave ($a = 1$), $G_\perp^{(e)}$ vanishes, while $G_z^{(e)}$ is given by the expression

$$G_z^{(e)}(s) = 4\pi e\theta(s)\cos(k_p s), \tag{43}$$

which coincides with the corresponding formulas presented in [23, 24].

4. WAKE FIELDS EXCITED BY A RECTANGULAR BUNCH

Here, we calculate and examine the fields driven by an electron bunch with a prescribed shape. We assume that the bunch electron density n_b is uniform ($n_b \ll n_0$) and denote the bunch length by d, so that

$$n_b(\xi) = n_b[\theta(\xi) - \theta(\xi - d)]. \tag{44}$$

We substitute (41), (42), and (44) into (22) to obtain expressions for the induced fields ahead of ($\xi > d$), inside ($0 \le \xi \le d$), and behind ($\xi < 0$) a bunch propagating in a plasma.

Ahead of the bunch ($\xi > d$), we have

$$E_z'(\xi) = 0, \tag{45}$$

$$\mathscr{E}^+(\xi) = -i\tilde{E}_0\frac{n_b}{n_0}(k_p d)\frac{\sqrt{a^4-1}}{a} \times \frac{\beta\Delta F}{4F^2 + (a^4-1)/\gamma^2 a^4}. \tag{46}$$

Inside the bunch ($0 \le \xi \le d$), we have

$$E_z'(\xi) = \tilde{E}_0\frac{n_b}{n_0}\frac{a\beta}{\lambda_+^2 - \lambda_-^2}\left[\frac{1}{\lambda_+}\left(\lambda_+^2 + \frac{a^4-1}{a^4} - 4\beta^2\gamma^4F^2\right) \times \sin\left(\frac{\lambda_+}{a}k_p(d-\xi)\right)\right. \tag{47}$$
$$\left. - \frac{1}{\lambda_-}\left(\lambda_-^2 + \frac{a^4-1}{a^4} - 4\beta^2\gamma^4F^2\right)\sin\left(\frac{\lambda_-}{a}k_p(d-\xi)\right)\right],$$

$$\mathscr{E}^+(\xi) = i\tilde{E}_0\frac{n_b}{n_0}\frac{\beta\sqrt{a^4-1}}{a} \times \left\{\frac{\Delta F}{4F^2 + (a^4-1)/\gamma^2a^4}k_p(d-2\xi)\right.$$
$$- \frac{\beta\gamma^2}{\lambda_+^2 - \lambda_-^2}\left[\frac{\lambda_+^2 - 2\beta\gamma^2 a\Delta F}{\lambda_+^3}\sin\left(\frac{\lambda_+}{a}k_p(d-\xi)\right)\right.$$
$$\left. - \frac{\lambda_-^2 - 2\beta\gamma^2 a\Delta F}{\lambda_-^3}\sin\left(\frac{\lambda_-}{a}k_p(d-\xi)\right)\right.$$
$$+ i\frac{a\Delta - 2\beta\gamma^2 F}{\lambda_+^2}\left[1 - \cos\left(\frac{\lambda_+}{a}k_p(d-\xi)\right)\right]$$
$$\left.\left. - i\frac{a\Delta - 2\beta\gamma^2 F}{\lambda_-^2}\left[1 - \cos\left(\frac{\lambda_-}{a}k_p(d-\xi)\right)\right]\right]\right\}. \tag{48}$$

Behind the bunch ($\xi < 0$), we have

$$E_z'(\xi) = \tilde{E}_0\frac{n_b}{n_0}\frac{a\beta}{\lambda_+^2 - \lambda_-^2} \times \left\{\frac{1}{\lambda_+}\left(\lambda_+^2 + \frac{a^4-1}{a^4} - 4\beta^2\gamma^4F^2\right)\left[\sin\left(\frac{\lambda_+}{a}k_p(d-\xi)\right)\right.\right.$$
$$\left. + \sin\left(\frac{\lambda_+}{a}k_p\xi\right)\right] - \frac{1}{\lambda_-}\left(\lambda_-^2 + \frac{a^4-1}{a^4} - 4\beta^2\gamma^4F^2\right)$$
$$\left.\times\left[\sin\left(\frac{\lambda_-}{a}k_p(d-\xi)\right) + \sin\left(\frac{\lambda_-}{a}k_p\xi\right)\right]\right\}, \tag{49}$$

$$\mathscr{E}^+(\xi) = i\tilde{E}_0\frac{n_b}{n_0}\frac{\beta\sqrt{a^4-1}}{a}\left\{\frac{\Delta F}{4F^2 + (a^4-1)/\gamma^2a^4}(k_p d)\right.$$
$$- \frac{\beta\gamma^2}{\lambda_+^2 - \lambda_-^2}\left[\frac{\lambda_+^2 - 2\beta\gamma^2 a\Delta F}{\lambda_+^3}\left(\sin\left(\frac{\lambda_+}{a}k_p(d-\xi)\right)\right.\right.$$
$$\left. + \sin\left(\frac{\lambda_+}{a}k_p\xi\right)\right) - \frac{\lambda_-^2 - 2\beta\gamma^2 a\Delta F}{\lambda_-^3}$$
$$\times\left(\sin\left(\frac{\lambda_-}{a}k_p(d-\xi)\right) + \sin\left(\frac{\lambda_-}{a}k_p\xi\right)\right)$$
$$+ i(a\Delta - 2\beta\gamma^2 F)\left[\frac{1}{\lambda_+^2}\left(\cos\left(\frac{\lambda_+}{a}k_p\xi\right)\right.\right.$$
$$\left. - \cos\left(\frac{\lambda_+}{a}k_p(d-\xi)\right)\right) - \frac{1}{\lambda_-^2}\left(\cos\left(\frac{\lambda_-}{a}k_p\xi\right)\right.$$
$$\left.\left.\left. - \cos\left(\frac{\lambda_-}{a}k_p(d-\xi)\right)\right)\right]\right]\right\}. \tag{50}$$

Here, we introduce the notation $\tilde{E}_0 = mc\omega_p/e$. Expression (45) implies that there is no longitudinal field ahead of the bunch ($\xi > d$). The transverse fields ahead of the bunch are unmodulated (i.e., independent of ξ) and are circularly polarized, and the field amplitude is proportional to the function F and the bunch length d. Note that the function F is proportional to the difference between the group velocity $v_g = k_0c^2/\omega_0$ of the induced transverse fields and the bunch velocity. If the group velocity of a transverse wave coincides with the bunch velocity ($F = 0$), then there are no transverse fields ahead of the bunch. In addition, it is easy to see that the magnetic field ahead of the bunch is proportional to F_0 and is absent in the long-wavelength (quasistatic) limit ($k_0 = 0$, or $F_0 = 0$).

The transverse fields ahead of the bunch are induced because the phase velocity $v_\varphi = \omega_0/k_0 > c$ of the pump wave is higher than the bunch velocity, regardless of the values of the parameters of the plasma and the pump wave. Consequently, some perturbations driven by the

pump wave and bunch in the plasma have a phase velocity above the bunch velocity and thereby can overtake the bunch.

According to (29)–(31), (48), and (50), the transverse fields inside and behind the bunch are modulated and circularly polarized. However, although the polarization vector of the transverse wave spans an entire circle, the circle's radius depends on the distance ξ from the bunch. In fact, from expressions (29)–(31), we have

$$E_x'^2 + E_y'^2 = E_r^2(\xi) + E_i^2(\xi) = E_{\max}^2(\xi), \quad (51)$$

$$B_x'^2 + B_y'^2 = B_r^2(\xi) + B_i^2(\xi) = B_{\max}^2(\xi). \quad (52)$$

In the general case, the amplitudes of the electric and magnetic fields, $E_{\max}(\xi)$ and $B_{\max}(\xi)$, are functions of ξ. Modulated transverse plasma waves are generated because of the excitation of the above two types of waves with frequencies $\omega_L\lambda_\pm$ and wave vectors $(\omega_L/u)\lambda_\pm$. The interaction between a pump wave and the two induced waves gives rise to oscillations with the combination frequencies $\omega_0 - \omega_L\lambda_\pm$ and $\omega_0 + \omega_L\lambda_\pm$ and combination wave vectors $k_0 - (\omega_L/u)\lambda_\pm$ and $k_0 + (\omega_L/u)\lambda_\pm$; the modulated wave results from the interference between these oscillations. If $\omega_0 > \omega_L\lambda_\pm$ (or, in dimensionless form, $a\Delta > \lambda_\pm$) and $k_0 > (\omega_L/u)\lambda_\pm$ (or, in dimensionless form, $\beta\sqrt{a^2\Delta^2 - 1} > \lambda_\pm$), the carrier wave is described by the transverse components $E_r(\xi)$ or $E_i(\xi)$. Otherwise, the carrier wave is described by the functions $\cos\zeta$ and $\sin\zeta$ in expressions (29) and (30).

We analyze the above formulas for the following, practically important parameter range: $n_0 < 10^{17}$ cm^{-3} ($\omega_p < 2 \times 10^{13}$ s^{-1}), $I_L \approx 10^{18}$–10^{20} W/cm^2 ($I_L = cE_0^2/4\pi$ is the pump wave intensity), $\omega_0 \approx 10^{15}$ s^{-1}, and $\gamma \approx 10$–10^3. For pump wave intensities ranging from 10^{18} to 10^{20} W/cm^2, the parameter a is in the interval $a \approx 1.02$–2. The parameter Δ lies in the range $\Delta > 50$.

In region I, formulas (40) imply that either $\gamma < \Delta$ or $\gamma > \Delta$. Formulas (45)–(50) are comparatively easy to analyze in the ranges $a\Delta \gg \gamma \gg 1$ and $1 \ll a\Delta \ll \gamma$. In the first range, formulas (34) and (35) give

$$4\gamma^4F^2 \approx a^2\Delta^2\left(1 - \frac{2\gamma^2}{a^2\Delta^2}\right) \gg \gamma^2 \gg 1, \quad (53)$$

$$\lambda_-^2 \approx 1, \quad \lambda_+^2 \approx 4\gamma^4F^2 \approx a^2\Delta^2 \gg \lambda_-^2. \quad (54)$$

Ahead of the bunch, the transverse electric and magnetic fields are equal in order of magnitude to $|\mathscr{E}^+| \approx |\mathscr{B}^+| \approx \tilde{E}_0(n_b/n_0)(k_pd)\gamma^2/2$ at $a > 1$. Inside and behind the bunch, the amplitude of waves with the frequency $\omega_L\lambda_+$ is much smaller than the amplitude of waves with the frequency $\omega_L\lambda_-$. According to expressions (47) and (49), the amplitude of longitudinal waves with the frequency $\omega_L\lambda_-$ is equal in order of magnitude to $\tilde{E}_0(n_b/n_0)a$, which is $\gamma^2(k_pd)/2a$ times smaller than the transverse wave amplitude ahead of the bunch. In the ranges $0 \le \xi \le d$ and $\xi < 0$, the dominant contributions to expressions (48) and (50) come from the first and third terms, in which case the third terms are approximately equal to $\tilde{E}_0(n_b/n_0)\gamma^2a$ (which exceeds the amplitude of the longitudinal waves by a factor of γ^2). Therefore, we have $E_i(\xi) \gg E_r(\xi) \approx 0$ and $B_r(\xi) \gg B_i(\xi) \approx 0$, so that we can write $E_x' \simeq -E_i(\xi)\sin\zeta$, $E_y' \simeq E_i(\xi)\cos\zeta$, $B_x' \simeq B_r(\xi)\cos\zeta$, and $B_y' \simeq B_i(\xi)\sin\zeta$. The oscillating terms in formulas (47)–(50) describe waves whose wavelengths increase as the pump wave becomes more intense. In the case of a short bunch such that $\pi d < a\lambda_p$ (where $\lambda_p = 2\pi/k_p$ is the wavelength of the longitudinal waves excited in the absence of a pump wave), the third oscillating terms in expressions (48) and (50) are larger than the first terms. In the case of a long bunch such that $\pi d > a\lambda_p$, the first term in expression (50) is larger than the third term. This is also true for a boundary region on the inside of a long bunch ($\pi|d/2 - \xi| > a\lambda_p/2$). In the central region of a long bunch ($\pi|d/2 - \xi| < a\lambda_p/2$), the main contribution to formula (58) comes from the third term.

Behind the bunch, the amplitude of the longitudinal and transverse waves is proportional to $2\sin(\pi d/a\lambda_p)$ and becomes maximum at $d = (n - 1/2)a\lambda_p$ ($n = 1, 2, \ldots$). Under the condition $d = (a\lambda_p)n$, no waves are excited behind the bunch.

Figures 3–6, which illustrate the numerical results obtained for induced fields from formulas (29)–(31) and (45)–(50), reveal all of the characteristic features described above. Consequently, a one-dimensional bunch propagating in a plasma in the presence of a pump wave with circular polarization excites a wave whose wavelength increases with increasing the pump wave intensity. The amplitude of a longitudinal wave is weakly sensitive to the energy of the bunch electrons (to the relativistic factor γ) and increases with the pump wave intensity. The amplitude of the transverse wave is larger than the amplitude of the longitudinal wave by a factor of γ^2. Thus, we can conclude that, in the range $\gamma \gg 1$, the excited wave is nearly transverse.

Now, we consider another limiting case, $\gamma \gg a\Delta \gg 1$. Instead of formulas (53) and (54), we obtain

$$4\gamma^4F^2 \approx \gamma^2\left(\frac{\gamma}{a\Delta}\right)^2 \gg 1, \quad (55)$$

$$\lambda_-^2 \approx 1, \quad \lambda_+^2 \approx \gamma^2\left(\frac{\gamma}{a\Delta}\right)^2 \gg \lambda_-^2. \quad (56)$$

Ahead of the bunch, the amplitudes of the transverse fields are equal in order of magnitude to $|\mathscr{E}^+| \approx |\mathscr{B}^+| \approx \tilde{E}_0(n_b/n_0)(k_pd)a^2\Delta^2/2$ at $a > 1$. Inside and behind the

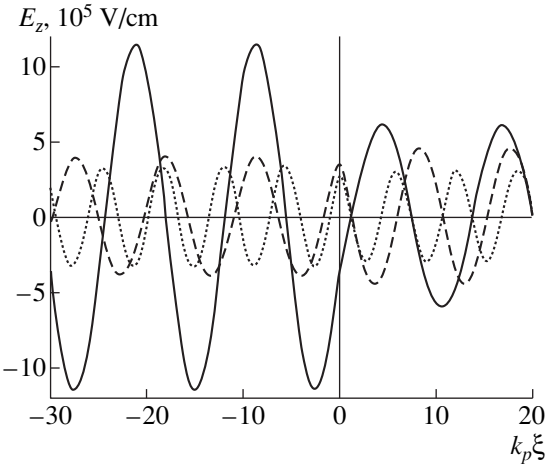

Fig. 3. Induced longitudinal electric field vs. ξ in region I for $n_0 = 10^{17}$ cm^{-3} ($k_p^{-1} = 1.7 \times 10^{-3}$ cm), $n_b = 10^{14}$ cm^{-3}, $\omega_0 = 3.77 \times 10^{15}$ s^{-1}, $\gamma = 50$, and $k_p d = 20$. The dotted curve was calculated in the absence of a pump wave ($E_0 = 0$), the dashed curve was obtained for $E_0 = 1.3 \times 10^{11}$ V/cm, and the solid curve refers to $E_0 = 2.5 \times 10^{11}$ V/cm.

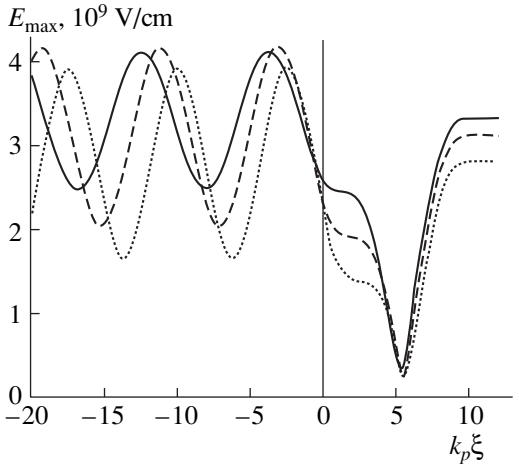

Fig. 4. Maximum induced transverse electric field $E_{max} = \sqrt{E_r^2(\xi) + E_i^2(\xi)}$ vs. ξ in region I for a bunch of length $10\ k_p^{-1}$. The dotted curve corresponds to $E_0 = 6.7 \times 10^{10}$ V/cm, the dashed curve corresponds to $E_0 = 8.8 \times 10^{10}$ V/cm, and the solid curve corresponds to $E_0 = 1.09 \times 10^{11}$ V/cm. The remaining parameters are the same as in Fig. 3.

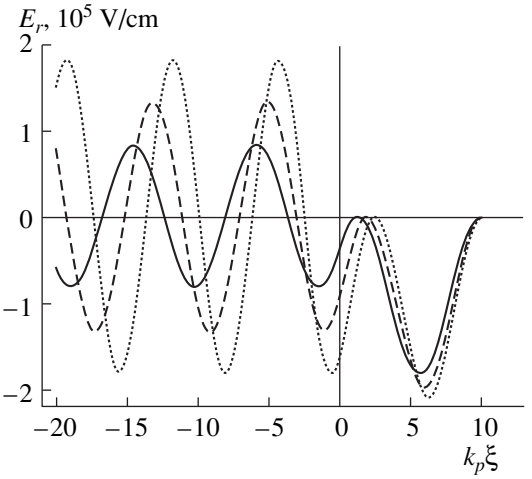

Fig. 5. Electric field $E_r(\xi)$ vs. ξ. The parameters and notation are the same as in Fig. 4.

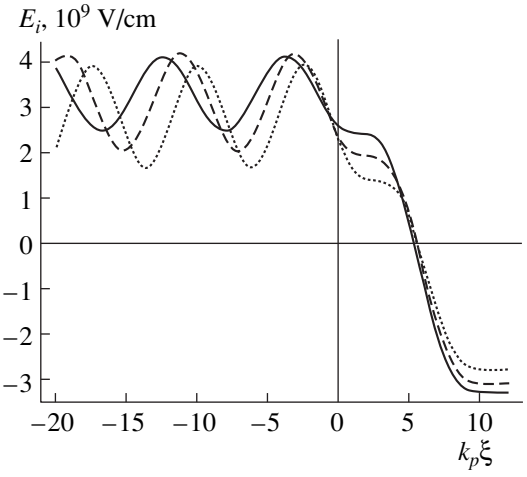

Fig. 6. Electric field $E_i(\xi)$ vs. ξ. The parameters and notation are the same as in Fig. 4.

bunch, the amplitude of waves with the frequency $\omega_L\lambda_+$ is again much smaller than the amplitude of waves with the frequency $\omega_L\lambda_-$. According to (47) and (49), the amplitude of longitudinal waves with the frequency $\omega_L\lambda_-$ remains constant and is approximately equal to $\tilde{E}_0 (n_b/n_0)a$, in which case the longitudinal field is $(k_p d)a\Delta^2/2$ times weaker than the transverse field ahead of the bunch. Inside and behind the bunch, the main contributions to the expressions describing transverse waves again come from the first and third terms. The third terms are equal to $\tilde{E}_0 (n_b/n_0)a(a\Delta)^2$, which exceeds the longitudinal wave amplitude by a factor of $(a\Delta)^2$. Note that, in the limit of very large γ ($\gamma \gg a\Delta$), the transverse fields are γ-independent but depend on the pump wave intensity. The remaining features are the same as those described above in the limit $\gamma \ll a\Delta$.

5. CONCLUSION

We have solved the problem of the excitation of linear wake waves by a one-dimensional electron bunch propagating in a plasma in the presence of a strong electromagnetic wave with circular polarization. We have derived equations describing induced electromagnetic fields. We have shown that there are three ranges of the parameter values of the bunch, pump wave, and plasma in which the equations derived have different solutions. Our analysis shows that, for certain parameters in the most interesting range (region I), the amplitude of the excited transverse waves grows as the energy of the bunch electrons increases until the relativistic factor of the bunch reaches a certain threshold value $\gamma \sim a\Delta$, above which the transverse wave amplitude becomes essentially independent of γ and grows as the intensity and frequency of the pump wave increase. The longitudinal field, which is shown to be weakly sensitive to γ, grows with increasing the pump wave intensity.

To conclude, note that, although much attention has been devoted to one-dimensional wake fields (see, e.g., [1–18] and the papers cited therein), a more realistic three-dimensional case is of greater importance from the standpoint of practical applications. We expect that the above characteristic features of the wake fields driven by a one-dimensional bunch will persist in three-dimensional bunches, in which case, however, new features may arise, stemming from the dependence on the radial coordinate.

ACKNOWLEDGMENTS

This work was supported in part by the International Science and Technology Center, project no. A-013.

REFERENCES

1. E. Esarey, P. Sprangle, J. Krall, and A. Ting, IEEE Trans. Plasma Sci. **24**, 252 (1996).
2. Ya. B. Faĭnberg, Fiz. Plazmy **23**, 275 (1997) [Plasma Phys. Rep. **23**, 251 (1997)].
3. P. Chen, Part. Accel. **20**, 171 (1987).
4. A. Ts. Amatuni, S. S. Elbakian, A. G. Khachatryan, and E. V. Sekhpossian, Part. Accel. **51**, 1 (1995).
5. P. Chen, J. M. Dawson, R. W. Huff, and T. Katsouleas, Phys. Rev. Lett. **54**, 693 (1985).
6. R. D. Ruth, A. W. Chao, P. L. Morton, and P. B. Wilson, Part. Accel. **17**, 171 (1985).
7. R. Keinigs and M. E. Jones, Phys. Fluids **30**, 252 (1987).
8. A. Ts. Amatuni, E. V. Sekhposyan, A. G. Khachatryan, and S. S. Elbakian, Fiz. Plazmy **21**, 1000 (1995) [Plasma Phys. Rep. **21**, 945 (1995)].
9. A. G. Khachatryan, A. Ts. Amatuni, E. V. Sekhposyan, and S. S. Elbakian, Fiz. Plazmy **22**, 638 (1996) [Plasma Phys. Rep. **22**, 576 (1996)].
10. Ya. B. Fainberg, N. Ayzatskij, V. Balakirev, *et al.*, in *Proceedings of the 15th International Workshop on Charged Particle Linear Accelerator, Alushta, 1997*, p. 16.
11. S. S. Elbakian, E. V. Sekhpossian, and A. G. Khachatryan, Preprint No. YerPhI-1511(11)-98 (Yerevan Physical Institute, Yerevan, 1998).
12. A. Ts. Amatuni, E. V. Sekhposyan, and S. S. Elbakian, Fiz. Plazmy **12**, 1145 (1986) [Sov. J. Plasma Phys. **12**, 662 (1986)].
13. J. B. Rosenzweig, Phys. Rev. Lett. **58**, 555 (1987).
14. J. B. Rosenzweig, IEEE Trans. Plasma Sci. **15**, 186 (1987).
15. J. B. Rosenzweig, Phys. Rev. A **38**, 3634 (1988).
16. A. G. Khachatryan, Phys. Plasmas **4**, 4136 (1997).
17. J. B. Dawson, Phys. Rev. **133**, 383 (1959).
18. A. I. Akhiezer and R. V. Polovin, Zh. Éksp. Teor. Fiz. **30**, 915 (1956) [Sov. Phys. JETP **3**, 696 (1956)].
19. M. V. Kalmykov and N. Ya. Kotsarenko, Izv. Vyssh. Uchebn. Zaved., Radiofiz. **19**, 1481 (1976).
20. L. Stenflo, Plasma Phys. **19**, 1187 (1977).
21. C. Max and F. Perkins, Phys. Rev. Lett. **29**, 1731 (1972).
22. C. S. Liu and V. K. Tripathi, *Interaction of Electromagnetic Waves with Electron Beams and Plasmas* (World Scientific, Singapore, 1994).
23. M. E. Jones and R. Keinigs, IEEE Trans. Plasma Sci. **15**, 203 (1987).
24. H. S. Kim, S. Yi, A. Amin, and K. E. Lonngren, Phys. Rev. E **50**, 3962 (1994).

Translated by I.A. Kalabalyk

Plasma Physics Reports, Vol. 26, No. 10, 2000, pp. 840–867. Translated from Fizika Plazmy, Vol. 26, No. 10, 2000, pp. 894–926.

PLASMA KINETICS

Rates of Thermonuclear Reactions in Dense Plasmas

V. N. Tsytovich* and M. Bornatici**

**Institute of General Physics, Russian Academy of Sciences, ul. Vavilova 38, Moscow, 117942 Russia*
e-mail: tsytov@td.lpi.ac.ru
***INFM, Department of Physics A. Volta, via Bassi 6, Pavia, 27100 Italy*
e-mail: bornatici@pv.infn.it

Received January 27, 2000; in final form, March 6, 2000

Abstract—The problem of plasma screening of thermonuclear reactions has attracted considerable scientific interest ever since Salpeter's seminal paper, but it is still faced with controversial statements and without any definite conclusion. It is of relevant importance to thermonuclear reactions in dense astrophysical plasmas, for which charge screening can substantially affect the reaction rates. Whereas Salpeter and a number of subsequent investigations have dealt with static screening, Carraro, Schafer, and Koonin have drawn attention to the fact that plasma screening of thermonuclear reactions is an essentially dynamic effect. In addressing the issue of collective plasma effects on the thermonuclear reaction rates, the first critical overview of most of the work carried out so far is presented and the validity of the test particle approach is assessed. In contrast to previous investigations, we base our description on the kinetic equation for nonequilibrium plasmas, which accounts for the effects on the rates of thermonuclear reactions of both plasma fluctuations and screening and allows one to analyze explicitly the effects of the fluctuations on the reaction rates. Such a kinetic formulation is more general than both Salpeter's approach and the recently developed statistical approaches and makes it possible to obtain a more comprehensive understanding of the problem. A noticeable result of the fluctuation approach is that the static screening, which affects both the interaction and the self-energy of the reacting nuclei, does not affect the reaction rates, in contrast with the results obtained so far. Instead, a *reduction* of the thermonuclear reaction rates is obtained as a result of the effect of plasma fluctuations related to the free self-energy of the reacting nuclei. A simple physical explanation of the slowing down of the reaction rates is given, and the relation to the dynamically screened test particle approach is discussed. Corrections to the reaction rates in the solar interior are calculated numerically. It is shown that the corrections to reactions involving ^{8}B and ^{7}Be may exceed 100%. The results obtained are discussed in connection with the solar neutrino problem. The range of applicability of the approach is also discussed. © *2000 MAIK "Nauka/Interperiodica".*

1. INTRODUCTION

There exist three main approaches used in the problem of thermonuclear reactions in dense plasmas: the approach of static screening first used by Salpeter [1], the approach of dynamic screening first used by Carraro *et al.* [2], and the general plasma fluctuation approach used in [3].

Below, we will consider a plasma consisting of electrons and different species of ions. We label different ions by subscripts i and j and electrons by the subscript e, whereas the subscript α is used to label all of the plasma species (electrons plus ions). The nuclear reactions between nuclei i and j will be considered, and the corresponding reaction rate will be denoted by R_{ij}.

The effect of static screening of nuclear reactions in a dense plasma was first considered by Salpeter [1] and since then extensively discussed in the literature [4–7] (a recent review of this issue was given by Ichimaru [8]). Dynamic screening was first considered by Carraro *et al.* [2] and subsequently discussed by Gruzinov [9] and Brown and Sawyer [10] with results differing from the earlier findings. Recent papers [11–14] have questioned the issue of screening altogether. A statistical description of nuclear reactions in a plasma was done by Brown and Sawyer [10] and Weneser [15]. More recently, the issue of the plasma screening of nuclear reactions was considered in [16–17]. Here, we will analyze critically some of the above papers with the aim of clarifying a few of the controversial points that have accompanied the issue of thermonuclear reactions in dense plasmas.

1.1. Salpeter's Enhancement Factor

Let us recall the main arguments by Salpeter. Thermonuclear reactions in a dense plasma usually occur at distances between nuclei much less than the screening distance. For the case of Debye screening, the potential energy of two nuclei i and j with charges Z_i and Z_j (in units of the absolute value of the electron charge e) is

$$U_{ij} = \frac{Z_i Z_j e^2}{r}\exp\left(-\frac{r}{d}\right) \approx \frac{Z_i Z_j e^2}{r} - \frac{Z_i Z_j e^2}{d} = U_{ij}^C - U_{ij}^S, \quad (1)$$

1063-780X/00/2610-0840$20.00

with

$$\frac{1}{d^2} = \sum_\alpha \frac{4\pi Z_\alpha^2 e^2 n_\alpha}{T} \equiv \sum_\alpha \frac{1}{d_\alpha^2}, \quad (2)$$

d being the Debye screening radius accounting for all plasma particles, whereas d_α refers to the Debye screening radius for particles of species α. In expression (2), T is the plasma temperature (in units of energy); n_α is the number density of species α; and the electron number density n_e is such that $n_e = \sum_i Z_i n_i$, according to the charge neutrality. With reference to expression (1), U_{ij}^C is the Coulomb energy of bare nuclei and $U_{ij}^S = Z_i Z_j e^2/d$ describes Salpeter's lowering of the Coulomb barrier due to static screening. Note that U_{ij}^S in expression (1) is constant and does not depend on the distance of the two nuclei. The nuclear reaction probability of bare nuclei $w_{ij}(E)$ depends on the relative kinetic energy E and after averaging over the thermal distribution $f(E)dE \propto \sqrt{E}\exp(-E/T)dE$ yields the rate of nuclear reaction R_{ij}. The constancy of U_{ij}^S allows us to write $E - U_{ij} = E + U_{ij}^S - U_{ij}^C$. Therefore, by replacing $w_{ij}(E)$ with $w_{ij}(E + U^S)$, we obtain that the rate R_{ij}, which takes into account the static screening effect, is equal to

$$R_{ij} \propto \sqrt{E - U_{ij}^S}\exp(U_{ij}^S/T)\exp(-E/T)w_{ij}(E)dE, \quad (3)$$

where the replacement of variable $E + U_{ij}^S \longrightarrow E$ is made. The integration over E leading to the reaction rate (3) contains in its integrand a product between the steeply decreasing Maxwellian factor $\exp(-E/T)$ and the steeply rising factor $\exp(-G_{ij}/\sqrt{E})$, the latter being connected with the probability $w_{ij}(E)$ with $G_{ij} = \sqrt{2}\pi Z_i Z_j e^2 \sqrt{\mu_{ij}}/\hbar$, μ_{ij} denoting the reduced nuclear mass [8]. The product attains its maximum at

$$E_{ij}^G = \left(\frac{G_{ij}T}{2}\right)^{2/3} = \left(\frac{\pi}{\sqrt{2}}\frac{Z_i Z_j e^2 \sqrt{\mu_{ij}}}{\hbar}T\right)^{2/3}, \quad (4)$$

to be referred to as the Gamow energy, which yields the typical energies at which nuclear reactions occur. For most thermonuclear reactions, the Gamow energy (4) is larger by a factor from 5 to 20 than the thermal energy T of the reacting nuclei; more explicitly, $E_{ij}^G/T = 14.145(Z_i^2 Z_j^2 \mu_{ij}/T_6)^{1/3}$ with $T_6 = T/10^6$ K. For the most interesting case $U_{ij}^S \ll E_{ij}^G$, we may assume $\sqrt{E - U_{ij}^S} \approx \sqrt{E}$ in the factor determining the phase volume when integrating over the thermal distribution. Thus, we obtain that the rate of nuclear reactions occurring in a vacuum should be multiplied by a constant factor to account for static screening:

$$R_{ij} = R_{ij}^{(0)}(1 + \Lambda_{ij}^S), \quad (5)$$

where $R_{ij}^{(0)}$ is the reaction rate in the absence of screening and

$$1 + \Lambda_{ij}^S = \exp\left(\frac{U_{ij}^S}{T}\right) = \exp\left(\frac{Z_i Z_j e^2}{Td}\right) \quad (6)$$

is referred to as Salpeter's enhancement factor. The enhancement can be substantial for $Z_i Z_j e^2/d \approx T$; however, even for $Z_i Z_j e^2/d \ll T$, it can amount to several percent, which can be relevant to such a problem as neutrino production in nuclear reactions. Salpeter's factor (6) increases with the charge Z of the reacting nuclei, which should be of relevance to the production of high energy neutrinos with reference to the solar neutrino problem.

1.2. Static versus Dynamic Screening

Salpeter's results, which rest on the assumption that the screening of the nuclear charge is due to static Debye screening, were later disputed on the basis that the screening of nuclei in nuclear reactions cannot be static, since the reacting nuclei move with velocities larger than the ion thermal velocity. On the other hand, investigations of plasma screening based on a statistical approach confirmed Salpeter's results. Let us analyze these two opposing findings.

We will consider here only nonrelativistic particles for which the particle field in a medium is determined mainly by the longitudinal dielectric permittivity $\varepsilon_{\mathbf{k},\omega}$, where $\mathbf{k}$ is the wave vector and ω is the frequency.

For reference later on, for a thermal collisionless plasma, the longitudinal dielectric permittivity is [18]

$$\varepsilon_{\mathbf{k},\omega} = 1 + \sum_\alpha \frac{1}{k^2 d_\alpha^2} W\left(\sqrt{\frac{m_\alpha}{2T}}\frac{\omega}{k}\right), \quad (7)$$

where d_α is the Debye radius of the particles of species α [see (2)] and

$$W(x) \equiv 1 + x\exp(-x^2)\left(i\sqrt{\pi} - 2\int_0^x \exp(t^2)dt\right) \quad (8)$$

is the plasma dispersion function. The collisionless dielectric permittivity (7) will be used here for fluctuations with frequencies much higher than the binary plasma particle collision frequency. Of interest are the asymptotic expressions

$$\varepsilon_{\mathbf{k},\omega} = 1 + \sum_\alpha \frac{1}{k^2 d_\alpha^2}, \quad (9)$$

which is valid to the lowest order in $\omega\sqrt{m_\alpha/2T}/k \ll 1$, and

$$\varepsilon_{\mathbf{k},\omega} = 1 - \frac{\sum_\alpha \omega_{p\alpha}^2}{\omega^2}, \quad \omega_{p,\alpha}^2 \equiv \frac{4\pi Z_\alpha^2 n_\alpha}{m_\alpha}, \tag{10}$$

which is valid to lowest order in $(\omega\sqrt{m_\alpha/2T}/k)^2 \gg 1$ (the cold plasma limit).

From the test particle approach, it is well known that a charge moving in a plasma is dynamically screened; i.e., its Fourier transformed potential is inversely proportional to $1/\varepsilon_{\mathbf{k},\mathbf{k}\cdot\mathbf{v}}$, the relevant dielectric function being evaluated at a frequency equal to $\mathbf{k}\cdot\mathbf{v}$, which is the Doppler shifted frequency of the field of a moving particle [18]. As a consequence, a particle moving with a velocity larger than the thermal velocity of the corresponding particle species in the system tends to "undress" as its velocity increases. The screening will become negligible for particles moving with velocities much higher than the corresponding thermal velocity. With reference to the reacting nuclei, whose typical energy is the Gamow energy (4), the characteristic velocities are higher than the ion thermal velocity but lower than the electron thermal velocity, so that the screening by plasma ions should be negligible, whereas the screening by electrons should be almost static. In this case, Salpeter's enhancement factor, which accounts for the contribution to the screening from both electrons and ions, should be reduced. Calculations along these lines were first performed by Carraro *et al.* [2], who, however, did not consider the self-energy of the reacting nuclei.

Let us discuss this point in more detail. In terms of the space-time Fourier transform, the polarization potential of a test nuclei of charge Z_i moving with velocity $\mathbf{v}$ has the standard form [18]

$$\phi_{\mathbf{k},\omega}^{\mathrm{pol}}(\mathbf{v}) = \frac{Z_i e}{2\pi^2 k^2}\delta(\omega - \mathbf{k}\cdot\mathbf{v})\left(\frac{1}{\varepsilon_{\mathbf{k},\omega}} - 1\right), \tag{11}$$

such that the corresponding space-time potential

$$\phi^{\mathrm{pol}}(\mathbf{r},\mathbf{v},t) = \int d\mathbf{k}\, d\omega\, \phi_{\mathbf{k},\omega}^{\mathrm{pol}}(\mathbf{v}) e^{i(\mathbf{k}\cdot\mathbf{r} - \omega t)} \tag{12}$$

is

$$\phi^{\mathrm{pol}}(\mathbf{r},\mathbf{v},t) = \frac{Z_i e}{2\pi^2}\int \frac{d\mathbf{k}}{k^2}\left(\frac{1}{\varepsilon_{\mathbf{k},\mathbf{k}\cdot\mathbf{v}}} - 1\right) e^{i\mathbf{k}\cdot(\mathbf{r} - \mathbf{v}t)}, \tag{13}$$

which, in the static limit ($\mathbf{v} = 0$), leads to the potential used by Salpeter.

Indeed, for $|\mathbf{k}\cdot\mathbf{v}| \ll \omega$, which corresponds to the static limit, which, in particular, applies to a particle at rest, one can approximate $\delta(\omega - \mathbf{k}\cdot\mathbf{v}) \approx \delta(\omega)$ in expression (11), so that, to the lowest order in $|\mathbf{k}\cdot\mathbf{v}|/\omega \ll 1$, expression (13) reduces to the spherically symmetric potential

$$\phi^{\mathrm{pol}}(r) = \frac{Z_i e}{2\pi^2}\int \frac{d\mathbf{k}}{k^2}\left(\frac{1}{\varepsilon_{\mathbf{k},0}} - 1\right) e^{i\mathbf{k}\cdot\mathbf{r}} = \frac{Z_i e}{r}\left(e^{-\frac{r}{d}} - 1\right), \tag{14}$$

the last equality being obtained by using the expression for the static ($\omega = 0$) dielectric permittivity, $\varepsilon_{k,0} = 1 + (kd)^{-2}$ [cf. (9)]. Salpeter's result is based just on the static potential (14) [cf. Section 1.1].

To account for the finite nuclei velocity, one has to refer to the polarization potential (13) instead of (14). In relation to the nuclear reaction between the nuclei i and j, it is necessary to know the corresponding polarization potential energy

$$\begin{aligned} U_{ij}^{\mathrm{pol}} &= \frac{1}{2}\int d\mathbf{r}\,\phi^{\mathrm{pol}}(\mathbf{r},t)\rho(\mathbf{r},t) \\ &= \frac{e}{2}\int d\mathbf{k}\, d\omega\, \phi_{\mathbf{k},\omega}^{\mathrm{pol}} e^{-i\omega t}[Z_i e^{i\mathbf{k}\cdot\mathbf{r}_i(t)} + (i \longrightarrow j)], \end{aligned} \tag{15}$$

where

$$\rho(\mathbf{r},t) = e[Z_i\delta(\mathbf{r} - \mathbf{r}_i(t)) + (i \longrightarrow j)] \tag{16}$$

is the charge density of the nuclei i and j, whose instantaneous positions at time t are $\mathbf{r}_i(t)$ and $\mathbf{r}_j(t)$, respectively. The notation $(i \longrightarrow j)$ indicates that one has to take the same as the preceding term with the index i replaced with j. Using expression (11) for two test ions yields

$$\begin{aligned} \phi_{\mathbf{k},\omega}^{\mathrm{pol}} &= \frac{e}{2\pi^2 k^2}\left(\frac{1}{\varepsilon_{\mathbf{k},\omega}} - 1\right) \\ &\times [Z_i\delta(\omega - \mathbf{k}\cdot\mathbf{v}_i)e^{-i\mathbf{k}\cdot\mathbf{r}_i(0)} + (i \longrightarrow j)] \end{aligned} \tag{17}$$

in the case of motion along straight trajectories, e.g., $\mathbf{r}_i(t) = \mathbf{r}_i(0) + \mathbf{v}_i t$. After substituting expression (17) into (15), we obtain that the result consists of two contributions: the first one is independent of the relative distance of the two nuclei and is referred to as the self-energy U_{ij}^{self} and the other depends on the relative distance between the two nuclei and is equal to the interaction energy U_{ij}^{int}. Explicitly, we have

$$U_{ij}^{\mathrm{pol}} \equiv U_{ij}^{\mathrm{pol,self}} + U_{ij}^{\mathrm{pol,int}}, \tag{18}$$

$$U_{ij}^{\mathrm{pol,self}} = \frac{e^2}{4\pi^2}\int \frac{d\mathbf{k}}{k^2}\left[Z_i^2\left(\frac{1}{\varepsilon_{\mathbf{k},\mathbf{k}\cdot\mathbf{v}_i}} - 1\right) + (i \longrightarrow j)\right], \tag{19}$$

$$\begin{aligned} &U_{ij}^{\mathrm{pol,int}} \\ &= \frac{e^2}{4\pi^2}\int \frac{d\mathbf{k}}{k^2}\left[Z_i Z_j e^{-(i\mathbf{k}\cdot(\mathbf{r}_j(t) - \mathbf{r}_i(t)))}\left(\frac{1}{\varepsilon_{\mathbf{k},\mathbf{k}\cdot\mathbf{v}_i}} - 1\right) + (i \longleftrightarrow j)\right], \end{aligned} \tag{20}$$

where $U_{ij}^{\text{pol, int}}$ [given by expression (20) and proportional to Z_iZ_j] is the polarization interaction energy of two dynamically screened nuclei and the self-energy $U_{ij}^{\text{pol, self}}$ [given by (19)] accounts for the corresponding self-energies of two nuclei also dynamically screened, the latter being proportional to Z_i^2 and Z_j^2. In the static limit, $U_{ij}^{\text{pol, int}}$ reduces to Salpeter's energy U_{ij}^S [cf. (1)]. After proceeding in the same way as Salpeter [1], we obtain that the effect on the nuclear reactions of the dynamic screening is described by the enhancement factor [2]

$$1 + \Lambda_{ij}^{\text{dyn}} = \left\langle \exp\left(-\frac{U_{ij}^{\text{pol, int}}}{T}\right)\right\rangle \equiv \exp\left(s_{ij}\frac{Z_iZ_je^2}{Td}\right), \quad (21)$$

where the brackets $\langle\ldots\rangle$ denote an average with respect to both the kinetic energy of the center of mass and the energy of the relative motion of the nuclei. A numerical evaluation of the dynamic screening factor s_{ij} occurring in expression (21) was carried out for hydrogen chain reactions in the solar interior, with the result that the enhancement of the thermonuclear reactions rates can be appreciably smaller ($s_{ij} \le 0.82$) than that obtained in the limit of static screening [2].

One should note that expression (19) for the self-energy is valid either for nondispersive media or for nuclei at rest. For moving nuclei, there will appear an additional term proportional to the derivative of the dielectric permittivity with respect to frequency, the frequency being determined by the same dynamic screening relation $\omega = \mathbf{k}\cdot\mathbf{v}$. Such a result will be shown below when discussing the self-energy problem in the present context. Here, it is sufficient to note that only the self-energy (19) [rather than the interaction energy (20)] is modified by dispersion. The fact that expression (19) does not properly account for the dispersion of the medium can be seen from the relation

$$\frac{1}{2}\int\rho(\mathbf{r}, t)\phi(\mathbf{r}, t)d\mathbf{r} = \frac{1}{8\pi}\int\phi\nabla\cdot(\varepsilon\mathbf{E})d\mathbf{r}$$
$$= -\frac{1}{8\pi}\int\varepsilon\mathbf{E}\cdot\nabla\phi d\mathbf{r} = \int\frac{\varepsilon E^2}{8\pi}d\mathbf{r}, \quad (22)$$

which is the same as relation (15), which has been the starting equation for the calculation of the energy. However, relation (22) does not take into account the dispersion of the dielectric function (dependence on ω and $\mathbf{k}$). In fact, it is well known that, in dispersive media, the expression for the energy contains $(\partial(\omega\varepsilon)/\partial\omega)$ instead of ε [19].

The issue of the self-energy of the reacting nuclei has been of particular concern in the evaluation of thermonuclear reaction rates. In [11], on using relation (15), where, however, the charge density $\rho(\mathbf{r}, t)$ is replaced by the polarization charge density (in terms of the Fourier transform, this amounts to $\rho_{\mathbf{k},\omega} \longrightarrow [(1/\varepsilon_{\mathbf{k},\omega}) - 1]\rho_{\mathbf{k},\omega}$), one obtains an expression that is referred to as "self-energy," although it is dependent on the relative distance of the nuclei, in contrast with relation (19), where such a dependence is absent. Then, the two reacting nuclei acquire additional energy $Z_iZ_je^2/2d$, with the result being that Salpeter's enhancement factor (6) becomes $\exp(3Z_iZ_je^2/2Td)$ [11]. Such a result was rejected in [12] on the basis that the additional energy $Z_iZ_je^2/2d$ is not related to the interaction energy of the two nuclei and, for both the case of thermodynamic equilibrium (as considered in [12]) and nuclei at rest, should be stored in a heat bath.

From the foregoing consideration, one should refer to expressions (15)–(20), which account for the total electrostatic energy, as shown in [19], the polarization energy in particular being taken into account through the dielectric permittivity.

The issue of the particle self-energy in dense thermal plasmas was extensively discussed in [15] on the basis of a statistical approach. A question that needs to be considered is whether the self-energy can affect the nuclear reaction rates. Note that, in general, the self-energy is velocity dependent. Although it is not part of the interaction energy, it should be added to the total energy. The total velocity dependent energy will consist of both the kinetic energy and self-energy. It is possible to divide the total velocity dependent energy of two interacting nuclei into the energy of the center of mass and the energy of relative motion only if the self-energy can be neglected.

We will prove later that the part of the self-energy related to static screening cancels completely from the rate of nuclear reactions.

1.3. Arguments against Dynamic Screening

The issue of dynamic screening of thermonuclear reactions has been a subject of debate. Gruzinov [9] has pointed out that the test particle approach seems to be in contradiction with the fact that in the Gibbs distribution kinetic and electrostatic energy factorize according to $\propto\exp(-\sum_i m_i v_i^2/2T)\exp(-\sum_{i,j} Z_iZ_je^2/rT)$. Because of this factorization, Gruzinov claims that the interaction energy cannot depend on the particle velocity and there should be no dynamic screening. This statement, as well as the explicit calculations of [9], requires however to be examined in detail. First of all, one can give an example for which the foregoing factorization takes place and the particles are nevertheless dynamically screened. This is the case of binary particle collisions in a plasma, for which it is well known that the particles collide being dynamically screened [18, 20]. The dynamic screening exists for both test particles and any particle collision, but, in the case of statistical equilibrium, one cannot recognize it due to a balance of direct and inverse processes.

According to [9], screening is purely static; it is assumed that the interacting nuclei are in an electrostatic fluctuating potential $\delta\phi(\mathbf{r})$ produced by all other particles, such a potential being independent of particle velocities. One can thus take, as in [9], the distribution function of nuclei in the form $f_{i,j} \propto \exp(-Z_{i,j}e\phi(\mathbf{r})/T)$. According to [9], the reaction rate R_{ij} should be proportional to the averaged product $\langle f_i f_j \rangle$, while in the absence of screening, it is proportional to $\langle f_i \rangle \langle f_j \rangle$. Therefore,

$$R_{ij} = R_{ij}^{(0)} \frac{\left\langle \exp\left(-\frac{(Z_i + Z_j)e\delta\phi}{T}\right)\right\rangle}{\left\langle \exp\left(-\frac{Z_i e\delta\phi}{T}\right)\right\rangle\left\langle \exp\left(-\frac{Z_j e\delta\phi}{T}\right)\right\rangle} = (1 + \Lambda_{ij}^G)R_{ij}^{(0)}, \quad (23)$$

so that, in the limit $Z_i e\phi/T \ll 1$, the parameter determining the enhancement of the rate of thermonuclear reactions takes the form

$$\Lambda_{ij}^G = \frac{Z_i Z_j e^2}{T^2}\langle(\delta\phi)^2\rangle. \quad (24)$$

Note that expression (23) is such that there is a cancellation of the terms $\propto Z_i^2$ and $\propto Z_j^2$; i.e., there is no contribution to rate (24) from the self-energy of the reacting nuclei. The plasma fluctuation theory is then used for the expression of the square of the fluctuating potential [9]

$$\langle(\delta\phi(\mathbf{r}))^2\rangle = \frac{T}{2\pi^2}\int\frac{d\mathbf{k}}{k^2}\left(1 - \frac{1}{\varepsilon_{\mathbf{k},0}}\right) = \frac{T}{d}, \quad (25)$$

which, along with expression (24), yields Salpeter's weak screening result:

$$\Lambda_{ij}^G = \frac{Z_i Z_j e^2}{Td} = \Lambda_{ij}^S. \quad (26)$$

The main objection to Gruzinov's procedure is the use of relation (25), since such a result of plasma fluctuation theory is specific to temporal fluctuations and dynamic screening, whereas here the fluctuating potential $\delta\phi(\mathbf{r})$ depends on space coordinate $\mathbf{r}$ only. More explicitly, in plasma fluctuation theory, one is dealing with quantities dependent on frequencies and wave vectors, namely,

$$\langle(\delta\phi(\mathbf{r}, t))^2\rangle = \int\frac{d\mathbf{k}d\omega}{(2\pi)^4}\langle(\delta\phi)^2\rangle_{\mathbf{k},\omega}. \quad (27)$$

Result (25) of [9] requires that

$$\langle(\delta\phi(\mathbf{r}))^2\rangle = \int\frac{d\mathbf{k}}{(2\pi)^3}\langle(\delta\phi)^2\rangle_{\mathbf{k}},$$
$$\langle(\delta\phi)^2\rangle_{\mathbf{k}} = \int\frac{d\omega}{2\pi}\langle(\delta\phi)^2\rangle_{\mathbf{k},\omega}, \quad (28)$$

the second of expressions (28) being, however, not available for time-independent fluctuations. Note that it is only the integration with respect to the frequency of the frequency dependent fluctuations that leads to expression (25) containing the static dielectric permittivity $\varepsilon_{\mathbf{k},0}$. In such an integration, all of the frequencies contribute, including high frequencies for which no adiabatic approximation can be used; i.e., the fluctuating potential cannot be considered as only depending on $\mathbf{r}$. The reason why it is the static dielectric permittivity that enters expression (25) has to do with the analytic properties of the dielectric permittivity itself, which has no poles in the upper part of the complex ω plane, so that the ω-integration in the second of expressions (28) can be performed by taking into account only the pole $\omega = 0$. The time (and, thus, frequency) dependence of the fluctuations is crucial. Another reason for the existence of a frequency dependence in the particle fluctuations is that Salpeter's result has to do with the finite plasma temperature, so that the particles move according to their thermal distributions, with the consequence that the fluctuations are necessarily frequency dependent. Furthermore, in the context of the plasma fluctuation theory, the change of the particle distribution function is found to be

$$\delta f \propto \int d\mathbf{k}d\omega\delta\phi_{\mathbf{k},\omega}\frac{(\mathbf{k}\cdot\mathbf{v})}{(\omega - \mathbf{k}\cdot\mathbf{v})}e^{i(\mathbf{k}\cdot\mathbf{r} - \omega t)}, \quad (29)$$

for which the contribution from all frequencies is included. Instead, in [9], it is simply $\delta f \propto \delta\phi(\mathbf{r})$. One should also note that, whereas Salpeter's result [1] stems from the effect on the reaction probability of the static screening of the reacting nuclei, Gruzinov's result [9] is obtained from considering (incorrectly) the change of the nuclear distributions. One might expect that the change of both the nuclei distributions and the reaction probability and possibly cross-effects thereof have to be accounted for.

1.4. Statistical versus Kinetic Approach

The use of a statistical approach seems to be most appropriate to describe the influence on the reaction rates of a plasma in thermal equilibrium. In this respect, an extensive analysis was carried out by Brown and Sawyer [10] on the basis of general quantum statistical mechanics to find out whether the screening of thermonuclear reactions is dynamic or static. Quantum statistical mechanics was adopted presumably because the process of tunneling through the Coulomb barrier relevant to nuclear reactions is a quantum effect. The result of [10] is that the reaction rate is independent of nuclei

velocities and, thus, screening should be static. Similar results were obtained by Ichimaru [8] and Weneser [15]. Here again, one wonders how these results can be reconciled with the test particle results, according to which the static screening for fast ions does not appear to be physical.

One can then wonder whether dynamic screening can be obtained by a statistical approach. In a recent paper [17], it is claimed that the potential felt by a test particle differs from that felt by a particle in statistical equilibrium. In principle, this should be correct because a test particle has a definite velocity and, as such, it should be subjected to a field that is different from that seen by an average thermal particle. On the other hand, a test particle can itself be one of the thermal particles. According to [17], the average potential felt by all particles is independent of the particle kinetic energy only in complete statistical equilibrium, which can indeed be expected on the basis of the detailed balance in statistical equilibrium, according to which any direct process is balanced by the corresponding inverse process and the probabilities of the direct and inverse processes are the same. In plasma physics, this is well known for the Coulomb collision integral, which vanishes for thermal particle distributions, whereas it accounts for dynamic screening of the colliding particles for any deviation from thermal equilibrium and the test particles are always dynamically screened when they interact with other particles by Coulomb forces. The two reacting nuclei play the same role as colliding test particles.

One should also note that the statistical approach has certain subtle aspects that one should worry about. First of all, one is dealing with the *rates* of nuclear reactions and, in this sense, the system considered *is not in total equilibrium.* In particular, with reference to nuclear reactions in which neutrinos are produced in either a single reaction or in a reaction which is a part of a cycle of nuclear processes, the system is optically thin, so that the neutrinos freely leave the system, with the result that no full thermal equilibrium exists. In fact, the inverse process for which the neutrinos are absorbed is not taken into account. Thus, what is of relevance is the *rate* of the reactions, which requires, in general, that the kinetics of the process be considered under conditions for which the direct and inverse processes are not balanced. Instead, in making use of a statistical approach, one might account as well for some of the inverse processes, even if one can argue that the matrix element is considered for the direct process rather than the inverse one. A proper description of the neutrinos' processes requires that only the direct (nonabsorbing) processes are considered, which is precluded within the frame of a statistical approach.

A second question concerns the "identification" of the reacting nuclei. In the statistical approach [10, 15], the reacting nuclei are singled out from the background plasma particles. Indeed, one should consider the reacting nuclei themselves as *plasma particles,* often referred to as *plasma particle excitations* [20, 21]. The reacting nuclei in a plasma are different from free nuclei and should be considered as plasma nuclei, just as the electrons in a solid are different from free electrons due to the electron–lattice interaction, thereby being electron excitations. In a statistical approach, one should account for these excitations in the form of an operator acting on the nuclei and the thermal distributions should refer to the excitations, since one can envisage an equilibrium state only for them. Once the reacting nuclei are considered plasma particles, the statistical approach yields the results obtained below in the frame of a general kinetic approach based on the plasma fluctuation description.

To further clarify the issue of dynamically screened charges, let us recall, based on the kinetic description of nonequilibrium systems, a few well-known results from both plasma physics [18, 20] and the physics of particle radiation and scattering of waves in plasmas [21].

A problem that has been considered for quite a long time concerns the Coulomb interactions of plasma particles and the corresponding kinetic description in terms of the Landau–Balescu collision integral. Such an integral is obtained for arbitrary nonequilibrium particle distributions averaged over plasma fluctuations and describes the interactions of dynamically screened plasma particles [18, 20]. The Landau–Balescu collision integral, which can also be obtained by a test particle approach, is one of the simplest examples of the relevance of dynamically screened plasma particles. There exists a rigid requirement that the test-particle approach leads to results coinciding with those obtained in the kinetic description and this requirement is fulfilled for the Landau–Balescu collision integral. In statistical equilibrium, the Landau–Balescu collision integral is equal to zero, which means that the *Maxwellian distribution is formed only for dynamically screened plasma particles.*

The transition radiation occurring at a plasma–vacuum boundary [21] is yet another process related to the screening of a charge self-field, which is inherent in a bare particle (in vacuum) becoming a dressed plasma particle. Similar to the process of transition radiation, a nucleus produced through a nuclear reaction in a plasma radiates as it acquires its polarization cloud on becoming a plasma particle. The radiation is due to rearrangement of the particle self-field. For nonrelativistic particles, the waves emitted in the process of particle self-field formation are mainly plasma waves.

A further process for which the notion of dressed plasma particles is important is the transition scattering of waves by plasma ions [21], the scattered wave being due to the oscillation of the ion screening cloud. In this process, the plasma ion scatters as a whole in such a way that the ion polarization cloud does not receive energy or momentum as a result of the conservation of energy and momentum in scattering.

In view of the limitations inherent in a statistical approach to the treatment of the nuclear reactions in a plasma, as mentioned above, it appears highly desirable to adopt a kinetic description, which permits one to deal with nonequilibrium particle distributions. Such a kinetic approach can rely on concepts and procedures already developed in the kinetic theory of plasmas, such as the notion of dressed plasma particles.

1.5. Fixed Polarization Charge Approach versus Fluctuation Approach

Salpeter's approach, as well as a number of subsequent approaches, is based on the assumption that the screening of the reacting nuclei is due to charges that are fixed around the nuclei, thus forming a polarization cloud that can be described by using Poisson's equation. One can find a detailed description taking into account the correlations between the polarization charges in the review by Ichimaru [8]. Recently, Gruzinov and Bahcall [16] evaluated nonlinear corrections to static screening by solving the quantum density matrix equation for the electron density in the vicinity of the reacting nuclei, the quantum approach being adopted for the electrons to account for the quantum uncertainty principle. The numerical solution of the nonlinear Poisson–Boltzmann equation is then used as a screened potential to calculate the enhancement of reaction rates; the result obtained agrees (within small uncertainties) with Salpeter's weak screening formula. Such a treatment again rests on the assumption that the screening process is static. The calculation of the electron density in the vicinity of the reacting nuclei was performed using a quantum-diffusion equation applicable in the case of Boltzmann statistics [22], as well as Fermi–Dirac and Maxwell–Boltzmann statistics [23]. With particular reference to the process of nuclear electron capture, it is again concluded that Salpeter's enhancement factor provides the leading corrections.

In contrast with the assumption of a fixed polarization cloud, the dressed plasma particles acquire their polarization clouds through plasma fluctuations, which thus play an important role in the description of dressed plasma particles in equilibrium as well as nonequilibrium plasmas. The effects of plasma fluctuations on nuclear reactions were investigated in [3].

With reference to the nuclear reaction rates in a fluctuating plasma, it is important to take into account that the reactions occur on time scales much shorter than those typical for the formation of nuclei screening clouds by fluctuations. Thus, the screening clouds undergo fluctuations in contrast with Salpeter's assumption of a fixed screening charge, the characteristic times of these fluctuations being related to the time taken by the background plasma particles to cross a Debye distance. As a result of the fluctuating nature of the plasma screening, the screening of the almost instantaneous nuclear reactions can be positive (enhancement of the reaction rate) or negative (slowing the reaction rate), so that the averaged (with respect to fluctuations) effect is likely to differ from the static or dynamic Debye screening.

The fluctuations relevant to the problem under consideration are due to plasma particle collisions, the corresponding frequency being quite high for a dense plasma (e.g., it is on the order of 10^{16} s^{-1} for the solar interior). With respect to the typical collision frequency, the nuclear reaction rates are smaller by many orders of magnitude. With reference to the nuclear reactions, along with the time of crossing the Coulomb barrier, which is very short as compared to the characteristic time scale of the fluctuations, there is the time scale related to the rates of nuclear reactions measuring how often the nuclei crosses the barrier, which is rather long as compared to the time scale of the fluctuations. As consequence of such a time ordering [3], the plasma effects on the nuclear reaction rates can be calculated by using the present fluctuation theory of nonequilibrium plasmas, the relevant fluctuations being the same as the ones due to the binary plasma collisions of dynamically screened plasma particles [3]. One can thus attribute the changes in nuclear reactions by plasma fluctuations to the effect of binary collisions.

According to [3], the plasma fluctuations in the absence of nuclear reactions are responsible for both the screening self-energy and the interaction energy. When the nuclei are far apart, the fluctuations create the self-energy cloud of each nuclei; on the other hand, when the nuclei approach close to each other and undergo nuclear reactions, the fluctuations responsible for the screening of the self-energy and the screening of interactions are not distinguishable and should therefore be treated together. This effect substantially changes the nuclear reaction rates [3].

1.6. Outline of the Content and Description of the Fluctuation Approach

The aim of this paper is to calculate the nuclear reaction rates in dense plasmas on the basis of the general fluctuation approach to nonequilibrium plasmas.

In Section 2, we recall the derivation of the binary collision integral for a plasma, because we will need the expressions for the plasma fluctuations in the absence of nuclear reactions to generalize the fluctuation approach to account for the nuclear reactions and to evaluate the influence of the fluctuations on the nuclear reaction rates. In a certain approximation, one can treat the effects of nuclear reactions on fluctuations, assuming that the reaction rates are not changed by fluctuations, and the corresponding inverse effects (namely, the influence of fluctuations on nuclear reaction rates), assuming that the fluctuations are not changed by nuclear reactions. In this limit, one refers equivalently to the change of nuclear reactions by fluctuations that produce the binary collisions or to the influence of collisions on nuclear reactions. In fact, such an approach

includes both the polarization effect and the effect of fluctuations responsible for the binary collisions, the two effects being treated together.

In Section 3, we introduce the microscopic probability of a nuclear reaction between the nuclei *i* and *j*, taking into account the effect of an external fluctuating potential, but neglecting the interaction of nuclei with any other particle, and generalize the usual approach by averaging the relevant kinetic equations with respect to fluctuations. The expression for the reaction rates of *dressed plasma nuclei* is finally obtained by expanding the probability in powers of the fluctuating potential. Following [3], we will show that the reaction rates with the effect of the fluctuations responsible for the binary collisions accounted for can be obtained for the case where the rates of nuclear reactions are much less than the frequency of the fluctuating field.

Section 4 is devoted to the self-energy issue and comprises the evaluation of the free energy related to the self-energy and the renormalization procedure applied to the equations for the nuclear reaction rates. The physical meaning of renormalization and the corresponding relation to the self-energy of the nuclei are discussed. Here, one is dealing with effects not specific to nuclear reactions, the general properties of dressed plasma particles are addressed, and the concept of dressed particles is emphasized. Renormalization is a necessary element in the calculation of the nuclear reaction rates, and the results of this section are used in subsequent sections.

In Section 5, the quantum description of tunneling is outlined and the corresponding probability is obtained in the presence of arbitrary fluctuating fields whose space and time variations occur over distances and time intervals significantly larger than the nuclear size and the crossing time of the potential barrier, respectively. With the expressions thus obtained, one can both assess the validity of the expansions in the fluctuating field and find the averaged kinetic equations that take into account the collective effects of the plasma particles on the two reacting nuclei.

In Section 6, we consider the specific case of a thermal plasma with thermal distributions of *plasma nuclei* and find that *there is complete cancellation of Salpeter-type terms, connected with the static screening, as well as the terms related to the static self-energy* [3]. Such a result stems from the interference of the fluctuations responsible for the screening effects on the interactions between the nuclei and the fluctuations responsible for the self-energy of each interacting nuclei. The nonzero contributions are related to the dynamically screened free energy of the two nuclei, in accordance with the test particle approach. The net effect is of the opposite sign as compared to Salpeter's result; i.e., *the rates of nuclear reactions in plasmas are slower than the corresponding rates in vacuum*, the slowing down being the greater, the higher are the nuclear charges. A simple physical explanation of the *Z*-dependence is given, which has to do with the decrease of the free energy related to the dynamically screened part of self-energy as the nuclei velocities increase to match the higher Gamow energy for higher *Z* [3].

In Section 7, numerical results for the nuclear reactions relevant to the solar interior are discussed in the connection with the solar neutrino problem.

In Section 8, issues concerning nonlinear fluctuations, the strong influence of fluctuations on the rate of nuclear reactions, the reaction rate in nonequilibrium and turbulent plasmas, and emission of plasma and acoustic waves during the nuclear reactions are addressed.

2. BINARY PLASMA PARTICLE COLLISIONS

The problem of binary Coulomb collisions in plasmas has been addressed on the basis of sophisticated correlation function methods. In this respect, early work was done by Bogolyubov [24] and Klimontovich [25], the topic being one of the most developed fields in plasma physics. Here, we outline the derivation of the plasma collision integral given by one of the authors in [20] with the aim of describing the dynamic screening in binary collisions, as well as including nuclear collisions. In the context of this section, we make a few general physical statements that are rarely emphasized in connection with the issue of binary plasma collisions. One such statement is that the correct procedure of getting a proper description of both collective and polarization effects in binary collisions is based on averaging over fluctuations. The generalization of the fluctuation approach developed for binary collisions is used to evaluate the influence on the rates of nuclear reactions of plasma fluctuations related to binary collisions.

2.1. Derivation of the Binary Coulomb Collision Integral with Dynamic Screening

Following the formalism of the kinetic theory of plasma fluctuations [18, 20], let us write the distribution function (e.g., for nuclei of species *i*) as

$$f_i(\mathbf{r}, \mathbf{p}, t) = \Phi_i(\mathbf{p}, t) + \delta f_i(\mathbf{r}, \mathbf{p}, t), \tag{30}$$

such that

$$\Phi_i(\mathbf{p}, t) = \langle f_i(\mathbf{r}, \mathbf{p}, t)\rangle \tag{31}$$

is the homogeneous distribution function of dressed particles, i.e., particles surrounded by their screening cloud. Here, the brackets $\langle\ldots\rangle$ denote the average with respect to fluctuations and δf_i is the fluctuating part of the distribution function, such that $\langle\delta f_i\rangle = 0$. The distribution function f_i is such that

$$n_i(\mathbf{r}, t) = \int \frac{d\mathbf{p}}{(2\pi)^3} f_i(\mathbf{r}, \mathbf{p}, t), \tag{32}$$

n_i being the number density of particles of species *i*.

The kinetic equation for f_i is

$$\frac{\partial f_i}{\partial t} + \mathbf{v}\cdot\frac{\partial f_i}{\partial \mathbf{r}} - Z_i e(\nabla\delta\phi)\cdot\frac{\partial f_i}{\partial \mathbf{p}} = 0, \tag{33}$$

the only effect of the fluctuating potential $\delta\phi$ being considered. By averaging Eq. (33) and afterwards subtracting the averaged equation from Eq. (33), we obtain the following two equations:

$$\frac{\partial \Phi_i}{\partial t} = Z_i e\frac{\partial}{\partial \mathbf{p}}\cdot\langle(\nabla\delta\phi)\delta f_i\rangle, \tag{34}$$

$$\frac{\partial \delta f_i}{\partial t} + \mathbf{v}\cdot\frac{\partial \delta f_i}{\partial \mathbf{r}} - Z_i e(\nabla\delta\phi)\cdot\frac{\partial \Phi_i}{\partial \mathbf{p}} = 0. \tag{35}$$

In Eq. (35), only the terms linear in fluctuations are kept. Assuming that the time variations of the averaged part of the distribution function are much slower than those of the fluctuating part, one obtains the solution of Eq. (35) in terms of the space-time Fourier transform

$$\delta f_{i,\mathbf{k},\omega}(\mathbf{p}) = \delta f^{(0)}_{i,\mathbf{k},\omega}(\mathbf{p}) - \frac{Z_i e\delta\phi_{\mathbf{k},\omega}}{\omega - \mathbf{k}\cdot\mathbf{v} + i0}\left(\mathbf{k}\cdot\frac{\partial \Phi_i}{\partial \mathbf{p}}\right). \tag{36}$$

On the right-hand side of Eq. (36), the first term is due to the free particle motion, the autocorrelation function of which is [20]

$$\langle \delta f^0_{i,\mathbf{k},\omega}(\mathbf{p})\delta f^0_{j,\mathbf{k}',\omega'}(\mathbf{p}')\rangle = \Phi_i(\mathbf{p})\delta_{i,j}\delta(\mathbf{p}-\mathbf{p}')\delta(\mathbf{k}+\mathbf{k}')\delta(\omega+\omega')\delta(\omega-\mathbf{k}\cdot\mathbf{v}), \tag{37}$$

and the second term is related to the electrostatic particle interaction, the corresponding fluctuating potential being obtained by using Poisson's equation

$$\delta\phi_{\mathbf{k},\omega} = \frac{4\pi e}{k^2\varepsilon_{\mathbf{k},\omega}}\left(-\int\frac{d\mathbf{p}}{(2\pi)^3}\delta f^{(0)}_{e,\mathbf{k},\omega}(\mathbf{p}) + \sum_i Z_i\int\frac{d\mathbf{p}}{(2\pi)^3}\delta f^{(0)}_{i,\mathbf{k},\omega}(\mathbf{p})\right). \tag{38}$$

In expression (38), both the contributions of electrons and ions are taken into account. The right-hand side of relation (38) contains the fluctuating distributions of noninteracting particles, whereas the contributions from the particle interactions are accounted for through the dielectric permittivity $\varepsilon_{\mathbf{k},\omega}$:

$$\varepsilon_{\mathbf{k},\omega} = 1 + \frac{4\pi e^2}{k^2}\left[\int\frac{d\mathbf{p}}{(2\pi)^3}\frac{1}{\omega-\mathbf{k}\cdot\mathbf{v}+i0}\left(\mathbf{k}\cdot\frac{\partial \Phi_e}{\partial \mathbf{p}}\right) + \sum_i Z_i^2\int\frac{d\mathbf{p}}{(2\pi)^3}\frac{1}{\omega-\mathbf{k}\cdot\mathbf{v}+i0}\left(\mathbf{k}\cdot\frac{\partial \Phi_i}{\partial \mathbf{p}}\right)\right]. \tag{39}$$

For the case where Φ_e and Φ_i are Maxwellian, expression (39) reduces to formula (7) with (8).

In expressions (36) and (39), the denominator $(\omega - \mathbf{k}\cdot\mathbf{v} + i0)$ accounts for the causality principle and should be dealt with according to (the Plemelj formula)

$$\frac{1}{\omega-\mathbf{k}\cdot\mathbf{v}+i0} = P\frac{1}{\omega-\mathbf{k}\cdot\mathbf{v}} - i\pi\delta(\omega-\mathbf{k}\cdot\mathbf{v}), \tag{40}$$

where P denotes the principal value. In view of relation (40), the imaginary part of the dielectric permittivity (39) is

$$\mathrm{Im}\,\varepsilon_{\mathbf{k},\omega} = -\frac{4\pi^2 e^2}{k^2}\int\frac{d\mathbf{p}}{(2\pi)^3} \times\left[\left(\mathbf{k}\cdot\frac{\partial \Phi_e}{\partial \mathbf{p}}\right) + \sum_i Z_i^2\left(\mathbf{k}\cdot\frac{\partial \Phi_i}{\partial \mathbf{p}}\right)\right]\delta(\omega-\mathbf{k}\cdot\mathbf{v}), \tag{41}$$

$$\mathrm{Im}\varepsilon_{\mathbf{k},\omega} = \frac{4\pi^2 e^2\omega}{Tk^2}\int\frac{d\mathbf{p}}{(2\pi)^3}\left[\Phi_e(\mathbf{p}) + \sum_i Z_i^2\Phi_i(\mathbf{p})\right]\delta(\omega-\mathbf{k}\cdot\mathbf{v}), \tag{42}$$

where expression (42) refers to a thermal plasma. The right-hand side of Eq. (34) is related to the collision integral; introducing expressions (36)–(38) into Eq. (34) yields the Landau–Balescu form of the collision integral [18, 20]

$$Z_i e\frac{\partial}{\partial \mathbf{p}}\cdot\langle\nabla(\delta\phi)\delta f_i\rangle \equiv I_i^{(C)} = I_{i,e} + \sum_j I_{ij}, \tag{43}$$

with

$$I_{ij} = 2Z_i^2 Z_j^2 e^4\int\frac{d\mathbf{p}'d\mathbf{k}}{(2\pi)^3}\left(\mathbf{k}\cdot\frac{\partial}{\partial \mathbf{p}}\right)\frac{\delta(\mathbf{k}\cdot\mathbf{v}-\mathbf{k}\cdot\mathbf{v}')}{k^4|\varepsilon_{\mathbf{k},\mathbf{k}\mathbf{v}}|^2} \times\left[\Phi_j(\mathbf{p}')\left(\mathbf{k}\cdot\frac{\partial \Phi_i(\mathbf{p})}{\partial \mathbf{p}}\right) - \Phi_i(\mathbf{p})\left(\mathbf{k}\cdot\frac{\partial \Phi_j(\mathbf{p}')}{\partial \mathbf{p}'}\right)\right]. \tag{44}$$

This integral describes the Coulomb collisions of dynamically screened particles, the screening being accounted for by the dielectric permittivity $\varepsilon_{\mathbf{k},\mathbf{k}\cdot\mathbf{v}}$. From this equation, one can obtain the expression for the change of the momentum of particle i per unit time in the form of an expression averaged with respect to the particle distribution and referred to as an average force acting on particle i. By comparing this force with the force acting on a test particle moving in a medium with the dielectric permittivity $\varepsilon_{\mathbf{k},\omega}$, one finds that these two forces are equal. This coincidence can be considered as a check on the theory of the collision integral valid for any nonequilibrium particle distribution, including the distribution corresponding to an ensemble of particles plus the test particle. The same statements should be true for nuclear reaction collisions in plasmas if they are described for the general case of nonequilibrium particle distributions. The dynamic screening described by expression (44) occurs for all plasma particles and this screening is due to fluctuations. The particles

described by expression (44) are the dressed plasma particles and their distribution is Maxwellian for equilibrium states, for which integral (44) vanishes. The undressed particles cannot be in an equilibrium state, and the corresponding distribution function varies in time until all plasma particles become dressed particles and reach the thermal distribution.

2.2. A Few Correlations of Fluctuations Accounting for Screening

The use of expressions (37) and (38) yields the autocorrelation function of the fluctuating potential,

$$\langle \delta\phi^2 \rangle = (4\pi e)^2 \int \frac{d\mathbf{p}\,d\mathbf{k}\,d\omega}{(2\pi)^6} \frac{1}{k^4 |\varepsilon_{\mathbf{k},\,\mathbf{k}\cdot\mathbf{v}}|^2} \times \left(\Phi_e(\mathbf{p}) + \sum_i Z_i^2 \Phi_i(\mathbf{p}) \right) \delta(\omega - \mathbf{k}\cdot\mathbf{v}), \tag{45}$$

which accounts for the effect of the dynamically screened particles through the dielectric permittivity evaluated at a frequency equal to $\mathbf{k}\cdot\mathbf{v}$. For the specific case of a thermal plasma, for which relation (42) holds, expression (45) takes the form

$$\langle (\delta\phi)^2 \rangle = -\frac{T}{2\pi^3} \int \frac{d\omega\,d\mathbf{k}}{\omega k^2} \mathrm{Im}\left(\frac{1}{\varepsilon_{\mathbf{k},\,\omega}} \right) \tag{46}$$

in agreement with the fluctuation–dissipation theorem. To carry out integration over ω in expression (46), let us first note the identity

$$\frac{1}{\omega} \mathrm{Im}\left(\frac{1}{\varepsilon_{\mathbf{k},\,\omega}} \right) = \mathrm{Im}\left[\frac{1}{\omega + i0} \left(\frac{1}{\varepsilon_{\mathbf{k},\,\omega}} - 1 \right) \right] + \pi\delta(\omega) \mathrm{Re}\left[\frac{1}{\varepsilon_{\mathbf{k},\,\omega}} - 1 \right]. \tag{47}$$

The first term on the right-hand side of identity (47) has no poles in the upper part of the complex ω plane. On account of its proportionality to $(1/\varepsilon_{\mathbf{k},\,\omega} - 1)$ and the analytical properties of dielectric permittivity for a thermal plasma, this term makes no contribution to integration over ω in expression (46). Thus, we obtain

$$\langle \delta\phi^2 \rangle = -\frac{T}{2\pi^2} \int \frac{d\mathbf{k}}{k^2} \left(\frac{1}{\varepsilon_{\mathbf{k},\,0}} - 1 \right). \tag{48}$$

We note that result (48) can also be obtained by applying the Kramers–Kronig relation [18, 19]:

$$P \int_{-\infty}^{\infty} d\omega \frac{1}{\omega - \omega'} \mathrm{Im}\left(\frac{1}{\varepsilon_{\mathbf{k},\,\omega}} \right) = \pi \left[\left(\mathrm{Re} \frac{1}{\varepsilon_{\mathbf{k},\,\omega'}} \right) - 1 \right]. \tag{49}$$

As already discussed in Section 1.3, result (48) accounts for the particle dynamic screening, notwithstanding the presence of the static dielectric permittivity $\varepsilon_{\mathbf{k},\,0}$.

As for the autocorrelation function of the fluctuating part of the distribution function, using the same procedure as before yields

$$\langle \delta f_i(\mathbf{p}) \delta f_j(\mathbf{p}') \rangle = \frac{4 Z_i Z_j e^2 \Phi_i(\mathbf{p}) \Phi_j(\mathbf{p}')}{T(2\pi)^3} \times \int d\mathbf{k}\,d\omega \frac{(\mathbf{k}\cdot\mathbf{v})(\mathbf{k}\cdot\mathbf{v}')}{k^2\omega} \times \left[\frac{1}{(\omega - \mathbf{k}\cdot\mathbf{v} + i0)(-\omega + \mathbf{k}\cdot\mathbf{v}' + i0)} \mathrm{Im} \frac{1}{\varepsilon_{\mathbf{k},\,\omega}} - \delta(\omega - \mathbf{k}\cdot\mathbf{v}) \frac{\pi}{(-\omega + \mathbf{k}\cdot\mathbf{v}' + i0)\varepsilon_{-\mathbf{k},\,-\omega}} + \delta(\omega - \mathbf{k}\cdot\mathbf{v}') \frac{\pi}{(\omega - \mathbf{k}\cdot\mathbf{v} + i0)\varepsilon_{\mathbf{k},\,\omega}} \right]. \tag{50}$$

By means of simple algebra, the expression within the square brackets divided by ω is converted to

$$-\mathrm{Im}\left\{ \frac{1}{(\omega + i0)\varepsilon_{\mathbf{k},\,\omega}(\omega - \mathbf{k}\cdot\mathbf{v} + i0)(\omega - \mathbf{k}\cdot\mathbf{v}' + i0)} \right\} - \pi\delta(\omega) \mathrm{Re}\left\{ \frac{1}{\varepsilon_{\mathbf{k},\,\omega}(\mathbf{k}\cdot\mathbf{v})(\mathbf{k}\cdot\mathbf{v}')} \right\}. \tag{51}$$

Again, the first term does not contribute to integration over ω due to the analytical properties of the dielectric permittivity [in contrast to identity (47), we do not need to subtract 1] and expression (50) reduces to

$$\langle \delta f_i(\mathbf{p}) \delta f_j(\mathbf{p}') \rangle = -\frac{Z_i Z_j e^2}{2\pi^2 T} \Phi_i(\mathbf{p}) \Phi_j(\mathbf{p}') \int \frac{d\mathbf{k}}{k^2} \left(\frac{1}{\varepsilon_{\mathbf{k},\,0}} \right). \tag{52}$$

Proceeding in the same way, for the correlation between the fluctuating particle distribution and the fluctuating potential, one obtains

$$\langle \delta f_i(\mathbf{p}) \delta\phi \rangle = \frac{Z_i e \Phi_i(\mathbf{p})}{2\pi^2} \int \frac{d\mathbf{k}}{k^2} \left(\frac{1}{\varepsilon_{\mathbf{k},\,0}} \right). \tag{53}$$

For the case where we include only the polarization fluctuating potential, we should substitute $1/\varepsilon_{\mathbf{k},\,0}$ with $(1/\varepsilon_{\mathbf{k},\,0} - 1)$ in formulas (52) and (53), whereas expression (48) remains unchanged.

3. FLUCTUATION-AVERAGED EQUATIONS FOR NUCLEAR REACTIONS IN PLASMAS

Let us now establish the equations governing the nuclear reactions in a nonequilibrium plasma with particular attention paid to the effects caused by plasma fluctuations. Of relevance to the nuclear reaction between the nuclei i and j is the tunneling probability

$w_{ij}(\mathbf{p}, \mathbf{p}')$, which is the probability relative to tunneling through the Coulomb barrier of nuclei i in the reaction with nuclei j and depends on both the momentum $\mathbf{p}$ of the particle i and the momentum $\mathbf{p}'$ of the particle j, both momenta being referred to the laboratory frame. The probability $w_{ji}(\mathbf{p}', \mathbf{p})$, entering the equation for nuclei j, is the corresponding tunneling probability of nuclei j. In the general case, $w_{ij}(\mathbf{p}, \mathbf{p}') \neq w_{ji}(\mathbf{p}', \mathbf{p})$ in the presence of fluctuations of the potential barrier, the fluctuations being induced by the fluctuating potential. We also note that, although the effects of the fluctuations of the potential barrier due to the presence of an external fluctuating potential are accounted for in w_{ij} and w_{ji}, neither the polarization nor the self-energy of the nuclei (both due to the presence of the plasma) are included. These latter effects need to be calculated separately. The probabilities w_{ij} and w_{ji} describe the tunneling in the absence of plasma particles but in the presence of the fluctuating potential. The total reaction rate should be obtained as sum of these two probabilities multiplied by the product of the nuclei distribution functions and then integrated over the phase volume. In the absence of fluctuations, the average distributions Φ_i and Φ_j in a thermal plasma are just the thermal distributions. Denoting the tunneling probabilities in the absence of fluctuations with $w_{ij}^{(0)}(\mathbf{p}, \mathbf{p}')$ and $w_{ji}^{(0)}(\mathbf{p}', \mathbf{p})$, the corresponding reaction rate $R_{ij}^{(0)}$ for bare nuclei is

$$R_{ij}^{(0)} = \frac{1}{1+\delta_{i,j}}\int\frac{d\mathbf{p}d\mathbf{p}'}{(2\pi)^6}(w_{ij}^{(0)}(\mathbf{p}, \mathbf{p}') + w_{ji}^{(0)}(\mathbf{p}', \mathbf{p}))\Phi_i^{(M)}(\mathbf{p})\Phi_j^{(M)}(\mathbf{p}'), \tag{54}$$

where the superscript $(^M)$ in the distribution functions means that they are Maxwellian (thermal). In terms of the total probability

$$\bar{w}_{ij}^{(0)}(\mathbf{p}, \mathbf{p}') = w_{ij}^{(0)}(\mathbf{p}, \mathbf{p}') + w_{ji}^{(0)}(\mathbf{p}', \mathbf{p}) = 2w_{ij}^{(0)}(\mathbf{p}, \mathbf{p}'), \tag{55}$$

the reaction rate (54) can be expressed as

$$R_{ij}^{(0)} = \frac{1}{1+\delta_{i,j}}\int\frac{d\mathbf{p}d\mathbf{p}'}{(2\pi)^6}\bar{w}_{ij}^{(0)}(\mathbf{p}, \mathbf{p}')\Phi_i^{(M)}(\mathbf{p})\Phi_j^{(M)}(\mathbf{p}'). \tag{56}$$

The effects of fluctuations will be assumed to be weak, the same as for the weak screening approximation in Salpeter's approach, which permits one to expand the probability in powers of $\delta\phi$:

$$w_{ij}(\mathbf{p}, \mathbf{p}') = w_{ij}^{(0)}(\mathbf{p}, \mathbf{p}') + \hat{w}_{ij}^{(1)}(\mathbf{p}, \mathbf{p}')\delta\phi + \hat{w}_{ij}^{(2)}(\mathbf{p}, \mathbf{p}')(\delta\phi)^2 \tag{57}$$

(and, analogously, for $w_{ji}(\mathbf{p}', \mathbf{p})$), where, in the general case, $\hat{w}^{(1)}$ and $\hat{w}^{(2)}$ are operators. One should recall that the probability of a nuclear reaction is, in general, very small, which means that the tunneling occurs rarely, but the time of the tunneling is very fast, so that, during the tunneling, the fluctuation potential, as well as the positions of the interacting nuclei, does not change appreciably. This will allow us to find explicitly the expressions for $\hat{w}_{ij}^{(1)}$ and $\hat{w}_{ij}^{(2)}$.

The kinetic equation governing the distribution function of nuclei i,

$$f_i(\mathbf{r}, \mathbf{p}, t) \equiv f_i(\mathbf{p}), \tag{58}$$

is

$$\frac{\partial f_i(\mathbf{p})}{\partial t} + \mathbf{v}\cdot\frac{\partial f_i(\mathbf{p})}{\partial \mathbf{r}} - Z_i e(\nabla\delta\phi)\cdot\frac{\partial f_i(\mathbf{p})}{\partial \mathbf{p}} = -\frac{1}{1+\delta_{i,j}}\int\frac{d\mathbf{p}'}{(2\pi)^3}w_{ij}(\mathbf{p}, \mathbf{p}')f_i(\mathbf{p})f_j(\mathbf{p}'). \tag{59}$$

The corresponding equation for $f_j(\mathbf{p}')$ is given by Eq. (59) with $i \longleftrightarrow j$ and $\mathbf{p} \longleftrightarrow \mathbf{p}'$. The right-hand side of Eq. (59) accounts for the nuclear reactions [cf. (33)].

By proceeding in the same way as for the derivation of the collision integral in Section 2.1 and taking into account expansion (57), one obtains from Eq. (59) the following two equations:

$$\frac{\partial\Phi_i(\mathbf{p})}{\partial t} = Z_i e\frac{\partial}{\partial\mathbf{p}}\cdot\langle(\nabla\delta\phi)\delta f_i(\mathbf{p})\rangle - \frac{1}{1+\delta_{i,j}}\int\frac{d\mathbf{p}'}{(2\pi)^3}\{w_{ij}^{(0)}(\mathbf{p}, \mathbf{p}')[\Phi_i(\mathbf{p})\Phi_j(\mathbf{p}') + \langle\delta f_i(\mathbf{p})\delta f_j(\mathbf{p}')\rangle] + \hat{w}_{ij}^{(1)}(\mathbf{p}, \mathbf{p}')[\Phi_i(\mathbf{p})\langle\delta\phi\delta f_j(\mathbf{p}')\rangle + \Phi_j(\mathbf{p}')\langle\delta\phi\delta f_i(\mathbf{p})\rangle] + \hat{w}_{ij}^{(2)}(\mathbf{p}, \mathbf{p}')\Phi_i(\mathbf{p})\Phi_j(\mathbf{p}')\langle\delta(\phi)^2\rangle\}, \tag{60}$$

$$\frac{\partial\delta f_i(\mathbf{p})}{\partial t} + \mathbf{v}\cdot\frac{\partial}{\partial\mathbf{r}}\delta f_i(\mathbf{p}) - Z_i e(\nabla\delta\phi)\cdot\frac{\partial\Phi_i(\mathbf{p})}{\partial\mathbf{p}} = -\frac{1}{1+\delta_{i,j}}\int\frac{d\mathbf{p}'}{(2\pi)^3}\{w_{ij}^{(0)}(\mathbf{p}, \mathbf{p}')[\Phi_i(\mathbf{p})\delta f_j(\mathbf{p}') + \Phi_j(\mathbf{p}')\delta f_i(\mathbf{p})] + \hat{w}_{ij}^{(1)}(\mathbf{p}, \mathbf{p}')\Phi_i(\mathbf{p})\Phi_j(\mathbf{p}')\delta\phi\} \tag{61}$$

and similar equations for Φ_j and δf_j. These equations generalize the corresponding equations for the binary plasma collisions to include the effects of nuclear reactions.

To proceed further, we note that the most interesting case is that for which any collisional process is much faster than the nuclear reaction, so that one can deal with the fluctuations by a perturbative method, taking the effect of binary collision fluctuations as a zero-order effect:

$$\delta f = \delta f^C + \delta f^N, \quad \delta f^N \ll \delta f^C, \tag{62}$$

where the superscripts C and N denote the effects due to Coulomb collisions and nuclear reactions, respectively. From Eq. (61), one then obtains an equation for δf^C, which, to lowest order in $|\delta f^N/\delta f^C| \ll 1$, is the same

as Eq. (35); δf^C is thus known and plays the role of a source in the equation for δf^N.

For completeness, we give the expression for $\delta f^{(N)}$, although it is really needed for the evaluation of the change of the rate of binary collisions by nuclear reactions and not for the rate of nuclear reactions (as shown below):

$$\delta f^{(N)}_{i,\mathbf{k},\omega}(\mathbf{p}) = -\frac{Z_i e}{\omega - \mathbf{k}\cdot\mathbf{v} + i0}\delta\phi^{(N)}_{\mathbf{k},\omega}\left(\mathbf{k}\cdot\frac{\partial\Phi_i(\mathbf{p})}{\partial\mathbf{p}}\right)$$
$$-\frac{i}{(1+\delta_{i,j})(\omega-\mathbf{k}\cdot\mathbf{v}+i0)}\int\frac{d\mathbf{p}'}{(2\pi)^3}[w^{(0)}_{ij}(\mathbf{p},\mathbf{p}')(\delta f^{(C)}_{i,\mathbf{k},\omega}(\mathbf{p})\Phi_j(\mathbf{p}') \tag{63}$$
$$+\delta f^{(C)}_{j,\mathbf{k},\omega}(\mathbf{p}')\Phi_i(\mathbf{p})) + \hat{w}^{(1)}_{ij}(\mathbf{p},\mathbf{p}')\delta\phi^{(C)}_{\mathbf{k},\omega}\Phi_i(\mathbf{p})\Phi_j(\mathbf{p}')].$$

Using this expression along with Poisson's equation, one finds the change of the fluctuating potential by the nuclear reactions; substituting it into expression (63) yields the effect of the nuclear reactions on the fluctuations, through both the probability and the fluctuations responsible for Coulomb collisions.

In the linear approximation for fluctuations related to nuclear reactions, the collision integral on the right-hand side of the averaged Eq. (60) can be written in the form

$$\frac{\partial\Phi_i(\mathbf{p})}{\partial t} = I^{(C)}_i(\mathbf{p}) + I^{(N)}_i(\mathbf{p}), \tag{64}$$

where $I^{(C)}_i$ is the Coulomb collision integral as given by expression (43) and I^N_i is

$$I^N_i(\mathbf{p}) = \frac{\partial}{\partial t}(\hat{I}^{(R)}_i(\mathbf{p})\Phi_i(\mathbf{p})) + Z_i e\frac{\partial}{\partial\mathbf{p}}\cdot\langle\delta f^{(C)}_i(\mathbf{p})\nabla\delta\phi^N$$
$$+\delta f^{(N)}_i(\mathbf{p})\nabla\delta\phi^{(C)}\rangle) - \frac{1}{1+\delta_{i,j}}\int\frac{d\mathbf{p}'}{(2\pi)^3}\{w^{(0)}_{ij}[\Phi_i(\mathbf{p})\Phi_j(\mathbf{p}') \tag{65}$$
$$+\langle\delta f^{(C)}_i(\mathbf{p})\delta f^{(C)}_j(\mathbf{p}')\rangle] + \hat{w}^{(2)}_{ij}\Phi_i(\mathbf{p})\Phi_j(\mathbf{p}')\langle(\delta\phi^{(C)})^2\rangle$$
$$+\hat{w}^{(1)}_{ij}[\langle\delta f^{(C)}_i(\mathbf{p})\delta\phi^{(C)}\rangle\Phi_j(\mathbf{p}') + \langle\delta f^{(C)}_j(\mathbf{p}')\delta\phi^{(C)}\rangle\Phi_i(\mathbf{p})]\}.$$

All the terms in (65) except for the first one are obtained in a straightforward manner. The first term is proportional to the time derivative of the averaged distribution function and is new with respect to the binary collision integral. In the derivation of the collision integral (44), we neglect the contribution from the time derivative of the averaged distribution function on the assumption that the corresponding time variation is much slower than the characteristic time of the fluctuations. To keep such a term would have been a higher (second) order correction to the collision integral. In contrast, in (65), the term proportional to the time derivative of the average distribution is accounted for, because here we are interested in the *rates* of the nuclear reactions; i.e., the nuclear reaction time dependences are relevant. We will show that this term is of the same order as the other terms occurring in (65). The new term is to be referred to as the *distribution function renormalization* term (hereafter, the superscript ^{R} stands for renormalization). The justification for such a notation is related to the fact that, by moving this term to the left-hand side of Eq. (64), we can write the left-hand side in the form

$$\frac{\partial}{\partial t}(\Phi_i(\mathbf{p}) - \hat{I}^{(R)}\Phi_i(\mathbf{p})) \equiv \frac{\partial}{\partial t}\Phi^{(R)}_i(\mathbf{p}), \tag{66}$$

where $\Phi^{(R)}_i$ is referred to as the renormalized distribution function. Below, we will show explicitly how such a renormalization can be performed.

The terms occurring in (65) that are proportional to the momentum derivative conserve the number of particles and are not related to the change of the nuclear reaction rate; they describe the influence of nuclear reactions on the binary collisions. Such terms do not contribute to expression (65) upon integrating with respect to the particle momentum; thus, we do not need to take them into account in calculating the reaction rates.

We are now able to express the reaction rates through the renormalized particle distributions assuming that the renormalization term is small and substituting in it the renormalized distribution function $\Phi^{(R)}_i$ [see (66)]:

$$\Phi_i(\mathbf{p}) = \Phi^{(R)}_i(\mathbf{p}) + \hat{I}^{(R)}\Phi^{(R)}_i(\mathbf{p}). \tag{67}$$

Since the renormalization effect is taken to be small, we need to take into account the difference between Φ_i and $\Phi^{(R)}_i$ and, analogously, the difference between Φ_j and $\Phi^{(R)}_j$ only in the zeroth-order term containing the product of the two averaged distribution functions $\Phi_i\Phi_j$; in such a way, all of the terms on the right-hand side of (65) are expressed through the renormalized distribution function.

A similar procedure is performed for the equation for Φ_j. The equations are then integrated with respect to the momenta and summed up to give the expression for the rate of nuclear reactions:

$$R_{ij} = \frac{1}{1+\delta_{i,j}}\int\frac{d\mathbf{p}'d\mathbf{p}}{(2\pi)^6}\{(w^{(0)}_{ij}(\mathbf{p},\mathbf{p}') + w^{(0)}_{ji}(\mathbf{p}',\mathbf{p}))$$
$$\times[\Phi^{(R)}_i(\mathbf{p})\Phi^{(R)}_j(\mathbf{p}') + \langle\delta f^{(C)}_i(\mathbf{p})\delta f^{(C)}_j(\mathbf{p}')\rangle]$$

$$+ w_{ij}^{(0)}(\mathbf{p}, \mathbf{p}')\Phi_j^{(R)}(\mathbf{p}')\hat{I}^{(R)}(\mathbf{p})\Phi_i^{(R)}(\mathbf{p})$$

$$+ w_{ji}^{(0)}(\mathbf{p}', \mathbf{p})\Phi_i^{(R)}(\mathbf{p})\hat{I}^{(R)}(\mathbf{p}')\Phi_j^{(R)}(\mathbf{p}')] \quad (68)$$

$$+ (\hat{w}_{ij}^{(1)}(\mathbf{p}, \mathbf{p}') + \hat{w}_{ji}^{(1)}(\mathbf{p}', \mathbf{p}))[\langle \delta f_i^{(C)}(\mathbf{p})\delta\phi^{(C)}\rangle\Phi_j^{(R)}(\mathbf{p}')$$

$$+ \langle \delta f_j^{(C)}(\mathbf{p}')\delta\phi^{(C)}\rangle\Phi_i^{(R)}(\mathbf{p})] + (\hat{w}_{ij}^{(2)}(\mathbf{p}, \mathbf{p}')$$

$$+ \hat{w}_{ji}^{(2)}(\mathbf{p}', \mathbf{p}))\langle(\delta\phi^{(C)})^2\rangle\Phi_i^{(R)}(\mathbf{p})\Phi_j^{(R)}(\mathbf{p}')\}.$$

This expression contains only the fluctuations in the absence of nuclear reactions. For an explicit evaluation of (68), we need to find both the renormalization and the changes in the probability of tunneling due to arbitrary fluctuations. As for the renormalization, it will be shown that the renormalized distribution function describes the "dressed" particles, i.e., the particle excitations in a plasma. In thermal equilibria, the particle excitations should have Maxwellian distributions, and, thus, the part of expression (68) proportional to $\Phi_i^{(R)}\Phi_j^{(R)}$ is just the reaction rate for bare nuclei $R_{ij}^{(0)}$ given by (56). It is therefore convenient to write (68) as [cf. (5)]

$$R_{ij} = (1 + \Lambda_{ij})R_{ij}^{(0)}, \quad (69)$$

where the quantity Λ_{ij}, which accounts for the change in the rate of nuclear reactions in plasmas, is more general than Salpeter's correction, because it takes into account in general form all fluctuating fields produced by other plasma particles.

4. RENORMALIZATION OF THE PARTICLE DISTRIBUTION FUNCTION

The renormalization of the distribution function is a technique used in most kinetic theories [26]. The reason why this effect is not taken into account in the problem of binary particle collisions is that it provides corrections to the collision integral to higher orders in the small parameter inherent in the linear approximation to fluctuations, namely, $(4\pi d^3 n/3)^{-1}$, which is the reciprocal of the number of particles in the Debye sphere. However, for the problem under consideration here, these corrections are important, being of the same order as the other ones.

Generally, any response function of the medium has an imaginary and a real part. For example, the collisions are related to the dissipative process and therefore yield an additional imaginary part to the dielectric permittivity. In considering the effects of fluctuations on the rate of change of the particle distribution function related to renormalization, we do not need to include the nuclear reaction effect since the time derivative itself is determined by the rate of nuclear reactions. We will make the assumption that the rate of change of the averaged particle distribution is much slower than the rate of change of the corresponding fluctuating part of the particle distribution. This assumption was already used in the derivation of the collision integral, but we will go one order higher and calculate the terms proportional to the first time derivative of the averaged distribution function. The fluctuations responsible for the renormalization of the distribution function are of a different power in frequency as compared to the fluctuations that determine the collision integral, and, in this sense, one finds an analogy with the real and imaginary parts of the plasma response. We also assume that the averaged distribution function is homogeneous, because we are interested in the *rates* of nuclear reactions in homogeneous plasmas.

4.1. Fluctuations against a Time-Dependent Background

The slowly varying distribution function Φ_i can be expanded about $t = 0$ so that

$$\Phi_i(t) = \Phi_i(0) + t\frac{\partial\Phi_i}{\partial t}(0), \quad (70)$$

where only the linear corrections are kept (below, the argument (0) by the time derivative will be omitted). Taking into account the time dependence of Φ_i, the fluctuating part of the distribution function is given by

$$\delta f_{i,\mathbf{k},\omega} = \delta f_{i,\mathbf{k},\omega}^{(0)} - \frac{Z_i e}{\omega - \mathbf{k}\cdot\mathbf{v} + i0}\int d\omega'\delta\phi_{\mathbf{k},\omega-\omega'}\left(\mathbf{k}\cdot\frac{\partial\Phi_{i,\omega'}}{\partial\mathbf{p}}\right). \quad (71)$$

The part of formula (71) connected with the particle free motion, $\delta f_{i,\mathbf{k},\omega}^{(0)}$, is the same as in expression (36), and the corresponding autocorrelation is given by relation (37), where Φ_i is time-independent. The term in formula (71) related to the particle interaction can be expressed through the time derivative of the average distribution. Since the latter is changing slowly as compared to the fluctuating part, one can take $\omega' \ll \omega$, so that

$$\delta\phi_{\mathbf{k},\omega-\omega'} \approx \delta\phi_{\mathbf{k},\omega} - \omega'\frac{\partial\delta\phi_{\mathbf{k},\omega}}{\partial\omega}. \quad (72)$$

Taking into account (72), from (71), one obtains

$$\delta f_{i,\mathbf{k},\omega} = \delta f_{i,\mathbf{k},\omega}^{(0)} - \frac{Z_i e\delta\phi_{\mathbf{k},\omega}}{\omega - \mathbf{k}\cdot\mathbf{v} + i0}\left(\mathbf{k}\cdot\frac{\partial\Phi_i}{\partial\mathbf{p}}\right) - i\frac{Z_i e}{\omega - \mathbf{k}\cdot\mathbf{v} + i0}\frac{\partial\delta\phi_{\mathbf{k},\omega}}{\partial\omega}\left(\mathbf{k}\cdot\frac{\partial}{\partial\mathbf{p}}\right)\frac{\partial\Phi_i}{\partial t}. \quad (73)$$

As for the last term in formula (73), which is proportional to the small derivative $\partial\Phi_i/\partial t$ (first-order quantity), one can use expression (38) for the fluctuating potential, thus neglecting the effect of the nuclear reactions. The value of $\delta\phi$ that is not modified by nuclear reactions can be used in the term that does not contain the time derivative of the averaged distribution. In fact, on substituting expression (73) into Poisson's equation,

one obtains that these corrections lead to an additional term in the time derivative of the dielectric permittivity. Comparing the contribution from this term with the other terms, one can see that its relative contribution is determined by the ratio of $(1/\varepsilon)(\partial\varepsilon/\partial t)$ to $(1/\Phi)(\partial\Phi)/\partial t$. The time dependence is related to nuclear reactions that occur at the Gamow energies, at which the dielectric permittivity, by virtue of $T/E_G \ll 1$, is close to unity and its time derivative is proportional to the small parameter T/E_G. Thus, expression (73) can be written in the form

$$\delta f_{i,\mathbf{k},\omega} = \delta f^{(C)}_{i,\mathbf{k},\omega} + \delta f^{(R)}_{i,\mathbf{k},\omega}, \tag{74}$$

where

$$\delta f^{(R)}_{i,\mathbf{k},\omega} = -i\frac{Z_i e}{\omega - \mathbf{k}\cdot\mathbf{v} + i0}\frac{\partial\delta\phi^{(C)}_{\mathbf{k},\omega}}{\partial\omega}\left(\mathbf{k}\cdot\frac{\partial}{\partial\mathbf{p}}\right)\frac{\partial\Phi_i}{\partial t}, \tag{75}$$

and $\delta f^{(C)}_i$ and $\delta\phi^{(C)}$ are given by expressions (36) and (38), respectively. Expression (75) yields the part of δf_i that is related to the renormalization of the distribution function. Substituting relation (74) into Eq. (43) leads to the equation for the renormalization:

$$\begin{aligned}&\frac{\partial}{\partial t}(\hat{I}^{(R)}_i(\mathbf{p})\Phi_i(\mathbf{p}))\\ &= iZ_i e\frac{\partial}{\partial\mathbf{p}}\cdot\int d\mathbf{k}d\mathbf{k}'d\omega d\omega'\mathbf{k}\langle\delta f^{(R)}_{i,\mathbf{k}',\omega'}(\mathbf{p})\delta\phi^{(C)}_{\mathbf{k},\omega}\rangle,\end{aligned} \tag{76}$$

where

$$\begin{aligned}\hat{I}^{(R)}_i(\mathbf{p})\Phi_i(\mathbf{p}) &= \frac{4(Z_i e)^2}{(2\pi)^3}\frac{\partial}{\partial\mathbf{p}}\cdot\int d\omega d\mathbf{k}\frac{\mathbf{k}(\mathbf{k}\cdot\mathbf{v})}{k^2}\\ &\times\left[\frac{1}{\omega - \mathbf{k}\cdot\mathbf{v} + i0}\frac{\partial}{\partial\omega}\mathrm{Im}\frac{1}{\omega\varepsilon_{\mathbf{k},\omega}}\right]\Phi_i(\mathbf{p}).\end{aligned} \tag{77}$$

In arriving at formula (77), we used expression (41) for the imaginary part of the dielectric permittivity and the relation [cf. (46)]

$$\begin{aligned}&\left\langle\delta\phi^{(C)}_{\mathbf{k}',\omega'}\frac{\partial}{\partial\omega}\delta\phi^{(C)}_{\mathbf{k},\omega}\right\rangle\\ &= -\frac{4T}{(2\pi)^3 k^2}\left(\frac{\partial}{\partial\omega}\mathrm{Im}\frac{1}{\omega\varepsilon_{\mathbf{k},\omega}}\right)\delta(\omega+\omega')\delta(\mathbf{k}+\mathbf{k}').\end{aligned} \tag{78}$$

4.2. Evaluation of the Renormalization

For the evaluation of the renormalization, we carry out the integral with respect to the frequency in expressions (77) in the same way that was used for the calculation of the correlations of fluctuating quantities in Section 2.2.

Let us write expressions (77) in the form

$$\hat{I}^{(R)}_i(\mathbf{p})\Phi_i(\mathbf{p}) = \frac{\partial}{\partial\mathbf{p}}\cdot\int d\mathbf{k}\mathbf{k}I^{(R)}_{i,\mathbf{p},\mathbf{k}}\Phi_i(\mathbf{p}), \tag{79}$$

where

$$\begin{aligned}&I^{(R)}_{i,\mathbf{p},\mathbf{k}}\\ &= \frac{4(Z_i e)^2}{(2\pi)^3 k^2}(\mathbf{k}\cdot\mathbf{v})\int d\omega\left[\frac{1}{\omega - \mathbf{k}\cdot\mathbf{v} + i0}\frac{\partial}{\partial\omega}\mathrm{Im}\frac{1}{\omega\varepsilon_{\mathbf{k},\omega}}\right].\end{aligned} \tag{80}$$

By integration by parts in formula (80), we use the following equalities:

$$\begin{aligned}&\mathrm{Re}\left(\frac{1}{(\omega - \mathbf{k}\cdot\mathbf{v} + i0)^2}\right)\mathrm{Re}\left(\frac{1}{\omega + i0}\right)\mathrm{Im}\left(\frac{1}{\varepsilon_{\mathbf{k},\omega}}\right)\\ &= \mathrm{Re}\left(\frac{1}{(\omega - \mathbf{k}\cdot\mathbf{v} + i0)^2(\omega + i0)}\right)\mathrm{Im}\left(\frac{1}{\varepsilon_{\mathbf{k},\omega}}\right)\\ &= \mathrm{Im}\left(\frac{1}{(\omega - \mathbf{k}\cdot\mathbf{v} + i0)^2(\omega + i0)\varepsilon_{\mathbf{k},\omega}}\right)\\ &- \mathrm{Re}\left(\frac{1}{\varepsilon_{\mathbf{k},\omega}}\right)\mathrm{Im}\left(\frac{1}{(\omega - \mathbf{k}\cdot\mathbf{v} + i0)^2(\omega + i0)}\right)\\ &= \mathrm{Im}\left(\frac{1}{(\omega - \mathbf{k}\cdot\mathbf{v} + i0)^2(\omega + i0)\varepsilon_{\mathbf{k},\omega}}\right)\\ &+ \mathrm{Re}\left\{\frac{\pi}{\varepsilon_{\mathbf{k},\omega}}\left[\frac{\delta(\omega)}{(\mathbf{k}\cdot\mathbf{v})^2} - \frac{\partial\delta(\omega - \mathbf{k}\cdot\mathbf{v})}{\partial\omega}\frac{1}{\omega}\right]\right\}.\end{aligned} \tag{81}$$

In the first part of equalities (81), we take into account that $\delta(\omega)\mathrm{Im}(\varepsilon_{\mathbf{k},\omega}) = 0$. The first term in the last part of these equalities does not contribute to the integration over ω in expression (79) due to both the analytical properties of the dielectric permittivity and the absence of poles in the upper part of the complex ω-plane for the other two factors (the same procedure was used for the evaluation of the correlations in Section 2.2). The two remaining terms can be integrated with respect to the frequency by using an integration by parts for the term containing the derivative of the δ-function. Thus, one obtains

$$\begin{aligned}&I^{(R)}_{i,\mathbf{p},\mathbf{k}}\\ &= \frac{(Z_i e)^2}{2\pi^2 k^2}\left\{\left[\frac{1}{(\mathbf{k}\cdot\mathbf{v})\varepsilon_{\mathbf{k},0}}\right] + \left[\omega\frac{\partial}{\partial\omega}\frac{1}{\omega}\mathrm{Re}\left(\frac{1}{\varepsilon_{\mathbf{k},\omega}}\right)\right]_{\omega = \mathbf{k}\cdot\mathbf{v}}\right\}\\ &= \frac{(Z_i e)^2}{2\pi^2 k^2}\left[\omega\frac{\partial}{\partial\omega}\frac{1}{\omega}\mathrm{Re}\left(\frac{1}{\varepsilon_{\mathbf{k},\omega}} - \frac{1}{\varepsilon_{\mathbf{k},0}}\right)\right]_{\omega = \mathbf{k}\cdot\mathbf{v}}.\end{aligned} \tag{82}$$

This result contains the dielectric permittivity taken both at $\omega = 0$ and $\omega = \mathbf{k}\cdot\mathbf{v}$; more explicitly, in formula (82), the difference between the expressions related to the dynamic and static screening occurs. The proportionality of result (82) to the square of the particle charge indicates that the renormalization is related to the self-energy of the particles, the $\mathbf{k}$-dependence of (82) also being similar to that for the self-energy (19).

As we already mentioned, we need to extend the derivation of the self-energy to the case of dispersive media.

4.3. The Particle Self-Energy and the Free Self-Energy

The energy conservation law requires the self-energy to be accounted for in nuclear collisions. The dependence of self-energy on the particle velocity, together with the fact that the particle velocities change during particle interactions, causes the self-energy itself to vary, which in turn affects the particle interactions. Here, we treat the self-energy as a perturbation that leads to the renormalization of the particle distribution function.

Let us derive the self-energy for dispersive media by making use of the general expression for the energy [19]. The energy E related to the electric field is

$$E = \frac{1}{4\pi}\int d\mathbf{r}\int_{-\infty}^{t} dt'\mathbf{E}(t')\cdot\frac{\partial\mathbf{D}(t')}{\partial t'}, \tag{83}$$

where $\mathbf{D}$ is the electrostatic induction, such that $\mathbf{D}_{\mathbf{k},\omega} = \varepsilon_{\mathbf{k},\omega}\mathbf{E}_{\mathbf{k},\omega}$. The time integration in expression (83) is performed, as usual, assuming that the contribution is zero at $t \longrightarrow -\infty$, which determines the constant in the corresponding expression of the energy. By expanding the fields in Fourier components, integrating over space, and making use of the expression for the field of the particle i [see (11)]

$$\mathbf{E}_{i,\mathbf{k},\omega}(\mathbf{v}) = -i\frac{Z_i e}{2\pi^2 k^2\varepsilon_{\mathbf{k},\omega}}\mathbf{k}\delta(\omega-\mathbf{k}\cdot\mathbf{v}), \tag{84}$$

one obtains the particle self-energy, labeled by the superscript s,

$$E_i^s(\mathbf{v}) = \frac{(Z_i e)^2}{4\pi^2}\int\frac{d\mathbf{k}}{k^2}d\omega d\omega'\left(\frac{\omega}{(\omega+\omega')\varepsilon_{-\mathbf{k},\omega'}} + \frac{\omega'}{(\omega+\omega')\varepsilon_{\mathbf{k},\omega}}\right)\delta(\omega+\omega')\delta(\omega-\mathbf{k}\cdot\mathbf{v}), \tag{85}$$

where symmetrization with respect to ω and ω' has been used. By expanding the integrand around $\omega' = -\omega$, from (85) one obtains

$$E_i^s(\mathbf{v}) = \frac{(Z_i e)^2}{4\pi^2}\int\frac{d\mathbf{k}}{k^2}\mathrm{Re}\left[\frac{1}{\varepsilon_{\mathbf{k},\omega}} - \omega\frac{\partial}{\partial\omega}\frac{1}{\varepsilon_{\mathbf{k},\omega}}\right]_{\omega=\mathbf{k}\cdot\mathbf{v}} = -\frac{(Z_i e)^2}{4\pi^2}\int\frac{d\mathbf{k}}{k^2}\mathrm{Re}\left[\omega^2\frac{\partial}{\partial\omega}\frac{1}{\omega\varepsilon_{\mathbf{k},\omega}}\right]_{\omega=\mathbf{k}\cdot\mathbf{v}}. \tag{86}$$

The first term in formula (86) is the same as that in expression (19), whereas the second term is due to the time dispersion of the medium. It is remarkable that the derivative of the dielectric permittivity enters formula (86) in the same combination as in expression (82) for the renormalization. One should note that, in contrast to the expression for the energy of waves for a dispersive medium, which is proportional to $(\partial/\partial\omega)(\omega\varepsilon)$, both the renormalization (82) and the particle self-energy (86) are proportional to $(\partial/\partial\omega)(1/\omega\varepsilon)$, which is related to the fact that the field strength depends on ω and, thus, the operator that should be applied to $1/\varepsilon$ is $-\omega^2(\partial/\partial\omega)(1/\omega)$.

Averaging expression (86) over the particle distribution $\Phi_i(\mathbf{p})$ yields the average self-energy per particle:

$$E_i^s = \frac{1}{n_i}\int\frac{d\mathbf{p}}{(2\pi)^3}E_i^s(\mathbf{v})\Phi_i(\mathbf{p}). \tag{87}$$

The results obtained so far are valid for arbitrary particle distributions (with the only constraint being that simplifications using the analytical properties of dielectric permittivity can be made when integrating over ω). For the specific case of a Maxwellian distribution, it is natural to normalize the particle momentum and velocity and the wave number to $\sqrt{m_i T}$, $\sqrt{T/m_i}$, and $1/d$, respectively, with d being the Debye length. Taking into account that the dielectric function is given by (7) and (8), we obtain that the temperature dependence is determined by the Debye length, which will obviously enter the denominator, and the energy should contain the factor $Z_i^2 e^2/d$. As a result, one can express the average particle self-energy (87) in the form

$$E_i^s = \lambda_i\frac{(Z_i e)^2}{d} \propto \frac{1}{\sqrt{T}}, \tag{88}$$

where the numerical coefficient λ_i can be obtained numerically for a given composition (abundance) of nuclei in the plasma.

In connection with the particle self-energy, one can find the corresponding particle free energy, F_i^s, which is related to the entropy S_i^s through [27]

$$S_i^s = -\left(\frac{\partial F_i^s}{\partial T}\right)_n, \tag{89}$$

where the derivative with respect to temperature is taken with density $n = N/V$ fixed, the total number of particles N being conserved by both the fluctuations and the corresponding collisions. As a consequence, one can refer the result to a single particle, the number of particles per unit volume, or the total number of particles. Below, the free energy per particle is considered.

On average, any work performed on an isolated system is zero; i.e.,

$$E_i^s - TS_i^s = 0, \tag{90}$$

which, along with relation (89), yields

$$E_i^s = -T\frac{\partial F_i^s}{\partial T}. \tag{91}$$

By using the same reasoning that led to expression (88), one obtains that $F_i^s \propto 1/\sqrt{T}$, and, thus, $T(\partial/\partial T)F_i^s = -F_i^s/2$, which then gives

$$F_i^s = 2E_i^s = -\frac{(Z_i e)^2}{2\pi^2}\int\frac{d\mathbf{k}}{k^2}\left(\omega^2\frac{\partial}{\partial\omega}\frac{1}{\omega\varepsilon_{\mathbf{k},\omega}}\right)_{\omega=\mathbf{k}\cdot\mathbf{v}}\Phi_i(\mathbf{p})\frac{d\mathbf{p}}{(2\pi)^3}. \quad (92)$$

Expression (92) is similar to that obtained for the renormalization of the particle distribution function [see (82)].

4.4. Physical Meaning of Renormalization

By calculating the average particle kinetic energy with the use of the renormalized distribution function along with expressions (67), (79), and (82), we obtain

$$\int\frac{d\mathbf{p}}{(2\pi)^3}\frac{p^2}{2m_i}\Phi_i(\mathbf{p}) = \int\frac{d\mathbf{p}}{(2\pi)^3}\left\{\frac{p^2}{2m_i} - \frac{Z_i^2e^2}{2\pi^2}\int\frac{d\mathbf{k}}{k^2}\left[\omega^2\frac{\partial}{\partial\omega}\left(\frac{1}{\omega\varepsilon_{\mathbf{k},\omega}} - \frac{1}{\omega\varepsilon_{\mathbf{k},0}}\right)\right]_{\omega=\mathbf{k}\cdot\mathbf{v}}\right\}\Phi_i^{(R)}(\mathbf{p}). \quad (93)$$

The quantity within the square brackets in expression (93) comprises the same term as that entering formula (92), from which the static screening is subtracted. The latter depends only on the total number of particles per unit volume, which is conserved by both fluctuations and collisions, so that it just adds a constant to expression (93). Although any energy is determined up to a constant, this constant in expression (93) cannot be arbitrary, since the constant is already chosen for each particle in the system. The average energy (93) yields the free energy along with a constant determined in such a way that only the free energy in excess of that related to the particles at rest is accounted for.

The physical meaning of the constant occurring in expression (93) is that the energy of the particles at rest is stored in the heath bath of the system and (93) represents the *energy of the excitations (dressed particles) in the plasma*. The concept of dressed (dynamically screened) plasma particles is thus relevant to the issue of the free energy associated with the self-energy of the particles, the same as for collisions in a plasma.

Even if considerations starting with expression (88) refer to a thermal system and are based on the concepts of entropy and free energy, results (92) and (93) obtained by virtue of the concept of renormalization are valid for any nonthermal distribution. Thus, the renormalization of the particle distribution function allows one to calculate the energy of the plasma excitations for any non-equilibrium system with arbitrary deviations from thermal equilibrium, when one cannot introduce the concept of entropy and free energy. Thus, one is able to treat the physics of excitations *for any system far from equilibrium*. This result, which appears to be new, has been obtained by virtue of the utilization of the kinetic approach applicable to any nonequilibrium system, the same as for derivation of the binary collision integral, which is valid as well for any nonequilibrium system.

With reference to a thermal system, the physical meaning of the renormalization is simple. The total energy of the system includes the free energy of the excitations, and, as a consequence, the thermal distribution of the dressed particles has to account for the energy of the excitations. One can recover the usual Maxwellian distribution of particles by means of proper renormalization. Thus, in thermal equilibrium, one can identify the renormalized distribution function for which the self-free energy is excluded, the latter being taken into account through additional renormalization terms.

On the basis of the foregoing arguments and with reference to thermal equilibrium, the rate of nuclear reactions in the presence of plasma fluctuations is thus given by expression (68), with the renormalized functions $\Phi_i^{(R)}$ and $\Phi_j^{(R)}$ replaced by the corresponding Maxwellian functions $\Phi_i^{(M)}$ and $\Phi_j^{(M)}$. The factor Λ_{ij} [see (69)] is thus

$$\begin{aligned}\Lambda_{ij} = \frac{1}{(1+\delta_{ij})R_{ij}^0}\int\frac{d\mathbf{p}'d\mathbf{p}}{(2\pi)^6}\{&(w_{ij}^{(0)}(\mathbf{p},\mathbf{p}') + w_{ji}^{(0)}(\mathbf{p}',\mathbf{p}))(\langle\delta f_i^{(C)}(\mathbf{p})\delta f_j^{(C)}(\mathbf{p}')\rangle)\\ &+ w_{ij}^{(0)}(\mathbf{p},\mathbf{p}')\Phi_j^{(M)}(\mathbf{p}')\hat{I}^{(R)}(\mathbf{p})\Phi_i^{(M)}(\mathbf{p})\\ &+ w_{ji}^{(0)}(\mathbf{p}',\mathbf{p})\Phi_i^{(M)}(\mathbf{p})\hat{I}^{(R)}(\mathbf{p}')\Phi_j^{(M)}(\mathbf{p}')\\ &+ (\hat{w}_{ij}^{(1)}(\mathbf{p},\mathbf{p}') + \hat{w}_{ji}^{(1)}(\mathbf{p}',\mathbf{p}))[\langle\delta f_i^{(C)}(\mathbf{p})\delta\phi^{(C)}\rangle\Phi_j^{(M)}(\mathbf{p}')\\ &+ \langle\delta f_j^{(C)}(\mathbf{p}')\delta\phi^{(C)}\rangle\Phi_i^{(M)}(\mathbf{p})] + (\hat{w}_{ij}^{(2)}(\mathbf{p},\mathbf{p}')\\ &+ \hat{w}_{ji}^{(2)}(\mathbf{p}',\mathbf{p}))\langle(\delta\phi^{(C)})^2\rangle\Phi_i^{(M)}(\mathbf{p})\Phi_j^{(M)}(\mathbf{p}')\},\end{aligned} \quad (94)$$

where $R_{ij}^{(0)}$ is the rate of nuclear reactions between bare nuclei, given by expression (56).

To proceed further with expression (94), we need to calculate $w^{(1)}$ and $w^{(2)}$, which account for the change in the probabilities of nuclear reactions in arbitrary fluctuating fields.

Before carrying out such a calculation, it is worthwhile to make a few comments. It seen from expression (94) that the contributions due to changes of the distribution functions by fluctuations are as important as the contributions due to the change of the probability, their combined effect also being relevant. From a general point of view, it does not appear to be possible to establish the relative weight of the different effects; hence, one should expect that all terms make contribu-

tions of the same order. Moreover, the renormalization of the distribution function is important and takes into account, by a perturbative method, the self-energy of the nuclei, which might yield effects of the same order of magnitude as Salpeter's corrections stemming from the polarization of the reacting nuclei. The approach used should permit one to clarify the controversy between the static and dynamic screenings.

5. CHANGE OF THE TUNNELING PROBABILITIES BY FLUCTUATION POTENTIALS

In this section, we will consider the issue of nuclear reactions of two bare nuclei in an arbitrary external fluctuating potential $\delta\phi(\mathbf{r}, t)$ (taken to be weak), such that a perturbative procedure is applicable. Our treatment generalizes Salpeter's approach.

As is known, nuclear reactions are due to tunneling of the nuclei through the Coulomb potential barrier. Here, we will use a quasi-classical description, which can be justified by the fact that both the width of the Coulomb barrier and the characteristic length of the fluctuating potential are considered to be significantly larger than the de Broglie wavelength of the nuclei. In this case, the wave function $\psi(\mathbf{r}_i, \mathbf{r}_j, t)$ of the two nuclei can be expressed through the action σ

$$\psi(\mathbf{r}_i, \mathbf{r}_j, t) = \exp\left(\frac{i}{\hbar}\sigma(\mathbf{r}_i, \mathbf{r}_j, t)\right). \tag{95}$$

On account of both the interaction potential energy U and the external potential $\delta\phi(\mathbf{r}, t)$, the equation for $\sigma \equiv \sigma(\mathbf{r}_i, \mathbf{r}_j, t)$ is [28]

$$\begin{aligned}\frac{1}{2m_i}\left(\frac{\partial\sigma}{\partial\mathbf{r}_i}\right)^2 + \frac{1}{2m_j}\left(\frac{\partial\sigma}{\partial\mathbf{r}_j}\right)^2 - \frac{i\hbar}{2m_i}\frac{\partial}{\partial\mathbf{r}_i}\cdot\frac{\partial}{\partial\mathbf{r}_i}\sigma \\ - \frac{i\hbar}{2m_j}\frac{\partial}{\partial\mathbf{r}_j}\cdot\frac{\partial}{\partial\mathbf{r}_j}\sigma = -\frac{\partial\sigma}{\partial t} - U - Z_i e\delta\phi(\mathbf{r}_i, t) \\ - Z_j e\delta\phi(\mathbf{r}_j, t).\end{aligned} \tag{96}$$

When solving Eq. (96), one should take into account that the width of the Coulomb barrier is larger than the characteristic scale length of the potential, whereas the tunneling time (i.e., the time taken by nuclei to cross the Coulomb barrier) is shorter than the characteristic time scale of $\delta\phi$. Let us solve Eq. (96) to the second order in $\delta\phi$. To the zero order in $\delta\phi$ (i.e., for the tunneling in the absence of a fluctuating potential), we have $\sigma = -Et + \sigma_0$, with E being the energy eigenvalue. To the zero order in $\hbar$, the exponent in the tunneling probability can be determined from the equation [28]

$$\frac{1}{2m_i}\left(\frac{\partial\sigma_0}{\partial\mathbf{r}_i}\right)^2 + \frac{1}{2m_j}\left(\frac{\partial\sigma_0}{\partial\mathbf{r}_j}\right)^2 = E - U, \tag{97}$$

which, on introducing the center of mass position $\mathbf{R}$ and the nuclei relative position $\mathbf{r}$

$$\mathbf{R} = \frac{m_i\mathbf{r}_i + m_j\mathbf{r}_j}{m_i + m_j}, \quad \mathbf{r} = \mathbf{r}_i - \mathbf{r}_j \tag{98}$$

can be written as

$$\begin{aligned}\frac{1}{2(m_i + m_j)}\left(\frac{\partial\sigma_0}{\partial\mathbf{R}}\right)^2 + \frac{1}{2\mu_{ij}}\left(\frac{\partial\sigma_0}{\partial\mathbf{r}}\right)^2 \\ = \frac{\mathbf{P}^2}{2(m_i + m_j)} + \frac{1}{2\mu_{ij}}\left(\frac{\partial\sigma_{0,0}}{\partial r}\right),\end{aligned} \tag{99}$$

$$\sigma_0 = \sigma_{0,0} + \mathbf{P}\cdot\mathbf{R}, \tag{100}$$

where

$$\mathbf{P} = m_i\mathbf{v}_i + m_j\mathbf{v}_j \quad \text{and} \quad \mu_{ij} = \frac{m_i m_j}{m_i + m_j}.$$

On the basis of Eq. (99), one obtains the standard equation for $\sigma_{0,0}$ containing the relative energy E_r and the relative distance r of the two nuclei [28]

$$\frac{1}{2\mu}\left(\frac{\partial\sigma_{0,0}}{\partial r}\right)^2 = E_r - U, \tag{101}$$

which yields the known probability of tunneling w (see [28], where this probability is denoted by D),

$$w = \exp\left(-\frac{2}{\hbar}\left|\int_{r_{t,1}}^{r_{t,2}} p_r dr\right|\right), \quad p_r \equiv \sqrt{2\mu(E_r - U)}, \tag{102}$$

where $r_{t,1}$ and $r_{t,2}$ are the turning points in the potential U for the given energy E_r.

To first order in $\delta\phi$, we look for a solution of Eq. (96) in the form $\sigma = \sigma_0 + \sigma_1$ with $\sigma_1 \ll \sigma_0$. In view of the fact that $\delta\phi$ is slowly varying over the distance $r_t \equiv r_{t,2} - r_{t,1}$, one can take $\delta\phi(\mathbf{r}_i, t) \approx \delta\phi(\mathbf{r}_j, t) = \delta\phi(\mathbf{R}, t)$, which corresponds to the replacements

$$\begin{aligned}\mathbf{r}_i &= \mathbf{R} + \frac{m_j}{m_i + m_j}\mathbf{r} \longrightarrow \mathbf{R}, \\ \mathbf{r}_j &= \mathbf{R} - \frac{m_i}{m_i + m_j}\mathbf{r} \longrightarrow \mathbf{R}.\end{aligned} \tag{103}$$

To the first order in $\delta\phi$, the relevant equation is

$$\begin{aligned}\frac{1}{\mu_{ij}}\left(\frac{\partial\sigma_{0,0}}{\partial r}\right)\frac{\mathbf{r}}{r}\cdot\frac{\partial\sigma_1}{\partial\mathbf{r}} \\ = -\frac{\partial\sigma_1}{\partial t} - \mathbf{V}\cdot\frac{\partial\sigma_1}{\partial\mathbf{R}} - (Z_i + Z_j)e\delta\phi(\mathbf{R}, t),\end{aligned} \tag{104}$$

with

$$\mathbf{V} = \frac{\mathbf{P}}{m_i + m_j} \tag{105}$$

being the velocity of the center of mass. By taking a Fourier transform with respect to both **R** and *t*, namely,

$$\sigma_1(r, \mathbf{R}, t) = \int d\mathbf{k} d\omega \sigma_{1,\mathbf{k},\omega}(r) \exp(i\mathbf{k}\cdot\mathbf{R} - i\omega t),$$
$$\delta\phi(\mathbf{R}, t) = \int d\mathbf{k} d\omega \delta\phi_{\mathbf{k},\omega} \exp(i\mathbf{k}\cdot\mathbf{R} - i\omega t), \quad (106)$$

one can rewrite (104) in the form

$$\frac{1}{\mu}\frac{\partial\sigma_{0,0}}{\partial r}\frac{\partial\sigma_{1,\mathbf{k},\omega}(r)}{\partial r} = i(\omega - \mathbf{k}\cdot\mathbf{V})\sigma_{1,\mathbf{k},\omega}(r) - (Z_i + Z_j)e\delta\phi_{\mathbf{k},\omega}. \quad (107)$$

Let us estimate the different terms entering (107). With reference to the left-hand side of (107), one finds that

$$\frac{1}{\mu}\frac{\partial\sigma_{0,0}}{\partial r} \approx \left(\frac{E_r}{\mu}\right)^{1/2} \approx v^G. \quad (108)$$

According to (101), v^G is the velocity corresponding to the Gamow energy (4); for estimates, we take $\partial\sigma_1/\partial r \approx \sigma_1/r_t$. On the other hand, the first term on the right-hand side of (107) is of the order $v_T\sigma_1/L_{\delta\phi}$, with v_T the nuclei thermal velocity and $L_{\delta\phi}$ the typical spatial scale length of $\delta\phi$. Thus, the term with σ_1 on the right-hand side of (107) is smaller than the left-hand side by a factor on the order of $(v_T/v^G)(r_t/L_{\delta\phi}) \ll 1$ and can be neglected. Taking into account (101), the solution to (107) is

$$\sigma_1(r, \mathbf{R}, t) = -(Z_i + Z_j)e\delta\phi(\mathbf{R}, t)\mu_{ij}\int\frac{dr}{\sqrt{2\mu_{ij}(E_r - U)}} = -(Z_i + Z_j)e\delta\phi(\mathbf{R}, t)\frac{\partial\sigma_{0,0}}{\partial E_r}, \quad (109)$$

with $\sigma_{0,0} = \int dr\sqrt{2\mu(E_r - U)}$. Thus, the effect of the first order in $\delta\phi$ can be obtained by expanding

$$\sigma = \int dr\sqrt{2\mu_{ij}[E_r - U - (Z_i + Z_j)e\delta\phi]}. \quad (110)$$

in $\delta\phi$. As a result, the effect of $\delta\phi$ reduces to a shift in energy E_r.

To the second order in $\delta\phi$, we obtain $\sigma_2 \propto \partial^2\sigma_{0,0}/2\partial E_r^2$; i.e., the energy shift described by (110) remains valid to the second order as well. The same shift in energy is obtained for the first-order (in $\hbar$) terms that determine the factor in front of the exponent in the quasi-classical description. Thus, the same shift in energy is obtained for the complete expression for the tunneling probability. With reference to the expansion in powers of $\delta\phi$ of the total probability of tunneling [see (57)], one obtains

$$w_{ij}^{(1)}(\mathbf{p}, \mathbf{p}') + w_{ji}^{(1)}(\mathbf{p}', \mathbf{p}) = (Z_i + Z_j)e\frac{\partial}{\partial E_r}w_{ij}^{(0)}(E_r), \quad (111)$$

$$w_{ij}^{(2)}(\mathbf{p}, \mathbf{p}') + w_{ji}^{(2)}(\mathbf{p}', \mathbf{p}) = \frac{1}{2}(Z_i + Z_j)^2 e^2\frac{\partial^2}{\partial E_r^2}w_{ij}^{(0)}(E_r), \quad (112)$$

with

$$\bar{w}_{ij}^{(0)}(\mathbf{p}, \mathbf{p}') \equiv w_{ij}^{(0)}(E_r). \quad (113)$$

Result (57), along with Eqs. (111)–(113), generalizes the approach used by Salpeter for the evaluation of the effect of the electrostatic potential related to the static charge screening on the tunneling probability. Here, we have dealt with an external fluctuating potential slowly varying in space and time.

6. PLASMA CORRECTIONS TO THE NUCLEAR REACTION RATES IN THERMAL PLASMAS

6.1. Cancellation of Salpeter's Enhancement Factor

Let us now go back to the general expression (94), which accounts for the change in the reaction rates by fluctuations in thermal plasmas. We first rearrange the renormalization terms occurring in expression (94) by using relation (79), expressing all of these terms through the product of the thermal distributions of the reacting nuclei. According to relations (79) and (82), for a thermal distribution, we obtain

$$\hat{I}_i^{(R)}(\mathbf{p})\Phi_i^{(M)}(\mathbf{p}) = \Phi_i^{(M)}(\mathbf{p})\left[-\int d\mathbf{k}\frac{\mathbf{k}\cdot\mathbf{v}}{T}I_{i,\mathbf{p},\mathbf{k}}^{(R)} + \int d\mathbf{k}\left(\mathbf{k}\cdot\frac{\partial I_{i,\mathbf{p},\mathbf{k}}^{(R)}}{\partial\mathbf{p}}\right)\right] = \Phi_i^{(M)}(\mathbf{p})(I_i^{(R,0)}(\mathbf{p}) + I_i^{(R,F)}(\mathbf{p})), \quad (114)$$

$$I_i^{(R,0)}(\mathbf{p}) = \frac{(Z_i e)^2}{2\pi^2 T}\int\frac{d\mathbf{k}}{k^2}\left(1 - \frac{1}{\varepsilon_{\mathbf{k},0}}\right) = \frac{(Z_i e)^2}{Td}, \quad (115)$$

$$I_i^{(R,F)}(\mathbf{p}) = \frac{(Z_i e)^2}{2\pi^2}\times\int\frac{d\mathbf{k}}{k^2}\left\{\frac{1}{T}\left[\omega^2\frac{\partial}{\partial\omega}\frac{1}{\omega}\mathrm{Re}\left(1 - \frac{1}{\varepsilon_{\mathbf{k},\omega}}\right)\right]_{\omega = \mathbf{k}\cdot\mathbf{v}}\right. + \left.\left(\mathbf{k}\cdot\frac{\partial}{\partial\mathbf{p}}\right)\left[\omega\frac{\partial}{\partial\omega}\frac{1}{\omega}\mathrm{Re}\left(\frac{1}{\varepsilon_{\mathbf{k},\omega}} - \frac{1}{\varepsilon_{\mathbf{k},0}}\right)\right]_{\omega = \mathbf{k}\cdot\mathbf{v}}\right\}, \quad (116)$$

where we have distinguished term (115) related to the static ($\omega = 0$) effect from term (116) describing the effect of the fluctuations and labeled by *F*. Taking into account Eqs. (111)–(114), we can write expression (94) in the form

$$\Lambda_{ij} = \Lambda_{ij}^{(0)} + \Lambda_{ij}^{(F)}, \quad (117)$$

where

$$\Lambda_{ij}^{(0)} = \frac{1}{(1+\delta_{ij})R_{ij}^0}\int\frac{d\mathbf{p}d\mathbf{p}'}{(2\pi)^6}\Big\{w_{ij}^{(0)}(E_r)$$
$$\times\Big[\langle\delta f_i^{(C)}(\mathbf{p})\delta f_j^{(C)}(\mathbf{p}')\rangle + \frac{1}{2}(I_i^{(R,0)}(\mathbf{p})$$
$$+ I_j^{(R,0)}(\mathbf{p}'))\Phi_i^{(M)}(\mathbf{p})\Phi_j^{(M)}(\mathbf{p}')\Big] + (Z_i+Z_j)e\frac{\partial w_{ij}^{(0)}(E_r)}{\partial E_r}$$
$$\times[\langle\delta f_i^{(C)}(\mathbf{p})\delta\phi^{(C)}\rangle\Phi_j^{(M)}(\mathbf{p}')$$
$$+ \langle\delta f_j^{(C)}(\mathbf{p}')\delta\phi^{(C)}\rangle\Phi_i^{(M)}(\mathbf{p})] + \frac{1}{2}(Z_i+Z_j)^2e^2$$
$$\times\frac{\partial^2 w_{ij}^{(0)}(E_r)}{\partial E_r^2}\langle(\delta\phi^{(C)})^2\rangle\Phi_i^{(M)}(\mathbf{p})\Phi_j^{(M)}(\mathbf{p}')\Big\}, \quad (118)$$

$$\Lambda_{ij}^{(F)} = \frac{1}{2(1+\delta_{ij})R_{ij}^0}\int\frac{d\mathbf{p}d\mathbf{p}'}{(2\pi)^6}w_{ij}^{(0)}(E_r)$$
$$\times(I_i^{(R,F)}(\mathbf{p}) + I_j^{(R,F)}(\mathbf{p}'))\Phi_i^{(M)}(\mathbf{p})\Phi_j^{(M)}(\mathbf{p}'). \quad (119)$$

When calculating the corrections to the probabilities due to the presence of a fluctuating potential (see Section 5), we have already accounted for the Coulomb interaction of two bare nuclei with the consequence that only the contribution from the interactions with other particles should be included in expression (118). Moreover, the vacuum self-energy, which can be dealt with through mass renormalization, should not be included in expression (118). On the other hand, the effects stemming from both the bare nuclei interaction and the vacuum self-energy are described by terms which are nonzero for $\varepsilon = 1$. As a consequence, to exclude these latter effects from expression (118) reduces simply to replacing $1/\varepsilon$ by $(1/\varepsilon - 1)$ in correlations (52) and (53) (the same result, as was mentioned above, can be obtained if correlations (52) and (53) are calculated with only the polarization potential accounted for), which are relevant to both the first term within the first square brackets and the two terms within the second square brackets on the right-hand side of expression (118).

On the basis of the foregoing prescription, let us calculate expression (118), whose terms are to be related only to the static dielectric permittivity or, more precisely, with $(1 - 1/\varepsilon_{\mathbf{k},0})$. Along with correlations (52) and (53), each term of expression (118) contains the product

$$\Phi_i^{(M)}\Phi_j^{(M)} \propto \exp\left(-\frac{\mathbf{p}^2}{2m_iT} - \frac{(\mathbf{p}')^2}{2m_jT}\right)$$
$$= \exp\left(-\frac{\mathbf{P}^2}{2(m_i+m_j)T} - \frac{E_r}{T}\right), \quad (120)$$

and the corresponding integration with respect to $\mathbf{p}$ and $\mathbf{p}'$ can be converted to the integration with respect to $\mathbf{P}$ and $\mathbf{p}_r$, where $\mathbf{P}$ and $\mathbf{p}_r$ are the momentum of the center of mass and the relative momentum, respectively. We then integrate by parts (with respect to E_r) the terms of expression (118) proportional to $(\partial w_{ij}^{(0)}/\partial E_r)$ and $(\partial^2 w_{ij}^{(0)}/\partial E_r^2)$. In carrying out these integrations, only the dominant contributions related to the first and second derivatives of the exponential in expression (120) are kept; i.e., the results from the integration by parts are the same as those obtained by the replacements

$$\left(\frac{\partial w_{ij}^{(0)}}{\partial E_r}, \frac{\partial^2 w_{ij}^{(0)}}{\partial E_r^2}\right) \longrightarrow \left(\frac{1}{T}, \frac{1}{T^2}\right)w_{ij}^{(0)}. \quad (121)$$

Note that the same approximation was used by Salpeter [1] and is accurate to the lowest order in the ratio of the thermal energy to the Gamow energy. On making use of relation (48) for the last term on the right-hand side of expression (118) and taking into account expression (56) for $R_{ij}^{(0)}$, expression (118) reduces to [we write out the terms in the same order as they appear in expression (118)]

$$\Lambda_{ij}^{(0)} = \frac{e^2}{2\pi^2T}\int\frac{d\mathbf{k}}{k^2}\left(1 - \frac{1}{\varepsilon_{\mathbf{k},0}}\right)\Big\{Z_iZ_j + \frac{1}{2}(Z_i^2 + Z_j^2)$$
$$- (Z_i+Z_j)^2 + \frac{1}{2}(Z_i+Z_j)^2\Big\} = 0. \quad (122)$$

We thus obtain a *remarkable result* that *the net effect on the nuclear reaction rates* of the four different contributions *connected with the static dielectric permittivity is zero.* This result, which *is one of the most important of this paper, is new* and differs radically from the findings obtained so far in regard to the issue under investigation. In particular, result (122) rejects the most popular Salpeter result (5) and (6). In this respect, one should note that Salpeter's term $Z_iZ_je^2/Td$ is just the Z_iZ_j term stemming from the last term within the curly brackets of expression (122) (recall that such a term is due uniquely to the fluctuating potential [see (118)].

6.2. Discussion of the Physics of Result (122)

Let us first note that, in the framework of the fluctuation approach adopted in the foregoing, one is dealing with correlation functions that are quantities of the second order in the fluctuations. From expression (122), it is seen that, along with terms proportional to Z_iZ_j, which will be referred to as interaction terms, there occur terms proportional to the square of the charge of the single nuclei, which will be referred to as static self-energy terms. Expression (122) contains all the interaction terms, which, as it appears, can be expressed through the static dielectric permittivity and the static

self-energy terms. According to expression (122), the net effect of the interaction terms on the nuclear reaction rates, on the one hand, and the static self-energy terms, on the other hand, is zero.

More precisely, the first term in the curly brackets of expression (122), which is equal to Salpeter's term $Z_iZ_je^2/Td$, stems from the first term on the right-hand side of expression (118) and is uniquely related to the fluctuations of the distribution function of the bare reacting nuclei. This term is the term dealt with by Gruzinov [9] through a procedure that has been disputed above (see Section 1.3). The difference from [9] is that, in the present consideration, the fluctuating potentials are time-dependent in accordance with the rule prescribed by binary collisions.

Two additional interaction terms appear in expression (122). The part of the last term that is proportional to Z_iZ_j is the Salpeter term [1]. The part of the third term that is proportional to Z_iZ_j results from the energy variation of the tunneling probability, which is proportional to the first derivative of the probability with respect to the nuclei relative energy, in combination with the fluctuation of the distribution function [cf. the term $\partial w_{ij}^{(0)}/\partial E_r$ in expression (118)]. This term is peculiar of our approach and does not seem to have been considered so far.

The net result of the three interaction contributions proportional to Z_iZ_j is zero; i.e., Salpeter's term plus the Gruzinov-type term are completely cancelled by the new "interference" term (the contribution from the third term proportional to Z_iZ_j).

As for the second term in expression (122), it is related to the static self-energy and is due to the static part of the renormalization effect, i.e., to the terms $I_i^{(R,0)}$ and $I_j^{(R,0)}$ in expression (118). The second term is canceled by the contributions from the terms proportional to Z_i^2 and Z_j^2 in expression (122). In respect to the terms proportional to $(Z_i^2 + Z_j^2)$ in expression (122), let us again note that the reacting nuclei (rather than bare nuclei) are to be considered as excitations endowed with the free energy related to the self-energy stemming from the plasma fluctuations. The cancellation of the self-energy terms in the static approximation reflects the fact that the static self-energy cannot affect the nuclear reactions and is, in fact, stored in the heath bath.

The Z_iZ_j part of the last term within the curly brackets of expression (122) (i.e., Salpeter's term) has also been obtained through a detailed statistical description [10] on the assumption of nonfluctuating Maxwellian distributions for the reacting bare nuclei, in contrast with our treatment of nuclei as excitations with fluctuating polarization clouds. These fluctuations lead to fluctuations in particle distributions. They are changed by interaction, and the effect proportional to the product of charges of interacting nuclei appears in the self-energy particle polarization clouds. In fact, the fluctuations that create the self-energy and the fluctuations responsible for the polarization effects are not separable, and their interference during nuclear reactions makes the net effect of static screening and static self-energy equal to zero.

As for the equality of the Gruzinov-type term, i.e., the first term of expression (122) and Salpeter's term, it appears that the fluctuations in the nuclei distribution function together with the change of the probability linear in the fluctuation potential yield an increase, on average, in the relative energy of the reacting nuclei, thus enhancing the reaction rates by the same amount as that resulting from the lowering of the potential barrier due to the fluctuation of the potential.

6.3. Explicit Evaluation of Plasma Corrections

Let us now evaluate the effect on the reaction rates of the dynamically screened part of the self-energy, which depends on the velocities of the two interacting nuclei, as described by expression (119), which is the only contribution to the change of the nuclear reaction rates in a plasma. Such an effect occurs under the resonant condition $\omega = \mathbf{k}\cdot\mathbf{v}$ [see (116)] and is easily obtained from the test-particle approach. Let us first rearrange the second term of relation (116) in a form more suitable to the evaluation of expression (119). In this regard,

(i) the integration over $\mathbf{k}$ is such that only the component of the corresponding integrand that is directed along $\mathbf{v}$ contributes; i.e., denoting the quantity within the square brackets by $g(\mathbf{k}\cdot\mathbf{v})$, one has

$$\frac{\partial}{\partial \mathbf{p}}\cdot[\mathbf{k}g(\mathbf{k}\cdot\mathbf{v})] \longrightarrow \frac{1}{m_i}\frac{\partial}{\partial \mathbf{v}}\cdot\left[\frac{(\mathbf{k}\cdot\mathbf{v})}{v^2}\mathbf{v}g(\mathbf{k}\cdot\mathbf{v})\right] = \frac{1}{m_i v^2}(\mathbf{k}\cdot\mathbf{v})\mathbf{v}\cdot\frac{\partial}{\partial \mathbf{v}}g(\mathbf{k}\cdot\mathbf{v}), \tag{123}$$

the last equality following from

$$\frac{\partial}{\partial \mathbf{v}}\cdot\left(\frac{(\mathbf{k}\cdot\mathbf{v})\mathbf{v}}{v^2}\right) = 0; \tag{124}$$

(ii) the part dependent on $\mathbf{k}\cdot\mathbf{v}$ can be expressed through an integral over ω by using the function $\delta(\omega - \mathbf{k}\cdot\mathbf{v})$; i.e.,

$$\begin{aligned}(\mathbf{k}\cdot\mathbf{v})\mathbf{v}\cdot\frac{\partial}{\partial \mathbf{v}}g(\mathbf{k}\cdot\mathbf{v}) &= \\ = \int d\omega\omega\left(\mathbf{v}\cdot\frac{\partial}{\partial \mathbf{v}}\right)(\delta(\omega-\mathbf{k}\cdot\mathbf{v})g(\omega)) &\\ = \int d\omega\omega g(\omega)\left(\mathbf{v}\cdot\frac{\partial}{\partial \mathbf{v}}\right)\delta(\omega-\mathbf{k}\cdot\mathbf{v}) &\\ = -\int d\omega\omega^2 g(\omega)\frac{\partial}{\partial\omega}\delta(\omega-\mathbf{k}\cdot\mathbf{v}),&\end{aligned} \tag{125}$$

where the last equality is based on

$$\mathbf{v}\cdot(\partial/\partial\mathbf{v})\delta(\omega-\mathbf{k}\cdot\mathbf{v}) = -(\mathbf{k}\cdot\mathbf{v})(\partial/\partial\omega)\delta(\omega-\mathbf{k}\cdot\mathbf{v}); \tag{126}$$

(iii) the integral over ω can be integrated by parts.

Using the notation of (116), one thus obtains

$$I_i^{(R,F)}(\mathbf{p}) = \frac{(Z_i e)^2}{2\pi^2 T}\mathrm{Re}\left\{\int\frac{d\mathbf{k}}{k^2}\left[\omega^2\frac{\partial}{\partial\omega}\frac{1}{\omega}\left(1-\frac{1}{\varepsilon_{\mathbf{k},\omega}}\right)\right]_{\omega=\mathbf{k}\cdot\mathbf{v}}\right. \tag{127}$$
$$\left. + \frac{T}{m_i v^2}\left[\frac{\partial}{\partial\omega}\omega^3\frac{\partial}{\partial\omega}\frac{1}{\omega}\left(\frac{1}{\varepsilon_{\mathbf{k},\omega}}-\frac{1}{\varepsilon_{\mathbf{k},0}}\right)\right]_{\omega=\mathbf{k}\cdot\mathbf{v}}\right\}.$$

Let us now return to expression (119), for which we make use of relation (120) along with the change of variables $(\mathbf{p},\mathbf{p}') \longrightarrow (\mathbf{P},\mathbf{p}_r)$, the corresponding Jacobian of the transformation being equal to 1. On adopting spherical coordinates, let us perform first the integration over the relative energy $E_r = p_r^2/2\mu$, with $\mu = m_i m_j/(m_i+m_j)$ the reduced mass. Recalling relation (56) along with identity (113), the part of expression (119) related to the integration over E_r is

$$\frac{1}{\int w_{ij}^{(0)}(E_r)\exp\left(-\frac{E_r}{T}\right)\sqrt{E_r}\,dE_r} \tag{128}$$
$$\times\int dE_r I_{i,j}^{(R,F)}(\mathbf{P},\hat{\mathbf{p}}_r,E_r)w_{ij}^{(0)}(E_r)\exp\left(-\frac{E_r}{T}\right)\sqrt{E_r}$$
$$\approx I_{i,j}^{(R,F)}(\mathbf{P},\hat{\mathbf{p}}_r,E_{ij}^G),$$

where the last (approximate) equality takes into account that the integrand of the preceding integral is peaked at the Gamow energy E_{ij}^G [see (4)]. It remains to carry out the angular integration over $\hat{\mathbf{p}}_r = \mathbf{p}_r/p_r$ and the integration over $\mathbf{P} = (m_i+m_j)V$. The velocities of the reacting nuclei occurring in expression (127) can be expressed in terms of the velocity of the center of mass $\mathbf{V}$ and the relative velocity $\mathbf{v}_r = \mathbf{v}_i - \mathbf{v}_j$:

$$\mathbf{v}_i = \mathbf{V} + \frac{m_j}{m_i+m_j}\mathbf{v}_r, \quad \mathbf{v}_j = \mathbf{V} - \frac{m_i}{m_i+m_j}\mathbf{v}_r. \tag{129}$$

The dielectric function $\varepsilon_{\mathbf{k},\mathbf{k}\cdot\mathbf{v}}$ occurring in (127) is given by expressions (7) and (8), with $\omega = \mathbf{k}\cdot\mathbf{v}$, and the argument of the function W in expression (7) can be expressed as

$$s_{\alpha,i} = \frac{\mathbf{k}\cdot\mathbf{v}}{k\sqrt{2}v_{T,\alpha}} = \frac{kVx + kv_r z\dfrac{m_j}{m_i+m_j}}{k\sqrt{2}v_{T,\alpha}} \tag{130}$$
$$= \sqrt{\frac{m_\alpha}{m_i+m_j}}\left(yx + \lambda_{i,j}z\frac{m_j}{m_i+m_j}\right),$$

$$s_{\alpha,j} = \frac{\mathbf{k}\cdot\mathbf{v}'}{k\sqrt{2}v_{T,\alpha}} = \frac{kVx - kv_r z\dfrac{m_i}{m_i+m_j}}{k\sqrt{2}v_{T,\alpha}} \tag{131}$$
$$= \sqrt{\frac{m_\alpha}{m_i+m_j}}\left(yx - \lambda_{i,j}z\frac{m_i}{m_i+m_j}\right),$$

where $v_{T,\alpha} = \sqrt{T/m_\alpha}$ is the thermal velocity of a plasma particle of species α (α includes both electrons and ions; i.e., $\alpha = \{e, j'\}$); x and z are the cosine of the angle between $\mathbf{k}$ and $\mathbf{V}$ and the cosine of the angle between $\mathbf{k}$ and $\mathbf{v}_r$, respectively; and

$$y = \frac{V}{\sqrt{2T/(m_i+m_j)}}, \quad \lambda_{ij} = \frac{v_{ij}^G}{\sqrt{2T/(m_i+m_j)}}, \tag{132}$$

where y is the velocity of the motion of the center of mass of the two nuclei normalized to the thermal velocity of the center of mass and λ_{ij} is the normalized velocity corresponding to the Gamow energy $v_{ij}^G = \sqrt{(2/\mu_{ij})E_{ij}^G}$, with μ_{ij} the reduced nuclear mass.

In terms of the quantities defined in expressions (132), the kinetic energy of the particle i that occurs in the second term of relation (127) can be expressed as

$$\frac{m_i v^2}{2T} \tag{133}$$
$$= \frac{m_i}{m_i+m_j}\left[y^2 + \frac{m_j}{m_i+m_j}\frac{(\mathbf{V}\cdot\mathbf{v})}{vV} + \lambda_{i,j}^2\left(\frac{m_i}{m_i+m_j}\right)^2\right]$$

The last term in expression (133) is dominant since the Gamow energy is much larger than the thermal energy, with the result being that the contribution from the term $T/m_i v^2$ in relation (127) is smaller than that corresponding to the first one. Substituting relation (127) into expression (119) yields

$$\Lambda_{ij}^F = \Lambda_{ij}^{F,0} + \delta\Lambda_{ij}^F. \tag{134}$$

The first and second terms in expression (134) stem from the first and second terms of relation (127), respectively (the numerical analysis shows that the contribution from the term with $\delta\Lambda_{ij}^F$ is no more than 10% of the first term). The first (dominant) term in expression (134)—$\Lambda_{ij}^{F,0}$—describes the effect of the nuclei free energy on the reaction rate. This effect tends to a *decrease* in the reaction rates, since $\Lambda_{ij}^{F,0}$ turns out to be negative.

The explicit evaluation of the two terms in expression (134) requires the integration over k, x, z, and y; as for integration over k in relation (127), it can be performed in the complex k-plane after transforming the

integral over k from 0 to ∞ to the integral over k from $-\infty$ to ∞. One thus obtains

$$\Lambda_{ij}^{F,0} = -\frac{e^2}{2\sqrt{\pi}Td}\int_{-1}^{1}dx\int_{-1}^{1}dz\int_{0}^{\infty}dy y^2\exp(-y^2)$$
$$\times\left\{Z_i^2\frac{\sum_\alpha\frac{1}{d_\alpha^2}(2s_{\alpha,i}^2W(s_{\alpha,i})+1)}{\sqrt{\left(\sum_\alpha\frac{1}{d_\alpha^2}W(s_{\alpha,i})\right)\left(\sum_\alpha\frac{1}{d_\alpha^2}\right)}}+(i\longrightarrow j)\right\} \quad (135)$$

and

$$\delta\Lambda_{ij}^{F} = -\frac{e^2}{2\sqrt{\pi}Td}\int_{-1}^{1}dx\int_{-1}^{1}dz\int_{0}^{\infty}dy y^2\exp(-y^2)$$
$$\times\left\{\frac{Z_i^2(m_i+m_j)}{m_iY_{ij}}\left[1-\frac{\sqrt{\sum_\alpha\frac{1}{d_\alpha^2}W(s_{\alpha,i})}}{\sqrt{\sum_\alpha\frac{1}{d_\alpha^2}}}\right.\right.$$
$$\left.-\frac{1}{2}\frac{\left(\sum_\alpha\frac{1}{d_\alpha^2}((1-2s_{\alpha,i}^2)W(s_{\alpha,i})-1)\right)^2}{\left(\sum_\alpha\frac{1}{d_\alpha^2}W(s_{\alpha,i})\right)^{3/2}\sqrt{\sum_\alpha\frac{1}{d_\alpha^2}}}\right. \quad (136)$$
$$\left.+\frac{\sum_\alpha\frac{1}{d_\alpha^2}((1-8s_{\alpha,i}^2+4s_{\alpha,i}^4)W(s_{\alpha,i})+2s_{\alpha,i}^2-1)}{\sqrt{\sum_\alpha\frac{1}{d_\alpha^2}W(s_{\alpha,i})}\sqrt{\sum_\alpha\frac{1}{d_\alpha^2}}}\right]$$
$$\left.+(i\longleftrightarrow j)\right\},$$

where $(i\longrightarrow j)$ and $(i\longleftrightarrow j)$ indicate that one should write the same term as the preceding one with i replaced by j and vice versa. With reference to expression (136), we have

$$Y_{ij} = \sqrt{\left(y^2+\frac{2m_jzxy\lambda_{ij}}{m_i+m_j}+\left(\frac{m_j\lambda_{ij}}{m_i+m_j}\right)^2\right)^2-\left(\frac{2m_jy\lambda_{ij}}{m_i+m_j}\right)^2(1-x^2)(1-z^2)}, \quad (137)$$

$$Y_{ji} = \sqrt{\left(y^2-\frac{2m_izxy\lambda_{ij}}{m_i+m_j}+\left(\frac{m_i\lambda_{ij}}{m_i+m_j}\right)^2\right)^2-\left(\frac{2m_iy\lambda_{ij}}{m_i+m_j}\right)^2(1-x^2)(1-z^2)}. \quad (138)$$

Let us note that in arriving at results (135) and (136), we used the expression for the derivative of the dielectric permittivity (7) [see (127)] and the equation for the dispersion function $W(s)$:

$$s\frac{dW(s)}{ds} = (1-2s^2)W(s)-1. \quad (139)$$

It is convenient to rewrite expression (134) in the form

$$\Lambda_{ij}^{F} = -\frac{e^2}{2Td}(Z_i^2(I_i+\delta I_i)+Z_j^2(I_j+\delta I_j)). \quad (140)$$

The relation between expressions (134) and (140) is straightforward; namely, I in expression (140) is related to the first term in expression (134) and δI in expression (140) is related to the second term in expression (134), while the expressions for I and δI are given by formulas (135) and (136), respectively.

One should note that the reciprocal of the square of the Debye length, $d_\alpha^{-2} = (4\pi e2/T)Z_\alpha^2 n_\alpha$ [see (2)], occurring in the summation in both the numerator and denominator of expressions (135) and (136) can be replaced by $Z_\alpha^2 n_\alpha$, because the remaining factors cancel each other. As for the electron contribution, since the electron thermal speed is larger than the velocity of the reacting nuclei so that $s_{e,i} \ll 1$ [see (130) and (131)], one can neglect (to lowest order in $s_{e,i}^2$) the electron contribution to $\sum_\alpha d_\alpha^{-2}s_{\alpha,i}^2W(s_{\alpha,i})$ and approximate $W(s_{e,i})\approx 1$ in the factor $\sum_\alpha d_\alpha^{-2}W(s_{\alpha,i})$ in the denominator of expression (135). Furthermore, the charge neutrality condition $n_e = \sum_i Z_i n_i$ is to be used. The first

term of expression (140) can then be written in the form

$$I_i = \frac{1}{\sqrt{\pi(1+Z_{\rm eff})}}\int_{-1}^{1}dx\int_{-1}^{1}dz\int_{0}^{\infty}dy\,y^2\exp(-y^2)$$
$$\times\left\{\frac{1+\sum_{j'}\frac{X_{j'}(Z_{j'})^2}{m_{j'}}(2(s_{j',i})^2W(s_{j',i})+1)\frac{1}{\sum_{j'}\frac{X_{j'}Z_{j'}}{m_{j'}}}}{\sqrt{1+\sum_{j'}\frac{X_{j'}(Z_{j'})^2}{m_{j'}}W(s_{j',i})\frac{1}{\sum_{j'}\frac{X_{j'}Z_{j'}}{m_{j'}}}}}\right\}. \quad (141)$$

The term I_j is obtained from (141) with $i \longrightarrow j$. In formula (141),

$$Z_{\rm eff} = \frac{\sum_{j'}\frac{X_{j'}Z_{j'}^2}{m_{j'}}}{\sum_{j'}\frac{X_{j'}Z_{j'}}{m_{j'}}}, \quad X_{j'} = \frac{m_{j'}n_{j'}}{\sum_{j'}m_{j'}n_{j'}}, \quad (142)$$

where $X_{j'}$ is the relative mass density abundance of the ions of species j'.

The term $\delta\Lambda_{ij}^F$ in formula (136) and, as consequence, the term δI_i in expression (140) can be expressed in terms of the same quantities as in formula (141).

In the limit for which $s_{j',i} \gg 1$ (i.e., the Gamow energy is significantly larger than the thermal energy of the reacting nuclei), one can make use of the asymptotic expansion $W(s) = -(1/2s^2)$, which is valid for the lowest significant order in $s^{-2} \ll 1$, and formula (141) yields $I_i^0 \approx 1/2\sqrt{1+Z_{\rm eff}}$. The corresponding asymptotic limit of expression (140) is

$$\Lambda_{ij}^{(F)} = -\frac{(Z_i^2+Z_j^2)e^2}{2\sqrt{1+Z_{\rm eff}}Td}. \quad (143)$$

Making use of expression (122) along with formulas (141) and (136), one obtains the Λ_{ij} correction that describes the plasma effects on the nuclear reaction rates [see (69)]. In this respect, we make the following two comments.

(i) $\Lambda_{ij} < 0$, in contrast with Salpeter's term $\Lambda_{ij}^S > 0$; i.e., the *plasma corrections to the reaction rates are negative* [cf. (143)].

(ii) In contrast with the Z_iZ_j scaling of Salpeter's static screening [see (6)], the plasma corrections to the nuclear reaction rates scale as the square of the nuclear charge [cf. (140)].Thus, for nuclear reactions involving high-Z nuclei, the slowing down of nuclear reaction rates is expected to be significant.

7. NUMERICAL RESULTS

7.1. Nuclear Reactions of the Hydrogen Cycle in the Solar Interior

For a quantitative evaluation of the plasma effects on the nuclear reaction rates, we consider the thermonuclear reactions relevant to the Sun's core.

The standard solar model provides the abundances of different ions for the central part of the solar interior [30–33]. For the mass abundances X_i and the quantity $Z_{\rm eff}$, defined by (142), the reference values are $X_{\rm H} = 0.3411$, $X_{\rm He} = 0.6387$, $X_{\rm C} = 0.00003$, $X_{\rm N} = 0.0063$, $X_{\rm O} = 0.0085$, $\sum_j Z_jX_j/m_j = 0.661$, and $Z_{\rm eff} = 1.551$. For a temperature of $T = 1.5$ keV and density of $n = 5 \times 10^{25}$ cm^{-3}, corresponding to the Sun's interior, we have $e^2/Td = 0.05$, which amounts to Salpeter's enhancement factor (6) equal to 5% for the (p, p) reaction. The results of numerical calculations are presented in Tables 1 and 2.

With reference to the most relevant reactions of the hydrogen cycle listed in the first column of Table 1, the values of the argument of the W function [see (141), (130), and (131)] are obtained from the relevant Gamow energies and the values of the parameter λ_{ij} determined by the Gamow energies are given in the second column of Table 1.

The values of both I_i, given by formula (141), and δI_i, obtained from formula (136) along with expression (140), as well as I_j and δI_j, occurring in expression (140), are

Table 1. Thermonuclear reactions of the hydrogen cycle for the Sun's core. The numerical results refer to the normalized Gamow velocity λ_{ij}, defined in (132); the integral quantities I, defined in (141); δI, given by (136) and (140); and the corresponding sum for each pair of fusing nuclei

Reaction	λ_{ij}	I_i	δI_i	$I_i + \delta I_i$	I_j	δI_j	$I_j + \delta I_j$
$p + p$	4.280	0.906	0.115	1.021	0.906	0.115	1.021
$p + {}^2$H	4.757	1.060	0.052	1.061	0.848	0.098	0.942
^{3}He + ^{3}He	8.150	0.888	0.040	0.928	0.888	0.040	0.928
^{3}He + ^{4}He	8.420	0.851	0.034	0.885	0.972	0.038	1.010
^{7}Li + p	10.234	1.144	–0.032	1.112	0.689	0.024	0.713
^{7}Be + p	11.264	1.127	–0.025	1.102	0.661	0.019	0.680

Table 2. With reference to the same reactions as in Table 1, the numerical results for $\Lambda_{ij}^{(F)}$, defined in (140); the corresponding asymptotic expression $\Lambda_{ij}^{(F,as)}$ [see (143)]; Salpeter's term $\Lambda_{ij}^{(S)} = Z_iZ_je^2/Td$ [see (6)]; the factor F_{ij} by which the reaction rates calculated based on Salpeter's enhancement should be divided; and the percentage deviation $(F_{ij} - 1)\%$

Reaction	$\Lambda_{ij}^{(F)}$	$\Lambda_{ij}^{(F,as)}$	$\Lambda_{ij}^{(S)}$	F_{ij}	$(F_{ij} - 1)\%$
$p + p$	−0.0510	−0.03	+0.05	1.106	10.6%
$p + {}^2\mathrm{H}$	−0.0514	−0.03	+0.05	1.107	10.7%
${}^3\mathrm{He} + {}^3\mathrm{He}$	−0.125	−0.2	+0.20	1.223	22.3%
${}^3\mathrm{He} + {}^4\mathrm{He}$	−0.125	−0.2	+0.2	1.223	22.3%
${}^7\mathrm{Li} + p$	−0.157	−0.250	+0.15	1.571	57.1%
${}^7\mathrm{Be} + p$	−0.266	−0.425	+0.2	2.087	108.7%

calculated for the two nuclei of each reaction and are presented in the third to eighth columns of Table 1 together with the sums $I_i + \delta I_i$ and $I_j + \delta I_j$. The values of both $\Lambda_{ij}^{(F)}$ and the corresponding asymptotic expansion, $\Lambda_{ij}^{(F,as)}$ [see (140) and (143)] are given in the second and third columns of Table 2. The values of Salpeter's term $\Lambda_{ij} = Z_iZ_je^2/Td$ are given in the fourth column of Table 2. The fifth column of Table 2 gives the factor

$$F_{ij} = \frac{1 + \Lambda_{ij}^{(S)}}{1 + \Lambda_{ij}^{(F)}} > 1, \qquad (144)$$

by which the reaction rates previously calculated on the basis of Salpeter's enhancement, due to static screening, should be divided to obtain the rates according to our treatment. The last column of Table 2 gives the change in the reaction rates (in percent).

From the numerical results presented in Tables 1 and 2, it follows that

(i) the δI corrections vary between 2 and 10%, the lower values corresponding to the higher values of the normalized Gamow velocity;

(ii) the value of $\left|\Lambda_{ij}^{(F)}\right|$ increases with the nuclear charge according to the $Z_i^2 + Z_j^2$ scaling in the asymptotic limit for which result (143) is valid;

(iii) the values obtained from the asymptotic approximation (143) tend to underestimate the exact value;

(iv) for the (^{7}Be, p) reaction, the requirement that $\Lambda_{ij}^{(F)} < 1$ is satisfied only marginally.

Let us again emphasize that the plasma effects on the nuclear reactions are such that the reaction rates are *slower* than the corresponding ones in vacuum; namely, the $\Lambda_{ij}^{(F)}$ corrections are negative. As a result, in particular, the reaction rates accounting for Salpeter's enhancement should be divided by the factor $F_{ij} > 1$ [see (144) and the last two columns of Table 2]. A significant (and only marginally acceptable with regard to our perturbative scheme) decrease in the rate of the (^{7}Be, p) reaction is expected to be relevant to the solar neutrino problem [30–33] (see also [34–37]). More specifically, from the solar neutrino experiments [34], it follows that the neutrino flux from the reaction ${}^8\mathrm{B} \longrightarrow {}^8\mathrm{Be} + e^+ + \nu$, where ^{8}B is produced through the reaction ${}^7\mathrm{Be} + p \longrightarrow {}^8\mathrm{B} + \gamma$, is reduced by about a factor of three with respect to the value predicted by a standard solar model [30–33]. The effect that the reduction of the rate of proton capture by ^{7}Be produces on the ^{8}B solar neutrino (see the last row of Table 2) is under investigation by means of a code for a standard solar model taking into account the plasma effects on the solar opacity as well [38, 39].

7.2. The ^{7}Be Electron Capture Rate

So far, we have referred to nuclear reactions characterized by the tunneling through the Coulomb barrier. Nuclear processes involving electron capture, instead, exhibit no Coulomb barrier, the electrons being attracted by the nuclei. The change of the electron function in the vicinity of the nuclei with respect to the plane wave function describing an electron far from the nuclei enhances the electron capture rate, which was first calculated by Bahcall [40] and then by Brown and Sawyer [23], as well as by Gruzinov and Bahcall [22]. Such an enhancement is accounted for in both (118) and (119) through the replacement $w_{ie}^{(0)} \longrightarrow \Lambda_i^B(v) w_{ie}^{(0)}$, such a replacement also being made in $R_{ij}^{(0)}$ in the denominator of both (118) and (119) with [22, 40]

$$\Lambda_i^B(v) = \frac{\dfrac{2\pi Z_i e^2}{v\hbar}}{1 - \exp\left(-\dfrac{2\pi Z_i e^2}{v\hbar}\right)}, \qquad (145)$$

Table 3. Plasma corrections to the (^{7}Be, e) reaction rate for the Sun's core [see (146)–(150)] and the factor F_{Be} by which the electron capture rate calculated based on Salpeter's enhancement should be divided

I_{Be}	δI_{Be}	I_e	δI_e	$F_{\mathrm{Be}} = \dfrac{1+\Lambda^{(S)}_{\mathrm{Be},e}}{1+\Lambda^{(F)}_{\mathrm{Be},e}}$
0.0558	−0.030	0.353	0.126	2.166

where v is the electron velocity. For the ^{7}Be + e reaction, the average of factor (145) with respect to the electron thermal distribution yields an enhancement factor of 3.18 for the value of the temperature of the solar interior [22, 40].

To proceed further, one should note that the Gamow energy is zero and the center of the mass system is approximately the same as the laboratory system, which permits us to carry out the averaging directly over the thermal distributions of both electron and nucleus momenta [see (120)].

We again obtain cancellation (122). Let us consider now corrections (140) along with formulas (135) and (136). As for the nuclei contribution, one can make use of the foregoing expressions with the argument of the W function equal to xy [see (130) or (131), where $\lambda_{ij} = 0$]. Moreover, the integration involving the electrons occurs in the form of the same factor in both the numerator and denominator and thus it cancels out. As for the electron contribution, one can neglect the contribution to the dielectric permittivity from the ions, taking into account that the ion velocity is significantly smaller than the electron velocity. For the specific case of the (^{7}Be + e) reaction, one obtains the following result [see (140)]:

$$\Lambda^{F}_{\mathrm{Be},e} = -\frac{e^2}{2Td}(16(I_{\mathrm{Be}}+\delta I_{\mathrm{Be}}) + I_e + \delta I_e), \qquad (146)$$

where

$$I_{\mathrm{Be}} = \frac{1}{\sqrt{\pi}(1+Z_{\mathrm{eff}})}\int_{-1}^{1} dx \int_{0}^{\infty} y^2 e^{-y^2} dy \times \frac{\sum_\alpha \frac{1}{d_\alpha^2}\left(2x^2y^2\frac{m_\alpha}{m_{\mathrm{Be}}}W\left(\sqrt{\frac{m_\alpha}{m_{\mathrm{Be}}}}xy\right)+1\right)}{\sqrt{\sum_\alpha \frac{1}{d_\alpha^2}W\left(\sqrt{\frac{m_\alpha}{m_{\mathrm{Be}}}}xy\right)}}, \qquad (147)$$

$$\delta I_{\mathrm{Be}} = \frac{1}{2\sqrt{\pi}}\int_{-1}^{1} dx \int_{0}^{\infty} dy e^{-y^2} \left\{ 1 - \frac{\sqrt{\sum_\alpha \frac{1}{d_\alpha^2}W\left(\sqrt{\frac{m_\alpha}{m_{\mathrm{Be}}}}xy\right)}}{\sqrt{1+Z_{\mathrm{eff}}}} - \frac{1}{2}\frac{\left[\sum_\alpha \frac{1}{d_\alpha^2}\left(1-2x^2y^2\frac{m_\alpha}{m_{\mathrm{Be}}}\right)W\left(\sqrt{\frac{m_\alpha}{m_{\mathrm{Be}}}}xy\right)-1\right]^2}{\sqrt{1+Z_{\mathrm{eff}}}\left[\sum_\alpha \frac{1}{d_\alpha^2}W\left(\sqrt{\frac{m_\alpha}{m_{\mathrm{Be}}}}xy\right)\right]^{3/2}} + \frac{\sum_\alpha \frac{1}{d_\alpha^2}\left(1-8x^2y^2\frac{m_\alpha}{m_{\mathrm{Be}}}+4x^4y^4\frac{m_\alpha^2}{m_{\mathrm{Be}}^2}\right)W\left(\sqrt{\frac{m_\alpha}{m_{\mathrm{Be}}}}xy\right)+2x^2y^2\frac{m_\alpha}{m_{\mathrm{Be}}}-1\right)}{\sqrt{(1+Z_{\mathrm{eff}})\sum_\alpha \frac{1}{d_\alpha^2}W\left(\sqrt{\frac{m_\alpha}{m_{\mathrm{Be}}}}xy\right)}} \right\}, \qquad (148)$$

$$I_e = \frac{1}{\int_0^\infty \frac{4y^2\exp(-y^2)dy}{\sqrt{\pi}}\Lambda^B_{\mathrm{Be}}(y)}\frac{1}{\sqrt{\pi}}\int_{-1}^{1} dx \int_{0}^{\infty} dy y^2 \times \exp(-y^2)\Lambda^B_{\mathrm{Be}}(y)\frac{(x^2y^2W(xy)+1)}{\sqrt{W(xy)(1+Z_{\mathrm{eff}})}}, \qquad (149)$$

$$\delta I_e = \frac{1}{\int_0^\infty \frac{4y^2\exp(-y^2)dy}{\sqrt{\pi}}\Lambda^B_{\mathrm{Be}}(y)}\frac{1}{\sqrt{2\pi}}\int_{-1}^{1} dx \int_{0}^{\infty} dy y^2 e^{-y^2}\Lambda^B_{\mathrm{Be}}(y) \times \left\{ 1 - \sqrt{\frac{W(xy)}{1+Z_{\mathrm{eff}}}} - \frac{[(1-2x^2y^2)W(xy)-1]^2}{\sqrt{1+Z_{\mathrm{eff}}}(W(xy))^{3/2}} \right. \qquad (150)$$

$$+\frac{(1-8x^2y^2+4x^4y^4)W(xy)+2x^2y^2-1}{\sqrt{(1+Z_{\rm eff})W(xy)}}\Bigg\}.$$

For the temperature of the solar interior, factor (145) is equal to $\Lambda^B_{\rm Be}(y) = (2.6/y)[1-\exp(-(2.6/y)]^{-1}$.

The numerical results for the integrals for the ^{7}Be electron capture relevant to the solar interior are given in Table 3, along with the factor $F_{\rm Be}$, by which the (^{7}Be + e) reaction rate evaluated according to Salpeter's approach should be *divided* to obtain our results.

A significant *decrease* in the reaction rate of electron capture by ^{7}Be is expected to reduce the flux of ^{7}Be solar neutrinos that are produced from the reaction $^7\mathrm{Be} + e \longrightarrow {}^7\mathrm{Li} + \nu$. Whether such a reduction can explain the strong deficit of ^{7}Be neutrinos measured in the solar neutrino experiments [34–37] is under investigation.

8. GENERAL DISCUSSION AND CONCLUSIONS

In this section, we touch upon a few issues related to the subjects developed in the preceding sections. The discussion is somewhat speculative and intends mainly to identify a number of topics that need further investigation. More specifically, we briefly discuss the effects on the reaction rates of both nonlinear fluctuations and turbulence, as well as the effects due to wave emission. The section ends with a few concluding remarks.

8.1. Nonlinear Fluctuations

The perturbation theory used to describe the plasma corrections to the rates of nuclear reactions can be extended to the next-order approximation in the fluctuations to account for nonlinear effects. One can proceed to make an expansion in the small parameter that is the ratio between the particle thermal energy and the Gamow energy and/or take into account only the terms with the largest power of Z, which contribute the most to the corrections. From a preliminary analysis, it follows that:

(i) The corrections due to nonlinear dielectric permittivities tend to be small since both the Gamow energy is large and the parameter related to the reciprocal of the number of particles in the Debye sphere is small. Moreover, the relative contribution of heavy ions to the nonlinear dielectric permittivities is $Z_i^2 n_i m_p/m_i$, which is small since $Z_i m_p/m_i \approx 2$ and $Z_i n_i/n_p \ll 1$ for heavy ions.

(ii) An additional renormalization is needed in fluctuation theory, which leads to proper treatment of the Landau poles.

(iii) The corrections related to the ions with large charges are the most important.

(iv) An extrapolation of these results to the case of a strong change of the reaction rates by plasma fluctuations leads to a substitution of the linear corrections obtained here by exponential ones.

8.2. Nuclear Reactions in Nonthermal and Turbulent Plasmas

The results obtained in the foregoing are valid for the general case of nonthermal plasmas, for which, however, the analytical properties of the dielectric functions (fluctuation-dissipation theorem) are, in general, no longer applicable. For arbitrary, non-thermal distributions, the sign of the effect of plasma fluctuations on the nuclear reaction rates is not determined and it can lead to either enhancement or suppression of the reactions. An electron distribution function of interest is the one accounting for drift motion, because it results from currents in a plasma related to strong magnetic fields, which are expected to be present in many stars and probably in the center of the Sun.

The results obtained in this work can be applied to turbulent fluctuations. For the case in which the particle distribution functions are thermal and the level of turbulent fluctuations is much higher than the thermal level and assuming that the frequency of fluctuations ω is much less than kv_T, one can generalize result (140) to

$$\Lambda_{ij} = -\frac{e^2}{2T^2}(Z_i^2+Z_j^2)\int d\mathbf{k}\,d\omega\,|\delta\phi|^2_{\mathbf{k},\omega}, \qquad (151)$$

where $|\delta\phi|^2_{\mathbf{k},\omega}$ describes the turbulent potential fluctuations

$$\langle(\delta\phi)^2\rangle = \int|\delta\phi|^2_{\mathbf{k},\omega}d\mathbf{k}\,d\omega. \qquad (152)$$

The corrections to the reaction rates described by expression (151) are always negative. With reference to the Sun, of particular relevance are the acoustic helioseismological fluctuations [41], which are mainly hydrodynamic fluctuations. The total energy density of these fluctuations is

$$(5/3)(1+Z_{\rm eff})\langle(\delta\phi)^2\rangle/d^2.$$

From the known level of the Sun's oscillations, we can estimate that, even for $Z_i = 8$ (^{16}O), corrections (151) are negligible (less than 0.01%). In this case, the assumption that the level of turbulent fluctuations is higher than the level of thermal fluctuations is not valid and the whole effect is described by thermal fluctuations as considered above. One can think of other types of fluctuations [42], including Langmuir waves, whose wave number spectrum, however, is very narrow since the number of particles in the Debye sphere is not large (about six) for parameters relevant to the solar interior.

In turbulent plasmas, the particle distributions often exhibit nonthermal (power-law) tails (see, e.g., [43]),

which can significantly affect the reaction rates. On the other hand, for the solar interior, the plasma relaxation time is of the order of N_d/ω_{pe} and the effects of nonthermal tails are thus negligible (see also [44]).

8.3. Emission of Waves in Nuclear Reactions

The self-energy of the fusing nuclei undergoes an abrupt change during nuclear reactions, which can result, in particular, in transition radiation [21]. The calculation of the energy emitted in longitudinal waves can be performed along the lines described in detail in [21]. Emission of electromagnetic waves is negligible for particles moving with nonrelativistic velocities. For the specific case of a nuclei moving along a straight trajectory with velocity **v** and disappearing in the reaction at the moment $t = 0$, the energy of transition radiation can be obtained as the work done by the electric field on the charge (integrated with respect to the entire time and volume):

$$E_i^{tr} = \int (\mathbf{E}\cdot\mathbf{j})\,d\mathbf{r}\,dt = \frac{2Z_i^2e^2}{\pi^2}\int d\mathbf{k}\frac{\omega_\mathbf{k}}{k^2\left|\omega_\mathbf{k}-\mathbf{k}\cdot\mathbf{v}\right|^2(\partial\varepsilon_{\mathbf{k},\omega}/\partial\omega)_{\omega=\omega_\mathbf{k}}}, \quad (153)$$

where **j** is the particle current density and $\omega_\mathbf{k}$ is the frequency of the plasma mode emitted. In the derivation of relation (153), we used the expression for the charge density $\rho_{\mathbf{k}\omega}$ of a nuclei that moves with a constant velocity until $t = 0$ and Poisson's equation

$$\rho_{\mathbf{k},\omega} = \frac{Z_ie}{i(\omega-\mathbf{k}\cdot\mathbf{v}+i0)(2\pi)^2}. \quad (154)$$

For Langmuir waves, the emission of which is most significant and for which $\omega_\mathbf{k} \gg kv_{Te}$, relation (153) yields

$$E_i^{tr,l} = \frac{4Z_i^2}{\pi d_e}f, \quad (155)$$

where f is the ratio between the maximum wavenumber and $1/d_e$, with d_e being the electron Debye length. Usually, this ratio is $f = 1/2$ or $1/3$.

From relation (155), it follows that the energy emitted is of the same order as the self-energy, in accordance with the general statement proved in the theory of transition radiation. This emission guarantees the conservation of the sum of all the self-energies relevant to both the reactions and the emitted waves. The emission of plasma waves is concomitant to any nuclear reaction occurring in a plasma.

The total power density Q_{ij} emitted due to the nuclear reaction $i + j \longrightarrow i' + j'$ is determined by

$$Q_{i,j}^l = \frac{1}{\tau_{ij}}(E_i^{tr,l}n_i + E_j^{tr,l}n_j + E_{i'}^{tr,l}n_{i'} + E_{j'}^{tr,l}n_{j'}), \quad (156)$$

where τ_{ij} is the time of the nuclear reaction. The level of the emitted Langmuir waves can be obtained from balancing emission power (156) by the Landau damping; i.e., $-2\gamma_L W^l = Q^l$, which, being normalized to the particle thermal energy, is of the order of $Z^2/\nu_{coll}\tau$, where ν_{coll} is the collision frequency. For all of the reactions in the solar interior (even with very large Z), this level is much less than the thermal fluctuation level. This means that the Langmuir waves are almost instantaneously absorbed as soon as they are emitted, so that taking into account only thermal fluctuations (as we did) is quite justified.

8.4. Concluding Remarks

In summary, we have obtained a remarkable result, according to which the rates of nuclear reactions occurring in a plasma are *slower* than those in vacuum. This result might be of particular relevance to the solar neutrino problem. Let us briefly summarize the basic concepts underlying our result.

(i) Only the fluctuation approach can provide an adequate description of the plasma effects on the rate of thermonuclear reactions.

(ii) The fluctuations responsible for binary plasma collisions are strictly connected to the fluctuations affecting the reaction rates.

(iii) The kinetic equations describing the binary plasma collisions due to fluctuations in nonequilibrium plasmas are generalized by taking into account the nuclear reactions, the general kinetic description of which is given for nonequilibrium plasmas.

(iv) The reacting nuclei are treated as plasma excitations, i.e., charges endowed with fluctuating self-energy clouds, which makes their interactions with plasma particles significantly different from the corresponding interactions of bare nuclei.

(v) The fluctuations causing the screening of the nuclei interactions and the fluctuations responsible for the nuclei self-energy are not separable, with the result being that the net effect on the nuclear reaction rates related to both the interaction energy and the static part of the self-energy seems to be zero.

(vi) The renormalization of the particle distribution function provides the free energy related to the self-energy of the plasma particles treated as plasma excitations.

(vii) The slowing-down of the thermonuclear reaction rates resulting from the plasma fluctuations is the same as that obtained in the context of the dynamically screened test particle approach.

(viii) A simple physical explanation of the slowing-down of the reaction rates by plasma fluctuations rests on a decrease in the dynamically screened part of the nuclei self-energy with increasing the velocity of the reacting nuclei.

Note added in the proof: The aim of this review is to describe the new possibilities of applying the fluctuation approach to calculating the rates of thermonuclear reactions in dense plasmas. Since the problem is formulated in such a

way for the first time, a further comprehensive development and implementation of this approach seem to be desirable and necessary. Among questions that can be raised are the following: (i) May there exist an additional effect of the distribution function renormalization when the additional fluctuations (63), induced by nuclear reactions, are taken into account? (ii) Whether the influence of the plasma correlations related to the difference between the two-particle distribution function and the product of two one-particle distribution functions is important? (iii) Are the corrections to the interaction canceled completely or not? For future improvements, one should keep in mind that, from the physical point of view, purely static plasma corrections are unacceptable.

ACKNOWLEDGMENTS

The work of V.N. Tsytovich was supported by the Cariplo Foundation for Scientific Research, Landau Network–Centro Volta, Italy. V.N. Tsytovich acknowledges the hospitality of Pavia University and Collegio Nuovo, Pavia, Italy.

REFERENCES

1. E. E. Salpeter, Aust. J. Phys. **7**, 373 (1954); D. D. Clyton, *Principles of Stellar Evolution and Nucleosynthesis* (Mc Graw-Hill, New York, 1968).
2. C. Carraro, A. Schafer, and S. E. Koonin, Astrophys. J. **331**, 565 (1988).
3. V. N. Tsytovich and M. Bornatici, Comments Plasma Phys. Controlled Fusion **1** (4) (2000).
4. E. E. Salpeter and H. M. van Horne, Astrophys. J. **155**, 183 (1969).
5. H. E. Dewitt, H. C. Graboske, and M. C. Cooper, Astrophys. J. **181**, 439 (1973).
6. B. Jancovici, J. Stat. Phys. **17**, 357 (1977).
7. H. E. Mitler, Astrophys. J. **212**, 513 (1977).
8. S. Ichimaru, Rev. Mod. Phys. **65**, 255 (1993).
9. A. V. Gruzinov, Astrophys. J. **496**, 503 (1998).
10. L. S. Brown and R. F. Sawyer, Rev. Mod. Phys. **69**, 411 (1997).
11. N. J. Shaviv and G. Shaviv, Astrophys. J. **468**, 433 (1996).
12. M. Brüggen and D. O. Gough, Astrophys. J. **488**, 867 (1997).
13. M. Sahrling and G. Chabrier, Astrophys. J. **493**, 879 (1998).
14. C. W. Johnson, E. Kolbe, S. E. Koonin, and K. Langanke, Astrophys. J. **392**, 320 (1992).
15. J. Weneser, Phys. Rev. D **52**, 640 (1995).
16. A. V. Gruzinov and J. N. Bahcall, Astrophys. J. **504**, 996 (1998).
17. G. Shaviv and N. J. Shaviv, Phys. Rep. **311**, 99 (1999).
18. S. Ichimaru, *Statistical Plasma Physics: Basic Principles* (Addison-Wesley, Reading, 1992).
19. L. D. Landau and E. M. Lifshitz, *Electrodynamics of Continuous Media* (Nauka, Moscow, 1982; Pergamon, New York, 1984).
20. V. N. Tsytovich, *Lectures on Nonlinear Plasma Kinetics* (Springer-Verlag, Berlin, 1995).
21. V. L. Ginzburg and V. N. Tsytovich, *Transition Radiation and Transition Dispersion* (Nauka, Moscow, 1984).
22. A. V. Gruzinov and J. N. Bahcall, Astrophys. J. **490**, 437 (1998).
23. A. V. Brown and R. F. Sawyer, Astrophys. J. **489**, 968 (1998).
24. N. N. Bogolyubov, in *Studies in Statistical Mechanics*, Ed. by J. de Boer and G. E. Uhlenbeck (Gostekhizdat, Moscow, 1946; Wiley, New York, 1961), Vol. 1.
25. Yu. L. Klimontovich, Usp. Fiz. Nauk **167**, 23 (1997) [Phys. Usp. **40**, 21 (1997)].
26. E. M. Lifshitz and L. P. Pitaevskiĭ, *Physical Kinetics* (Nauka, Moscow, 1979; Pergamon, Oxford, 1981).
27. L. D. Landau and E. M. Lifshitz, *Statistical Physics* (Nauka, Moscow, 1964; Pergamon, Oxford, 1980).
28. L. D. Landau and E. M. Lifshitz, *Quantum Mechanics: Non-Relativistic Theory* (Nauka, Moscow, 1956; Pergamon, Oxford, 1977).
29. V. N. Tsytovich, Zh. Éksp. Teor. Fiz. **42**, 457 (1962) [Sov. Phys. JETP **15**, 320 (1962)].
30. J. N. Bahcall, *Neutrino Astrophysics* (Cambridge Univ. Press, Cambridge, 1989).
31. J. N. Bahcall, R. T. Pinsonneault, and G. J. Wasserburg, Rev. Mod. Phys. **67**, 781 (1995).
32. C. Ciacio, S. Degl'Innocenti, and B. Ricci, Astron. Astrophys., Suppl. Ser. **123**, 449 (1997).
33. P. Morel, B. Pichon, J. Provost, and G. Berthomieu, Astron. Astrophys. **350**, 275 (1999).
34. T. A. Kirsten, Rev. Mod. Phys. **71**, 1213 (1999).
35. A. Dar and G. Shariv, Phys. Rep. **311**, 115 (1999).
36. V. S. Berezinsky, G. Fiorentini, and M. Lissia, Phys. Lett. B **365**, 185 (1998).
37. B. Ricci, S. Degl'Innocenti, and G. Fiorentini, Phys. Rev. C **52**, 1095 (1995).
38. V. N. Tsytovich, R. Bingham, U. de Angelis, *et al.*, Astropart. Phys. **5**, 197 (1996).
39. V. N. Tsytovich, R. Bingham, U. de Angelis, and A. Forlani, Usp. Fiz. Nauk **166**, 113 (1996) [Phys. Usp. **39**, 103 (1996)].
40. J. N. Bahcall, Phys. Rev. **128**, 1297 (1962).
41. S. Degl'Innocenti, W. A. Dziembowski, G. Fiorentini, and B. Ricci, Astropart. Phys. **7**, 77 (1997).
42. J. Montalban and E. Schatzman, Astron. Astrophys. **351**, 347 (1999).
43. N. N. Aleksandrov and A. N. Starostin, Zh. Éksp. Teor. Fiz. **113**, 1661 (1998) [JETP **86**, 903 (1998)].
44. S. Turk-Chieze, Phys. Rep. **150**, 1 (1995).

Translated by V.N. Tsytovich

Plasma Physics Reports, Vol. 26, No. 10, 2000, pp. 868–874. Translated from Fizika Plazmy, Vol. 26, No. 10, 2000, pp. 927–933.

PLASMA DYNAMICS

Microexplosion of a Hot Point in an X-Pinch Constriction

G. V. Ivanenkov*, S. A. Pikuz*, D. B. Sinars, V. Stepnievski***, D. A. Hammer**, and T. A. Shelkovenko***

**Lebedev Institute of Physics, Russian Academy of Sciences, Leninskiĭ pr. 53, Moscow, 117923 Russia*

***Laboratory of Plasma Studies, 369 Upson Hall, Cornell University, Ithaca, NY 14853, USA*

***Institute of Plasma Physics and Laser Microfusion, Warsaw 49 Hery 23, Poland*

Received November 22, 1999; in final form, April 20, 2000

Abstract—The dynamics of an X-pinch in the diode of a high-power nanosecond current generator is studied experimentally and theoretically. The X-ray backlighting technique with subnanosecond time resolution and micron space resolution made it possible to trace both the formation of the constriction before the X-ray burst and the subsequent breaking and decay of the constriction. The radiative MHD model allowed simulation of the main characteristics of the process, including the formation of a minidiode and constriction, microexplosion of the hot point, and the generation of shock waves, followed by breaking of the constriction. © *2000 MAIK "Nauka/Interperiodica".*

Nanosecond explosions of thin wires are usually accompanied by the formation of constrictions and hot points. The physical picture of the associated processes remains unclear because of the insufficient resolution of the conventional experimental techniques. In this study, we apply the novel X-ray backlighting technique [1, 2] using X-pinches as radiation sources to trace the processes with a time resolution higher than 0.5 ns and space resolution about 1 μm. This allows us to approach the scale length of hot points and provides better insights into these objects in comparison with our previous works [3]. Recent experiments [4] showed that the most interesting processes are localized within ±2 ns around the X-ray burst.

In this paper, the dynamics of an X-pinch in the diode of a high-power nanosecond current generator is studied both experimentally and theoretically. Using two X-pinches that play the role of radiation sources and, at the same time, are the subjects of inquiry (Fig. 1c) allowed us to trace the evolution of the constriction in detail.

Experiments were carried out in the XP device (470 kA, 0.5 Ω, 100 ns) at Cornell University. Pairs of crossed 1-cm-long and 12.7-, 17-, 25-, or 30-μm-diameter molybdenum wires exploded in a diode. X radiation was detected by photoconductive diamond detectors. Signals were recorded with the help of a Tektronix 684B oscillograph with 0.4-ns time resolution. The spatial resolution of X-ray images depended on a number of factors (the size of a hot point, its distance from the object and film, and the types of filters and films used) and was estimated as ≃1 μm by digitizing photos with a Nikon LS-2000 scanner. Films of different sensitivities (Kodak RAR 2497, DEF, and Mikrat VE) were loaded as "sandwiches" with a 12.5-μm-thick Ti foil in front of them, which allowed us to obtain several images in various X-ray spectral regions.

Two X-pinches in the diode were positioned in parallel, irradiating each other. The time delay of X-ray bursts was specified by choosing the difference between load masses, taking into account the results from previous studies. It is important that, when pinches were arranged in pairs in the diode, the inductive coupling of loads allowed us to reduce the number of hot-point bursts to 1–2, which ensured a fairly high quality of the photos. The optimization of the source dimensions made it possible to operate in the spectral range of 1–5 Å covering the Ti-foil pass band of 2.5–4 Å. In this scheme, only the total current was measured, whereas the currents of individual X-pinches were assumed to be nearly the same, attaining 200–230 kA at maximum. In addition to molybdenum X-pinches, we investigated tungsten X-pinches; however, the database for the latter was substantially smaller. For this reason, below, we only present the data for molybdenum X-pinches with 17-μm wires.

The images in Fig. 1a clearly demonstrate two basic types of structures in the discharge: a minidiode (the central region where the wires are crossed and the constriction is formed) and cores positioned along the axes of initial wires and surrounded by a plasma corona. One can also see axial jets that are adjacent to the minidiode and have the same density as the corona. In this paper, our attention is mainly focused on the processes occurring in the minidiode; a more detailed description of results obtained in the experiments with X-pinches is the subject of a separate paper.

The minidiode images in Fig. 1a demonstrate that, when approaching the instant of the X-ray burst, the characteristic time scale of the constriction implosion

1063-780X/00/2610-0868$20.00

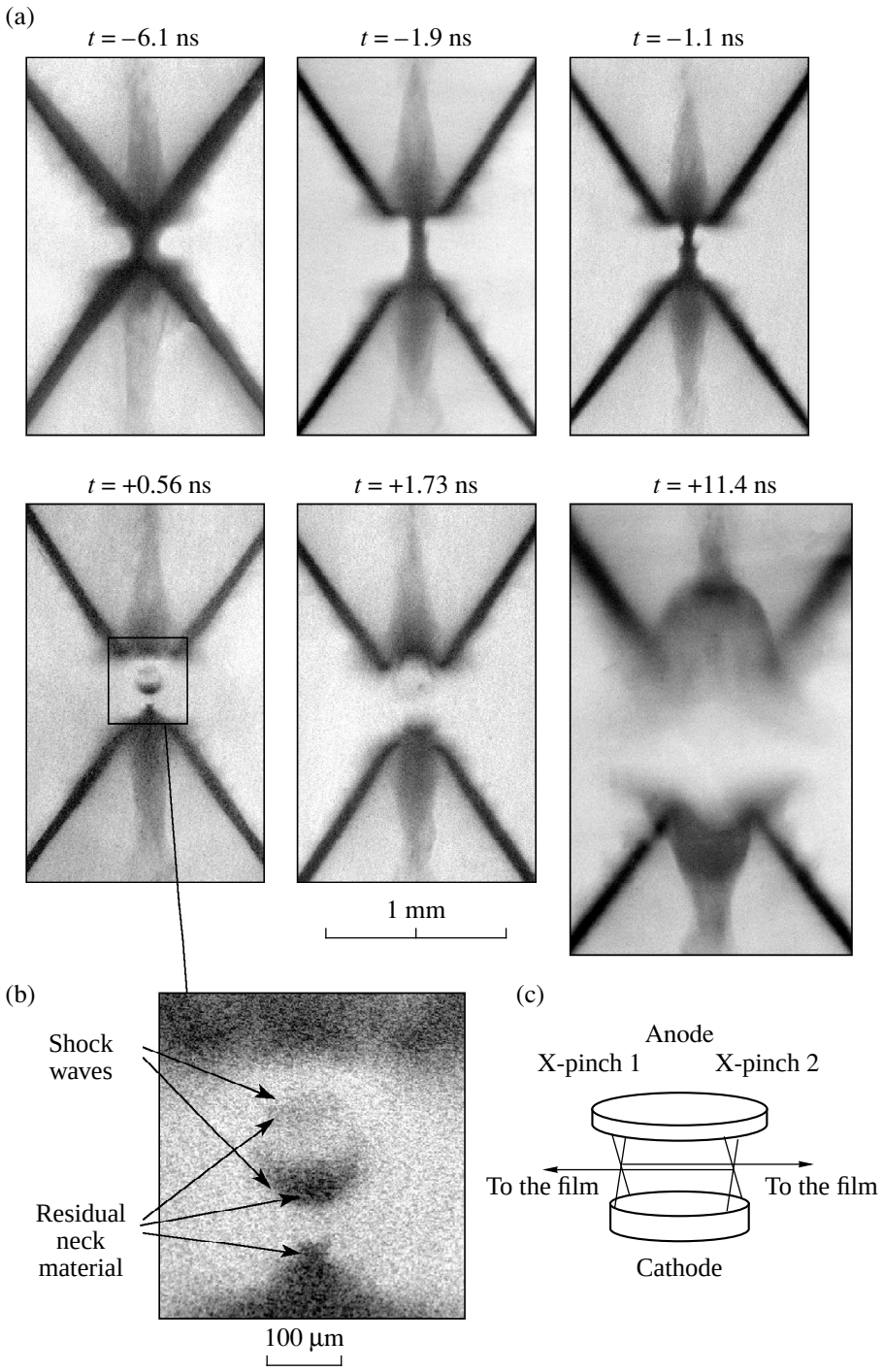

Fig. 1. (a, b) X-ray images of an X-pinch and (c) schematic of the experiment.

reduces from an initial value of 10 ns to ~5 ns before the burst and, then, to less than 0.5 ns. Thus, even 2 ns before the burst, there is no evidence of the formation of a narrow neck in the constriction, but it is clearly seen 1 ns later. According to measurements, the hot-point burst is almost instantaneous: its actual duration was shorter than the resolution of the apparatus (i.e., shorter than 0.4 ns). The currents flowing at this instant through each of the two X-pinches were usually about 150–170 kA.

After the burst, the time scale of the process increases. A rapid emptying of the minidiode occurs. In the last frame in Fig. 1a, one can see how the "minielec-

trodes" bounding this region are extruded by a flow of dense plasma expelled from the minidiode. These processes are similar to those occurring when a body flying at a high speed collides with an obstacle: fragments of a matter flying apart are seen, while, in the middle, we see how the minielectrodes are gradually extruded into the space between the almost immobile cores. Note that the dimensions of the plasma objects and cores gradually increase (the spatial scale is the same in all of the frames).

All these data refer to molybdenum, which turns out to be the most convenient metal for the experiments due to such factors as the absence of hard bremsstrahlung that is produced by an electron beam in the last stage of the constriction and worsens the images and a high intensity of radiation emitted from the minimum-size plasma region in the probing spectral range of 2–5 Å. However, a similar dynamics was observed for other metals, in particular tungsten, which was chosen for numerical calculations. This choice was motivated merely by a simpler modeling of a tungsten plasma, which has a higher optical thickness. The necessity of such calculations is dictated by the lack of experimental data on the rate of processes occurring in X-ray bursts because the available time resolution is insufficient.

Unlike the previous models [5, 6], here we used the experimental data to formulate the boundary conditions. The following facts were taken into consideration. Undoubtedly, the geometry of a discharge through crossed wires is, as a whole, more complicated than that through a single wire because the plane in which the wires are positioned plays a decisive role, determining the azimuthal inhomogeneity and the three-dimensional (3D) geometry of the magnetic field. In the region where the wires cross, an essentially 3D expansion (unlike quasi-cylindrical expansion, as in the other discharge regions) of the material occurs. The role of these factors is not yet completely understood, and the theoretical analysis encounters difficulties. Hence, it is reasonable to use a simplified two-dimensional model of the phenomenon in order to adequately describe only the most important region, namely, the constriction. We assume that the minidiode is autonomous, whereas the other parts of the X-pinch merely serve to supply the current. At the initial instant (which was chosen to correspond to a certain instant after the current start-up), the immobile plasma column was assumed to be in equilibrium and to have the shape of a paraboloid of revolution (Fig. 2). The radius of the minor cross section of the plasma column in the center was equal to 100 μm, and, at the ends, it was equal to 150 μm. The length of the fragment of interest was 400 μm[1] The density distribution corresponded to a pair of wires 10 μm in diameter. The current at $t = 0$ was assumed to be 50 kA; then, it increased by a sinusoidal law to 300 kA within 50 ns. The temperature (which determines the average ion charge Z through the Moor formula) was chosen according to the Bennet formula, and its profile decayed exponentially with depth. The temperature at the plasma surface was estimated as 16 eV. We note that variations in these parameters (the initial current was decreased to 10 kA and the temperature was increased to 3 eV) did not change the calculation results significantly.

We used the generalized version [6] of the model [7]. Along with the electron and ion temperatures, we introduced the radiative temperature. The model included the MHD equations of continuity and motion, the equation for heat transfer by particles, the equation for radiation transfer in an optically dense medium (with the transition to a transparent plasma in the outer plasma layers), the equations of ionization kinetics in the average-charge approximation, and the equation describing the generation of a magnetic field. The equation of state incorporated the effects related to the nonideal character of the ion component and quantum degeneration of electrons; in addition to [6], the contribution from radiation was also taken into account. In other respects, the model was almost the same in [7]: as previously, we used the Braginskii transport coefficients and assumed the resistance to be anomalous due to ion-acoustic, modified Buneman, or hybrid turbulence. We used the same power approximations for the averaged Planck and Rossealand mean free paths of photons and took into account the processes of electron impact ionization, photorecombination, and three-body recombination. The dependence of the ionization energy on Z was obtained by interpolating the available data for free ions; a correction for increasing the ionization threshold and evanescence of higher excited levels under the action of ion microfields was introduced. The numerical algorithm was developed according to the D'yachenko free-point method improved by Jach [8]. At the lateral boundaries, we applied the usual symmetric conditions, according to which the constriction, in fact, was considered to be a very short column. At the ends, the condition $v_z = 0$ did not exclude the numerical diffusion of the calculation points through the boundaries, thus imitating the plasma outflow along the axis from the constriction. In computations, we used 15×60, 20×80, or 25×100 meshes. In all cases, we obtained similar results.

After a short phase of adaptation to physical conditions, the results of computations (Fig. 2) describe the physical evolution of the constriction. In the initial stage of evolution, we observe the development of slow MHD processes with a characteristic time of 10 ns and subsonic velocities of about $\simeq 10^5$ cm/c. Thus, by time $t = 5$ ns, one can see the ionization wave approaching the axis and the heating of wire material by the current. The maximum values of the temperature ($\simeq 30$ eV) and ion charge are observed behind the wave front, whereas the maximum density values are observed ahead of the

[1] This geometry and dimensions approximately correspond to the photos presented in Fig. 1 for the instant ~15 ns before the burst.

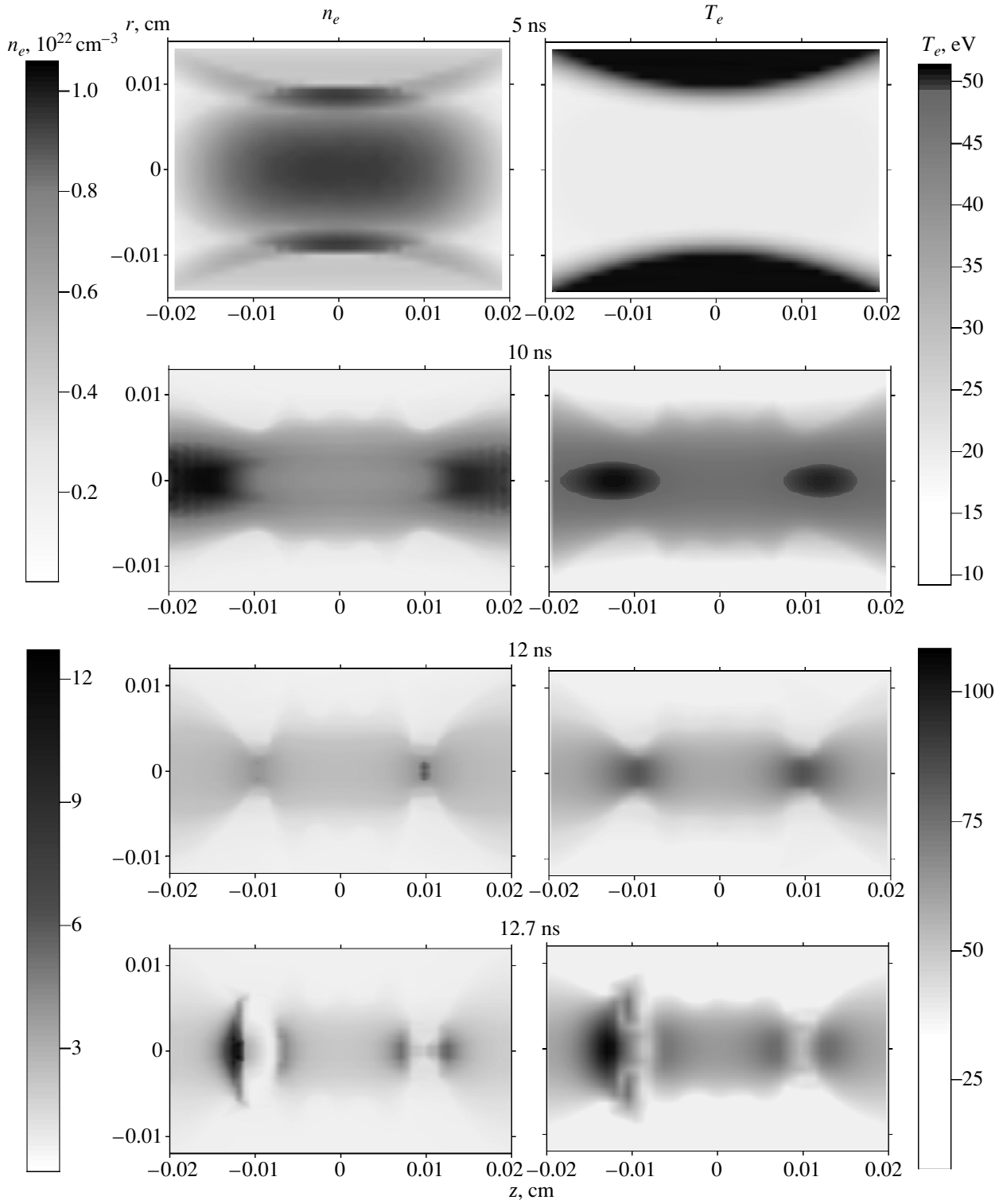

Fig. 2. Electron temperature and density distributions in an X-pinch calculated using the two-dimensional model at different instants.

wave front, in the center of the minidiode. The heated plasma behind the front expands gradually. In the axial region and at the ends, the plasma flows slowly out from the minidiode at velocities of (3–4) $\times 10^4$ cm/s, the velocity of the plasma flowing toward the cathode being higher than that flowing toward the anode. Shock

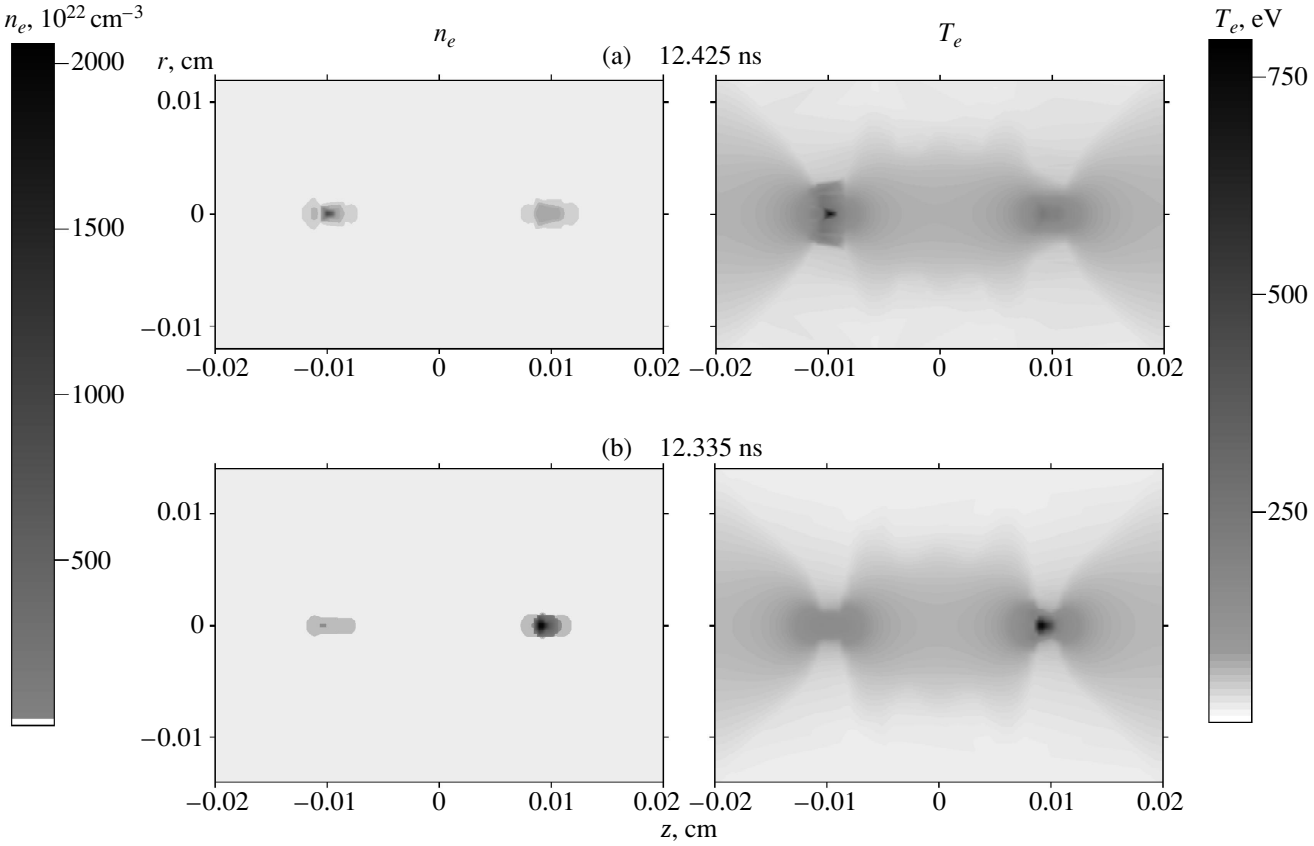

Fig. 3. States of the maximum compression of an X-pinch: (a) basic and (b) weakly perturbed versions.

waves are absent, the temperature near the anode is lower than near the cathode, and the compression ratio is still small.

The slow phase ends by the instant $t = 10$ ns. This time coincides with the time needed to heat the plasma volume near the constriction: $\tau \simeq a^2/2\pi\chi$, where $a \simeq 100$ μm is the constriction radius and $\chi = 2\kappa/3n_i \sim Z^{-1}T^{5/2}$ is the electron thermal diffusivity (with κ being the thermal conductivity). Behind the collapsing heating wave, the magnetic viscosity $\chi_m = c^2/4\pi\sigma \sim ZT^{-3/2}$ attains a value of about $\simeq 5 \times 10^4$ cm^2/s and the Reynolds magnetic number is $\mathrm{Rm} = va/\chi_m < c_s a/\chi_m \simeq 0.1$ (with $c_s = (ZT/m_i)^{1/2} \simeq 7 \times 10^5$ cm/s being the speed of sound). Under these conditions, it is diffusion that governs the penetration of the current and the magnetic field into the plasma. The time $\tau_m = a^2/2\pi\chi_m$ required for the penetration is shorter than 1 ns, and the released Joule heat power density at a current of $I \simeq 100$ kA attains a value of $j^2/\sigma = 2I^2/\pi^2c^2a^2\tau_m \simeq 10$ TW/cm^3. These are the conditions under which a rapid compression of the constriction begins.

Further, two necks appear in the constriction near its ends. The centers of the necks are located at distances of one-fourth of the constriction length from the ends. The temperature is maximum in the centers of the necks, whereas the density is maximum near the constriction ends. Near the points where the constriction cross section is minimum, the plasma moves at a velocity close to the speed of sound, whereas in the middle of the constriction, the plasma motion remains subsonic. As a result, during the following 2 ns, the plasma radius in the minimum cross sections reduces by several times to form two narrow necks with a maximum electron temperature of $T_e \simeq 80$ eV and density of $n_e \simeq 4.5 \times 10^{22}$ cm^{-3}. Further evolution is accompanied by an enhancement of the emission intensity and proceeds more rapidly. As soon as 400 ps later, the radius of the anode constriction decreases to 1 μm; 20 ps later, by the instant of maximum compression $t = 12.425$ ns (when the current is 145 kA), a small-sized region of strongly inhomogeneous plasma of radius $\simeq 0.1$ μm arises (the Rosseland mean free path of photons becomes nearly equal to this value). The abrupt decrease in the implosion velocity from higher than 5×10^6 cm/s to zero results in plasma heating, the electron temperature attains a value of $T_e = 0.9$–1 keV, and the ion temperature is $T_i = 1.1$–1.6 keV for $Z = 32$–35. The anomalous

conductivity is less than 1%, the electron density attains (2–3) × 10^{25} cm^{-3}, and the pressure is 30–50 Gbar. First, the ion temperature T_i reaches its maximum, then the average charge Z reaches its maximum, and finally T_e does. Only after this, the constriction radius becomes minimum. Sometimes, the constriction can undergo several rapid compressions with a period of 10–20 ns. The energy loss from this small-sized, but very hot and dense region is evidently insufficient for the constriction to evolve gradually, and the series of compressions is finished with a microexplosion followed by sharp expansion and the formation of shock waves. The shock fronts are clearly seen at t = 12.7 ns. Here, one can also see an anisotropy of the expansion and the formation of a break in the plasma near the anode. At first, this is merely a region of strongly lowered density; however, at $t > 12.7$ ns, the number of carriers in this region becomes insufficient to maintain the Ohmic current, and we have to stop the computation. Probably, this points to a tendency toward the generation of beams. Note that the velocity with which the plasma flows out from the constriction is always relatively low ($\simeq 10^5$ cm/s), so that intense axial plasma flows from the constriction can appear only when shock waves arrive at the ends. We should also emphasize that the dominant hot point appears spontaneously on either the anode or cathode side of the constriction at a distance of one-fourth of the constriction length from the ends (Fig. 3). Note that this is in spite of asymmetry that is introduced into the model by the influence of the current-generated magnetic field on the plasma kinetic coefficients.

We also note that the characteristic temporal and spatial scales of the solution, as well as the current at the instant of the burst, are in good agreement with the experiment. Even in the slow phase of compression, we observe an increasing deviation of the shape of the converging current-heating wave from cylindrical. The mechanism for this phenomenon is related, probably, to the onset of instability. The deformation of the free surface according to the symmetry of the problem leads to a situation when two toroidal vortices rotate in counter directions in each half of the constriction: at the ends and in the middle of the constriction, the plasma moves from the axis toward the surface, whereas between them, the plasma moves in the opposite direction. Further, when the velocity of this motion reaches and then exceeds the velocity of fast magnetic sound, this motion transforms into a cumulative heating of the material, which manifests itself as an anisotropic explosion. The formed shock waves mainly propagate toward the minidiode ends. The axial plasma flow arising behind the explosion fronts is accompanied by a decrease in the maximum density against the background of the increase in the density at the periphery. The plasma break is seen in the images corresponding to t = 12.7 ns in Fig. 2.

In essence, all of the above said is directly related to the effect observed in Figs. 1a and 1b. During the implosion, the characteristic time scale of compression decreases by four orders of magnitude, the constriction radius reduces by one thousand times, and the above-listed parameters of the material attain a fusion level. The limiting ion charge W corresponds to an ionization energy of ~2 keV, and the radiation is emitted as a high-intensity X-ray burst. Down to a radius of $\simeq 1$ μm, the implosion proceeds symmetrically in both minimum cross sections equally distant from the ends; however, further, a dominant hot point arises under the action of occasional factors. The Ohmic impedance of this point $R \simeq 1$ Ω falls just within the region of usual values of the loads matched to a moderate-power high-current generator. This allows us to estimate the maximum flux of radiation energy from the formed hot point under the simplest assumption that the radiative loss is equal to the released Joule heat. For the neck radius $a \simeq 0.1$ μm and current $I \simeq 150$ ka, the volume current density is equal to $\simeq 3RI^2/4\pi a^3$; consequently, the energy flux is $\simeq RI^2/4\pi a^2 \simeq 1.5 \times 10^{19}$ W/cm^2. The corresponding pressure of ≃5 Gbar is quite comparable with the pressure produced by the plasma particles and evidently plays an important role in the plasma compression. Apparently, these hot-point parameters are somewhat overestimated because, for instance, it is assumed that the total current flows through the small-sized constriction.

As a whole, the numerical solution describes fairly well the processes observed (in particular, the explosion of the hot point and the generation of shock waves) and is consistent with the time-integrated spectral measurements [3]. A detailed comparison of the plasma parameters in hot points requires X-ray spectral diagnostics with a high time resolution. As for the breaking of the construction, we note that, although this effect was observed in [3], an explanation of this phenomenon is still lacking. Note also that the insufficient time resolution of optical interferometry cannot assure a true result and only the data obtained in this study confirm the existence of the effect in question.

ACKNOWLEDGMENTS

We thank S.Yu. Gus'kov and Ya.S. Dimant for fruitful discussions and S.L. Nedoseev for valuable remarks. This work was supported in part by the Sandia National Laboratory (grant no. DE-FG02-98ER54496 and contract no. BD-9356).

REFERENCES

1. D. H. Kalantar and D. A. Hammer, Phys. Rev. Lett. **71**, 3806 (1993); T. A. Shelkovenko, S. A. Pikuz, A. R. Mingaleev, and D. A. Hammer, Bull. Am. Phys. Soc. **42**, 2051 (1997).
2. S. Yu. Gus'kov, G. V. Ivanenkov, A. R. Mingaleev, *et al.*, Pis'ma Zh. Éksp. Teor. Fiz. **67**, 531 (1998) [JETP Lett. **67**, 559 (1998)]; G. V. Ivanenkov, A. R. Mingaleev,

S. A. Pikuz, *et al.*, Zh. Éksp. Teor. Fiz. **114**, 1216 (1998) [JETP **87**, 663 (1998)]; Fiz. Plazmy **25**, 851 (1999) [Plasma Phys. Rep. **25**, 783 (1999)]; T. A. Shelkovenko, S. A. Pikuz, A. R. Mingaleev, and D. A. Hammer, Rev. Sci. Instrum. **70**, 667 (1999).

3. S. M. Zakharov, G. V. Ivanenkov, A. A. Kolomenskiĭ, *et al.*, Pis'ma Zh. Tekh. Fiz. **8**, 1060 (1982) [Sov. Tech. Phys. Lett. **8**, 456 (1982)]; Fiz. Plazmy **13**, 206 (1987) [Sov. J. Plasma Phys. **13**, 115 (1987)]; G. V. Ivanenkov, A. R. Mingaleev, S. A. Pikuz, *et al.*, Fiz. Plazmy **22**, 403 (1996) [Plasma Phys. Rep. *22*, 363 (1996)].
4. T. A. Shelkovenko, S. A. Pikuz, D. A. Hammer, *et al.*, Phys. Plasmas **6**, 2840 (1999).
5. E. L. Cochran and J. Davis, Phys. Fluids B **2**, 1238 (1990).
6. G. V. Ivanenkov and W. Stepniewski, Fiz. Plazmy **26**, 24 (2000) [Plasma Phys. Rep. **26**, 21 (2000)].
7. G. V. Ivanenkov and W. Stepniewski, Fiz. Plazmy **22**, 528 (1996) [Plasma Phys. Rep. **22**, 479 (1996)].
8. V. F. D'yachenko, Zh. Vychisl. Mat. Mat. Fiz. **5**, 680 (1965); K. Jach and E. Wlodarczyk, J. Tech. Phys. (Warsaw) **27**, 85 (1986).

Translated by N.F. Larionova

Plasma Physics Reports, Vol. 26, No. 10, 2000, pp. 875–880. Translated from Fizika Plazmy, Vol. 26, No. 10, 2000, pp. 934–939.

PLASMA DYNAMICS

One-Dimensional Hybrid Model of a Stationary Plasma Thruster

A. I. Morozov* and V. V. Savel'ev**

**Institute of Nuclear Fusion, Russian Research Centre Kurchatov Institute, pl. Kurchatova 1, Moscow, 123182 Russia*
***Keldysh Institute of Applied Mathematics, Russian Academy of Sciences, Miusskaya pl. 4, Moscow, 125047 Russia*

Received April 18, 2000

Abstract—A one-dimensional hybrid model of the dynamics of atoms, ions, and electrons in the channel of a stationary plasma thruster is developed. The relevant set of integrodifferential equations is studied numerically. The results obtained are compared with the results of previous calculations based on a hydrodynamic model. It is shown that, with the use of one fitting parameter (the channel resistance), the calculated integral characteristics agree well with the experimental ones. The current–voltage characteristic is obtained. The general features of low-frequency oscillations that have been revealed in numerical simulations using the model proposed are also in fairly good agreement with experimental results. The value of the electron thermal conductivity is estimated. © *2000 MAIK "Nauka/Interperiodica".*

1. INTRODUCTION

To our knowledge, a self-consistent one-dimensional model incorporating a set of time-dependent hydrodynamic equations describing the dynamics of atoms and ions in the channel of a stationary plasma thruster (SPT) and a supplementary integral equation for the discharge circuit was first formulated in [1] and investigated in detail in [2]. As follows from [2], even in this relatively simple model, the behavior of the system is nontrivial and very complicated. Clearly, a reasonable approach to developing the theory of the processes occurring in SPTs is to develop and study a series of increasingly complicated, but more adequate models.

In this paper, results are presented from a numerical study of a hybrid one-dimensional model of the processes occurring in SPTs. In this model, briefly outlined in [1], the ion dynamics is described by a kinetic equation, whereas the dynamics of atoms and electrons is described by hydrodynamic equations. The electron energy equation is also used, which makes it possible to understand the role of the electron heat conduction.

Here, our attention is primarily focused on three issues: (i) the correspondence between the local and integral characteristics of a plasma flow in the hydrodynamic and hybrid models, (ii) the character of the ion distribution function in different cross sections of the channel, and (iii) the influence of heat conduction on the discharge characteristics.

2. FORMULATION OF THE PROBLEM

The development of a theoretical model for the SPT processes occurring with characteristic times $\tau \geq \tau_d$, where τ_d is the drift time,[1] is facilitated by the absence of azimuthally asymmetric oscillations in an operating thruster [3]. Hence, as a first step, it is reasonable to restrict ourselves to a one-dimensional model of the dynamics of electrons, atoms, and ions. We assume that, throughout the channel, ions are singly ionized.

Let the x-axis be directed along the channel; V be the longitudinal ion velocity; and the points $x = 0$ and $x = L$ correspond to the anode and outlet from the channel (cathode), respectively.

The basic parameters of a hybrid model are the ion distribution function $f(x, V, t)$, the neutral density $n_a(x, t)$, the electron temperature $T(x, t)$, and the longitudinal electric current $J(t)$. The basic equations of the model are the kinetic equation for ions with a mass M

$$\frac{\partial f}{\partial t} + V\frac{\partial f}{\partial x} + \frac{e}{M}E\frac{\partial f}{\partial V} = \beta(T)nn_a\delta(V - V_a), \qquad n = \int f(V)dV, \tag{1}$$

the continuity equation for neutrals

$$\frac{\partial n_a}{\partial t} + V_a\frac{\partial n_a}{\partial x} = -\beta nn_a, \tag{2}$$

where $V_a = \text{const} > 0$ is the neutral velocity; the energy balance equation for electrons

$$\frac{3}{2}n\left(\frac{\partial T}{\partial t} + V_e\frac{\partial T}{\partial x}\right) + nT\frac{\partial V_e}{\partial x} = \frac{\partial}{\partial x}\left(\kappa_e\frac{\partial T}{\partial x}\right) + J_eE - \alpha\beta(T)nn_a, \tag{3}$$

where $V_e = -\dfrac{J_e}{en} = -\dfrac{J - J_i}{en}$ is the longitudinal (current) electron velocity; and, finally, the equation for the

[1] $\tau_d = 2\pi R/u_E$, where R is the average channel radius and u_E is the velocity of the azimuthal electric drift.

electric circuit

$$L_c\frac{\partial J}{\partial t} + RJ + \int_0^L E dx = U_0, \quad (4)$$

where U_0 is the e.m.f. of the power supply source and L_c and R are the inductance and resistance of the circuit.

Taking into account that the model is one-dimensional and the discharge current is independent of x, the longitudinal electric field is described by Ohm's law:[2]

$$E = \frac{J - enV}{\sigma(x)}. \quad (5)$$

The right-hand side of Eq. (1) describes the electron impact ionization, $\beta(T)$ being the ionization rate coefficient. On the right-hand side of Eq. (3), κ_e is the electron thermal conductivity across the magnetic field and α is the cost of ionization. In Eq. (5), $\sigma(x)$ is the plasma conductivity; in our case, it depends only on the transverse magnetic field, which is a parameter of the model:[3]

$$\sigma(x) = \sigma_0\left(\frac{H_0}{H(x)}\right)^2, \quad \sigma_0 = \text{const}, \quad H_0 = \text{const}, \quad (6)$$

where H_0 is the magnetic field at the outlet from the channel and $H(x)$ is the profile of the transverse magnetic field.

For the set of Eqs. (1)–(4), we impose quite arbitrary initial conditions and the following time-independent boundary conditions: at $x = 0$ (anode), we specify $n_a = n_{a0}$, $\partial T/\partial x = 0$, $f = f_0(V)$ for $V > 0$ and, at $x = L$ (the outlet from the channel), we set $T = T_0$. As $f_0(V)$, we used the function

$$f_0(V) = \frac{\pi}{2}\frac{n_0}{V_0^2}V\exp\left(-\frac{\pi}{4}\left(\frac{V}{V_0}\right)^2\right),$$

where n_0 and V_0 (the density and average velocity of ions at the anode) are the parameters.

The function $\sigma(x)$ in (6) depends on the profile of the transverse magnetic field. As in [2], this field is described by the expression

$$H(x) = H_0(h_0 + (1 - h_0)(x/L)^2), \quad h_0 = H(0)/H_0,$$

which is consistent with actual magnetic field profiles in SPTs.

[2] We neglect the longitudinal pressure gradient.

[3] Here, we take into account the fact that, under actual conditions, $\omega_e\tau_e \gg 1$.

It only remains to define the functions $\beta(T)$ and κ_e. They were taken in the following form:

$$\beta = \begin{cases} 0, & T < T^*, \\ \beta_0\left(\frac{T}{T^*} - 1\right), & T > T^*, \quad \beta_0 = \text{const}, \end{cases} \quad (7)$$

$$\kappa_e = \kappa_0\frac{T}{H}, \quad \kappa_0 = \text{const}. \quad (8)$$

Expression (7) for β was obtained by approximating the experimental and calculated data for Xe with $\beta_0 = 2.2 \times 10^{-8}$ cm^3/s and $T^* = 4$ eV. The choice of the thermal conductivity κ_e in the form (8) is quite arbitrary because theoretical or experimental data on its value for the SPT conditions are still unavailable.

For further analysis and numerical solution, it is convenient to go over to dimensionless units. Let L (the channel length) be the unit length; n_{a0} (the initial atom density) be the unit density; $E_0 = U_0/L$ be the unit electric field; V_0 (the initial mean ion velocity) be the unit velocity; $t_0 = L/V_0$ (the transit time) be the unit time; and $I_0 = U_0/R_{ch}$ be the unit electric current, where $R_{ch} = L/\sigma_0$ is the resistance of the channel with a cross section $S = 1$ cm^2. In these units, the problem is described by the following dimensionless parameters:

$$\mu = \frac{eU_0}{MV_0^2}, \quad \nu = \frac{\beta_0 n_{a0} L}{V_0}, \quad \chi = \frac{en_{a0}V_0R_{ch}}{U_0},$$

$$l = \frac{L_cV_0}{LR_{ch}}, \quad r = \frac{R}{R_{ch}}, \quad \bar{\alpha} = \frac{\alpha}{T_0}, \quad (9)$$

$$\bar{\kappa}_0 = \frac{\kappa_0}{LV_0n_{a0}}, \quad \varsigma = \frac{eU_0}{T_0}, \quad \bar{T}^* = \frac{T^*}{T_0}.$$

The problem formulated above was solved numerically by the difference method. When approximating the hydrodynamic part of the set of Eqs. (1)–(4), we used the FCT method [4]. When solving the kinetic equation, we used the positive second-order difference scheme [5]. A standard mesh used in our calculations was 100×150 steps in x and V, respectively.

3. RESULTS OF CALCULATIONS

3.1. Estimates of the Parameters

The one-dimensional hybrid model formulated above significantly simplifies the real process. Nevertheless, it turns out to be fairly complicated and multiparametric, which renders the general analysis of the set of equations quite laborious.

At the same time, the calculations using a hydrodynamic model [2] showed that the behavior of the system is rather nontrivial and depends strongly on the parameters of the model. For this reason, in this study, we restrict ourselves to the range of SPT parameters that is

of current interest: the mass flow rate is $\dot{m} = 2$–4 mg/s, the discharge voltage is $U_0 = 200$–400 V, and the working gas is Xe [6].

Let us estimate the basic dimensionless parameters (9). Let the mass flow rate be $\dot{m} = 3$ mg/s. If the channel cross-section area is equal to $\simeq 25$ cm^2, then, for the neutral density at the anode, we have $n_{a0} \simeq 10^{13}$ cm^{-3} and the neutral velocity near the anode is equal to $V_a \simeq 4 \times 10^4$ cm/s. The ion velocity near the anode is assumed to be $V_0 \simeq 2 \times 10^5$ cm/s (the ion energy is $\simeq 3$ eV). For a channel length of $L \simeq 3$ cm, we have $t_0 \simeq 15$ μs. From here, we obtain the following estimates:

$$\mu \approx \frac{1}{6}U_0(B), \quad \nu \approx 10, \quad V_a \approx 0.2.$$

Under typical experimental conditions, we have $T_0 \sim 20$ eV, $T^* = 4$ eV, $\alpha = 40$ eV, and $U_0 = 300$ V; therefore, we obtain

$$\mu = 50, \quad \bar{\alpha} \approx 2, \quad \varsigma \approx 15, \quad \bar{T}^* \approx 0.2.$$

Some difficulty is encountered in estimating the value of the channel resistance R_{ch} and, consequently, the parameter χ:

$$\chi \approx 0.9\frac{R_{ch}}{U_0}, \quad [R_{ch}] = \Omega\ \text{cm}^2.$$

In [2], we estimated R_{ch} from the requirement that, for $U_0 = 300$ V, the time-independent hydrodynamic model should give the proper discharge current $J \approx 3$ A. Calculations show that this requirement is satisfied with $R_{ch} \simeq 8 \times 10^4\ \Omega$ cm^2. Thus, we have

$$\chi \approx 7 \times 10^4/U_0.$$

For the parameters l, r, and h_0, we take the values corresponding to the experimental conditions:

$$l \approx 10^{-2}, \quad r \approx 10^{-3}, \quad h_0 \approx 0.1.$$

The choice of the thermal conductivity will be discussed below.

3.2. Comparison between the Hydrodynamic and Hybrid Models

Apparently, it is hard to expect that two different models might give close results (even if qualitatively) in all cases. However, it could be expected that at least the average values of various physical characteristics will be close. For this reason, we begin the presentation of the results obtained using the hybrid model from the case when both models have steady-state solutions. We assume now that $\beta(T) \equiv$ const so that the equation for T is not needed.

We assume that $\mu = 10$, $\nu = 7$, $\chi = 15$, $V_{a0} = 0.3$, and $n_0 = 0.02$. In this case, both models give (by the establishing method) a steady-state solution. The discharge currents in the hydrodynamic and hybrid models are equal to 8.72 and 8.76, respectively. The channel voltages are the same and are equal to $U = \int E\,dx = 0.95$. There is not only a qualitative, but also a quantitative agreement between the results, even in the spatial profiles of the main SPT parameters (Fig. 1).

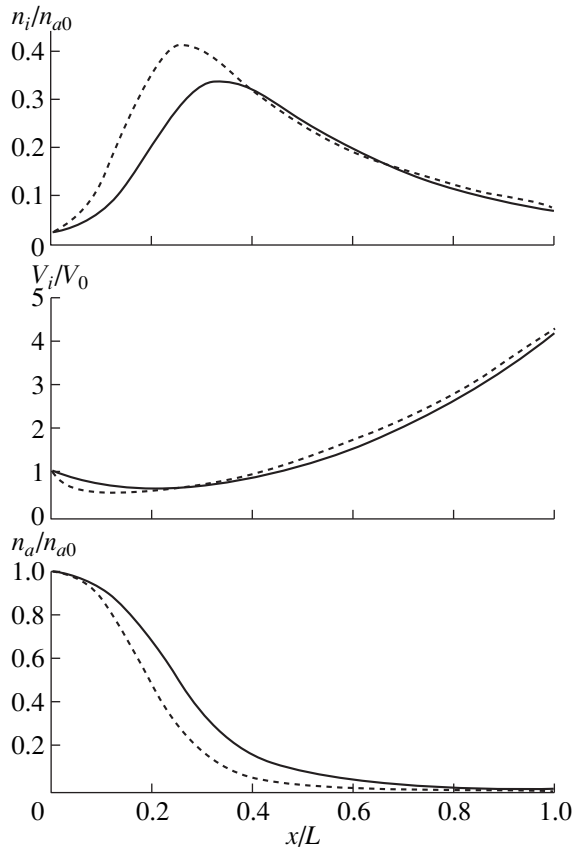

Fig. 1. Steady-state spatial profiles of the ion density, ion velocity, and neutral density calculated using the hydrodynamic (solid line) and hybrid (dashed line) models.

Now, let us compare the current–voltage (I–V) characteristics obtained using the two models. Calculations show that the I–V characteristics for both models almost coincide in the range 200–600 V. The closest coincidence was obtained for the channel voltages. As μ decreases (at $\mu\chi$ = const, i.e., when only the voltage is varied), the plasma flow becomes unstable and the solution becomes nearly periodic. In the hybrid model, this occurs at a lower value of μ than for the hydrodynamic model. As μ decreases further, the solution becomes nonperiodic; in this case, the transition again occurs earlier in the hydrodynamic model. Thus, the hybrid model turns out to be more stable.

A comparison of the time dependences of the main SPT parameters at $\beta(T) \equiv$ const shows that, although the time dependences obtained with the two models are different, there is good agreement for the fundamental

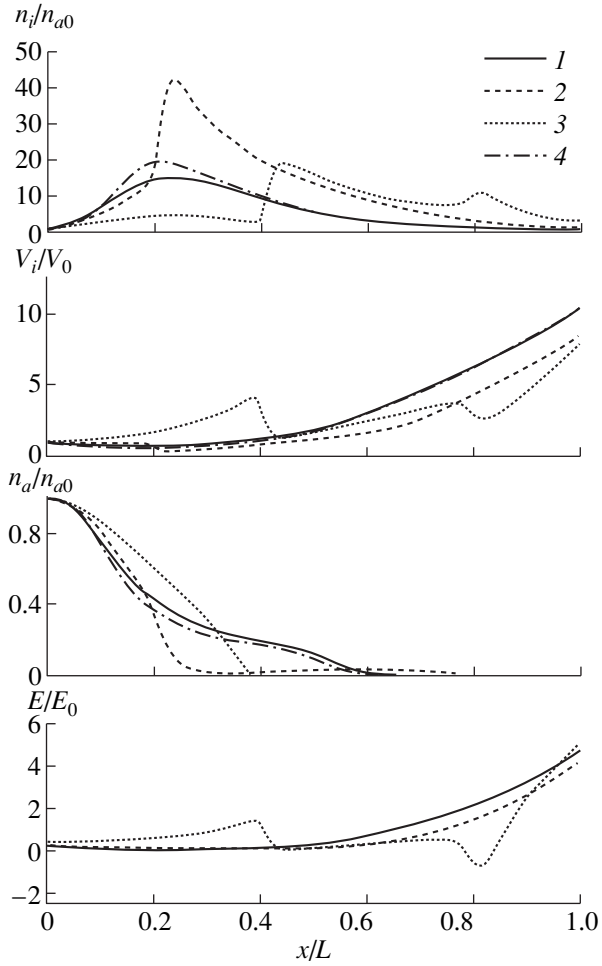

Fig. 2. Spatial profiles of the ion density, ion velocity, neutral density, and electric field calculated using the complete hybrid model at t/t_0 = (*1*) 3.9, (*2*) 4.4, (*3*) 5.2, and (*4*) 5.8.

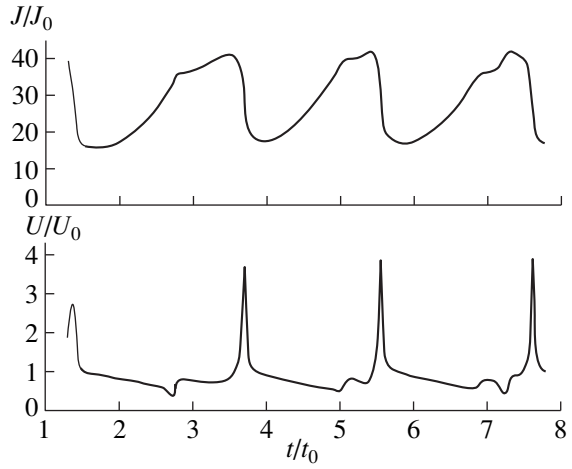

Fig. 3. Waveforms of the discharge current and channel voltage.

low-frequency (with a period of ~30 μs) component and the total oscillation amplitude.

The low-frequency oscillations observed in the hybrid model are associated with the ionization of the inflowing working gas and resemble the rarefaction-wave instability. Thus, it is not surprising that, when a fully ionized plasma is injected into the SPT channel, the solution always arrives at a steady-state regime. We note another characteristic feature of the one-dimensional model in the parameter range of interest, namely, the absence of high-frequency transit oscillations at a frequency of ~300 kHz that are usually observed in experiments. The reason for this is not yet understood.

3.3. Complete Model

Below, we will consider the complete set of Eqs. (1)–(5) of the hybrid model. We assume that U_0 = 300 V ($\mu = 50$, $\chi = 80$) and set $\nu = 10$ and $\kappa_0 = 1$. In this case, the flow does not arrive at a steady state. Figure 1 shows the *x*-profiles of the main SPT parameters at different instants. The presented spatial distributions of the density, ion velocity, and electric field are typical for all of the runs. By $x = 0.25$, the gas is almost fully ionized. Then, the flow accelerates to an average velocity of about $8V_0$ ($\approx 1.6 \times 10^6$ cm/s. The temperature T varies only slightly (due to high electron thermal conductivity in this case). The electron velocity increases rapidly near the anode and attains ≈ 10 $V_0 = 2 \times 10^6$ cm/s.

Figure 3 shows the waveforms of the current J and the channel voltage U. The flow oscillates almost periodically with a main period of ≈ 2 $t_0 = 30$ μs. The average current is nearly $24.2I_0$. The current and voltage oscillations are in antiphase. Figure 2 covers nearly one oscillation period.

An important feature observed in both the experiments and numerical simulations is that the neutral component is rather conservative. It is seen from Fig. 2 that, over a certain spatial interval near the entrance to the channel, the neutral density $n_a(x, t)$ remains nearly constant and the neutral density oscillations occur only at a sufficiently large distance from the entrance. After a breakdown occurs in the region where the neural density is relatively high, a plasma bunch is formed and then propagates as a single entity along the channel. As it approaches the outlet from the channel, the next breakdown occurs and so on. As the voltage varies in the range 150 V < U_0 < 600 V, the behavior of the system qualitatively remains the same. The only parameter that varies is the main oscillation period, which decreases as the voltage increases.

Figure 4 shows the *I–V* characteristic of the system (i.e., the dependence of the time-averaged current $\langle J \rangle$ on U_0) in the range of 150–600 V (in dimensional units). The *I–V* characteristic is nearly a straight line

and, as previously, depends only slightly on the model used.

3.4. Ion Distribution Function

Unlike the hydrodynamic model [2], the hybrid model allows us to determine the ion distribution function in different cross sections at different instants.

From Eq. (1) and the results of calculations, it follows that, if a fully ionized plasma is injected into the channel, then, in the steady state, the shape of the ion distribution function $f(\varepsilon)$ (where $\varepsilon = MV^2/2 + e\varphi$ and φ is the electric potential) does not change but only shifts along the energy axis. If a weakly ionized gas is injected into the channel, then, in the steady state, $f(\varepsilon)$ increases along the x-axis until the plasma flow reaches the boundary of the ionization region at a certain point x^*. Further, at $x > x^*$, the magnitude and the shape of the distribution function $f(\varepsilon)$ remain unchanged. The width of the distribution function over ε depends on the potential drop across the ionization region. As a function of velocity, the ion distribution function $f(V)$ decreases.

In the presence of oscillations, the behavior of the ion distribution function cannot be described in such a simple way. As an example, Fig. 5 shows the differential density of the ion flux $Vf(V)$ at $x = 0$, 0.5, and 1 at different instants for the same parameter values as in Figs. 2 and 3. The ion velocities at the outlet ($x = 1$) lie in the range 8×10^5–2.4×10^6 cm/s. For these parameter values, the transformation factor ζ defined as the ratio of the average energy of the ions leaving the channel to the average channel voltage is equal to

$$\zeta = \frac{\langle \varepsilon_i \rangle}{\langle eU \rangle} = 0.63,$$

which agrees well with the experimental data [3, 6].

3.5. Influence of Electron Heat Conduction

The processes occurring in the SPT channel should be substantially affected by electron heat conduction. Indeed, the electrons play a key role in the ionization of the injected gas. However, they can gain the required energy ε only if they cover a distance of $\delta \sim \varepsilon/E_i$ when moving toward the anode (here, E_i is the characteristic electric field strength in the ionization region). Therefore, if the electron thermal conductivity is set to zero, intense oscillations should arise in the channel, which should be accompanied by a shift of the ionization region toward the anode or even by quenching of the discharge. The above calculations were performed either with T = const or with a fairly high thermal conductivity. In both cases, strong oscillations of the temperature T are absent, whereas in the experiment, oscillations of T with an amplitude five to six times higher than the average level are sometimes observed. To estimate the actual value of the thermal conductivity in the SPT, we performed calculations at different values of the parameter κ_0. The calculations showed that, in our model, the ionization of the gas injected into the channel is negligibly small at $\kappa_0 \le 0.1$.

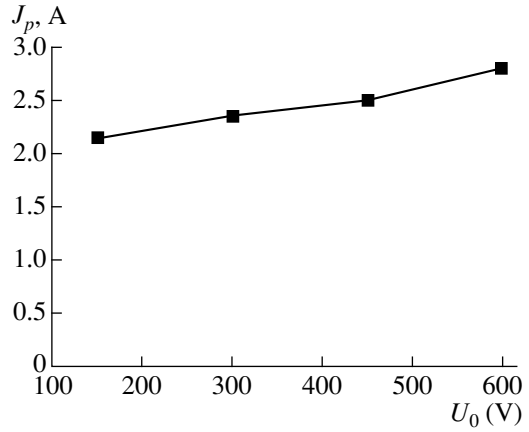

Fig. 4. Waveforms of the discharge current and channel voltage.

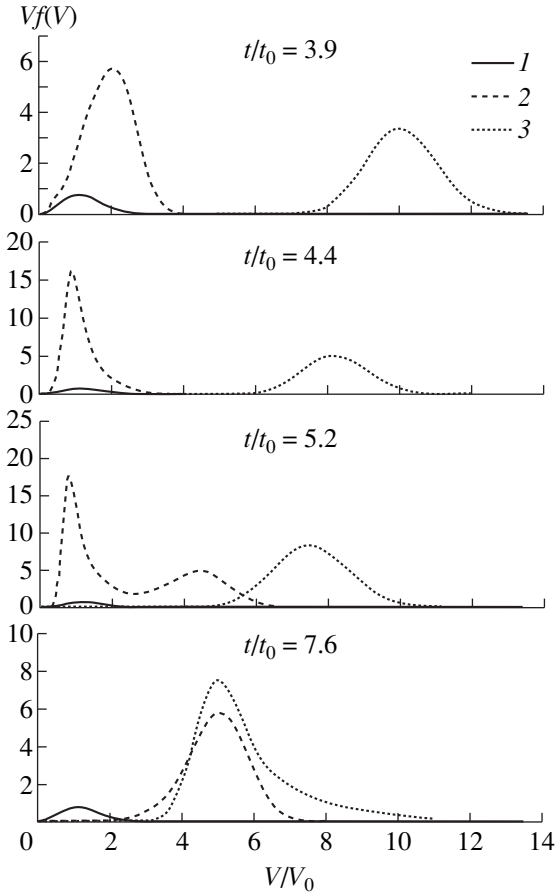

Fig. 5. Function $V(f(V)$ in different cross sections of the channel at x = (*1*) 0, (*2*) 0.5L, and (*3*) L at different instants.

4. CONCLUSION

The results of a numerical study of the hybrid model of an SPT allow us to draw the following conclusion. Although the one-dimensional hybrid model ignores many important details (in particular, the interaction of electrons with the channel wall, the non-Maxwellian electron distribution, and the two-dimensional character of the plasma flow), it provides, as a whole, a reasonable qualitative description of the processes occurring in actual SPTs. The model allows one to describe the ionization instability and the formation of the ion distribution function and to clarify the role of electron heat conduction. With one or two fitting parameters (for instance, the channel resistance), the model gives reasonable values for the integral characteristics of an SPT.

ACKNOWLEDGMENTS

We thank A.I. Bugrova and her collaborators from the Moscow Institute of Radio Electronics and Robotics for fruitful discussions. This work was supported in part by the SEP Company (France) and the Russian Foundation for Basic Research, project no. 00-01-00395.

REFERENCES

1. A. I. Morozov and V. V. Savel'ev, in *Proceedings of the 24th International Electric Propulsion Conference, Moscow, 1995*, Report IEPS 95-161.
2. A. I. Morozov and V. V. Savel'ev, Fiz. Plazmy **26**, 238 (2000) [Plasma Phys. Rep. **26**, 219 (2000)].
3. A. I. Morozov, in *Plasma Accelerators*, Ed. by L. A. Artsimovich (Mashinostroenie, Moscow, 1973), p. 85.
4. E. S. Oran and J. P. Boris, *Numerical Simulation of Reactive Flows* (Elsevier, New York, 1987; Mir, Moscow, 1990).
5. P. Smolarkiewicz, J. Comput. Phys. **54**, 325 (1984).
6. A. I. Morozov, A. I. Bugrova, A. V. Desyatskov, *et al.*, Fiz. Plazmy **23**, 587 (1997) [Plasma Phys. Rep. **23**, 587 (1997)].

Translated by N.F. Larionova

Plasma Physics Reports, Vol. 26, No. 10, 2000, pp. 881–888. Translated from Fizika Plazmy, Vol. 26, No. 10, 2000, pp. 940–947.

NONLINEAR PHENOMENA

Effect of Losses due to the Residual Electron Energy on the Temporal Profile of a Femtosecond Ionizing Laser Pulse

M. V. Chegotov

Institute for High Energy Densities, Associated Institute for High Temperatures, Russian Academy of Sciences, Izhorskaya ul. 13/19, Moscow, 127412 Russia

Received November 12, 1999; in final form, March 16, 2000

Abstract—A study is made of the combined action of the losses associated with overcoming the ionization potential barrier and those associated with the residual energy acquired by the electrons on a laser pulse propagating in a gas and ionizing it. It is shown that, depending on the laser and gas parameters, the losses due to overcoming the ionization potential barrier may be either larger or smaller than those associated with the residual electron energy. However, for pulses that penetrate sufficiently deeply into the gas, the residual energy–related losses are always larger than the ionization potential–related losses because of the steepening of the laser pulse profile during ionization. *© 2000 MAIK "Nauka/Interperiodica".*

1. INTRODUCTION

At present, the interaction of short intense laser pulses (with a duration of $\tau_{imp} < 100$ fs and a peak intensity of $I_{max} > 10^{16}$ W/cm^2) with matter is being actively studied both experimentally and theoretically (see, e.g., [1]). Success in experimental research in this field is mainly a consequence of the progress achieved in creating compact high-power devices capable of generating femtosecond laser pulses (so-called T^3 lasers). Experimental progress in turn stimulates theoretical investigations associated with possible applications of short intense laser pulses. A problem common to many practical applications is the change in the parameters of a laser pulse as it propagates in matter. In particular, both the frequency spectrum (see, e.g., [2]) and the temporal profile [3] of a pulse propagating in a gas and ionizing it change in time. The deformation of the laser pulse profile due to the loss of part of the pulse electromagnetic energy that is expended on ionizing gas atoms and exactly corresponds to overcoming the ionization potential barrier was studied in my earlier paper [3]. However, it should be noted that the nonadiabatic nature of gas ionization by the field of a short intense laser pulse gives rise to an additional energy loss: part of the electromagnetic energy is converted into so-called residual electron energy (REE) [4–6]. Gil'denburg *et al.* [6] asserted (without any justification) that the losses associated with the REE are larger than those due to overcoming the ionization potential barrier. For brevity, these loss channels will be referred to as residual energy–related losses (REL) and ionization potential–related losses (IPL). Andreev *et al.* [7] investigated the REE as a function of the laser and gas parameters and showed that, during ionization, the REE increases with the laser field intensity I as $I^{3/2}$. For this reason, it can be expected that the fraction of REL in the total energy loss will be large.

This paper is aimed at investigating how a laser pulse propagating in a gas and ionizing it is affected by both IPL and REL. We show that, depending on the relation between the IPL and REL, the substances under tunneling ionization conditions may be divided into two groups. If the electron shells of the gas atoms have comparatively low ionization energies (e.g., the electron shells of hydrogen atoms and the outer shells of the atoms of such gases as argon, krypton, and carbon), then, in the region where the laser pulse enters the gas, the IPL are larger than the REL. If the electron shells of the gas atoms have higher ionization energies (e.g., the electron shells of helium and neon atoms and the inner shells of heavy atoms), then, immediately at the entrance to the region occupied by the gas, the IPL are smaller than the REL. Note also that, even in the case of comparatively low ionization energies, the steeper the laser pulse profile, the larger the REL in comparison with the IPL. This indicates that the relation between REL and IPL changes as the pulse penetrates deeper into the plasma. In fact, a laser pulse propagating in a gas is eroded due to ionization [3]. The pulse profile becomes steeper, thereby raising the laser field intensity at which ionization occurs. As a result, as the laser pulse penetrates deep into the gas, the REL will inevitably start to dominate over the IPL, in which case the inverse effect of the ionization-related losses on the pulse profile will be substantially larger than that

1063-780X/00/2610-0881$20.00

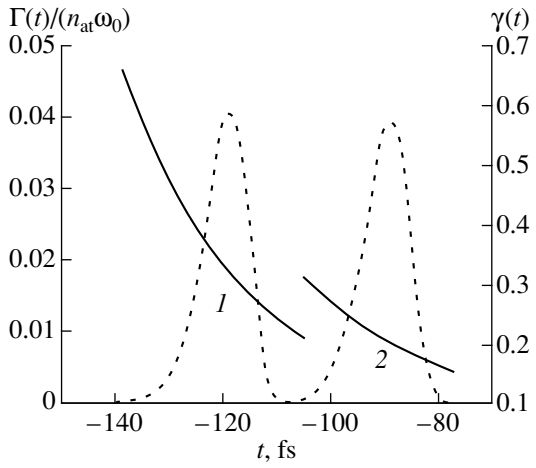

Fig. 1. The source term $\Gamma(t)$ (dotted curve) describing the production of free electrons during ionization of a helium gas by a Gaussian laser pulse with the duration τ_{imp} = 100 fs, peak intensity $I_{max} = 10^{17}$ W/cm^2, and wavelength $\lambda = 0.8$ μm (the scale on the left). The source term is normalized to the laser frequency ω_0 and the initial density n_{at} of neutral atoms. Curves *1* and *2* give the Keldysh parameter γ for ionization of neutral atoms and singly charged ions, respectively (the scale on the right). The zero time corresponds to the pulse center.

in the absence of REL and the erosion rate will increase.

We will study the role of IPL and REL in the ionization process using a one-dimensional model of laser pulse propagation. From an experimental standpoint, the one-dimensional model applies to laser pulses with sufficiently large transverse dimensions. In addition, we may hope (see, e.g., [3]) that the one-dimensional approximation will make it possible to determine the ionization-related losses for laser pulses guided with preformed plasma channels (e.g., in capillary discharges [8]), in which case the diffractive spreading is prevented by the focusing refraction effects if the profile of the refractive index across the channel is appropriately adjusted.

Of course, ionization is not the only possible mechanism for laser energy losses. However, an important feature of ionization-related losses is that the time required for ionization of an atom (or ion) is comparatively short and is independent of the particle density. For laser pulses with a sufficiently high intensity, the ionization time is approximately equal to several half-periods of the rapid oscillations of laser radiation (see [3, 7, 9], the discussion below, and Fig. 1). As a result, in the case of interaction between a short laser pulse with a sufficiently high intensity and a gas with a comparatively low density, the collision-induced losses of laser energy are insignificant in comparison with the ionization-related losses (see, e.g., [9]). In particular, the fraction of laser energy that is expended on exciting gas atoms and/or molecules is unimportant when the laser wavelength satisfies none of the resonance conditions [10]. In the case of interaction between a comparatively short laser pulse with a nonrelativistic maximum intensity ($I_{max} < 10^{18}$ (λ[μm])^2 W/cm^2) and a low-density gas (such that the density n_e of the ionization-produced free electrons is lower than the critical plasma density n_c for the given laser wavelength λ), we can neglect the losses resulting from stimulated Raman scattering (see, e.g., [11, 12]) and the associated excitation of plasma waves, which trap the electrons and accelerate them to high energies (see, e.g., [13]). Note that ionization processes can have a substantial impact on the propagation dynamics of relativistic laser pulses even in the case of light gases, which are characterized by low ionization energies. For example, the steepening of the laser pulse profile because of the pulse erosion during ionization significantly facilitates the onset of the self-modulational instability of the pulse, accompanied by the generation of an intense wake field [14].

2. BASIC EQUATIONS

Since, in the interaction between a short intense laser pulse and a comparatively low-density gas, ionizing inelastic collisions of free electrons with ions and neutral particles occur on time scales longer than the pulse duration [9], we neglect electron-impact ionization and consider only ionization by the laser field. According to the classical paper by Keldysh [15], in the interaction between the electromagnetic field and a gas, the plasma is produced via two different mechanisms—multiphoton ionization and tunneling ionization—depending on the value of the Keldysh parameter γ. Below, we will show that, for the short intense laser pulses under consideration, the γ values are such that the gas atoms and ions are ionized predominantly through the tunneling mechanism, in which case the initial velocity of free electrons is zero [16, 17]. However, since free electrons originate at different phases of the electric field of a laser pulse, part of the laser energy is converted into the REE [4, 5].

In order to describe the combined action of the IPL and REL, we turn to the approach developed in [3] and the results obtained in [7]. We consider a laser pulse with the electric field $\mathbf{E} = \mathbf{e}_z\mathscr{E}(x, t) = \mathbf{e}_z E(x, t)\cos(\omega_0 t - k_0 x)$; frequency ω_0; and amplitude $E(x, t)$, which varies slowly on the time scale $2\pi/\omega_0$. Let the pulse be linearly polarized along the z-axis and propagate along the x-axis. The REE, which is defined as the mean kinetic energy q acquired from the electromagnetic field by a free electron that originates in the vicinity of the point x during ionization, has the form (cf. [7])

$$q(x) = \frac{1}{n_e(\infty, x)} \times \int_{-\infty}^{\infty} \frac{\partial n_e(t, x)}{\partial t}\left(\sqrt{m^2c^4 + \mathbf{p}_\infty^2(t, x)c^2} - mc^2\right)dt,$$

where $n_e(t, x)$ is the electron density in the vicinity of the point x at the time t, $\mathbf{p}_\infty(t, x)$ is the momentum of an electron originating at the time t after the passage of the pulse, m is the mass of an electron, and c is the speed of light. The slowly varying amplitude $E(x, t)$ of a one-dimensional laser pulse satisfies the relationship [18]

$$\sqrt{m^2c^4 + \mathbf{p}_\infty^2(t, x)c^2} - mc^2 = \frac{e^2E^2(x, t)}{2m\omega_0^2}\sin^2(\omega_0 t - k_0 x),$$

where the electrons are assumed to originate at a zero initial velocity.

Since the rate $\partial n_e/\partial t$ at which the density of free electrons increases is governed by the ionization of both neutral atoms and ions (regardless of their ionization state), the time derivative $\partial n_e/\partial t$ can be written as

$$\frac{\partial n_e}{\partial t} = \sum_a \sum_{k=0}^{Z_a - 1} w_{a,k} n_{a,k},$$

where $n_{a,k}$ is the density of the ions stripped to the ionization state k ($k = 0$ corresponds to a neutral atom) in a gas of species a with the nuclear charge number Z_a. The probability $w_{a,k}$ for an ion in the related ionization state to be ionized per unit time is determined by the Ammosov–Delone–Kraĭnov formula [19, 20]

$$w_{a,k}(\mathscr{E}) = \omega_{\text{at}}\frac{e^1}{2\pi}\frac{(k+1)^2}{n_*^4}\left[4e^1\frac{(k+1)^3}{n_*^4}\frac{E_{\text{at}}}{|\mathscr{E}|}\right]^{2n_* - 1} \times \exp\left(-\frac{2}{3}\frac{(k+1)^3}{n_*^3}\frac{E_{\text{at}}}{|\mathscr{E}|}\right),$$

where $n_* = (k+1)\sqrt{U_H/U_{a,k}}$, U_H is the potential for ionization of a hydrogen atom from the ground state, $E_{\text{at}} \approx 5.1 \times 10^9$ V/cm is the electric field strength of an atom, $U_{a,k}$ is the potential for ionization of an ion in the kth ionization state in a gas of species a to an ion in the $[k+1]$th ionization state, $\omega_{\text{at}} \approx 4.1 \times 10^{16}$ s^{-1} is the atomic frequency, and $e^1 \approx 2.72$ is the base of natural logarithms.

To express the REE through the quantities that vary slowly on the time scale $2\pi/\omega_0$, we substitute the above relationships into the formula for q:

$$q(x) = \frac{e^2}{2n_e(\infty, x)m\omega_0^2} \times \sum_a \sum_{k=0}^{Z_a - 1} \int_{-\infty}^{\infty} n_{a,k} w_{a,k}(\mathscr{E}) E^2(x, t)\sin^2(\omega_0 t - k_0 x)\,dt.$$

Here, the integral can be represented as the sum of integrals over the time intervals $\pi/(2\omega_0)$. Evaluating each of the integrals asymptotically and carrying out the summation, we find

$$q(x) = \frac{1}{n_e(\infty, x)}\sum_a \sum_{k=0}^{Z_a - 1} \int_{-\infty}^{\infty} n_{a,k} W_{a,k}(E) R_{a,k}(x, t)\,dt.$$

Here,

$$R_{a,k}(x, t) = \frac{3\hbar\omega_0}{\sqrt{2}}\left(\frac{Q_p(x, t)}{U_{a,k}}\right)^{3/2} \times \left\{1 + \frac{9}{16}(8n_* - 15)\left(\frac{U_H}{U_{a,k}}\right)^{3/2}\frac{|E(x, t)|}{E_{\text{at}}} + \frac{135}{32}\left[(n_* - 2)(4n_* - 9) - \frac{1}{16}\right]\left(\frac{U_H}{U_{a,k}}\right)^3\frac{|E(x, t)|^2}{E_{\text{at}}^2}\right\}, \quad (1)$$

$$W_{a,k}(E) = \omega_{\text{at}}\sqrt{3}\left(\frac{e^1}{\pi}\right)^{3/2}\frac{(k+1)^2}{n_*^{4.5}} \times \left[4e^1\frac{(k+1)^3}{n_*^4}\frac{E_{\text{at}}}{|E|}\right]^{2n_* - 1.5}\exp\left(-\frac{2}{3}\frac{(k+1)^3}{n_*^3}\frac{E_{\text{at}}}{|E|}\right), \quad (2)$$

where $Q_p(x, t) = e^2|E(x, t)|^2/(4m\omega_0^2)$ is the ponderomotive potential of an electron. The expression in braces in (1) contains the first three terms of the asymptotic series with the expansion parameter $\alpha_k \equiv (U_H/U_{a,k})^{3/2}|E(x, t)|/E_{\text{at}}$ [7]. According to [7], in the region of intense ionization of the ions in the kth ionization state in gases with comparatively light atoms (with the nuclear charge number $Z < 10$), we have $\alpha_k \ll 1$. Expression (1) is just the mean fraction of laser energy that is converted into the REE in the tunneling ionization event. The quantity $W_{a,k}$ in (2) is the probability $w_{a,k}$ averaged over $2\pi/\omega_0$ [19, 20].

The total ionization-related energy loss $\tilde{U}_{a,k}$ is the sum of the REL and IPL:

$$\tilde{U}_{a,k} = U_{a,k} + R_{a,k}. \quad (3)$$

Consequently, in one-dimensional geometry, the laser pulse intensity $I(x, t) = (c/8\pi)|E(x, t)|^2$ evolves according to the equation (cf. [3])

$$\left(\frac{\partial}{\partial x} + \frac{1}{c}\frac{\partial}{\partial t}\right)I = -\sum_a \sum_k W_{a,k} n_{a,k} \tilde{U}_{a,k}, \quad (4)$$

and the time evolution of the density $n_{a,k}$ of the ions in the kth ionization state in a gas of species a is described

by the set of equations

$$\frac{\partial n_{a,0}}{\partial t} = -W_{a,0}n_{a,0},$$
$$\frac{\partial n_{a,k}}{\partial t} = -W_{a,k}n_{a,k} + W_{a,k-1}n_{a,k-1}, \quad (5)$$
$$\frac{\partial n_{a,Z_a}}{\partial t} = W_{a,Z_a-1}n_{a,Z_a-1}, \quad k = 1, \ldots, Z_a - 1,$$

where $W_{a,k}$ is the probability of ionization of an ion in the kth ionization state (or, at $k = 0$, of an atom) in a gas of species a per unit time. In Eq. (4), we neglect time dispersion and assume the electron density to be low ($n_e \ll n_c$, where $n_c = m\omega_0^2/4\pi e^2$ is the critical electron density). Equation (4) correctly describes the evolution only of the laser intensity I that varies sufficiently gradually (such that $\partial \ln I/\partial x < \omega_0/c$ and $\partial \ln I/\partial t < \omega_0$), and it yields merely rough estimates when $\partial \ln I/\partial x \sim \omega_0/c$ and $\partial \ln I/\partial t \sim \omega_0$.

Equations (5) describe how the ion densities evolve under the conditions of both multiphoton ionization and tunneling ionization. It is precisely the ionization mechanism that governs the dependence of $W_{a,k}$ on the laser and gas parameters. If, at the time t at which ionization occurs, the Keldysh parameter $\gamma = \omega_0\sqrt{2mU_{a,k}}/|e||E(x, t)|$ (where e and m are the charge and mass of an electron) is larger than unity, then the gas particles are ionized through the multiphoton mechanism, whereas, for $\gamma < 1$, ionization occurs via the tunneling mechanism [15, 21]. Under the conditions of tunneling ionization, the probability $W_{a,k}$ of ionization by linearly polarized laser radiation is described by formula (2). Substituting the specified dependence $E(x, t)$ into (2) and (4), we determine the point on the laser pulse profile and, accordingly, the γ value that correspond to ionization of an ion in the kth ionization state. Figure 1 illustrates the results of the related calculations carried out for a Gaussian laser pulse with the duration $\tau_{imp} = 100$ fs, peak intensity $I_{max} = 10^{17}$ W/cm^2, and wavelength $\lambda = 0.8$ μm in helium. We can see that, in the regions of the most intense ionization (which correspond to the peaks in the time evolution of $\Gamma \equiv \sum_a \sum_k W_{a,k} n_{a,k}$) in a laser field, the Keldysh parameter is equal to $\gamma \approx 0.3 < 1$ in the case of ionization of neutral atoms and $\gamma \approx 0.2 < 1$ when helium nuclei are produced by ionization of singly charged ions. For the same laser pulse propagating in hydrogen, we have $\gamma \approx 0.7 < 1$ near the maxima of Γ. As $U_{a,k}$ and I_{max} increase or τ_{imp} decreases, the γ values at the peaks in Γ fall off. This indicates, in particular, that the role of the tunneling ionization mechanism increases as the laser pulse erodes when penetrating deeper into the gas. In fact, as the pulse erodes, its profile becomes steeper, thereby raising the intensity at which ionization occurs. Hence, we are justified in assuming that ionization occurs via the tunneling mechanism.

Note that the time evolution $\Gamma(t)$ superimposed on the evolving laser pulse profile is seen as a sequence of narrow peaks: the number of peaks is equal to the maximum possible degree of ionization for the given type of gas and the adopted parameters of the laser pulse, and the width of each peak is approximately equal to several half-periods of the laser radiation (Fig. 1). Such a high localization within the pulse temporal profile indicates that ionization by the laser field is threshold in nature. The threshold intensity $I_{a,k}^{th}$ for ionization of an ion in the kth ionization state in a gas of species a can be estimated using the model in which ionization is assumed to occur due to the reduction in the potential barrier [22, 23]. In this model, an electron is assumed to be in the potential field $U(z) = -(k+1)e^2/|z| - e\mathscr{E}_z z$, which is a superposition of the Coulomb field of an ion with the charge $(k+1)|e|$ and the electric field $\mathbf{E}$ of the laser pulse. Under the condition $\hbar\omega_0 \ll U_{a,k}$, the laser field is quasistatic. According to the model of [22, 23], ionization occurs at the field strength $|\mathscr{E}_z| = E = E_{a,k}^{th}$ at which $U_{max}(z) = -U_{a,k}$. The threshold intensity $I_{a,k}^{th} = c|E_{a,k}^{th}|^2/8\pi$ of laser radiation can be estimated from the threshold electric-field strength:

$$I_{a,k}^{th} = \frac{c}{128\pi}\frac{U_{a,k}^4}{e^6(k+1)^2}. \quad (6)$$

Formula (6) was obtained without consideration of the dynamic nature of ionization. The threshold intensity depends, in particular, on the shape, duration, and maximum intensity of the laser pulse. For example, for singly and doubly charged helium ions, the threshold intensity is lower than that corresponding to the peaks in $\Gamma(t)$ by approximately 25%, and, in the case of hydrogen, it is lower by a factor of two. We substitute estimate (6) into (1) and divide the resulting expression by $U_{a,k}$ in order to better understand the relative fractions of REL and IPL in the total ionization-related losses. In particular, for a laser pulse with the above parameters, we have

$$R_{H,0}(I_{H,0}^{th})/U_{H,0} \approx 0.094$$

for nitrogen and

$$R_{He,0}(I_{He,0}^{th})/U_{He,0} \approx 0.71,$$
$$R_{He,1}(I_{He,1}^{th})/U_{He,1} \approx 1.51$$

for helium.

Determining $R_{a,k}/U_{a,k}$ from the laser pulse amplitude $|E(x, t)|$ at which $\Gamma(t)$ reaches its maximum yields

$$R_{\mathrm{H},0}/U_{\mathrm{H},0} \approx 0.235, \quad R_{\mathrm{He},0}/U_{\mathrm{He},0} \approx 1.1,$$
$$R_{\mathrm{He},1}/U_{\mathrm{He},1} \approx 2.0.$$

These values are larger than the $R_{a,k}/U_{a,k}$ values found from the threshold intensity (6) by approximately a factor of 1.5–2. However, even in this case, we can see that $R_{\mathrm{H},0}/U_{\mathrm{H},0} \ll 1$ and that $R_{\mathrm{He},k}/U_{\mathrm{He},k}$ is larger than or about unity. The fact that, depending on the laser and gas parameters, the ratio $R_{a,k}/U_{a,k}$ can be either larger or smaller than unity follows from expression (1). We actually have

$$\frac{R_{a,k}}{U_{a,k}} \approx \frac{3}{\sqrt{2}}\frac{\hbar\omega_0}{U_{a,k}}\left(\frac{Q_p}{U_{a,k}}\right)^{3/2},$$

so that, in the theory of tunneling ionization, the ratio $R_{a,k}/U_{a,k}$ is a product of the small and large parameters: $\hbar\omega_0/U_{a,k} \ll 1$ and $(Q_p/U_{a,k})^{3/2} \gg 1$ [15, 17].

As the pulse penetrates deeper into the gas and its profile becomes steeper, the relative fractions of REL and IPL can be estimated as follows. For the cases with and without REL, we integrate Eq. (4) over t from $-\infty$ to $+\infty$ to obtain

$$\frac{\partial}{\partial x}\int_{-\infty}^{+\infty} I(x, t)dt = -\sum_a\sum_k \int_{-\infty}^{+\infty} W_{a,k}n_{a,k}\tilde{U}_{a,k}dt,$$

$$\frac{\partial}{\partial x}\int_{-\infty}^{+\infty} I(x, t, R = 0)dt = -\sum_a\sum_k U_{a,k}\int_{-\infty}^{+\infty} W_{a,k}n_{a,k}dt.$$

The right-hand sides of these relationships are proportional to the laser energy losses per unit length. Consequently, as a function of the penetration depth of the pulse into the gas, the level of REL relative to the level of IPL, $k(x)$, can be estimated as

$$k(x) = \left[\frac{\partial}{\partial x}\int_{-\infty}^{+\infty} I(x, t)dt - \frac{\partial}{\partial x}\int_{-\infty}^{+\infty} I(x, t, R = 0)dt\right]\Big/\frac{\partial}{\partial x} \times \int_{-\infty}^{+\infty} I(x, t, R = 0)dt \quad (7)$$
$$= \sum_a\sum_k \int_{-\infty}^{+\infty} R_{a,k}W_{a,k}n_{a,k}dt\Big/\sum_a\sum_k U_{a,k}\int_{-\infty}^{+\infty} W_{a,k}n_{a,k}dt.$$

Since, in the case of ionization of electron-rich atoms, the electrons are ejected out of many different atomic shells, formula (7) describes the shell-averaged REL and IPL.

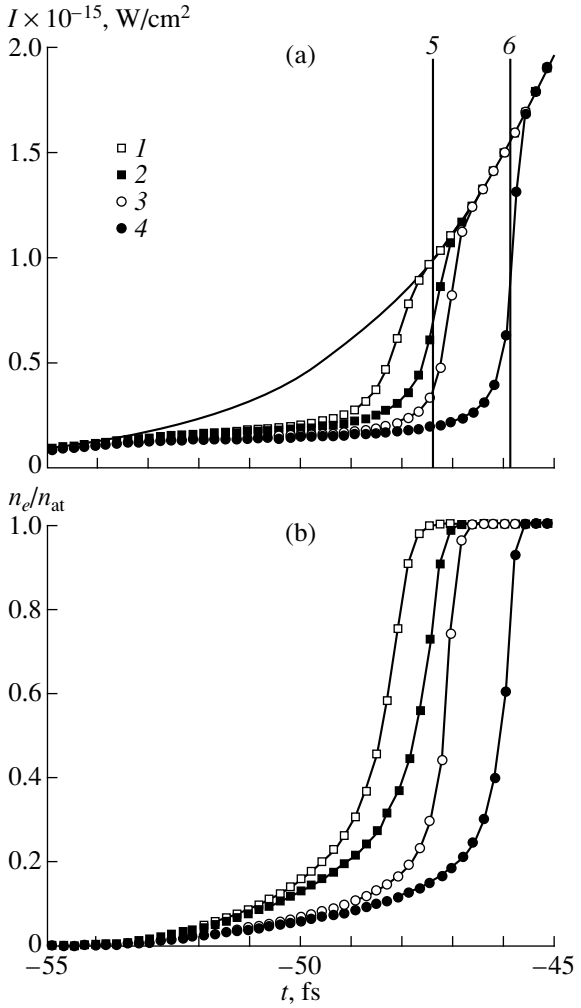

Fig. 2. Time evolutions of (a) the intensity of a Gaussian laser pulse (with the parameters $I_{\max} = 10^{18}$ W/cm^2, $\tau_{\mathrm{imp}} = 30$ fs, and $\lambda = 0.8$ μm) propagating in a hydrogen gas with the initial atom density $n_{\mathrm{at}} = 5 \times 10^{18}$ cm^{-3} and (b) the density n_e of the ionization-produced free electrons in units of n_{at} in the accompanying frame. The zero time corresponds to the pulse center. Curves *1* and *2* are for the penetration depth $x \approx 1$ mm obtained with and without consideration of the REL, respectively; curves *3* and *4* are for the penetration depth $x \approx 2$ mm obtained with and without consideration of the REL, respectively. The solid curve shows the initial laser pulse profile. The vertical lines illustrate the positions $f_{\mathrm{H},0}$ of the ionization front that were obtained from Eq. (8) for the penetration depths (*1*) $x \approx 1$ mm and (*2*) $x \approx 2$ mm, with the REL taken into account.

3. RESULTS OF A NUMERICAL SOLUTION

Equations (1)–(5) were solved numerically for different gases and laser pulses with different parameters. Figure 2a illustrates the evolution of a laser pulse with a Gaussian profile $I_0(t) = I_{\max}\exp(-4\ln 2t^2/\tau_{\mathrm{imp}}^2)$ (where $I_{\max} = 10^{18}$ W/cm^2, $\tau_{\mathrm{imp}} = 30$ fs, and $\lambda = 0.8$ μm) at the

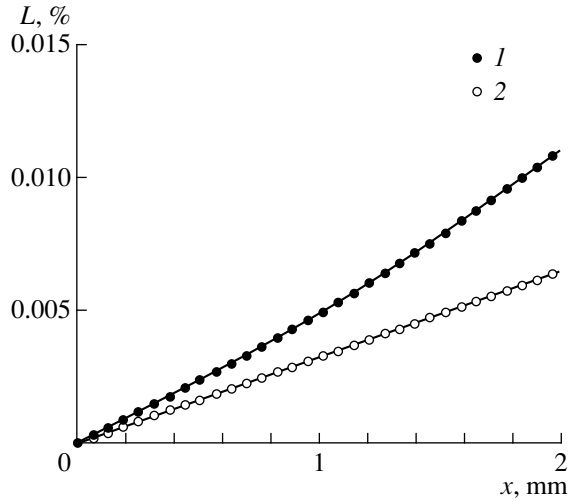

Fig. 3. Energy loss level $L(x)$ (%) vs. the penetration depth of the pulse into the gas (*1*) with and (*2*) without consideration of the REL. The parameters are the same as in Fig. 2.

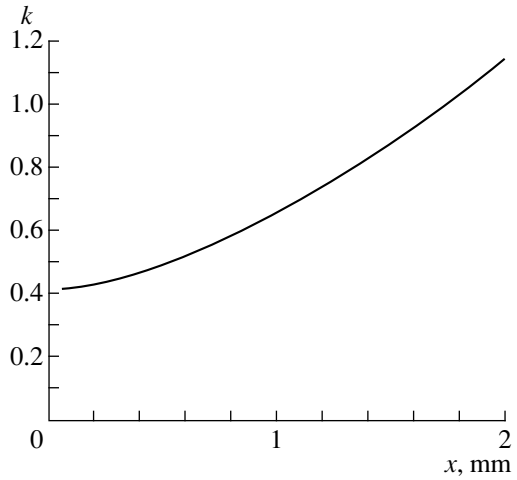

Fig. 4. The level of REL relative to the level of IPL, $k(x)$, determined from Eq. (8) vs. the penetration depth x of the pulse into the gas, for the same parameters as in Fig. 2.

entrance $x = 0$ to the region occupied by a hydrogen gas with the initial atom density $n_{at} = 5 \times 10^{18}$ cm^{-3}, which corresponds to a pressure of 0.186 atm. The results were obtained with and without consideration of REL ($I(x, t)$ and $I(x, t, R = 0)$, respectively). In both cases, the pulse erodes only in the region where the pulse intensity I changes abruptly. It is this region in which the electron density increases sharply (Fig. 2b); generally, this region corresponds to the ionization front where the ions in the kth ionization state in a gas of species a are ionized to ions in the $[k + 1]$th state. As the coordinate $f_{a,k}$ of this ionization front on the laser pulse profile in the accompanying frame of reference $f = t - x/c$, we can adopt the point at which the pulse intensity I changes most abruptly due to the ionization of an ion in the kth ionization state in a gas of species a. In the region where the pulse enters the gas, the ionization fronts on the pulse profiles $I(x, t)$ and $I(x, t, R = 0)$ are close to one another. However, as the pulse propagates in a gas, the distance between the coordinates $f_{H,0}$ and $f_{H,0}(R = 0)$ of the ionization fronts increases: the rate of pulse erosion due to REL is significantly higher than that due to IPL. As a result, as the pulse penetrates deeper into the gas, the rate of ionization-related energy losses with allowance for both REL and IPL becomes higher than that in the case in which only IPL are taken into account. Figure 3 displays the energy losses

$$L(x) = \int_{-\infty}^{+\infty} I(x, t)dt \left[\int_{-\infty}^{+\infty} I_0(t)dt\right]^{-1} - 1$$

as a function of the penetration depth of the pulse into the gas with and without consideration of REL for the same parameters as in Fig. 2. In the latter case, the dependence $L(x)$ is seen to be linear, in agreement with the theoretical predictions made in [3].

Since the ionization front on the laser pulse profile is narrow, we can analyze Eqs. (4) and (5) in a way similar to what we did in [3]. As a result, we arrive at an equation that is analogous to Eq. (15) in [3] and determines the coordinate $f_{a,k}$ of the ionization front on the

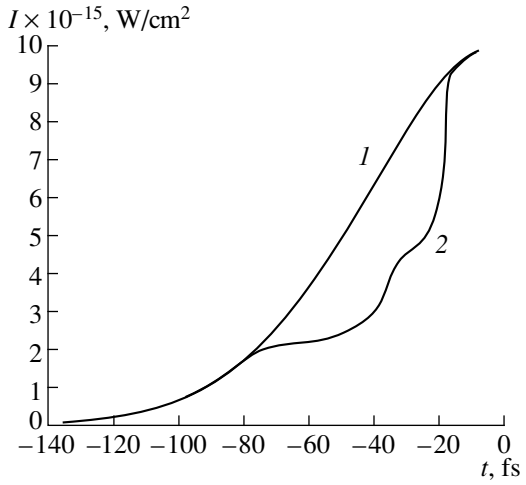

Fig. 5. Time evolutions of the intensity of a Gaussian laser pulse (with the parameters $I_{max} = 10^{16}$ W/cm^2, $\tau_{imp} = 100$ fs, and $\lambda = 0.8$ μm) in the accompanying frame at (*1*) the entrance to and (*2*) at the exit from the region occupied by the gas of doubly charged carbon ions with the initial atom density $n_{C,2} = 5 \times 10^{18}$ cm^{-3}. The zero time corresponds to the pulse center.

pulse profile as a function of the penetration depth of the pulse into the gas:

$$\int_{-\infty}^{f_{a,k}} \left(\int_{I_{a,k}^{th}}^{I_0(t)} \frac{dI}{1 + R_{a,k}(I)/U_{a,k}} \right) \theta(I_0(t) - I_{a,k}^{th}) dt = n_{\text{at},a} U_{a,k} x, \quad (8)$$

where $R_{a,k}(I)$ is the REE (3) as a function of the laser pulse intensity I and $\theta(p)$ is the Heaviside step function, which is defined as $\theta(p) = 0$ for $p < 0$ and $\theta(p) = 1$ for $p \geq 0$. At $R_{a,k} = 0$, Eq. (8) passes over to Eq. (15) from [3], which implies that L is a linear function of x. In Fig. 2, the vertical lines correspond to the positions $f_{\text{H},0}$ of the ionization front that were obtained from Eq. (8) for the indicated depths of penetration of the pulse into a hydrogen gas with the REL taken into account.

The ionization-induced erosion of the propagating laser pulse causes the ionization front to become steeper and to displace toward higher intensities on the pulse profile. As a result, the level of REL relative to the level of IPL increases with x. Figure 4, which shows the function $k(x)$ calculated from (7), demonstrates the validity of this conclusion.

4. CONCLUSIONS

The features of the propagation of a laser pulse in hydrogen that are illustrated in Figs. 2–4 also apply to laser pulse propagation in other gases. In particular, it is of interest to compare the total laser energy losses measured by Ehrlich *et al.* [8] in experiments on the propagation of a laser pulse with the parameters $I_{\max} = 10^{16}$ W/cm^2, $\tau_{\text{imp}} = 100$ fs, and $\lambda = 0.8$ μm through a capillary discharge initiated in polypropylene with the total ionization-related energy losses, including the REL. Under the experimental conditions of [8], an incompletely ionized substance is carbon contained in polypropylene. Since the ionization energy of doubly charged carbon ions is comparatively high (higher than the ionization energies of hydrogen and carbon atoms by a factor of approximately four), we can assume that, in the channel of a capillary discharge, the carbon ions are doubly charged and their density is equal to $n_{\text{C},2} = 5 \times 10^{18}$ cm^{-3}. Solving Eqs. (4) and (5) under these conditions and assuming that at the entrance to the capillary discharge the laser pulse is Gaussian in shape, we obtain the pulse profile at the exit from a capillary channel of length $x \approx 1$ cm (see Fig. 5). With the REL taken into account, the ionization-related losses are approximately equal to 13% of the total energy losses, whereas, without allowance for the REL, they are equal to 8%. Note that, under the optimum channeling conditions in the experiments of [8], the total energy losses were approximately equal to 16% of the input laser energy. Hence, the main fraction (80%) of the net energy loss of the laser pulse during its propagation through a capillary discharge in the experiments of [8] may be attributed precisely to the ionization-related losses, including the REL, which in turn may be as large as 40% of the total ionization-related energy losses.

The erosion of the propagating laser pulse accompanied by the steepening of its profile raises the REE. The REE may be comparable to the temperature of the ionization-created free electrons, because they obey an anisotropic Maxwellian velocity distribution function [17, 20]. Three-dimensional particle-in-cell simulations of the interaction between a linearly polarized ionizing laser pulse and a gas [24] confirm that, after the passage of the pulse, free electrons obey an anisotropic Maxwellian distribution with the peak temperature $T_{e,z}$ along the polarization direction (the z-axis) and that the REE q is related to the peak temperature by $T_{e,z} = 2q$. As a result, the electron temperature in the laser-produced plasma varies along the path of the pulse. This circumstance may be particularly important for creating active media by short intense laser pulses in X-ray lasers.

ACKNOWLEDGMENTS

This work was supported in part by the Russian Foundation for Basic Research (project no. 98-02-16263) and INTAS (grant no. 97-10236).

REFERENCES

1. *Proceedings of ICONO'98. Ultrafast Phenomena and Interaction of Superstrong Laser Fields with Matter: Nonlinear Optics and High-Field Physics, Moscow, 1998* [Proc. SPIE **3735** (1999)].
2. W. M. Wood, C. W. Siders, and M. C. Downer, Phys. Rev. Lett. **67**, 3523 (1991).
3. M. V. Chegotov, Izv. Akad. Nauk, Ser. Fiz. **63**, 1088 (1999).
4. N. H. Burnett and P. B. Corkum, J. Opt. Soc. Am. B **6**, 1195 (1989).
5. B. M. Penetrante and J. N. Bardsley, Phys. Rev. A **43**, 3100 (1991).
6. V. B. Gil'denburg, V. I. Pozdnyakova, and I. A. Shereshevskii, Phys. Lett. A **203**, 214 (1995).
7. N. E. Andreev, M. V. Chegotov, M. E. Veisman, *et al.*, Proc. SPIE **3735**, 242 (1999).
8. Y. Ehrlich, C. Cohen, A. Zigler, *et al.*, Phys. Rev. Lett. **77**, 4186 (1996).
9. N. E. Andreev, M. V. Chegotov, M. E. Veĭsman, *et al.*, Pis'ma Zh. Éksp. Teor. Fiz. **68**, 566 (1998) [JETP Lett. **68**, 592 (1998)].
10. N. B. Delone and V. P. Kraĭnov, *Atom in a Strong Light Field* (Atomizdat, Moscow, 1978), p. 205.
11. P. Mounaix, D. Pesme, W. Rozmus, and M. Casanova, Phys. Fluids B **5**, 3304 (1993).
12. P. Mounaix and D. Pesme, Phys. Plasmas **1**, 2579 (1994).

13. D. W. Forslund, J. M. Kindel, W. B. Mori, *et al.*, Phys. Rev. Lett. **54**, 558 (1985).
14. V. V. Goloviznin, P. W. van Amersfoort, N. E. Andreev, and V. I. Kirsanov, Phys. Rev. E **52**, 5327 (1995).
15. L. V. Keldysh, Zh. Éksp. Teor. Fiz. **47**, 1945 (1964) [Sov. Phys. JETP **20**, 1307 (1964)].
16. P. B. Corcum, N. H. Burnett, and F. Brunel, Phys. Rev. Lett. **62**, 1259 (1989).
17. N. B. Delone and V. P. Krainov, J. Opt. Soc. Am. B **8**, 1207 (1991).
18. P. C. Clemmow and J. P. Dougherty, *Electrodynamics of Particles and Plasmas* (Addison-Wesley, New York, 1990; Mir, Moscow, 1996).
19. M. V. Ammosov, N. B. Delone, and V. P. Kraĭnov, Zh. Éksp. Teor. Fiz. **91**, 2008 (1986) [Sov. Phys. JETP **64**, 1191 (1986)].
20. N. B. Delone and V. P. Kraĭnov, Usp. Fiz. Nauk **168**, 531 (1998) [Phys. Usp. **41**, 469 (1998)].
21. F. Ilkov, J. E. Decker, and S. L. Chin, J. Phys. B **25**, 4005 (1992).
22. R. R. Freeman and P. H. Bucksbaum, J. Phys. B **24**, 325 (1991).
23. J. H. Eberly, J. Javanainen, and K. Rzazewski, Phys. Rep. **204**, 331 (1991).
24. N. E. Andreev, M. E. Veĭsman, M. G. Cadjan, and M. V. Chegotov, Fiz. Plazmy **26** (10) (2000) [Plasma Phys. Rep. **26** (10) (2000)].

Translated by O.E. Khadin

Plasma Physics Reports, Vol. 26, No. 10, 2000, pp. 889–892. Translated from Fizika Plazmy, Vol. 26, No. 10, 2000, pp. 948–951.

BEAMS IN PLASMA

Wakefield Excitation by a Relativistic Electron Bunch in a Magnetized Plasma

V. A. Balakirev, I. V. Karas', and G. V. Sotnikov

National Science Center Kharkov Institute of Physics and Technology, ul. Akademicheskaya 1, Kharkov, 310108 Ukraine

Received March 7, 2000

Abstract—The excitation of a wake wave by a relativistic electron beam in an unbounded magnetized plasma and a plasma waveguide is studied theoretically. It is shown that, in a waveguide partially filled with a plasma, the energy that the electrons of the accelerated beam can gain is 37 times higher than the energy of the electrons of the beam generating wakefield. © *2000 MAIK "Nauka/Interperiodica".*

The idea of accelerating particles by means of collective fields in plasmas and unneutralized charge particle beams was originated as far back as 1956 by V.I. Veksler, G.I. Budker, and Ya.B. Fainberg [1–3]. Interest in the methods for collective acceleration of charged particles increased considerably after the development and fabrication of new high-power energy sources such as lasers, high-current relativistic electron beams, and superpower microwave generators. In 1979, Tajima and Dawson [4] and, in 1985, Chen *et al.* [5] suggested new, modified versions of Fainberg's method for particle acceleration by space charge density waves in a plasma [3]: they proposed to excite accelerating fields by laser pulses and relativistic electron bunches.

We think that the most promising acceleration method is to excite accelerating fields in a plasma by an individual relativistic electron bunch, because this excitation mechanism is nonresonant in nature and, therefore, is weakly sensitive to the longitudinal plasma density variations observed in experiments. Additionally, in order to avoid phenomena such as electromagnetic filamentation or slipping instability [6–9], it is worthwhile to apply a stabilizing external longitudinal magnetic field [10], which not only serves to suppress instabilities but also gives rise to a large number of new wave branches, thereby substantially expanding the possibilities of the wake field acceleration scheme.

1. Let us determine the wake field generated by an axisymmetric relativistic electron bunch propagating along the z-axis in a magnetized plasma, assuming that the ions are immobile and neglecting the electron thermal motion. We write the bunch current in the form

$$\mathbf{j}_{\text{ext}} = -I_0 \frac{\psi(r)}{2\pi} T\left(t - \frac{z}{V_0}\right)\mathbf{e}_z, \qquad (1)$$

where I_0 is the peak total bunch current, t is the time, z and r are the longitudinal and radial coordinates, and the unit vector $\mathbf{e}_z$ is aligned with the external magnetic field $\mathbf{H}_0 = H_0\mathbf{e}_z$ and indicates the propagation direction of the bunch. The radial and longitudinal profiles of the bunch current are described by the functions $\psi(r)$ and $T\left(t - \frac{z}{V_0}\right)$ (such that $\max T = 1$), respectively. Formula (1) describes the bunch current density under the assumption that the bunch propagates as a single entity, i.e., in the rigid-bunch approximation. The function $\psi(r)$ satisfies the normalization condition

$$\int_0^{r_b} \psi(r) r dr = 1,$$

where r_b is the maximum radius of the bunch.

We pass over to the Fourier transforms of the electric field $\mathbf{E}$, the magnetic field $\mathbf{H}$, and the bunch current density (1). Then, the Maxwell equations take the form

$$kE_{\omega\varphi} = k_0 H_{\omega r}, \quad kH_{\omega\varphi} = k_0(\varepsilon_1 E_{\omega r} + i\varepsilon_2 E_{\omega\varphi}),$$

$$\frac{1}{r}\frac{d}{dr} r E_{\omega\varphi} = ik_0 H_{\omega z},$$

$$\frac{dH_{\omega r}}{dr} - ikH_{\omega r} = ik_0(\varepsilon_1 E_{\omega\varphi} - i\varepsilon_2 E_{\omega r}), \qquad (2)$$

$$\frac{dE_{\omega z}}{dr} - ik_{\omega r} = ik_0 H_{\omega\varphi},$$

$$\frac{1}{r}\frac{d}{dr} r H_{\omega\varphi} = ik_0\varepsilon_3 E_{\omega z} - \frac{2I_0}{c}\psi(r)T(\omega),$$

where $k = \omega/V_0$; $k_0 = \omega/c$; $\varepsilon_1 = 1 - \dfrac{\omega_{pe}^2(\omega + i\nu)}{\omega[(\omega + i\nu)^2 - \omega_{He}^2]}$;

$\varepsilon_2 = \dfrac{\omega_{pe}^2\omega_{He}}{\omega[(\omega + i\nu)^2 - \omega_{He}^2]}$; $\varepsilon_3 = 1 - \dfrac{\omega_{pe}^2}{\omega(\omega + i\nu)}$; ω_{pe} and ω_{He} are the Langmuir frequency and gyrofrequency of

1063-780X/00/2610-0889$20.00

the plasma electrons, respectively; ν is the effective collision frequency; and φ is the azimuthal coordinate.

It is convenient to reduce the first-order differential equations (2) to the following coupled second-order differential equations for the longitudinal components of the electric and magnetic fields:

$$\begin{aligned}
&\frac{1}{r}\frac{d}{dr}r\frac{dH_{\omega z}}{dr} + p_H^2 H_{\omega z} \\
&= -ikk_0\frac{\varepsilon_2\varepsilon_3}{\varepsilon_1}E_{\omega z} - k\frac{\varepsilon_2}{\varepsilon_1}\frac{2I_0}{c}\psi(r)T(\omega), \\
&\frac{1}{r}\frac{d}{dr}r\frac{dE_{\omega z}}{dr} + p_E^2 E_{\omega z} \\
&= ikk_0\frac{\varepsilon_2}{\varepsilon_1}H_{\omega z} + i\frac{(k_0^2\varepsilon_1 - k^2)}{k_0\varepsilon_1}\frac{2I_0}{c}\psi(r)T(\omega),
\end{aligned} \tag{3}$$

where

$$p_H^2 = k_0^2\frac{\varepsilon_1^2 - \varepsilon_2^2}{\varepsilon_1} - k^2, \quad p_E^2 = k_0^2\varepsilon_3 - k^2\frac{\varepsilon_3}{\varepsilon_1}.$$

The inhomogeneous equations (3) have the solution

$$\begin{aligned}
H_{\omega z} &= i\pi\frac{I_0}{c}T(\omega)\frac{k\varepsilon_2}{\varepsilon_1} \\
&\times\int[A_1 G(\lambda_1 r_0, \lambda_1 r) - A_2 G(\lambda_2 r_0, \lambda_2 r)]r_0 dr_0\psi(r_0), \\
E_{\omega z} &= -\pi\frac{I_0}{c}T(\omega)\frac{1}{k_0\varepsilon_3} \\
&\times\int[B_1 G(\lambda_1 r_0, \lambda_1 r) - B_2 G(\lambda_2 r_0, \lambda_2 r)]r_0 dr_0\psi(r_0).
\end{aligned} \tag{4}$$

Here,

$$A_i = \frac{\lambda_i^2}{\lambda_1^2 - \lambda_2^2}, \quad B_i = \frac{\lambda_i^2(p_H^2 - \lambda_i^2)}{\lambda_1^2 - \lambda_2^2};$$

the transverse wavenumbers of the ordinary and extraordinary waves, $\lambda_{1,2}$, which are defined as the roots of the biquadratic equation

$$\lambda^4 - \lambda^2(p_E^2 + p_H^2) - k^2k_0^2\varepsilon_3\left(\frac{\varepsilon_2}{\varepsilon_1}\right)^2 + p_E^2 p_H^2 = 0, \tag{5}$$

are equal to

$$\lambda_{1,2}^2 = \frac{p_E^2 + p_H^2}{2} \pm \sqrt{\frac{(p_E^2 - p_H^2)^2}{4} + k^2k_0^2\varepsilon_3\left(\frac{\varepsilon_2}{\varepsilon_1}\right)^2},$$

$$G(\lambda_i r_0, \lambda_i r) = \begin{cases} H_0^{(1)}(\lambda_i r)J_0(\lambda_i r_0), & r > r_0, \\ H_0^{(1)}(\lambda_i r_0)J_0(\lambda_i r), & r < r_0, \end{cases}$$

where $J_0(\lambda_i r)$ and $H_0^{(1)}(\lambda_i r)$ are the Bessel and Hankel functions, respectively.

In the ultrarelativistic limit, we can set $V_0 = c$, in which case the transverse wavenumbers become

$$\lambda_{1,2}^2 = \frac{k_0^2}{\varepsilon_1}[\varepsilon_2(\varepsilon_1 - 1) \pm \varepsilon_2\sqrt{\varepsilon_3}]. \tag{6}$$

In the frequency range $\omega^2 < \omega_{pe}^2$, the transverse wavenumbers are complex quantities.

In the limit of a strong magnetic field ($\omega_{He}^2 \gg \omega_{pe}^2$), the transverse wavenumbers are equal to

$$\lambda_1^2 = k_0^2 - k^2, \quad \lambda_2^2 = (k_0^2 - k^2)\varepsilon_3.$$

For simplicity, we consider an infinitely thin ring-shaped bunch of radius r_b such that

$$\psi(r) = \frac{\delta(r - r_b)}{r_b}, \quad T(\omega) = 1. \tag{7}$$

The electric field at the axis $r = 0$ of the bunch can be represented in integral form:

$$E_z = -\frac{1}{2}\frac{Q_0}{V_0^2\gamma_0^2}\int_{-\infty}^{\infty}\exp(-i\omega t)H_0^{(1)}(k_\perp r_b)\omega d\omega, \tag{8}$$

where Q_0 is the total charge of the bunch, γ_0 is its relativistic factor, and $k_\perp^2 = (k_0^2 - k^2)\varepsilon_3$. Note that $k_\perp^2 > 0$. Consequently, in the frequency range $\omega < \omega_{pe}$, the bunch emits electromagnetic waves in the radial direction.

Expression (8) can be rewritten in the form

$$E_z = -\frac{iQ_0}{2V_0^2\gamma_0^2}\frac{d}{dt}\int_{-\infty}^{\infty}e^{-i\omega t}H_0^1(k_\perp r_b)d\omega, \tag{9}$$

We evaluate the integral in (9) (see [11]) to obtain the expression for the longitudinal component of the electric field

$$E_z = \frac{Q_0\omega_{pe}^2\tau}{V_0^2\gamma_0^2(\tau^2 + \mu^2)}\left\{\sin\sqrt{\tau^2 + \mu^2} + \frac{\cos\sqrt{\tau^2 + \mu^2}}{\sqrt{\tau^2 + \mu^2}}\right\}, \tag{10}$$

where

$$\tau = \omega_{pe}\left(t - \frac{z}{V_0}\right), \quad \mu = \frac{\omega_{pe}r_b}{V_0\gamma_0}.$$

Far behind the bunch, the wake field falls off as $1/\tau$, because the group velocity of plasma oscillations in a strong magnetic field is finite. Because of the emission of plasma waves from the axial region, the wake field decreases in the longitudinal direction.

2. Let us consider a waveguide partially filled with a plasma, i.e., a waveguide with a vacuum gap between the plasma surface $r = a$ and the conducting wall $r = b$. We assume that the waveguide is placed in an external magnetic field.

In order to derive a dispersion relation for the eigenmodes of this plasma waveguide, it is necessary to determine the electromagnetic fields in the vacuum gap $a < r < b$ and to match them with the plasma fields through the boundary conditions at the plasma surface. The boundary conditions are imposed in a standard way: the tangential components of the electric and magnetic fields are assumed to be continuous at the plasma surface. It is convenient to write the resulting dispersion relation in the form

$$\mathrm{Det}\, A = 0, \tag{11}$$

Here, the components of the matrix A are as follows:

$$A_{11} = 1, \quad A_{12} = 1, \quad A_{13} = -1, \quad A_{14} = 0,$$

$$A_{21} = \Gamma_1 \frac{\omega}{c\lambda_1}\frac{J_1(\lambda_1 a)}{J_0(\lambda_1 a)}, \quad A_{22} = \Gamma_2 \frac{\omega}{c\lambda_2}\frac{J_1(\lambda_2 a)}{J_0(\lambda_2 a)},$$

$$A_{23} = -1, \quad A_{24} = \frac{\omega}{cw}, \quad A_{31} = \Gamma_1, \quad A_{32} = \Gamma_2,$$

$$A_{33} = 0, \quad A_{34} = Q(wa), \quad A_{41} = \varepsilon_3 \frac{\omega}{c\lambda_1}\frac{J_1(\lambda_1 a)}{J_0(\lambda_1 a)},$$

$$A_{42} = \varepsilon_3 \frac{\omega}{c\lambda_2}\frac{J_1(\lambda_2 a)}{J_0(\lambda_2 a)}, \quad A_{43} = -\frac{\omega}{cw}F_1(wa), \quad A_{44} = 0,$$

where

$$Q(wa) = \frac{I_0(wa)K_1(wb) + K_0(wa)I_1(wb)}{I_1(wa)K_1(wb) - I_1(wb)K_1(wa)},$$

$$F_1 = \frac{I_0(w_p r_b)\cdot \Delta_0(wr_b, wb)}{I_0(w_p a)\cdot \Delta_0(wa, wb)},$$

$$w = \sqrt{\frac{\omega^2}{V_0^2} - \frac{\omega^2}{c^2}}, \quad w_p = \frac{\omega}{V_0}\sqrt{1 - \left(\frac{V_0}{c}\right)^2 \varepsilon_3},$$

$$\Delta_0(wr, wb) = I_0(wr)K_0(wb) - I_0(wb)K_0(wr),$$

$$\Gamma_{1,2} = \frac{1}{2\varepsilon_1}\left\{(\varepsilon_1 - \varepsilon_3)\left(\varepsilon_1 - \frac{k^2}{k_0^2} - \varepsilon_2^2\right)\right.$$

$$\left. \pm \left[\left((\varepsilon_1 - \varepsilon_3)\left(\varepsilon_1 - \frac{k^2}{k_0^2}\right) - \varepsilon_2^2\right)^2 + 4\varepsilon_2^2\varepsilon_3\frac{k^2}{k_0^2}\right]^{1/2}\right\},$$

$$\lambda_{1,2} = \frac{k_0}{2\varepsilon_1}\left\{(\varepsilon_1 + \varepsilon_3)\left(\varepsilon_1 - \frac{k^2}{k_0^2}\right) - \varepsilon_2^2\right.$$

$$\left. \pm \left[\left((\varepsilon_1 - \varepsilon_3)\left(\varepsilon_1 - \frac{k^2}{k_0^2}\right) - \varepsilon_2^2\right)^2 + 4\varepsilon_2^2\varepsilon_3\frac{k^2}{k_0^2}\right]^{1/2}\right\}.$$

The field distribution over the waveguide cross section is governed by the transverse wavenumber. The ranges $\lambda_{1,2}^2 > 0$ and $\lambda_{1,2}^2 < 0$ correspond to the spatial and surface modes, respectively. The complex values of $\lambda_{1,2}^2$ refer to a hybrid mode. The boundaries of the region where $\lambda_{1,2}$ are complex are determined by the inequalities

$$\omega_1 > \omega > \omega_2,$$

where

$$\omega_{1,2} = kc\frac{2\omega_{pe}^2 + \omega_{He}^2 \pm (\omega_{pe}^4 + \omega_{He}\omega_{pe}^2 - \omega_{He}^2 k^2 c^2)^{1/2}}{\omega_{He}^2 + 4k^2c^2}. \tag{12}$$

In order for a relativistic electron bunch to excite a hybrid mode, the relativistic factor of the bunch should satisfy the condition

$$\gamma_0 > \frac{\omega_{He}}{2\omega_{pe}}. \tag{13}$$

The electromagnetic field distribution and the frequency of a hybrid mode that synchronously accompanies the bunch were obtained numerically for the following parameters of the plasma waveguide: $\omega_{He}/\omega_{pe} = 6.3$, $\omega_{pe}a/c = 23.3$, $b/a = 2.4$, and $\gamma_0 = 4.6$, in which case the frequency of the wake hybrid mode is equal to $0.35\omega_{pe}$. We found that, at the radius $r/a = 0.8$, the profile of the absolute value of the longitudinal component of the electric field has a pronounced peak, which corresponds to an energy conversion factor equal to

$$R_E = \left|\frac{E_{z\max}}{E_{z(r=0)}}\right| = 37.$$

Note that, the energy conversion factor is defined as the ratio of the amplitude of the electric field accelerating a driven bunch to the amplitude of the electric field decelerating a driving bunch (the bunch exciting the wakefield). Such a large value of R_E indicates that the maximum energy the driven bunch can gain during acceleration is significantly higher (by a factor of R_E) than the initial energy of the driving bunch.

Hence, we have shown that, for a certain relation among the parameters of the plasma–bunch–magnetic-field system, the hybrid nature of the wake waves, which are excited by a relativistic electron bunch in a magnetized plasma and are a superposition of the surface and spatial modes, makes it possible to accelerate the driven bunch to the maximum energy $\varepsilon_{\max}$,

$$\varepsilon_{\max} = mc^2(R_E\gamma_0 - 1), \tag{14}$$

which is many times higher than the initial energy of the driving bunch (even when the bunch is initially unmodulated in the longitudinal direction).

REFERENCES

1. V. I. Veksler, in *Proceedings of CERN Symposium on High-Energy Physics, Geneva, 1956*, Vol. 1, p. 80.
2. G. I. Budker, in *Proceedings of CERN Symposium on High-Energy Physics, Geneva, 1956*, Vol. 1, p. 68.
3. Ya. B. Fainberg, in *Proceedings of CERN Symposium on High-Energy Physics, Geneva, 1956*, Vol. 1, p. 84.
4. T. Tajima and J. M. Dawson, Phys. Rev. Lett. **43**, 267 (1979).
5. P. Chen, J. M. Dawson, T. Katsouleas, *et al.*, Phys. Rev. Lett. **54**, 693 (1985).
6. T. Katsouleas, Phys. Rev. A **33**, 2066 (1986).
7. R. Keinigs and M. E. Jones, Phys. Fluids **30** (1), 252 (1987).
8. Ya. B. Faĭnberg, Fiz. Plazmy **23**, 275 (1997) [Plasma Phys. Rep. **23**, 251 (1997)].
9. Ya. B. Faĭnberg, Fiz. Plazmy **26**, 362 (2000) [Plasma Phys. Rep. **26**, 335 (2000)].
10. A. Ts. Amatuni, E. V. Sekhposyan, A. G. Khachatryan, and S. S. Elbakian, Fiz. Plazmy **21**, 1000 (1995) [Plasma Phys. Rep. **21**, 945 (1995)].
11. A. P. Prudnikov, Yu. A. Brychkov, and O. I. Marichev, *Integrals and Series*, Vol. 2: *Special Functions* (Nauka, Moscow, 1983; Gordon and Breach, New York, 1986).

Translated by I.A. Kalabalyk

Plasma Physics Reports, Vol. 26, No. 10, 2000, pp. 893–901. Translated from Fizika Plazmy, Vol. 26, No. 10, 2000, pp. 952–960.

LOW-TEMPERATURE PLASMA

Effect of Continuous Current during Pauses between Successive Strokes on the Decay of the Lightning Channel

N. L. Aleksandrov*, É. M. Bazelyan, and M. N. Shneider*****

**Moscow Institute of Physics and Technology, Institutskiĭ proezd 9, Dolgoprudnyĭ, Moscow oblast, 141700 Russia*

***Krzhizhanovskiĭ Power Engineering Institute, Leninskiĭ pr. 19, Moscow, 117927 Russia*

****Princeton University, Princeton, NJ, 08543 USA*

Received March 23, 2000

Abstract—A one-dimensional model is used to study the dynamics of the hydrodynamic parameters of the lightning channel in the return stroke and after the pulse current is damped. The effect of the continuous residual electric current during pauses between the successive strokes on the plasma cooling in the channel is analyzed. It is shown that a continuous electric current, which is several orders of magnitude lower than the peak current in the return stroke, is capable of maintaining the channel conductivity. This effect cannot be explained merely by Joule heating but is largely governed by the fact that the turbulent heat transport is substantially suppressed. In this case, even a continuous current as low as 50–100 A is capable of maintaining the conductivity of the lightning channel at a level at which only M-components can develop in the channel rather than the dart leader of the subsequent stroke. © *2000 MAIK "Nauka/Interperiodica".*

1. INTRODUCTION

Two out of every three lightning discharges are multistroke lightning flashes. In such a flash, each stroke begins with the so-called leader stage, during which a cloud-to-ground ionization wave produces a well-conducting channel in air [1]. The leaders of subsequent strokes (which are called a dart leaders) differ strongly in character from the first leader of a negative lightning flash, which is called the stepped leader because it descends in a series of very rapid steps. When the leader traverses the distance from the cloud to the ground, the lightning flash evolves into the return stroke accompanied by the main energy release.

During the pause between the strokes, which lasts from several tens to several hundreds of milliseconds, the channel conductivity is maintained by a quasisteady current of 100–200 A. Current pulses with a duration of 100–1000 μs and an amplitude from several tens of A to several hundred kA (the so-called M-components) may be superimposed on the quasisteady current. In the course of these pulses, the channel is observed to be very bright.

Although the problem of the nature of the dart leader, after which the lightning flash evolves into the return stroke, has been widely discussed in the literature, there are basically no studies devoted to modeling this phenomenon. Different ideas were set forth regarding the nature of the dart leader: it was interpreted, e.g., as a shock wave in an electron gas [2]; as an electromagnetic wave in the channel, which plays the role of the waveguide [3]; and as an ionization wave similar to the wave at the streamer head [4, 5]. An analysis of the results of observations of lightning flashes [6] supports the last hypothesis.

One of us [4] advanced the hypothesis that the dart leader and M-components both stem from the same cause: the channel formed by the preceding stroke began to be affected by new charged centers (convective cells) in a thundercloud. Which of these two phenomena (the dart leader or M-components) will occur depends mainly on the channel conductivity at the time the new cells come into play. The high conductivity of a strongly heated channel ensures that the potential decreases sufficiently uniformly and gradually from the cloud to the ground. As a result, the grounded channel is recharged in a wavelike fashion and the ionization effects are insignificant. Numerical modeling performed in [4] showed that the global parameters of the recharging process are similar to those of the M-components. The conditions in a heated channel whose conductivity at the time the new cells come into play is sufficiently low (such that the linear resistance exceeds 10^3 Ω/m) are favorable for the onset of a cloud-to-ground ionization wave whose parameters are typical of the dart leader. Hence, the occurrence of the subsequent stroke in the channel formed by the preceding stroke is largely governed by the dynamics of the channel cooling.

In this paper, we apply a one-dimensional model to numerically investigate hydrodynamic processes in the lightning channel during the return stroke and during pauses between successive strokes. The model incorporates the main mechanisms for heat transport and takes into account the possible residual electric current in the decaying channel. We show that the parameters charac-

1063-780X/00/2610-0893$20.00

terizing the cooling of air in the channel depend strongly on the comparatively low residual channel current. We clarify the nature of this dependence and show that it does not stem merely from the conventional Joule heating but is also attributed to the fact that, in a channel with a sufficiently high continuous current, the turbulent heat transport is substantially suppressed. We draw the conclusion that a low (50–100 A) residual current can serve to maintain the channel conductivity at a level at which, according to [4], only the M-components can develop in the channel rather than the dart leader of the subsequent strokes. This conclusion agrees qualitatively with the data from natural observations.

2. MODEL OF THE LIGHTNING CHANNEL IN THE RETURN STROKE

We consider the onset of a lightning channel in unperturbed cold air at atmospheric pressure for the following pulse currents characteristic of the return stroke of a lightning discharge:

$$I = I_a t/\tau_f \quad \text{for} \quad t \le \tau_f$$

and

$$I = (I_a - I_{\text{res}})\exp[-(t-\tau_f)/\tau^*] + I_{\text{res}} \quad \text{for} \quad t \ge \tau_f.$$

Here, $I_a \sim 30$–100 kA is the current amplitude in the return stroke of a lightning discharge, $I_{\text{res}} \sim 0$–500 A is the post-discharge current amplitude, $\tau_f = 5.5$ μs is the rise time of the linear front of the current pulse, and $\tau^* = 140$ μs is the characteristic damping time of its trailing edge.

In calculations, we followed the paper by Shneider [7], who applied the same approach to solve an analogous problem of the effect of the residual current on the cooling of the post-arc channel but for essentially different parameter values.

It is convenient to solve the standard one-dimensional gas-dynamic equations in the Lagrangian mass coordinates, $dm = \rho r dr$:

$$\begin{aligned} \frac{\partial r}{\partial t} &= u, \\ \frac{1}{\rho} &= \frac{1}{2}\frac{\partial r^2}{\partial m}, \\ \frac{\partial u}{\partial t} &= -r\frac{\partial}{\partial m}(p+Y), \\ \frac{\partial \varepsilon}{\partial t} + (p+Y)\frac{\partial}{\partial t}(1/\rho) &= Q. \end{aligned} \tag{1}$$

We supplement Eqs. (1) with the equation of state for air:

$$p = (\gamma-1)\rho\varepsilon = \frac{\gamma-1}{\gamma}\rho h, \quad \gamma(T) = c_p/c_v, \tag{2}$$

where ε and $h = \varepsilon + p/\rho$ are the internal energy and enthalpy per unit mass; r is the radial coordinate; u, ρ, and p are the air velocity, mass density, and pressure; Y is an artificially introduced viscosity; and the source term Q accounts for the Joule heating of air by the current flowing in the channel, heat transport, and heat losses due to emission and heat conduction: $Q = Q_J + Q_{\text{rad}} + Q_\lambda$. Since similar problems have been solved by many authors, we will not dwell on a detailed description of the numerical algorithm.

The problem treated in [9] is the most similar in formulation to our problem. Paxton *et al.* analyzed radiation in the multigroup diffusion approximation [11] (in [8, 10], the absorption coefficient was assumed constant). In this approximation, the radiation diffusion equation is solved for each kth spectral group,

$$\frac{1}{r}\frac{\partial}{\partial r}\left(\frac{r}{3\kappa_\nu}\frac{\partial U_\nu}{\partial r}\right) + \kappa_\nu(U_{p\nu} - U_\nu) = 0 \tag{3}$$

with the boundary conditions $\left.\frac{\partial U_\nu}{\partial r}\right|_{r=0} = 0$ and $W_{r_N} = -\frac{c}{3\kappa_\nu}\left.\frac{\partial U_\nu}{\partial r}\right|_{r_N} = \frac{c}{2}U_\nu|_{r_N}$, where r_N is a point at the boundary of the computation region. Here, U_ν is the spectral density of the radiation energy, $U_{p\nu}$ is the equilibrium radiation-energy density, κ_ν is the absorption coefficient for radiation of frequency ν, and $\mathbf{W}_\nu = -\frac{c}{3\kappa_\nu}\operatorname{grad} U_\nu$ is the radiation-energy flux. The emission-induced energy losses are written as

$$Q_{\text{rad}} = -\frac{1}{\rho}\sum_k \operatorname{div}\mathbf{W}_k = \frac{c}{\rho}\sum_k \kappa_\nu(U_{k\nu} - U_{kp\nu}). \tag{4}$$

The contribution of the molecular heat conduction to Q has the form

$$Q_\lambda = -\frac{1}{\rho}\operatorname{div}\mathbf{q}_\lambda = \frac{1}{\rho}\frac{1}{r}\frac{\partial}{\partial r}\left(r\lambda\frac{\partial T}{\partial r}\right) = \frac{1}{\rho}\frac{\partial}{\partial m}\left(\rho r^2\lambda\frac{\partial T}{\partial m}\right), \tag{5}$$

where $\lambda = \lambda(T)$ is the molecular thermal conductivity. The local Joule heating intensity is described by the formula

$$Q_J = \frac{E^2\sigma}{\rho}, \tag{6}$$

where $\sigma = \sigma(T)$ is the plasma conductivity, $E(t) = IR$ is the electric field strength, and $R(t) = 1/\int_r 2\pi r\sigma(T(r,t))dr$ is the linear resistance of the channel.

In calculations, the radiation spectrum was divided into three spectral groups. Within each group, the absorption coefficient was assumed independent of the frequency and equal to the Planck-averaged value over

the given group. In partitioning the radiation spectrum into groups, we adopted the following boundaries: 0.01–6.52, 6.52–9.96, and 9.96–247 eV. The absorption coefficients $\kappa_\nu \equiv \kappa_\nu(\rho, T)$ for the corresponding spectral groups incorporate light absorption, inverse bremsstrahlung, and photoabsorption. These coefficients were used in the form of the interpolation tables that were compiled from the data of [12, 13]. This three-group approach to describing radiation was employed to model a light-erosive plasma flare [13], a magnetoplasma compressor [14], and a pulsed arc discharge in air [15]. The air temperature T was described by the dependence $T(\varepsilon, \rho)$ determined by interpolating the data from the tables presented in [16]. The high-temperature range $T > 10^4$ K was described by the interpolation formula for the specific internal energy of air [17]. We also took into account the dependence $\gamma(T)$. The conductivity of a plasma channel, the partial content of air (with taking into account molecular dissociation and ionization up to doubly charged ions), and the thermal conductivity of air as functions of the air temperature T were found from the data presented in [8].

The initial channel radius was set to be $r_0 \sim 0.1$ cm, the initial air temperature being $T(r, 0) = T_0 + T(0, 0)/(1 + r^2/r_0^2)$, where $T_0 = 300$ K and $T(0, 0) \sim 10\,000$ K. Our simulations showed that, during the discharge evolution, the solution rapidly "forgets" the initial conditions.

3. NUMERICAL RESULTS

For Joule heating intensities characteristic of the lightning discharges under discussion, the expansion of the lightning channel gives rise to a high-power shock wave (SW). Radial profiles of the air parameters in the channel and in the SW at different instants for I_a = 100 kA are shown in Fig. 1 (for $t \le 300$ μs) and Fig. 2 (for $t > 300$ μs). For the other current pulses of interest to us, the lightning discharges develop in a similar manner.

During the development of the spark channel, the emitted radiation plays a key role in the overall energy balance and energy transport. Our simulations show that a significant fraction of the emitted radiant energy is absorbed at the channel boundary, thereby heating the nearest layers of the cold air. When the air temperature in the channel is high ($T > 10^4$ K), the molecular heat conduction plays a minor role in the energy balance. As time elapses, the rate at which the energy is lost via the emitted radiation decreases and, when the air temperature in the channel falls to $T(0) < 8000$ K (in the case at hand, this occurs at $t > 1$ ms), the energy losses are governed primarily by molecular heat conduction.

The postdischarge channel is cooled via molecular heat conduction on very long time scales. Thus, under the assumption that heat diffusion is described by the enhanced molecular thermal conductivity $\chi_\lambda = \lambda/c_p\rho \approx 50$ cm^2/s (this corresponds to $T = 10^4$ K), the thickness of the layer of air heated over a time interval of 10^{-2} s is $\delta r = (\chi t)^{1/2} \approx 0.7$ cm, which is much smaller than typical channel radii for the current pulses under consideration. However, if the air in the postdischarge channel evolves into a turbulent state, the cooling and expansion rates of the channel both become much higher. The mechanisms responsible for the loss of stability of the channel boundaries and the onset of the turbulent motion of air in the channel will be considered in the next section.

In Figs. 1 and 2, one can clearly see the phase of the negative pressure drop. This phase is known in the theory of explosions (see, e.g., [18]) and can be explained as follows. The air pressure in the expanding channel inevitably falls to $p = p_0 = 1$ atm, but the channel itself continues to expand by inertia, in which case the pressure drop becomes negative (the phase of the negative pressure drop at $p < p_0$) and the channel stops expanding. Then, the air begins to contract and is compressed in the channel, so that the air pressure and temperature grow. In the next section, we will show that a slowed contraction of air toward the channel axis is one of the possible mechanisms for the onset of the hydrodynamic Rayleigh–Taylor instability in the region of large density gradients at the channel boundary. The Rayleigh–Taylor instability may give rise to the turbulent motion of air in the channel, in which case the channel is cooled and expands at much higher rates.

Our simulations revealed that, on time scales longer than 1 ms, a low (in comparison with the peak value) residual current I_{res} has a substantial impact on the cooling process (Fig. 3). In the absence of the residual current ($I_{res} = 0$), the air temperature in the channel continuously decreases, while even a low residual current can terminate the cooling process and maintain a relatively high conductivity in the channel. The higher the residual current, the earlier the air cooling in the channel stops. The channel fairly rapidly evolves into a quasisteady free arc in air with a characteristic longitudinal electric field of about $E \sim 5$–8 V/cm (Fig. 3) [19].

4. HYDRODYNAMIC INSTABILITY OF THE BOUNDARY OF THE POST-ARC CHANNEL

The air pressure in the cooled channel becomes approximately equal to the pressure of the surrounding air when the air temperature in the channel is still high: $T \sim 10^4$ K. The air temperature continues to decrease, while the pressure remains essentially constant. Since, during this process, the air density in the channel increases, the air should come into the channel from its edge. This unstable reverse radial air flow gives rise to the turbulent air motion in the channel. According to present-day opinions [7], the main cause for the naturally observed hydrodynamic instability is the Ray-

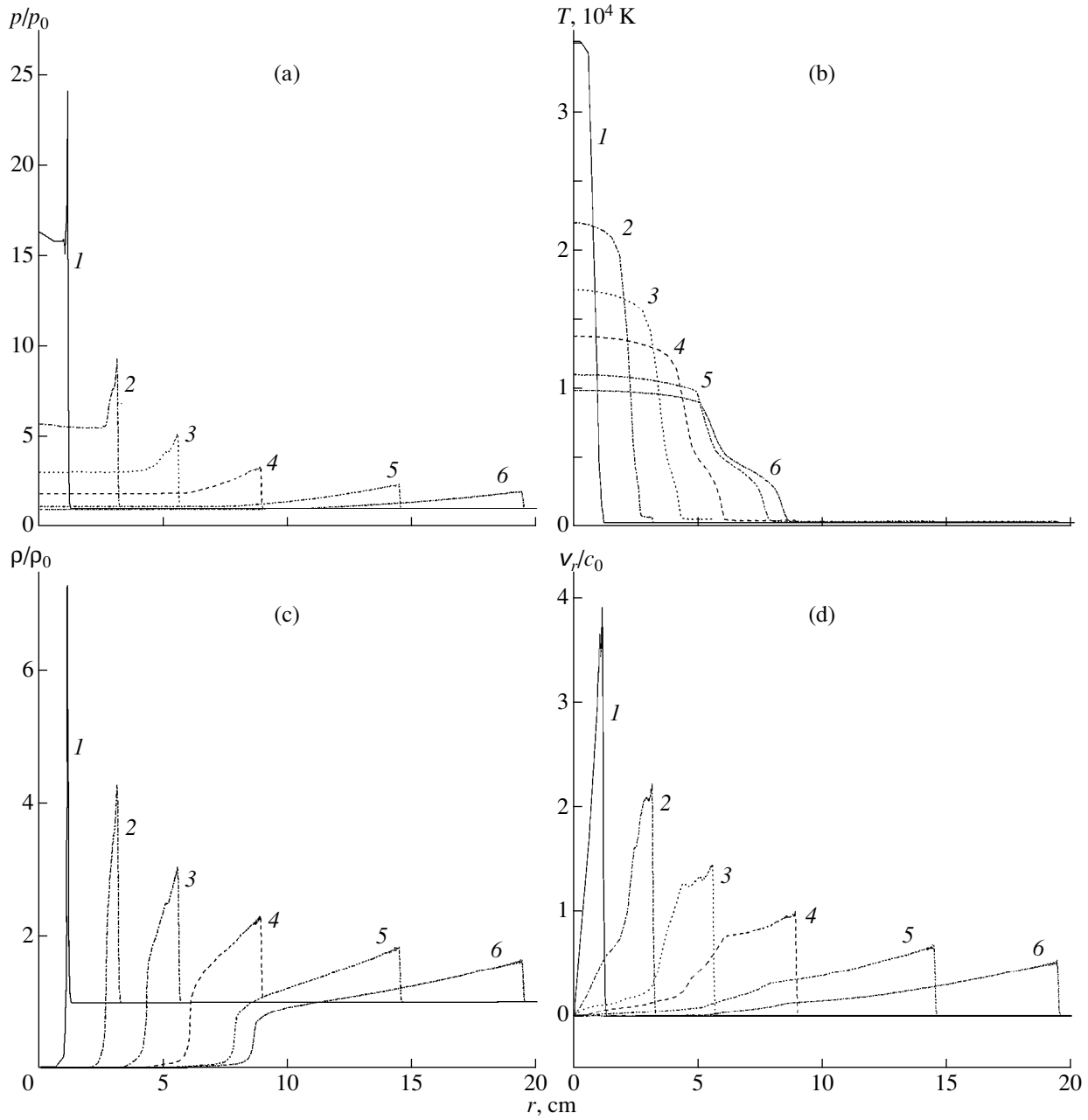

Fig. 1. Radial profiles of the (a) pressure, (b) temperature, (c) density, and (d) relative velocity (Mach number) of air for a current pulse with the amplitude I_a = 100 kA at different times in the interval $t \le 300$ μs: (*1*) 5, (*2*) 20, (*3*) 50, (*4*) 100, (*5*) 200, and (*6*) 300 μs.

leigh–Taylor instability [20] in the peripheral channel region where the density gradient is large. The Rayleigh–Taylor instability can occur in the transient layer at the channel boundary if the boundary contracts toward the channel axis at a slowed rate. The channel boundary can move in such a manner only when the pressure and density gradients at the boundary are oppositely directed, which corresponds to the condition $\nabla p \nabla \rho < 0$. The representative radial profiles of the air pressure and density are shown in Fig. 4 on an enlarged scale. The profiles were calculated for I_a = 100 kA at the instants t = 200 μs (when the channel continues to expand by inertia) and t = 800 μs (when the channel boundary contracts). At the boundary of the expanding channel, we have $\nabla p \nabla \rho > 0$ (Fig. 4a), so that the expansion process is stable. A higher pressure of the surrounding air terminates the expansion, and the channel starts to contract. As the volume of the channel decreases, the pressure in the channel increases and acts to prevent further air contraction, in which case the pressure and density gradients inevitably become oppositely directed, $\nabla p \nabla \rho < 0$ (Fig. 4b), thereby giving rise

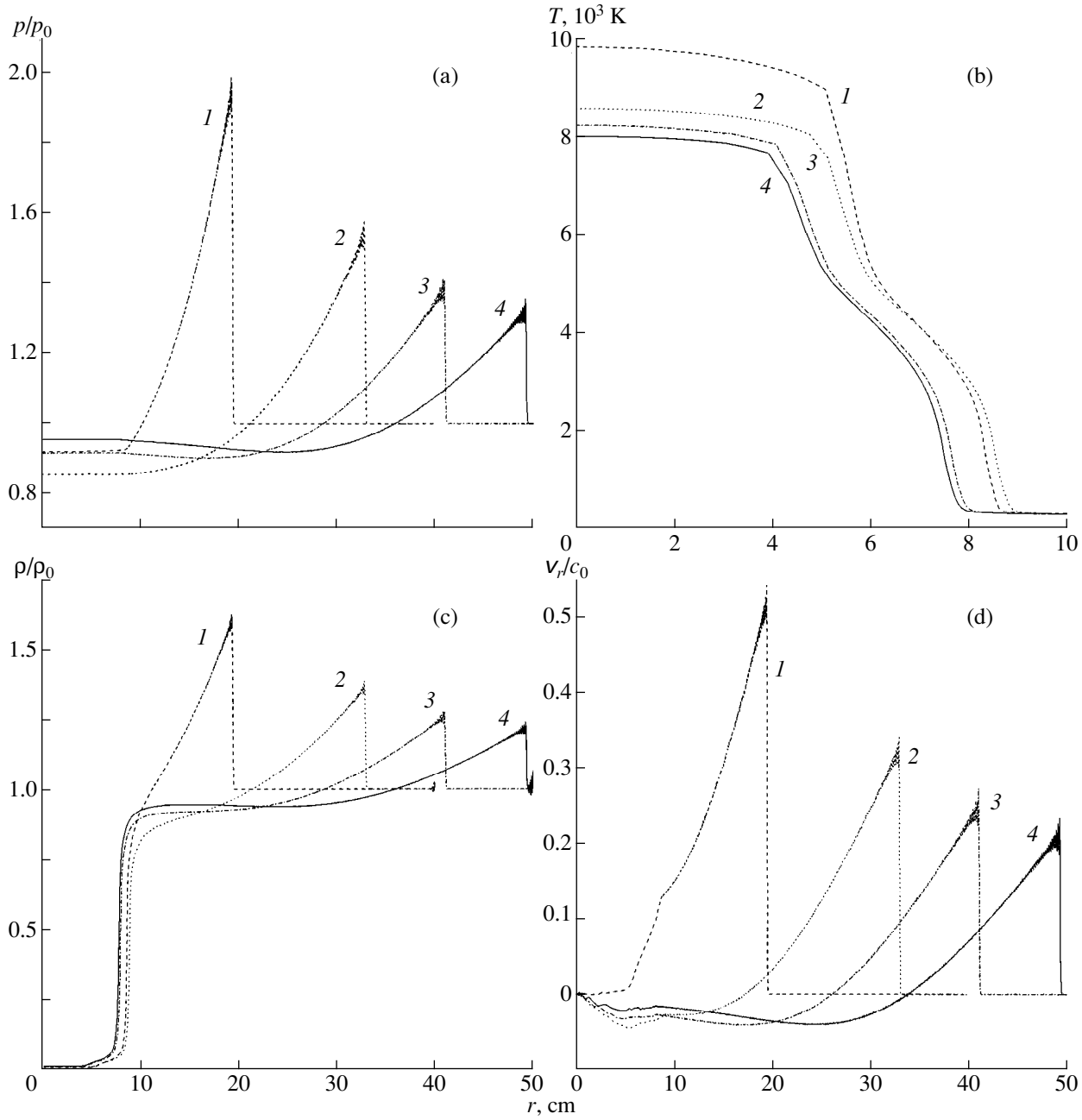

Fig. 2. Radial profiles of the (a) pressure, (b) temperature, (c) density, and (d) relative velocity (Mach number) of air for a current pulse with the amplitude I_a = 100 kA at different times in the interval $t \geq 300$ μs: (*1*) 300, (*2*) 600, (*3*) 800, and (*4*) 1000 μs.

to the Rayleigh–Taylor instability. Taking into account the fact that the air density in the channel satisfies the condition $\rho \ll \rho_0$, we can estimate the time scale on which the Rayleigh–Taylor instability develops as $\tau_{inst} \sim (2\pi \ddot{r}/\lambda_w)^{-1/2}$, where λ_w is the perturbation wavelength ($\delta r < \lambda_w \leq r$) and δr is the thickness of the boundary layer where the density gradient is large. For example, for our numerical results obtained at I_a = 100 kA, this estimate yields $10^{-4} < \tau_{inst} < 10^{-3}$, which is comparable to the duration of the phase of the negative pressure drop. We emphasize that this estimate applies only to the linear instability stage. Such involved problems as the nonlinear stage of the hydrodynamic instability and the evolution of air into a developed turbulent motion in the postarc channel require a separate analysis and go beyond the scope of this paper. However, the results from experimental investigations of the processes in the postarc channel (in particular, schlieren photographs) (see, e.g., [21, 22]) permit us to suggest that, in order of magnitude, the above estimate for τ_{inst} gives a correct duration of the nonlinear stage.

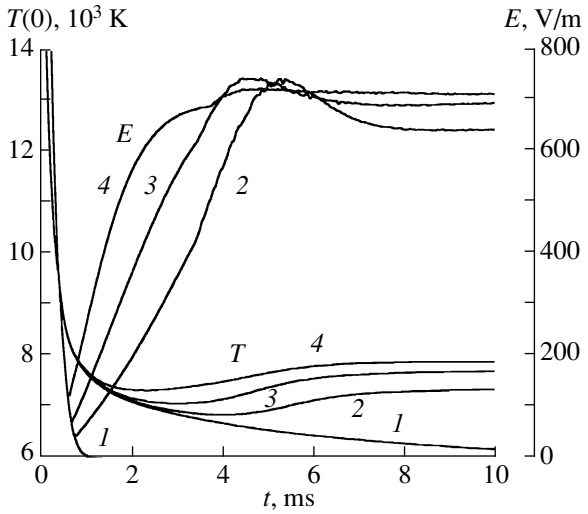

Fig. 3. Time evolutions of the air temperature at the channel axis and the averaged (over the channel cross section) electric field for I_a = 30 kA and for different residual currents I_{res} = (*1*) 0, (*2*) 25, (*3*) 50, and (*4*) 100 A.

5. ISOBARIC STAGE OF TURBULENT COOLING

In our study, we describe the turbulent cooling of the channel using the model that was considered in detail in [7] (an analogous model, which differs from our model only in that it neglects the spatial dependence of the averaged thermodynamic parameters of air in the channel, was used in [23, 24]). As before, we describe the cooling process by the one-dimensional Lagrangian equations (1). We also assume that the air pressure is constant and take into account only velocity pulsations, neglecting the pulsations of the remaining parameters.

According to Boussinesq's hypothesis, the turbulent shear deformations can be related to the mean deformation rate through the effective scalar turbulent viscosity η_T. By analogy with the kinetic theory of gases, the turbulent viscosity coefficient η_T can be represented as

$$\eta_T = \rho v_T L_T, \qquad (7)$$

where v_T is the characteristic velocity of turbulent pulsations and L_T is their characteristic spatial scale. It is natural to assume that

$$v_T = c_1\sqrt{\overline{u'^2}} \approx c_1\sqrt{2K_T} \text{ and } L_T = c_2 r_{ch},$$

where c_1 and c_2 are numerical coefficients on the order of unity, which should be adjusted to achieve the best agreement with the natural observations; $K_T = \overline{u_i' u_i'}/2 \approx W_T/2\pi\int_0^{r_{ch}(t)}\rho r dr$ is the kinetic energy of turbulent motion of the air per unit mass; W_T is the total linear kinetic energy of turbulent pulsations in the channel; and r_{ch} is the channel radius.

Taking into account the fact that heat diffusion from the cooled channel is governed by the molecular and turbulent transport processes (the latter process is far more intense), we introduce the effective thermal diffusivity χ_{eff} and thermal conductivity λ_{eff} [24]:

$$\chi_{eff} = \chi_\lambda + \chi_T = \frac{\lambda}{c_p\rho}\left(1 + \frac{\chi_T\rho}{\lambda/c_p}\right) \equiv \frac{\lambda_{eff}}{c_p\rho},$$

$$\lambda_{eff}(T) \equiv \lambda(T)\left(1 + \frac{\chi_T\rho}{\lambda/c_p}\right), \quad \chi_T \sim v_T L_T = \eta_T/\rho,$$

where χ_λ and λ are the associated molecular transport coefficients.

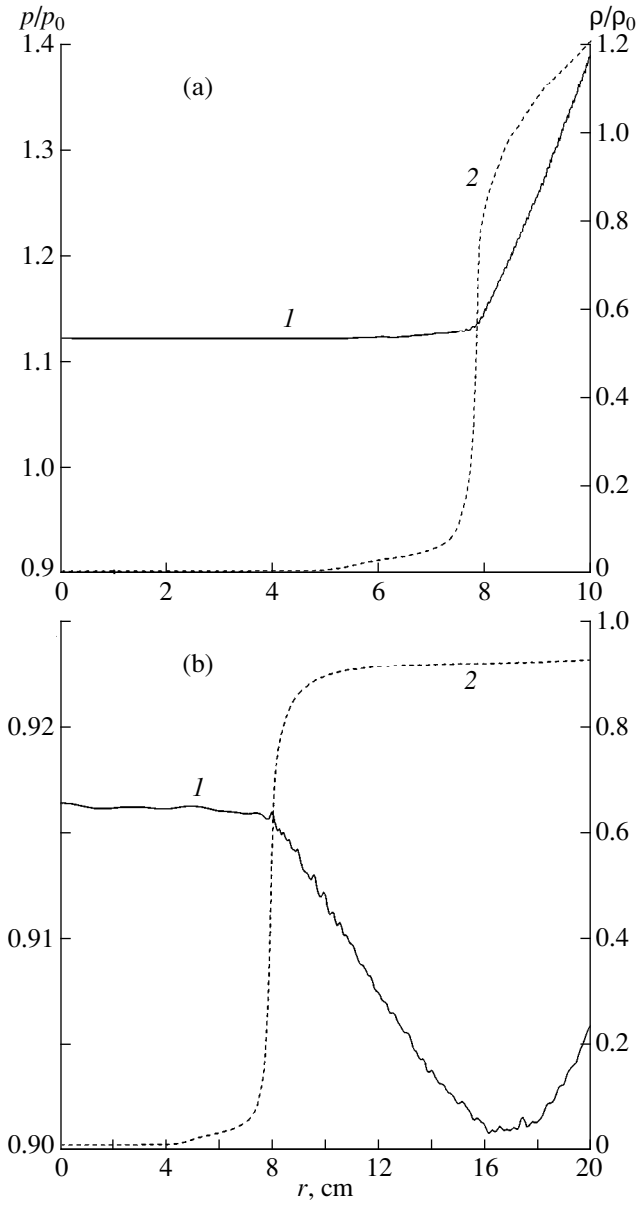

Fig. 4. Radial profiles of the (*1*) pressure and (*2*) density of air in the channel and its vicinity in the stages of (a) expansion (at t = 200 μs) and (b) contraction (at t = 800 μs) for I_a = 100 kA.

Outside the cooled channel, the air flow is laminar. During the cooling process, the kinetic energy of the air flow contracting toward the channel axis is converted into the energy of turbulent pulsations (except for a fraction of the kinetic energy that is converted into the thermal energy via air viscosity). As was shown in the previous section, the conditions for the onset of a hydrodynamic instability at the channel boundary are satisfied during the reverse radial motion of the boundary toward the axis, when the air pressure in the channel increases from the minimum value to atmospheric pressure. Consequently, we can assume that, when the channel boundary starts to contract toward the axis, the kinetic energy of turbulent pulsations of the air begins to flow into the channel. The energy influx per unit channel length is described by the equation [23, 24, 7]

$$\dot{W}_T = 2\pi r_{ch}\rho(r_{ch})\Lambda(t)(u_n + \dot{r}_{ch})u_n^2/2 - 2\pi\Omega(\nu)\int_0^{r_{ch}}\rho r dr, \quad u_n + \dot{r}_{ch} < 0, \tag{8}$$

where $\dot{r}_{ch}$ is the velocity of the conditional channel boundary and $u_n(r_{ch})$ is the air flow velocity through the boundary with respect to the immobile axis. The quantity $\Lambda(t)$ accounts for the delay of the onset of turbulent air motion in the channel; we can approximately set $\Lambda(t) = 1 - \exp[-(t - t_p)/\tau_{inst}]$, where t_p is the instant at which the channel boundary starts to contract, thereby giving rise to the hydrodynamic instability. The term

$$\Omega \approx \nu k^2 \overline{u'^2} \approx 2\nu k^2 K_T, \quad k \approx 2\pi/r_{ch} \tag{9}$$

accounts for the fraction of the kinetic energy of turbulent pulsations that is converted into thermal energy via the air viscosity, which is described by the kinematic viscosity coefficient $\nu(T)$.

If there is a heat source that acts to prevent air cooling in the channel (e.g., the air is Joule-heated by the residual current), then the cold air (and, accordingly, the kinetic energy) stops flowing into the channel. In this case, only the kinetic energy of turbulent pulsations dissipates in the channel:

$$\dot{W}_T = -2\pi\Omega(\nu)\int_0^{r_{ch}}\rho r dr \approx -2\nu k^2 W_T, \quad u_n + \dot{r}_{ch} > 0. \tag{10}$$

Equations (8) and (10) should be supplemented with the initial condition

$$W_T(t_p) = 0.$$

Equations (8) and (10) and expression (9) are valid under the assumption that the total kinetic energy of turbulent pulsations is accumulated in the longest scale pulsations such that $L_T \sim r_{ch}(t)$. Here, we neglect cascading of the kinetic energy of turbulent pulsations to shorter scale lengths, because the estimates carried out on the basis of the model of [23, 24] show that, for the range of Reynolds numbers characteristic of the longest scale pulsations ($\mathrm{Re} \approx \sqrt{\overline{u'^2}}\, r_{ch}/\nu(T) \sim 10$–$10^2$), the time scale on which the ionized air evolves into a fully developed turbulent state is comparable to or even longer than the time interval over which the decaying channel is stabilized by the residual current.

In our one-dimensional model, turbulent air motion is incorporated through the formal replacement $p + Y \longrightarrow p + Y + 2\rho K_T$ in Eqs. (1). We also must supplement the right-hand side of the energy balance equation with the effective thermal conductivity $\lambda_{eff}(T)$ and additional source term $Q_T = +\Omega(\nu)$, starting from the instant $t = t_p$.

Figure 5 illustrates the results of simulation of the turbulent cooling of the channel at I_a = 100 and 30 kA for different residual currents I_{res}. We can see that, with no residual current present, the turbulent pulsations enhance the rate at which the channel is cooled. As a result, the thermal conductivity falls to zero and the plasma in the channel rapidly decays. In contrast, a low (in comparison with the peak value) residual current is capable of stopping the cooling of the channel and maintaining a relatively high air temperature and thermal conductivity at levels typical of the quasisteady free arc. In this case, each discharge-current pulse is characterized by its own minimum residual current I_{res}, which stabilizes the decaying channel. At I_a = 100 kA, the channel is stabilized at $I_{res} \approx 100$ A. On the other hand, the residual current $I_{res} \approx 40$ A is sufficient to prevent the channel with I_a = 30 kA from decaying.

Under the conditions that we adopted for the stabilization stage, the electric field in the channel was found to be about $(1\text{–}2) \times 10^4$ V/m, which is far above the electric field in Fig. 3. This discrepancy stems from the fact that, for the same temperature and same channel radius, the field E_T in a turbulence-stabilized channel is stronger than the corresponding field E_λ in a turbulence-free channel by virtue of the estimate $E_T \sim E_\lambda(\lambda_{eff}/\lambda)^{1/2}$, which follows from the quasisteady balance condition for the Joule heat release in the channel and heat losses through the channel boundary.

6. DISCUSSION OF NUMERICAL RESULTS

Our simulations revealed that the residual current plays an important role in the stabilization of a cooled arc channel and the suppression of the originating turbulent pulsations. Even when the pulse current is extremely high (about 100 kA), no turbulent pulsations occur if the continuous residual current is sustained at a level of 100 A, which is a typical current during pauses between strokes of a lightning discharge. Consequently, if the gas-discharge processes in a cloud are capable of ensuring a continuous current at a level of at

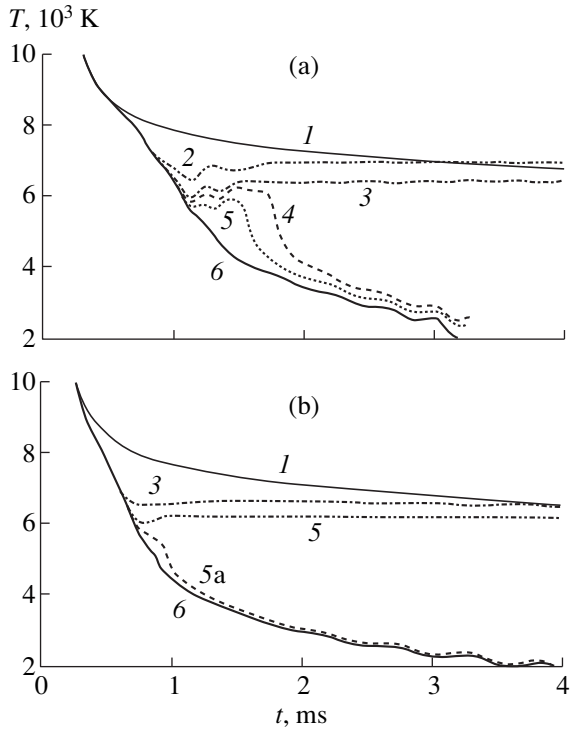

Fig. 5. Time evolutions of the air temperature at the channel axis for I_a = (a) 100 and (b) 30 kA. Profile (*1*) was calculated neglecting turbulent pulsations, and the remaining profiles were obtained with turbulent pulsations taken into account for the residual currents I_{res} = (*2*) 200, (*3*) 100, (*4*) 75, and (*5*) 50, (*5*a) 35, and (*6*) 0 A.

least 10^3 of the pulse current, then the turbulent pulsations cannot destroy the lightning channel as the pulse current is being damped. In other words, the cloud-to-ground channel continues to exist after the return stroke of a lightning discharge. According to our model simulations, this channel is in a transient stage, in which the channel radius (which is equal approximately to 5–8 cm because of the expansion of the channel in the return stroke) is noticeably larger than the radius of the steady arc channel. Presumably, for this reason, the air temperature in the channel is somewhat lower. Nevertheless, the air temperature is maintained by the accompanying residual current at a level of 6000–7000 K, which is typical of a quasisteady free arc. On a time scale of about 1 ms, on which the thermodynamically equilibrium state is reached, the plasma conductivity in a channel heated to 6000 K is about 1 $(\Omega\ \text{cm})^{-1}$ and the linear resistance R_0 of a channel with a radius of about 5 cm is estimated to be 2 Ω/m.

On the one hand, for characteristic distances between the cloud and the ground ($l \approx 3000$ m), the estimated value of the linear channel resistance R_0 is sufficient for the total channel resistance to be as high as $R_{ch} = R_0 l \gg Z$, where $Z \approx 500$–$600\ \Omega$ is the wave resistance of the lightning channel. This indicates that any process associated with the recharging of the channel is aperiodic. As a result, an aperiodic process will eventually result in the diffusion of the potential and current rather than the propagation of weakly damped waves of the potential and current. On the other hand, a linear resistance on the order of 1 Ω/m is insufficient for the electric field to exceed the ionization threshold in any region of the channel not only for the continuous current during pauses between the successive strokes but also for the typical current of the dart leader of the subsequent strokes, which are characterized by currents of about 10^3 A.

It is the regime of the propagation of electric perturbations that is peculiar to the M-components. It was shown in [4, 25] that the perturbation that propagates diffusivity upward and is driven, e.g., when an intracloud leader with a high potential U comes into contact with the grounded channel under consideration is rapidly damped and the initially steep fronts of the potential and current flatten and become as long as several hundreds of meters. Such phenomena are characteristic of the M-components.

Presumably, the so-called dart leader is also generated when an intracloud leader comes into contact with the grounded channel. However, the data from optical measurements can most likely be interpreted as resulting from the propagation of a cloud-to-ground ionization wave along the already developed channel rather than from another reason. The front of such an ionization wave is narrow and its main parameters (in particular, velocity) are analogous to those of the ionization wave at the streamer head. For a cloud-to-ground ionization wave to be excited, the linear resistance of the channel should be at least three orders of magnitude higher than that maintained by the continuous current during pauses between the successive strokes [4]. The above analysis allows us to conclude that such a high linear resistivity can be achieved only when the current in the channel terminates. This conclusion agrees with field observations [6, 26], according to which the generation of the dart leader of each successive stroke is always preceded by a decrease in the channel current to nearly zero.

REFERENCES

1. M. A. Uman, *The Lightning Discharge* (Academic, New York, 1987).
2. H. Jurenka and E. Barreto, J. Geophys. Res. D **90**, 6219 (1985).
3. J. E. Borovsky, J. Geophys. Res. D **100**, 2697 (1995).
4. É. M. Bazelyan, Fiz. Plazmy **21**, 497 (1995) [Plasma Phys. Rep. **21**, 470 (1995)].
5. V. Cooray, J. Atmos. Electr. **16**, 145 (1996).
6. V. Rakov, J. Geophys. Res. D **103**, 1879 (1998).
7. M. N. Shneider, Paper No. 2000-0721 (AIAA, Reno, NY, 2000).

8. M. N. Plooster, Phys. Fluids **13**, 2665 (1970); **14**, 2111 (1970).
9. A. H. Paxton, R. L. Gardner, and L. Baker, Phys. Fluids **29**, 2736 (1986).
10. M. Akram, J. Phys. D **29**, 2137 (1996).
11. B. N. Chetverushkin, *Numerical Simulations of the Problems of Dynamics of a Radiative Gas* (Nauka, Moscow, 1985).
12. I. V. Avilova, L. M. Biberman, V. S. Vorob'ev, *et al.*, *Optical Properties of Hot Air* (Nauka, Moscow, 1970).
13. M. A. El'yashevich, G. S. Romanov, and Yu. S. Stankevich, in *Proceedings of IV All-Union Conference "Dynamics of Radiative Gas"* (Mosk. Gos. Univ., Moscow, 1981), p. 90.
14. S. I. Ananin and T. A. Lepsheĭ, Preprint No. 325 Inst. Fiz. AN BSSR (Inst. of Physics, Academy of Science of BSSR, Minsk, 1984).
15. Yu. K. Bobrov, V. V. Vikhrev, and I. N. Fedotov, Fiz. Plazmy **14**, 1222 (1988) [Sov. J. Plasma Phys. **14**, 715 (1988)].
16. N. M. Kuznetsov, *Thermodynamic Functions and Shock Adiabats of Air at High Temperatures* (Mashinostroenie, Moscow, 1965).
17. Ya. B. Zel'dovich and Yu. P. Raizer, *Physics of Shock Waves and High-Temperature Hydrodynamic Phenomena* (Nauka, Moscow, 1966; Academic, New York, 1966, 1967).
18. F. A. Baum, K. P. Stanyukovich, and B. I. Shikhter, *Physics of Explosion* (Gos. Izd. Fiz. Mat. Lit., Moscow, 1959).
19. Yu. P. Raizer, *Gas Discharge Physics* (Nauka, Moscow, 1987; Springer-Verlag, Berlin, 1991).
20. G. Taylor, Proc. R. Soc. London, Ser. A **201**, 192 (1950).
21. J. P. Greig, R. E. Pechacek, and M. Releigh, Phys. Fluids **28**, 2357 (1985).
22. J. M. Picone, J. P. Boris, J. P. Greig, *et al.*, J. Atmos. Sci. **38**, 2056 (1981).
23. M. N. Shneĭder, Teplofiz. Vys. Temp. **31**, 406 (1993); **32**, 57 (1994); Paper No. 95-1994 (AIAA, San Diego, CA, 1995).
24. M. N. Shneĭder, Zh. Tekh. Fiz. **68** (2), 30 (1998) [Tech. Phys. **43**, 159 (1998)]; Paper No. 97-2360 (AIAA, Atlanta, GA, 1997).
25. V. A. Rakov, R. Thottappillil, M. A. Uman, *et al.*, J. Geophys. Res. D **100**, 25701 (1995).
26. R. J. Fisher, G. H. Schnetzer, R. Thottappillil, *et al.*, J. Geophys. Res. D **98**, 22887 (1993).

Translated by G.V. Shepekina

Plasma Physics Reports, Vol. 26, No. 10, 2000, pp. 902–908. Translated from Fizika Plazmy, Vol. 26, No. 10, 2000, pp. 961–968.

LOW-TEMPERATURE PLASMA

Self-Consistent Model of a Pulsed Air Discharge Excited by Surface Waves

O. A. Ivanov and V. A. Koldanov

Institute of Applied Physics, Russian Academy of Sciences, ul. Ul'yanova 46, Nizhni Novgorod, 603600 Russia

Received January 27, 2000

Abstract—A complete self-consistent electrodynamic model of a pulsed gas discharge excited by surface waves is developed. The model allows one to calculate both the initial phase of the discharge front propagation and the parameters of the produced plasma. The spatiotemporal evolution of the electromagnetic field and plasma parameters at the discharge front is investigated for the first time. It is shown that discharge propagation is mainly governed by a breakdown wave in an inhomogeneous electric field at the leading edge of the ionization front. It is found that the effect of the electric field enhancement in the plasma resonance region significantly affects the velocity of the breakdown wave. The results of calculations agree well with experimental data.

1. INTRODUCTION

Microwave gas discharges excited by electromagnetic surface waves (SW) are promising for wide application in various plasma technologies [1–7]. The parameters of SW discharge plasmas can be easily controlled by changing the frequency and power of the exciting radiation. Continuous SW discharges can be sustained at radiation frequencies from 1 MHz to 40 GHz over a wide range of pressures from 10^{-5} torr to atmospheric pressure in various types of plasma reactors and gas-discharge tubes.

In addition, pulsed SW discharges have attracted considerable interest. In the pulsed mode, microwave radiation with a higher power and frequency can be used; consequently, it is possible to attain higher densities of electrons, radicals, and excited molecules as compared to the continuous mode. Furthermore, in the pulsed mode, a high peak microwave power can be attained at a low level of the average power, which makes it possible to avoid strong gas heating.

The electron density N_c in SW discharge plasmas exceeds the value $N_d \geq N_c(1 + \varepsilon)$, where $N_c = m(\nu^2 + \omega^2)/4\pi e^2$ is the critical electron density, m and e are the electron mass and charge, $\omega = 2\pi f$ is the circular frequency of the microwave radiation (f is the radiation frequency), ε is the permittivity of the tube wall, and ν is the electron–molecule collision frequency. For f = 10 GHZ, we have $N_c \geq 10^{12}$ cm^{-3}. It follows from here that the electron density increases substantially with increasing the microwave frequency in the range $\nu < \omega$. The microwave power needed to sustain the discharge also increases in this case. Hence, in order to excite large-volume discharges by short-wavelength radiation, it is necessary to use high-power microwave sources.

Although there are many experimental works on pulsed SW discharges [8–15], a theoretical model describing the time evolution of such a discharge is still lacking. The mechanism governing the propagation of the ionization front of the SW discharge is not yet understood, and both the field structure and plasma parameters at the front are still unknown.

In this paper, based on the finite-difference time-domain (FDTD) method, we develop a numerical self-consistent model of a pulsed discharge. The model allows one to calculate both the initial phase of SW propagation and the parameters of the produced plasma. The theoretical analysis is based on the experimental results obtained for discharges produced with a novel SW launcher [15, 16] operating at the E_{01} mode of a circular waveguide. The results obtained are also applicable to pulsed discharges produced by using conventional launchers because the spatial distribution of electromagnetic fields and plasma in SWs is independent of the type of launcher.

2. DESCRIPTION OF THE NUMERICAL MODEL

At present, fairly well developed self-consistent models of a continuous SW discharge are available [6, 7, 17]. These models are usually based on the time-independent Helmholtz equation for the complex electric field amplitudes and balance equations for particles and electron energy, complemented with appropriate boundary conditions. Depending on the dominant mechanism for electron loss, diffusion or recombination regimes for sustaining the discharge can be realized. Solving the above equations simultaneously, one can determine the steady-state structure of the field and the distribution of electron density N_e along the gas-discharge tube. It is evident that such an approach is inap-

1063-780X/00/2610-0902$20.00

plicable for describing the unsteady processes in pulsed SW discharges.

In this paper, the processes of SW excitation are described using a numerical model based on the FDTD method proposed in [18] and successfully used now to calculate the parameters of plasma reactors (see, e.g., [19]). The method is based on the direct solution of the Maxwell equations on a specially adapted space-time mesh.

Calculations were carried out for an SW launcher used in the experiments [15, 16] and shown schematically in Fig. 1. In the experiments, magnetron radiation at the wavelength $\lambda = 3$ cm was generated as the $H_{10}^{\square}$ rectangular-waveguide mode, which then was converted into the H_{11}^{O} circular-waveguide mode and, finally, into the E_{01}^{O} beyond-cutoff circular-waveguide mode with the help of a wave converter [20]. A thin metal diaphragm whose diameter was somewhat larger than that of the gas-discharge tube was installed at the exit from the launcher. The diameter of the diaphragm aperture was chosen such that, in the absence of a discharge, a considerable fraction of the power of the E_{01}^{O} mode was reflected from the diaphragm. In this case, a standing wave that was formed in the launcher facilitated the ignition of the discharge over a wide range of gas pressures; another favorable factor was an increase in the electric field amplitude at the diaphragm edge. At the same time, an SW propagating along the tube wall freely penetrated through the aperture of the diaphragm. Thus, the launcher was, in fact, a so-called surfaguide (a waveguide launcher of surface waves) [3] in which the diaphragm and the coupling aperture were oriented in the propagation direction of the electromagnetic wave in the waveguide. The discharge was ignited in quartz tubes with inner diameter $2a = 4$–6 mm, outer diameter $2R = 6$–20 mm, and length $L = 30$–100 cm. The tubes were positioned along the axis of the circular waveguide. The experiments were conducted at an air pressure of $p = 0.1$–10 torr (see [15] for details).

When modeling the discharge, we consider only azimuthally symmetric surface E-waves with $\mathbf{E} = \mathbf{e}_z E_z + \mathbf{e}_r E_r$ and $\mathbf{H} = \mathbf{e}_\phi H_\phi$. The Maxwell equations were written in cylindrical coordinates:

$$\frac{\partial H_\phi}{\partial t} = c\left(\frac{\partial E_z}{\partial r} - \frac{\partial E_r}{\partial z}\right),$$

$$\frac{\partial E_r}{\partial t} = -\frac{c}{\varepsilon}\frac{\partial H_\phi}{\partial z} - 4\pi j_r, \qquad (1)$$

$$\frac{\partial E_z}{\partial t} = \frac{c}{\varepsilon}\frac{1}{r}\frac{\partial r H_\phi}{\partial r} - 4\pi j_z,$$

where c is the speed of light and $\mathbf{j} = \mathbf{e}_z j_z + \mathbf{e}_r j_r$ is the plasma-current density. The dielectric permittivity ε of the tube material was assumed to be $\varepsilon = 4$; outside of the tube, we set $\varepsilon = 1$.

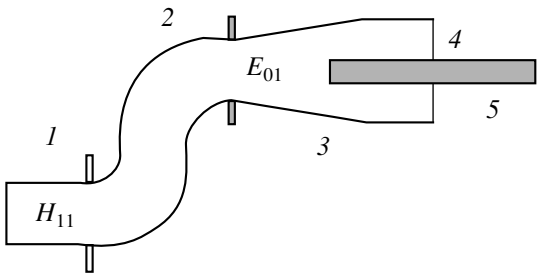

Fig. 1. Schematic of the surface-wave launcher: (*1*) $H_{11}^{\square} \longrightarrow H_{11}^{O}$ mode converter, (*2*) $H_{11}^{O} \longrightarrow E_{01}^{O}$ mode converter, (*3*) horn, (*4*) diaphragm, and (*5*) gas-discharge tube.

In calculations, we used the mesh shown in Fig. 2a. According to the FDTD method, the electric field values at nodal points of the mesh at the time $t + dt$ were computed from the known field values at the time t. The electric and magnetic fields were computed at different nodal points of the same mesh taking into account that, according to Eqs. (1), the time variations in the electric field **E** are caused by the spatial variations in the magnetic field **H** and vice versa. Thus, new values of E_z were first computed throughout the entire calculation region and, then, the values of E_r and H_ϕ were computed. The spatial step of the mesh ($h = 0.5$–1 mm) was chosen depending on the discharge-tube diameter. The time step was chosen from the condition $h > cdt$ ensuring the stability of the numerical scheme and was equal to nearly 1/50 of the microwave oscillation period.

Figure 2b illustrates the geometry of the model used in calculations. This geometry completely matched the launcher schematic shown in Fig. 1. The boundary conditions corresponded to a vanishing of the tangential components of the electric field on metal surfaces. A source was modeled by specifying the electric and magnetic currents exciting the E_{01} mode propagating in the $+z$-direction along the circular waveguide. The diaphragm diameter D and the tube diameter were chosen in compliance with the experimental conditions. The part of the discharge tube outside the exciter was surrounded by a cylinder with a well-absorbing wall. The cylinder radius was chosen to be much larger than the characteristic attenuation length of the SW electric field outside the tube, which excluded the influence of the absorber on the conditions of SW propagation. In this case, microwave power radiated from the discharge was absorbed at a fairly large distance from the tube axis. In this way, we modeled the conditions of SW propagation along a tube placed in free space. The initial electron density distribution was assumed to be uniform both along the axis and in the radial direction, and its value varied within the range 10^6–10^9 cm^{-3}. Estimates show that such an electron density ahead of the ioniza-

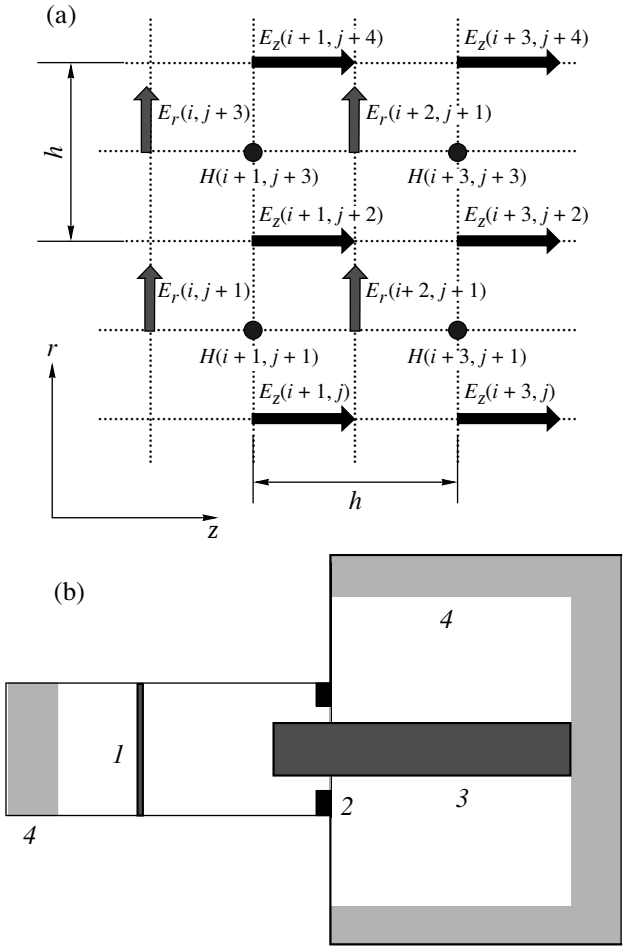

Fig. 2. (a) FDTD mesh in cylindrical coordinates and (b) the launcher scheme used in calculations: (*1*) exciter of E_{01}^{O} mode, (*2*) metal diaphragm, (*3*) quartz tube, and (*4*) absorber.

tion front can be produced by UV radiation from the discharge or by electron flows arising due to either diffusion or the action of a ponderomotive force. In addition, the calculations show that variations in the initial density N_0 have little or no effect on the spatiotemporal dynamics of the discharge and only lead to a change in the propagation velocity of the ionization wave.

As in [19], the equation for the plasma-current density entering Eq. (1) was written in the simplest form:

$$\frac{\partial \mathbf{j}}{\partial t} = \frac{e^2}{m} N_e \mathbf{E} - \nu \mathbf{j}, \qquad (2)$$

where $\nu(s^{-1}) = 5 \times 10^9 p$ [21] is the frequency of electron–molecule collisions in air. The set of Eqs. (1)–(2) was complemented with the electron balance equation

$$\frac{\partial N_e}{\partial t} = (\nu_i(|E_e|) - \nu_a) N_e - \alpha N_e^2 + D_a \Delta N_e, \qquad (3)$$

where α is the dissociative recombination coefficient; ν_i and ν_a are the ionization and attachment rates, respectively; and D_a is the ambipolar diffusivity. The ionization rate is a sharp function of the effective electric field $E_e = |\mathbf{E}|\nu/(\nu^2 + \omega^2)^{0.5}$. In calculations, we used the values of ν_a, D_a, and α from [21] and the dependence $\nu_i(E_e/p)$ given in [22].

Calculations were performed for gas pressures $p \geq 1$ torr, which were not too low so that the electron mean free path $L_e = V_{Te}/\nu$ (where V_{Te} is the electron thermal velocity) was less than the radius of the gas-discharge tube and the characteristic scale length of the electric field inhomogeneity Λ_E. In addition, at high pressures, the characteristic electron heat-conductivity length $L_T = L_e/\delta^{0.5}$ was less than Λ_E (here, $\delta \sim 10^{-3}$–10^{-2} is the fraction of electron energy lost in a collision with a molecule). The relaxation time of the electron temperature $\tau_e \sim 1/\delta\nu$ at such pressures was also shorter than the characteristic time τ_E of the electric field variations related to the propagation of the discharge ($\tau_E \sim \Lambda_E/V_f$, where V_f is the ionization-front velocity). Under these conditions, the relation between the ionization rate ν_i and the electric field strength has a local character: $\nu_i = \nu_i(E_e)$. The influence of gas heating in the initial phase of the discharge was neglected because the ionization-front velocities observed in experiments [12, 15] substantially exceeded the speed of sound in air.

3. RESULTS OF CALCULATIONS AND DISCUSSION

The self-consistent evolution of the electric field and electron density in an SW discharge was investigated by numerically solving the set of Eqs. (1)–(3). The calculations showed that the gas breakdown initially occurs in the part of the tube that is located inside the waveguide. When the electron density in this region approaches the critical density ($N_e \geq 10^{12}$ cm^{-3}), an SW is formed there and the ionization front begins to propagate along the tube. The initiation of the discharge, excitation of an SW, and its absorption in a plasma result in a significant decrease in the microwave power reflected from the launcher back toward the waveguide. The time dependence of the reflection coefficient is shown in Fig. 3. It is seen from the figure that up to 90% of the incident microwave power can be converted into an SW. This value coincides with experimental data [15, 16]. Oscillations of the calculated reflected signal (which were also observed in [15, 16]) may be attributed to the reflection of the SW from the propagating front of the discharge.

Figure 4 shows the spatiotemporal dynamics of the propagation of the ionization front in gas-discharge tubes of different diameters. The calculations show that the dynamics and structure of the discharge depend substantially on the gas pressure and the discharge tube diameter. Thus, at low gas pressures in small-diameter

tubes (when $pa < 1$ torr cm), the electron density starts growing in the center of the discharge tube. Figure 5 shows the characteristic radial profiles of the amplitudes of E_z and E_r components of the electric field and electron density N_e at different instants for this case. It is seen from the figure that, in the region where the electron density reaches its critical value N_c, both electric field components are significantly enhanced because of the plasma resonance. Note that the existence of the plasma resonance for the E_r-component of the SW field was observed experimentally [23]. The increase in the ionization rate in this field leads to an increase in the electron density and to the displacement of the discharge boundary toward the discharge tube wall. Further, the electron density continues growing and the distribution $N_e(r)$ flattens. At the same time, the electric field amplitude is redistributed over the tube cross section. As the discharge front propagates far away from the given cross section, the electron density distribution in this cross section becomes quasi-uniform (the electron density even somewhat increases from the tube axis to the periphery), the electric field reaches its maximum near the tube wall, and the electric field profile takes a form characteristic of steady-state SWs.

As the gas pressure and tube diameter increase ($pa \geq$ 1 torr cm), the electron density starts growing near the tube wall, where the electric field is maximum. In this case, the effect of the enhancement of the electric field in the plasma resonance region is not so pronounced and occurs on both sides of the maximum of the $N_e(r)$ profile. The resonance is less pronounced near the tube wall because of a steeper gradient of the electron density in this region. As time elapses, the $N_e(r)$ profile broadens, shifts toward the tube axis, and becomes more uniform. At the same time, the axial region with a decreased electron density continues to exist. Therefore, in the quasi-steady stage, the discharge takes the form of a plasma tube aligned with the quartz tube. The spatiotemporal dynamics of the discharge at higher air pressures is shown in Fig. 6.

The self-consistent evolution of the longitudinal profiles of the E_z component of the electric field and electron density is shown in Fig. 7. Calculations show that the electron density in the plasma column is substantially (by more than one order of magnitude) higher than the critical density $N_c = 10^{12}$ cm^{-3}. In the quasi-steady phase, the electron density gradually decreases from the launcher toward the end of the plasma column. These data agree well with experimental results [24].

At the discharge front, where the electron density gradient is maximum, one can see a sharp maximum of the amplitude of the electric field E_z, which is related to the plasma resonance. In this case, as is seen from the figure, the enhanced ionizing field penetrates into the neutral gas ahead of the discharge front to a depth of several centimeters. It is the avalanche growth of the

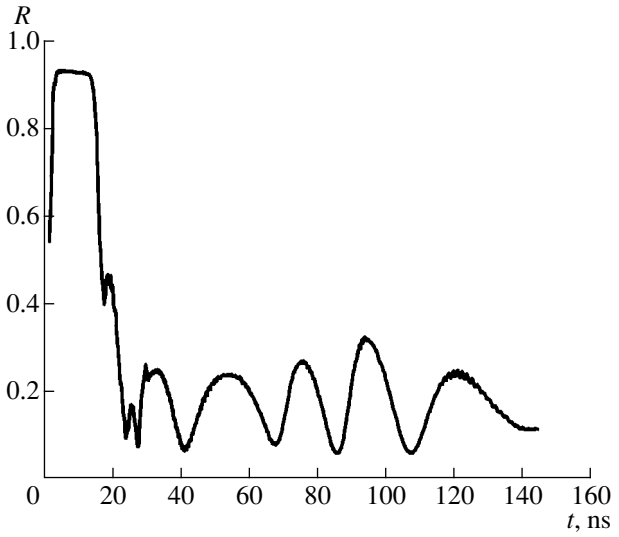

Fig. 3. Time dependence of the microwave reflection coefficient. The incident microwave power is $P = 50$ kW, the gas pressure is $p = 1.5$ torr, and the tube diameter is $2a = 8$ mm.

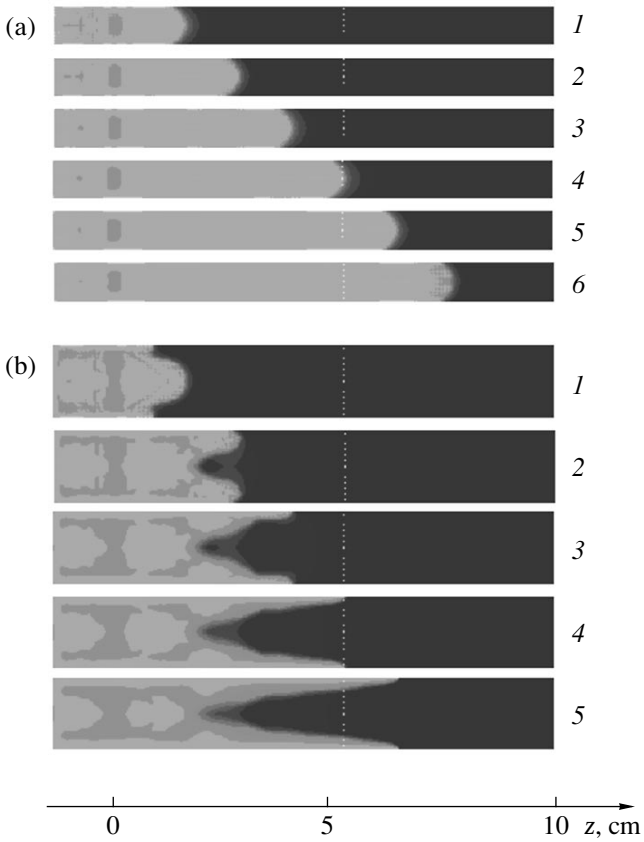

Fig. 4. Spatiotemporal dynamics of the electron density at the ionization front for $p = 1.5$ torr and tube diameters of (a) $2a = 8$ mm at the instants (*1*) 30, (*2*) 50, (*3*) 70, (*4*) 85, (*5*) 100, and (*6*) 130 ns and (b) $2a = 15$mm at the instants (*1*) 40, (*2*) 510, (*3*) 260, (*4*) 370, and (*5*) 500 ns.

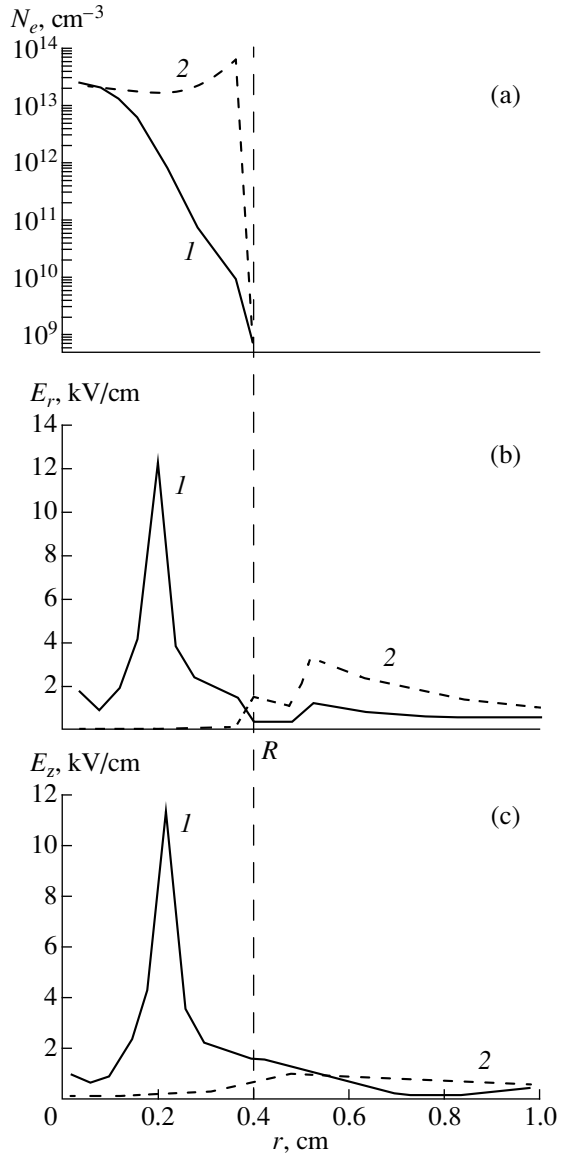

Fig. 5. Radial profiles of (a) the electron density and (b) E_r and (c) E_z components of the electric field at the instants (*1*) 85 and (*2*) 130 ns for P = 50 kW, p = 1.5 torr, $2a$ = 8 mm, and z = 5 cm.

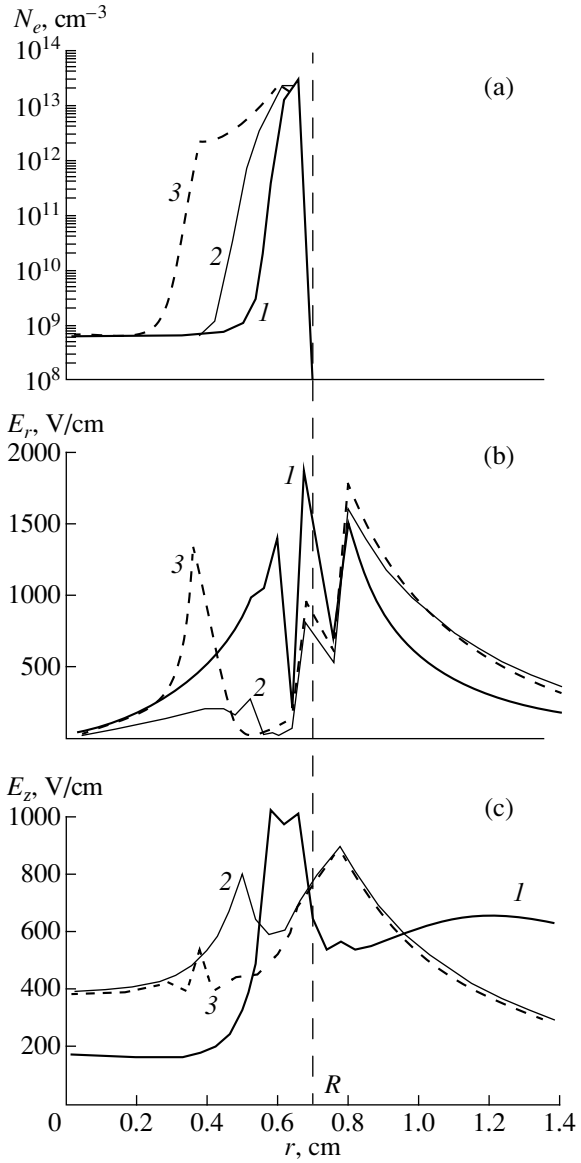

Fig. 6. The same as in Fig. 5 for the gas pressure p = 4 torr and tube diameter $2a$ = 15 mm for the instants (*1*) 350, (*2*) 430, and (*3*) 600 ns.

electron density in this field that causes the ionization front to move along the discharge tube. Note that the decrease in the electric field ahead of the ionization front in an SW was also observed in experiments [12, 15]. The enhancement of the field becomes less pronounced as the gas pressure (and, consequently, the electron–molecule collision frequency) increases. In addition, the electric-field amplitude at the front falls far away from the launcher because of the SW absorption. Behind the ionization front (in the plasma column), the electric-field strength falls sharply to a certain quasi-steady level sufficient to sustain the discharge.

Figure 8 shows the position of the discharge front Z_f as a function of time for different pressures and discharge tube diameters. In calculations, the front coordinate was specified as a point at which the electron density reached the critical value N_c. Figure 9 shows how the calculated discharge front velocity varies along the tube. For comparison, the experimental data [15] on the variation in the ionization-front velocity are also shown. It is seen from the figure that, at higher gas pressures, the increase in the collision frequency ν and, consequently, the increase in the damping rate of the SW with increasing the distance from the launcher result in a decrease in the discharge propagation veloc-

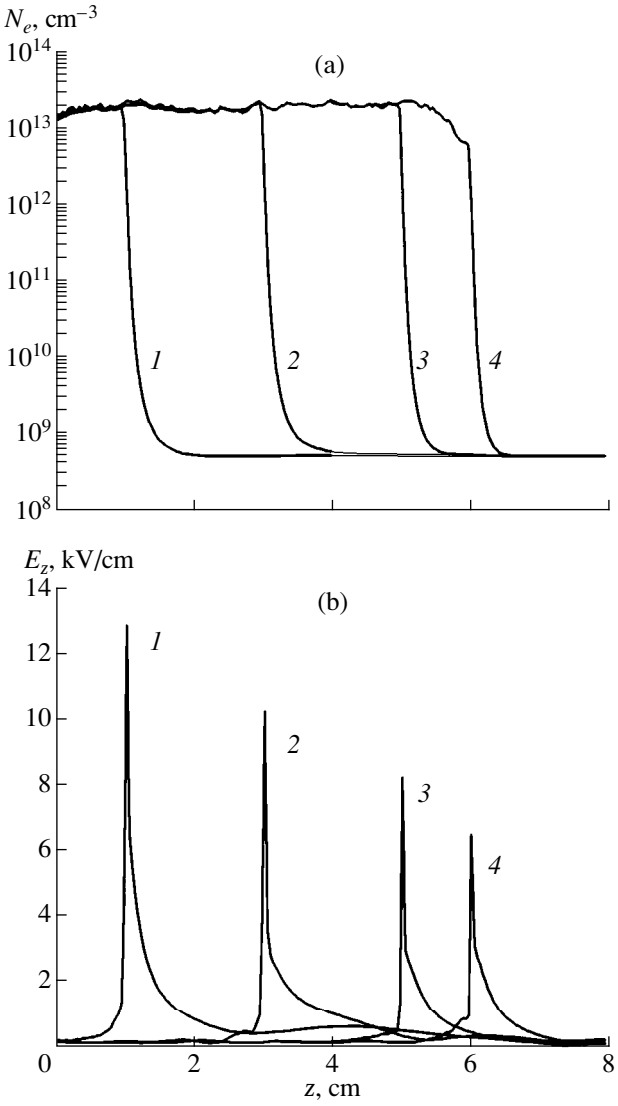

Fig. 7. Longitudinal profiles of (a) the electron density and (b) E_z component of the electric field at the instants (*1*) 32, (*2*) 70, (*3*) 100, and (*4*) 130 ns for P = 50 kW, p = 4 torr, $2a$ = 8 mm, and r = 2 mm.

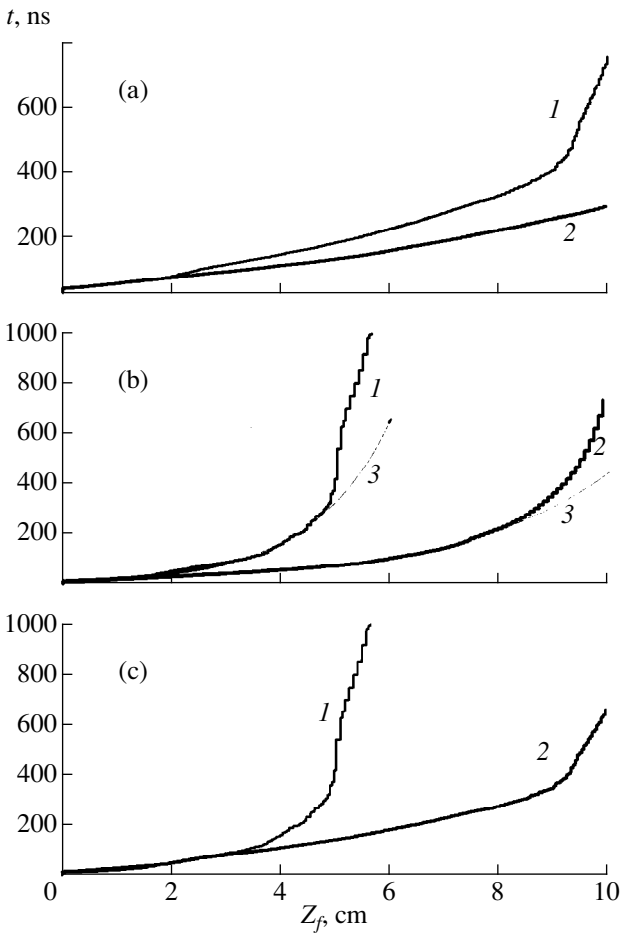

Fig. 8. The position of the ionization front as a function of time for P = 50 kW (a) at a pressure of p = 1.5 torr for tube diameters of (*1*) 14 and (*2*) 8 mm, (b) at a pressure of p = 4 torr for tube diameters of (*1*) 14 and (*2*) 8 mm (curve *3* shows the $Z_f \sim \ln(\beta t)$ approximation), and (c) for a tube diameter of $2a$ = 14 mm at air pressures of (*1*) 4 and (*2*) 1.5 torr.

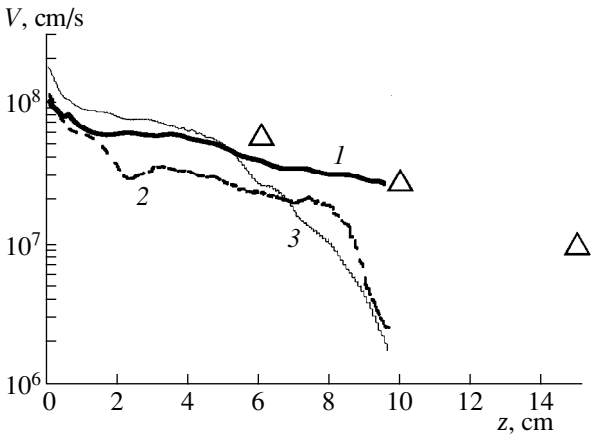

Fig. 9. Profiles of the ionization-front velocity along the discharge tube at P = 50 kW for (*1*) p = 1.5 torr and $2a$ = 8 mm, (*2*) p = 1.5 torr and $2a$ = 14 mm, and (*3*) p = 4 torr and $2a$ = 8 mm; triangles show the experimental data [5] for p = 1.5 torr and $2a$ = 8 mm.

ity. A similar effect is observed with increasing the inner diameter of the quartz tube. Actually, in this case, both the volume of the plasma column and the absorbed microwave power per unit length in the discharge increase; consequently, the SW damping rate also increases. Note that the position Z_f of the ionization front as a function of time is well approximated by the dependence $Z_f \sim \ln(\beta t)$, where β is the factor depending on the air pressure and tube radius. This dependence points to an exponential drop in the SW field amplitude along the tube axis and is characteristic of a breakdown wave [12, 15]. At large distances from the launcher where the discharge approaches its steady-state length, one can see a sharp decrease in the propagation velocity of the discharge front and, thus, a deviation from the

exponential function. In this region, because of the SW damping, the microwave field amplitude and the ionization rate decrease below the level needed for rapid gas breakdown ahead of the discharge front. Therefore, the breakdown-wave mechanism for the fast propagation of the discharge front changes to a slower mechanism for the front propagation along the electron-density gradient due to the ambipolar diffusion of charged particles [12, 25, 26].

4. CONCLUSION

In this paper, based on the FDTD method, a numerical electrodynamic model of a pulsed SW discharge has been developed. The model allows one to calculate both the initial phase of SW propagation and the plasma parameters in the quasi-steady regime. The self-consistent evolution of the radial and axial profiles of the electric field and plasma density at the discharge front is investigated. It is found that the discharge dynamics depends strongly on the gas pressure and the discharge tube diameter. It is shown that the electron density in an SW produced by high-power microwave radiation in the 3-cm-wavelength range is more that one order of magnitude higher than the critical density for the microwave frequency and attains the values $N_e \geq 10^{13}$ cm^{-3}. It follows from calculations that a strong ionizing electric field penetrates into the neutral-gas region at the SW front. This confirms the previously proposed mechanism for discharge front propagation related to a breakdown wave [12]. It is found that the effect of the electric field enhancement in the plasma resonance region at the leading front of the discharge significantly affects the propagation velocity of the SW front. It is shown that, at the distance where the discharge approaches its steady-state length, the breakdown-wave mechanism changes to a slower diffusion mechanism for the front propagation along the electron-density gradient.

ACKNOWLEDGMENTS

This work was supported in part by the Netherlands Organization for Scientific Research (NWO), project no. 047.011.000.01.

REFERENCES

1. M. Moisan, C. M. Ferreira, Y. Hajlaoui, *et al.*, Rev. Phys. Appl. **17**, 707 (1982).
2. M. Moisan and Z. Zakrzewski, J. Phys. D **24**, 1025 (1991).
3. M. Moisan, Z. Zakrzewski, R. Pantel, and P. Leprince, IEEE Trans. Plasma Sci. **12** (3), 203 (1984).
4. C. F. M. Borges, L. St.-Onge, M. Moisan, and A. Gicquel, Thin Solid Films **274**, 3 (1996).
5. C. M. Ferreira and M. Moisan, in *Proceedings of NATO Advanced Research Workshop "Microwave Discharges: Fundamentals and Applications," Sozopol, Bulgaria, 1998* (Plenum, New York, 1998).
6. I. Zhelyazkov and V. Atanassov, Phys. Rep. **255**, 79 (1995).
7. C. M. Ferreira and M. Moisan, Phys. Scr. **38**, 382 (1988).
8. E. Bloet, P. Leprince, M. Llamas Blasco, and J. Marec, Phys. Lett. **83A**, 391 (1981).
9. M. Llamas, V. Colomer, and M. Rodríguez-Vidal, J. Phys. D **18**, 2169 (1985).
10. A. Gamero, J. Cotrino, A. Sola, and V. Colomer, J. Phys. D **21**, 1275 (1988).
11. A. Gamero, A. Sola, J. Cotrino, and V. Colomer, J. Appl. Phys. **65**, 2199 (1989).
12. A. Bohle, O. Ivanov, A. Kolisko, *et al.*, J. Phys. D **29**, 369 (1996).
13. D. Grozev, K. Kirov, K. Makasheva, and A. Shivarova, IEEE Trans. Plasma Sci. **25**, 415 (1997).
14. D. Grozev, K. Kirov, and A. Shivarova, J. Phys. IV **8**, 307 (1998).
15. O. A. Ivanov, A. M. Gorbachev, V. A. Koldanov, *et al.*, J. Phys. IV **8**, 317 (1998).
16. A. L. Vikharev, O. A. Ivanov, and A. L. Kolysko, Pis'ma Zh. Tekh. Fiz. **22** (20), 28 (1996) [Tech. Phys. Lett. **22**, 832 (1996)].
17. Yu. M. Aliev, I. Ghanashev, H. Schluter, and A. Shivarova, Plasma Sources Sci. Technol. **3**, 216 (1994).
18. K. S. Yee, IEEE Trans. Antennas Propag. **14**, 302 (1966).
19. W. Tan and T. A. Grotjohn, J. Vac. Sci. Technol. A **12**, 1216 (1994).
20. D. V. Vinogradov and G. G. Denisov, Izv. Vyssh. Uchebn. Zaved., Radiofiz. **33** (6), 726 (1990).
21. Yu. P. Raĭzer, *Gas Discharge Physics* (Nauka, Moscow, 1987; Springer-Verlag, Berlin, 1991).
22. A. L. Vikharev, V. B. Gil'denburg, O. A. Ivanov, *et al.*, Fiz. Plazmy **12**, 1503 (1986) [Sov. J. Plasma Phys. **12**, 870 (1986)].
23. S. Grosse, in *Advanced Technologies Based on Wave and Beam Generated Plasmas*, Ed. by H. Schluter and A. Shivarova (Kluwer, Dordrecht, 1999) [NATO Sci. Ser. High Technol. **67**, 517 (1999)].
24. O. A. Ivanov and V. A. Koldanov, in *Advanced Technologies Based on Wave and Beam Generated Plasmas*, Ed. by H. Schluter and A. Shivarova (Kluwer, Dordrecht, 1999) [NATO Sci. Ser. High Technol. **67**, 511 (1999)].
25. V. E. Semenov, Fiz. Plazmy **8**, 613 (1982) [Sov. J. Plasma Phys. **8**, 347 (1982)].
26. A. L. Vikharev, O. A. Ivanov, and A. N. Stepanov, Fiz. Plazmy **14**, 53 (1988) [Sov. J. Plasma Phys. **14**, 32 (1988)].

Translated by N.F. Larionova

Plasma Physics Reports, Vol. 26, No. 10, 2000, pp. 909–913. Translated from Fizika Plazmy, Vol. 26, No. 10, 2000, pp. 969–973.

LOW-TEMPERATURE PLASMA

Gas-Dynamics of the Propagation of a Microwave Discharge Excited by the H_{10} Waveguide Mode

É. B. Kulumbaev and V. M. Lelevkin

Kyrgyz–Russian Slavic University, Bishkek, 720000 Kyrgyzstan

Received February 16, 2000; in final form, April 3, 2000

Abstract—A two-dimensional gas-dynamic model is applied to calculate the characteristics of the steady-state propagation of a microwave discharge excited by the H_{10} waveguide mode. The stream pattern is found on the basis of gas dynamics of a slowly propagating discharge, taking into account the non-one-dimensional character of the gas flow ahead of the discharge front. The calculated values of the propagation velocity agree with the experimental results. © *2000 MAIK "Nauka/Interperiodica".*

1. INTRODUCTION

The theory of microwave discharge propagation due to heat conduction implies that continuous motion of the leading front of the discharge toward the source of electromagnetic energy is caused by gas heating associated with the convective outflow of the energy dissipated in the discharge [1, 2]. An analysis of the processes in the frame of reference related to the plane front of a discharge is based on the equation of the energy balance, the one-dimensional continuity equation, and the wave equation for a monochromatic electromagnetic wave. The velocity of gas flowing into the discharge is the parameter to be determined and is treated as the normal propagation velocity of the discharge in a cold gas [2]. An experimental investigation of the microwave discharge propagation in a rectangular waveguide filled with air at atmospheric pressure was carried out in [3]. In the steady stage of propagation, the microwave discharge is located in the midplane (with respect to the wide wall) of the waveguide and is stretched out along the electric field lines. In this stage, the discharge absorbs and reflects about 75 and 25% of the incident power, respectively. A comparison of the numerical and experimental results showed [2] that the measured values of the discharge propagation velocity [3] significantly exceed the calculated ones. The authors of [2] explain this discrepancy by the fact that, under the experimental conditions of [3], the propagation of the discharge was analogous to combustion in a tube with a closed end. It was supposed in [4] that, during the discharge propagation, a fraction of the gas is expelled toward the waveguide walls and flows around the discharge; as a result, the gas is not entirely heated to the maximum temperature. A two-dimensional model of the gas flow ahead of the front of an optical discharge made it possible to explain the difference between the measured velocity of the discharge propagating toward the laser [5, 6] and the normal velocity of a slowly propagating optical discharge [7–9]. The mechanism for this phenomenon was considered in [7, 8] using as an example a cold gas flowing around a hot gaseous sphere. In [9], the gas-dynamics of a slowly propagating discharge was considered with allowance for Bernoulli's relation, taking into account the non-one-dimensional paraxial motion of the gas ahead of the discharge front.

In this paper, we propose a two-dimensional gas-dynamic model of the propagation of a microwave discharge excited by the H_{10} waveguide mode. A gas-dynamic regime of discharge propagation is found. The results obtained are compared with the experiment. The model [9] is considered to be suitable for estimating the discharge propagation velocity.

2. MODEL

2.1. Basic Assumptions

We consider a microwave discharge in a rectangular waveguide of cross section $a \times b$ (Fig.1) under the experimental conditions of [3]. The plasma exists due to dissipation of the electromagnetic energy of the TE wave with the components $\mathbf{E}(0; E_y = E; 0)\exp(i\omega t - ikz)$, $\mathbf{B}(B_x; 0; B_z)\exp(i\omega t - ikz)$. The wave passes through the discharge and is partially reflected from it. We assume that the flow is subsonic and laminar and the plasma is in local thermodynamic equilibrium. The variations of the parameters along the electric field direction are neglected.

2.2. Basic Equations

The plasma parameters are described in Cartesian coordinates related to the discharge front (Fig. 1). The model includes the following set of equations consist-

1063-780X/00/2610-0909$20.00

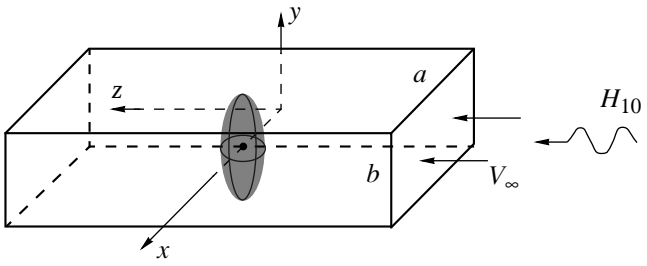

Fig. 1. Schematic of a waveguide microwave discharge.

ing of the time-independent continuity, Navier–Stokes, energy balance, and wave equations:

$$\frac{\partial}{\partial x}(\rho u) + \frac{\partial}{\partial z}(\rho w) = 0,$$

$$\rho u\frac{\partial u}{\partial x} + \rho w\frac{\partial u}{\partial z} = -\frac{\partial p}{\partial x} + 2\frac{\partial}{\partial x}\left(\eta\frac{\partial u}{\partial x}\right) + \frac{\partial}{\partial z}\left[\eta\left(\frac{\partial u}{\partial z} + \frac{\partial w}{\partial x}\right)\right] - \frac{2}{3}\frac{\partial}{\partial x}\left[\eta\left(\frac{\partial u}{\partial x} + \frac{\partial w}{\partial z}\right)\right],$$

$$\rho u\frac{\partial w}{\partial x} + \rho w\frac{\partial w}{\partial z} = -\frac{\partial p}{\partial z} + \frac{\partial}{\partial x}\left[\eta\left(\frac{\partial u}{\partial z} + \frac{\partial w}{\partial x}\right)\right] + 2\frac{\partial}{\partial z}\left(\eta\frac{\partial w}{\partial z}\right) - \frac{2}{3}\frac{\partial}{\partial z}\left[\eta\left(\frac{\partial u}{\partial x} + \frac{\partial w}{\partial z}\right)\right], \quad (1)$$

$$\rho u C_p\frac{\partial T}{\partial x} + \rho w C_p\frac{\partial T}{\partial z} = \frac{\partial}{\partial x}\left(\lambda\frac{\partial T}{\partial x}\right) + \frac{\partial}{\partial z}\left(\lambda\frac{\partial T}{\partial z}\right) + \frac{1}{2}\sigma E^2,$$

$$\frac{\partial^2 E}{\partial x^2} + \frac{\partial^2 E}{\partial z^2} + \frac{\omega^2}{c^2}\left(\varepsilon - i\frac{\sigma}{\omega\varepsilon_0}\right)E = 0.$$

Here, $\mathbf{V} = (V_x = u, V_y = 0, V_z = w)$ is the plasma velocity; p is the pressure; T is the temperature; ρ, C_p, η, and λ are the density, heat capacity, viscosity, and thermal conductivity, respectively; $\varepsilon = 1 - \sigma/\varepsilon_0\nu_e$ is the permittivity; $\sigma = e^2 n_e \nu_e/m_e(\omega^2 + \nu_e^2)$ is the electric conductivity; ν_e is the effective collision frequency; n_e, e, and m_e are the electron density, charge, and mass, respectively; $k = \sqrt{(\omega/c)^2 - (\pi/a)^2}$ is the longitudinal wavenumber; c is the speed of light; and ε_0 is the absolute permittivity.

2.3. Boundary Conditions

The boundary conditions at the contour of the rectangular integration region $0 \le x \le a/2$, $-L \le z \le L$ (Fig. 1) are set as follows.

(i) At the entrance ($z = -L$), we assume that the cold gas flow is uniform and the electromagnetic field is a superposition of the incident and reflected electromagnetic waves:

$$u = 0,\ w = V_\infty,\ T = T_\infty,$$
$$E = [E_I\exp(-ikz) + E_R\exp(ikz)]\sin(\pi x/a) \quad (2)$$
$$\text{for } z = -L.$$

(ii) At the exit end ($z = L$), we assume that the gas flows out freely and there is a transmitted electromagnetic wave:

$$p = p_0,\ u = 0,\ \partial(\rho w)/\partial z = 0,\ \partial T/\partial z = 0,$$
$$E = E_T\exp(-ikz)\sin(\pi x/a) \text{ for } z = L. \quad (3)$$

(iii) At the axis $x = a/2$, we impose the symmetry conditions

$$\partial p/\partial x = 0,\ u = 0,\ \partial w/\partial x = 0,\ \partial T/\partial x = 0,$$
$$\partial E/\partial x = 0 \text{ for } x = (a/2). \quad (4)$$

(iv) At the side boundary ($x = 0$), we assume the conditions of sliding (in the laboratory frame, it would be "sticking") over the cold, perfectly conducting walls of the channel:

$$u = 0,\ w = V_\infty,\ T = T_\infty,\ E = 0 \text{ for } x = 0. \quad (5)$$

Here, E_I, E_R, and E_T are the amplitudes of the incident, reflected, and transmitted waves of the H_{10} mode, respectively. When formulating the boundary conditions for E, we consider the dimensions a and b as those of a monomode waveguide that allow the main H_{10} wave to pass but cause the higher harmonics that emerge in the discharge area in the course of numerical solution to vanish before reaching the boundary $z = \pm L$.

2.4. Solution Technique

To solve the above set of equations numerically, we use the finite-difference scheme on a nonuniform rectangular grid. The control volume method is used to make the equations discrete. The pressure pattern is computed by means of the SIMPLE numerical code [10]. The velocity V_∞ is regarded as given, and the microwave power P_I is iteratively determined from the temperature T_* at the point ($a/2$, 0) [9]. The singularities of the solution to the wave equation are related to the numerical realization of the boundary conditions reduced to emission conditions:

$$\frac{\partial E}{\partial z} - ikE = -2ikE_I\exp(-ikz)\sin(\pi x/a) \quad (6)$$
$$\text{for } z = -L,$$

$$\frac{\partial E}{\partial z} + ikE = 0 \text{ for } z = L. \quad (7)$$

Since the wave equation determines the electric field amplitude accurate to a constant factor, condition (6) is substituted by the expression $\tilde{E} = \sin(\pi x/a)$ at $z = -L$. The iterative character of the right boundary condition is left unchanged. The obtained numerical solution $\tilde{E}(x, z)$ is to be scaled ($E(x, z) = K_E\tilde{E}(x, z)$) with the coefficient $K_E = |E_*|/|\tilde{E}|$ at $x = a/2$ and $z = 0$. The modulus $|E_*(a/2, 0)|$ provides the energy balance for the current values of the sought variables (at a given iteration step) in the control volume with temperature T_*. Based on the obtained field $E(x, z)$, we calculate the amplitudes E_I, E_R, and E_T and the corresponding microwave powers $P_{I, R, T} = kE^2_{I, R, T}\, ab/4\mu_0\omega$.

3. RESULTS

We calculated the characteristics of a microwave discharge in air at atmospheric pressure based on the experimental data from [3]: $a = 22.9$ mm; $b = 10.2$ mm; $\omega/2\pi = 10$ GHz; $T_* = 4500$ K; and $V_\infty = 0.5$, 1, 1.5, and 2 m/s. The parameters of air plasma at atmospheric pressure were taken from [7, 11]. The electron density was taken from the computed equilibrium composition. The dependence of the electron collision rate on temperature was derived from the values of the conductivity σ_0 at $\omega = 0$; namely, $\nu_e = e^2n_e/m_e\sigma_0$.

As is seen from Figs. 2 and 3 ($V_\infty = 1$ m/s), the inflowing cold gas forms an abrupt (thermal and gas-dynamic) leading front of the microwave discharge. The elevated pressure region formed near the front deflects the paraxial flow in the transverse direction. The bulk of the gas flows around the high-temperature region of the discharge. After the paraxial cold gas flow has entered the discharge, it is heated, expands, and occupies the high-temperature region. A quasi-homogeneous flow takes place behind the front. The interaction between the plasma and the electromagnetic field leads to condensing of the lines $|\mathbf{E}| = \text{const}$ at the discharge front. The superposition of the incident ($P_I = 0.97$ kW) and reflected ($P_R = 0.75$ kW) electromagnetic waves results in a standing wave. A power of 0.23 kW/cm is dissipated in the discharge. The discrepancy with the measured value of the reflected power [3] is caused by the transformation of the incident electromagnetic wave (the H_{10} mode) into other types of waves, thus enabling the microwave power transfer in the discharge along the y direction.

In the laboratory frame, the gas bulk flows around the high-temperature region ($T > 4000$ K), which corresponds to pushing the cold gas toward the waveguide walls by the propagating microwave discharge. At the front, oppositely directed gas flows are formed: the cold gas flow is directed toward the discharge propagation direction and the hot gas flow is directed toward the center of the discharge. The existence of these flows was established in experiments with an optical discharge [6].

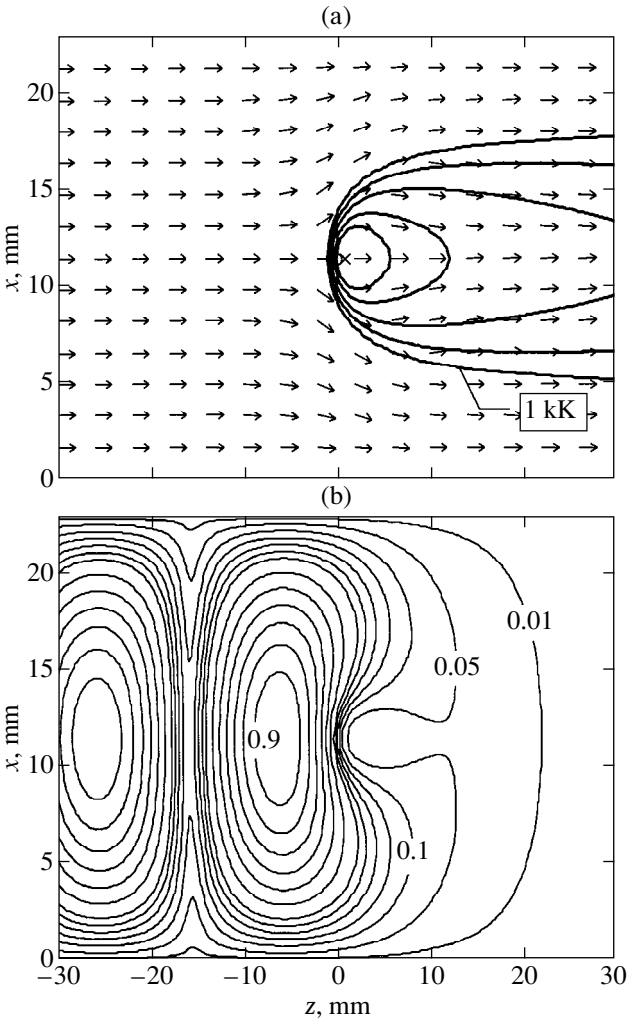

Fig. 2. (a) Velocity field and isotherms (the temperature increment is 1000 K) and (b) the contour lines of the electric field $E(x, z)/E_{\max}$ ($E_{\max} = 1.55$ kV) in a microwave discharge.

At $V_\infty = 0.5$, 1.5, and 2 m/s, the stream and gas-heating patterns do not change qualitatively. The measured [3] and calculated dependences of the observed discharge propagation velocity on the microwave power are in fair agreement (Fig. 4). At $V_\infty > 2$ m/s, it is impossible to obtain a convergent solution: there are iterative oscillations of the temperature and velocity behind the discharge front. In this case, the numerical procedure remains stable as a whole and the plasma parameters at the discharge head are almost independent of the oscillations at the right border. Similar instabilities took place when calculating a continuous optical discharge in the flow of atmospheric air [12].

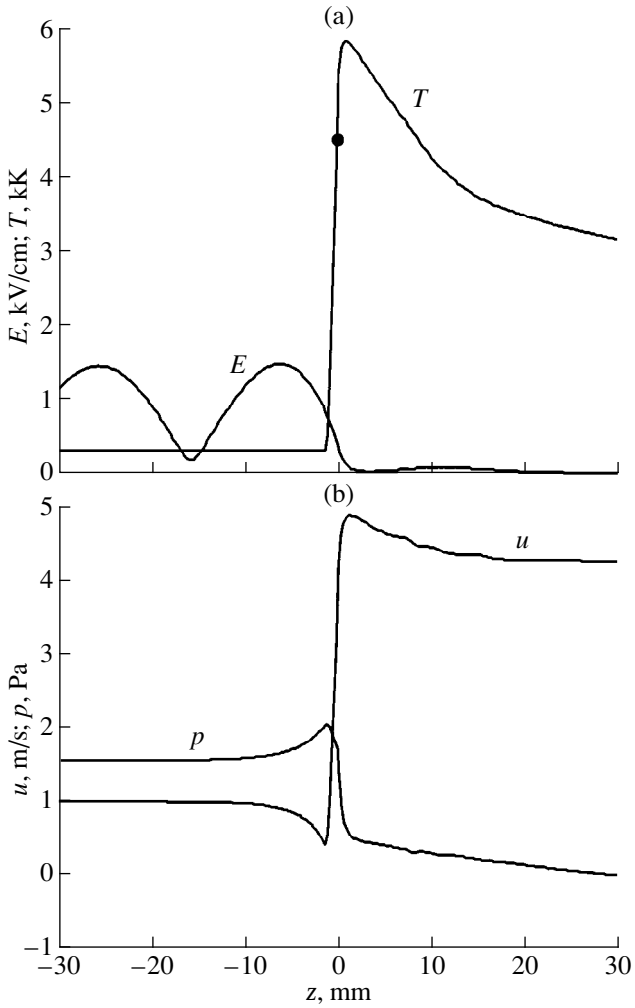

Fig. 3. The *z*-profiles of (a) the electric field and temperature and (b) the pressure and velocity at $x = a/2$.

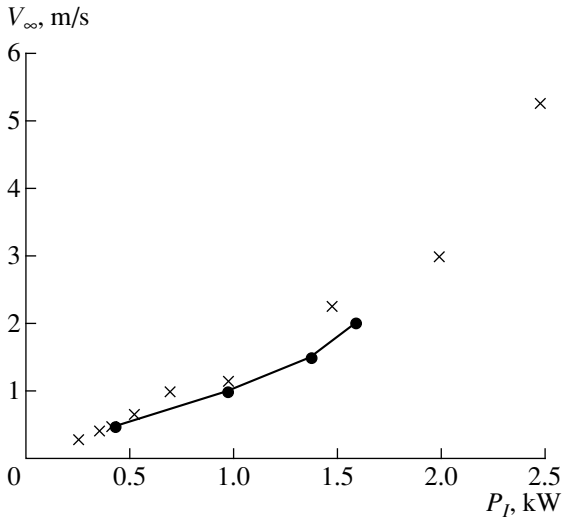

Fig. 4. The measured (crosses) [3] and calculated (circles) propagation velocity of a microwave discharge vs. the electromagnetic power.

The calculated gas-dynamic pattern of a discharge is almost identical to that of a moving optical discharge [9]. The gas dynamics of the microwave discharge propagation is described by the expressions

$$V_0 = \frac{\rho_\infty/\rho_0}{\sqrt{2\rho_\infty/\rho_0 - 1}}V_\infty, \quad V_1 = \frac{1}{\sqrt{2\rho_\infty/\rho_0 - 1}}V_\infty, \qquad \Delta p_1 = \frac{2(\rho_\infty/\rho_0 - 1)}{2\rho_\infty/\rho_0 - 1}\frac{\rho_\infty V_\infty^2}{2} \tag{8}$$

obtained from the solution to the gas-dynamic problem of slow combustion [13], which was supplemented with Bernoulli's relation in order to account for the non-one-dimensional motion of gas ahead of the discharge front [9]. Here, ρ_0 and V_0 are the mass density and velocity of the gas in the discharge and Δp_1 is the excess pressure occurring as a result of the velocity drop from V_∞ to V_1 during the motion of the gas toward the front.

At $V_\infty = 1$ m/s and $T_0 = 5840$ K, the velocities estimated in accordance with (8) are $V_1 \approx 0.2$ m/s and $V_0 \approx 3.5$ m/s (the minimum and maximum calculated values are 0.4 and 4.8 m/s, respectively). The observed propagation velocity of the microwave discharge front is related to the normal velocity of the discharge propagation, which, in the one-dimensional model, is defined by the expression $V_\infty \approx V_1\sqrt{2\rho_\infty/\rho_0}$ [2].

4. CONCLUSIONS

A gas-dynamic regime of the propagation of a microwave discharge excited by the H_{10} waveguide mode is obtained by numerical modeling. An analysis of the gas-dynamic pattern of the discharge allows one to explain the difference between the observed velocity at which the discharge front propagates toward the electromagnetic wave source and the normal velocity of a slowly propagating discharge. The calculated values of the microwave discharge propagation velocity agree with experiment.

REFERENCES

1. Yu. P. Raizer, *Laser-Induced Discharge Phenomena* (Nauka, Moscow, 1974; Consultants Bureau, New York, 1977).
2. Yu. P. Raĭzer, Zh. Éksp. Teor. Fiz. **61**, 222 (1971) [Sov. Phys. JETP **34**, 114 (1972)].
3. W. Best and W. L. Ford, Microwave J. **4** (10), 91 (1961).
4. V. M. Batenin, I. I. Klimovskiĭ, G. V. Lysov, and V. N. Troitskiĭ, *Microwave Plasma Generators: Physics, Technique, and Applications* (Énergoatomizdat, Moscow, 1988).
5. F. V. Bunkin, V. I. Konov, A. M. Prokhorov, *et al.*, Pis'ma Zh. Éksp. Teor. Fiz. **9**, 609 (1969) [JETP Lett. **9**, 371 (1969)].

6. I. A. Bufetov, A. M. Prokhorov, V. B. Fedorov, and V. K. Fomin, in *Slowly Burning Laser Plasma and Optical Discharges* (Nauka, Moscow, 1988).
7. Yu. P. Raĭzer, *The Physics of Gas Discharge* (Nauka, Moscow, 1992).
8. K. G. Gus'kov, Yu. P. Raĭzer, and S. T. Surzhikov, Kvantovaya Élektron. (Moscow) **17**, 937 (1990).
9. V. Ts. Gurovich, É. B. Kulumbaev, and V. M. Lelevkin, Fiz. Plazmy **24**, 1010 (1998) [Plasma Phys. Rep. **24**, 943 (1998)].
10. S. Patankar, *Numerical Heat Transfer and Fluid Flow* (McGraw-Hill, New York, 1980; Énergoatomizdat, Moscow, 1984).
11. V. S. Éngel'sht, V. Ts. Gurovich, G. A. Desyatkov, *et al.*, *The Theory of Electric Arc Column* (Nauka, Novosibirsk, 1990), Vol. 1.
12. S. T. Surzhikov and A. A. Chentsov, Fiz. Plazmy **22**, 1054 (1996) [Plasma Phys. Rep. **22**, 957 (1996)].
13. L. D. Landau and E. M. Lifshitz, *Fluid Mechanics* (Nauka, Moscow, 1988; Pergamon, Oxford, 1987).

Translated by N.N. Ustinovskiĭ

Plasma Physics Reports, Vol. 26, No. 10, 2000, pp. 914–916. Translated from Fizika Plazmy, Vol. 26, No. 10, 2000, pp. 974–976.

PLASMA KINETICS

Electron Distribution Function in a Two-Temperature Plasma with Cold Ions

S. A. Maĭorov

Institute of General Physics, Russian Academy of Sciences, ul. Vavilova 38, Moscow, 117942 Russia

Received November 12, 1999; in final form, March 4, 2000

Abstract—By modeling the dynamics of a large ensemble of particles, it is shown that slow electrons in a two-temperature plasma are in equilibrium with the electron component rather than with cold ions. The result of cooling by a cold ion component is that the number of the low-energy electrons only slightly exceeds that in the equilibrium Maxwellian distribution. © *2000 MAIK "Nauka/Interperiodica".*

1. INTRODUCTION

Due to the large ion-to-electron mass ratio, electron and ion plasma components may obey Maxwellian distributions with different temperatures. Such a system may be steady if equilibrium is sustained in each subsystem (e.g., when the electron component in a discharge is heated with an RF field, whereas the ions are in equilibrium with a neutral gas). It may also be quasi-steady (e.g., after the pulsed heating of the electron component). In the latter case, each subsystem acquires its own temperature and then the temperatures equalize. Of interest is the problem of how the electron distribution function differs from Maxwellian in the low-energy region. It is the low-energy electrons that determine the recombination flux and, thus, the ion level populations, ion line emission, and possible population inversion. Since the cross section for Coulomb scattering decreases with energy, the slow electrons undergo the most intense cooling in Coulomb collisions with cold ions. This effect influences the formation of a quasi-steady electron distribution function in a two-temperature plasma in the course of temperature equalization.

In a recent paper [1] based on the analysis of Boltzmann's equation with the Landau collisions integral for a two-temperature plasma, it was concluded that the fraction of the low-energy electrons

$$Y \approx \frac{m_e}{m_i} z n_e, \tag{1}$$

where z is the ion charge number and n_e is the electron density, would be in quasi-equilibrium with the cold heavy plasma component (ions or, under certain conditions, neutral atoms) and would possess its temperature. This conclusion, being very important for X-ray lasers with recombination pumping [2], requires additional verification. Computer simulations based on *ab initio* principles for an ensemble of classical Coulomb particles [3, 4] can provide such verification. In this paper, we consider the equalization of electron and ion temperatures due to Coulomb collisions.

2. NUMERICAL SIMULATION OF THE DYNAMICS OF A LARGE ENSEMBLE OF PARTICLES

Let us consider a fully ionized plasma consisting of ions with mass m_i and positive charge $+ze$ and electrons with mass m_e and charge $-e$. The plasma is modeled by the method of molecular dynamics. We consider the time evolution of a system consisting of $n(1 + z)$ particles housed in a cube with specularly reflecting walls. The trajectories of n ions and zn electrons are determined by solving the Newton equations

$$d^2 r_k / dt^2 = F_k / m_k, \quad F_k = \sum_{l \neq k}^{n(z+1)} f_{kl}, \tag{2}$$
$$k = 1, 2, \ldots, n(z + 1);$$

where $r_k(t)$ is a radius-vector of the kth particle with mass m_k and charge q_k. The Coulomb interaction force f_{kl} for a distance between the particles of less than r_0 was taken to be equal to the interaction force between uniformly charged interpenetrating spheres of diameter r_0 [3]. Such a modification of the Coulomb force at short distances eliminates a singularity at a zero distance and reduces the equation stiffness caused by the short-range collisions. The adopted value of r_0 is much less than the mean interparticle distance ($r_0 \ll N^{-1/3}$, where N is the particle number density); in our runs, we set $r_0 = 0.025N^{-1/3}$. Additional runs were carried out in order to estimate the influence of the r_0 value on the characteristics a Coulomb system [4]. A particle–particle method [3] was used to solve the set of Eqs. (2). The nearest neighbors were separated out to enhance the accuracy of numerical integration.

A fully ionized plasma with $z = 1$, $N_i = 10^{18}$ cm^{-3}, and initial electron and ion temperatures of $T_e = 10$ eV

1063-780X/00/2610-0914$20.00 © 2000 MAIK "Nauka/Interperiodica"

and T_i = 1 eV, respectively, was investigated. In order to embrace a greater number of slow electrons, the ion-to-electron mass ratio was chosen to be 20. According to (1), for these plasma parameters, the fraction of electrons possessing the temperature of ions (T_i = 1 eV) would amount to 5%. The total number of particles in the system to be modeled was taken to be $(1 + z)n$ = 4000. The system dynamics was computed over the time interval $t_0 = 12.8 \times 10^{-12}$ s, which substantially exceeds the time during which a steady-state electron energy distribution is established but is less than the time of equalization of electron and ion temperatures. Over the time t_0, the energy exchange between the cold and hot components leads to a 3% drop in the electron temperature.

Figure 1 presents the calculated electron kinetic-energy distribution function. To make an analysis of the distribution function in the low-energy region more convenient, a logarithmic energy scale is adopted. The calculated electron distribution function differs from Maxwellian at most by 30% in that region. The time evolution of the electron kinetic energy is illustrated in Fig. 2 by the example of electrons with a low initial kinetic energy. The solid curve shows the evolution of the kinetic energy of an electron whose total energy at the initial instant is positive ("free" electron), and the dashed curve corresponds to an electron with a negative total initial energy ("bound" electron). In both cases, electrons acquire kinetic energy rather than stay in equilibrium with cold ions.

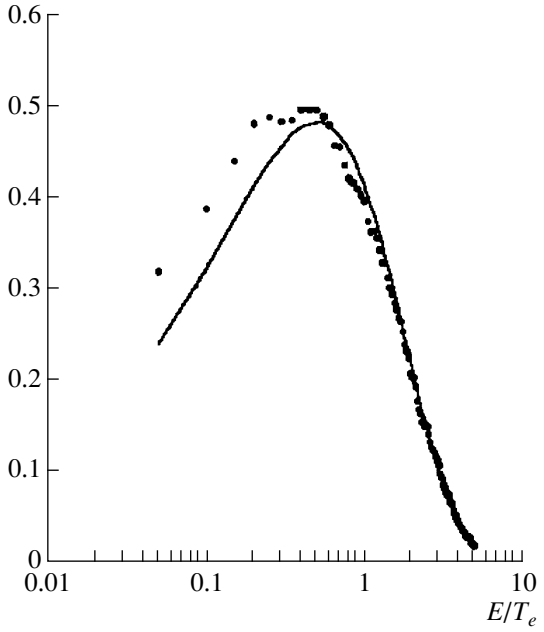

Fig. 1. Electron kinetic-energy distribution function: the solid curve is the Maxwellian distribution; dots show the results of numerical simulations.

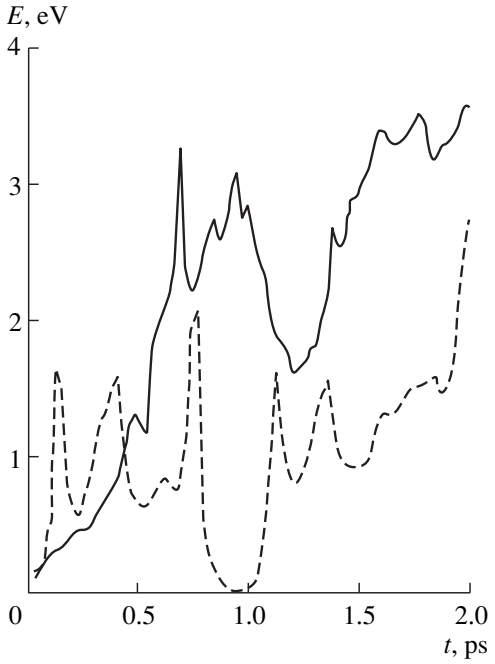

Fig. 2. Time evolution of the kinetic energy of electrons with low initial energies.

3. DISCUSSION OF THE RESULTS OF NUMERICAL SIMULATION

The results of our calculations show that the increase in the fraction of slow electrons is fairly small. Taking into account that this increase was a hundredfold magnified by the chosen ion-to-electron mass ratio, we can expect that, for a real mass ratio, the population of ion levels will hardly be influenced by this effect. The electron distribution stated in [1] was obtained based on the spherical cavity effect (first noted by Belyaev and Budker [5]), which implies that a probe particle does not exchange energy with faster particles under the condition that the distribution function is spherically symmetric in velocity space. It is of interest to explore the spherical cavity effect, in particular, its influence on collisional relaxation in a two-temperature plasma.

An analogy with electrostatics (the Trubnikov–Rosenblut potentials) leads to a formal consequence that the slowest particle is not able to acquire any energy at all. However, it is obvious that the applicability of this result is limited, especially, in the case of slow particles. The evolution of slow electrons in Fig. 2 clearly demonstrates that the spherical cavity effect does not apply to slow particles. It was pointed out by Sivukhin ([6], p. 123) that the spherical cavity effect stems from neglecting the dependence of the Coulomb logarithm on the relative particle velocity. In deriving this effect, a low momentum transfer per collision (straight-trajectory approximation) and the binary nature of collisions were also assumed. However, a slow particle interacts simultaneously with many others

and the binary-collision approximation is hardly applicable in this case.

4. DISCUSSION OF THE RESULTS OF [1] AND CONCLUSIONS

In [1], two subjects are discussed: the level population and the formation of a group of cold electrons with a temperature equal to the ion temperature. As for the first issue, I will make just one remark. The author used the cross-section value (referring to Zel'dovich and Raĭzer [7]) that provides the right asymptotic behavior at high energies and could be applied to ionization from the ground state. For the excitation of higher levels, Dravin's cross sections are commonly used. They have another asymptotics: for an excess energy of 0 to 2.85 (in units of transition energy), the cross section is assumed to be constant (namely, 0.302 in dimensionless units [8]). As the energy increases, the asymptotic used in [1] becomes valid. This difference can essentially affect the populations. The second issue is of more interest, being the major statement of paper [1]. Of course, there is certain logic in that study; a formal analogy with heat supports this. However, in my opinion, the effect is just a consequence of approximations under which the Landau collisions integral is derived. The numerical simulations confirm this opinion. An example of energy trajectories of initially slow electrons that should not acquire energy, but successfully do it in the numerical simulation (in full accordance with common sense), is most convincing. In the parameter region where the ideality approximation is violated, i.e., when the electron energy is on the order of its potential energy (the case of highly excited states), the collisions cannot be described by the Rutherford formula because of collective interaction. As was pointed out by Sivukhin, the Coulomb logarithm is substantially altered in this region and cannot be factored out of the integral sign.

It is worthwhile to make a terminological remark. It is reasonable to talk about the second temperature only when the temperatures differ greatly. The local slope of the distribution function on a logarithmic scale is not a temperature. An interaction stronger than the Coulomb one is known to be able to decrease the distribution function in a certain energy range, but nobody speaks about the temperature of the subtracted (or added) part of the distribution function. The temperature is either a thermodynamic parameter or a factor in the exponent index of the Maxwellian distribution (which, by the way, is also a thermodynamic characteristic of an ideal gas). The only advantage of defining the temperature from the slope of the distribution function (the derivative of logarithm of the distribution function without statistical weight) is that it coincides with the true temperature in the case of a Maxwellian distribution. If we determine the temperature from the distribution function itself (rather than from its slope), then, in the region where the distribution function is increased, the temperature will be negative. Sometimes, the population inversion is referred to as a state with a negative temperature.

Paper [1] is based on the binary-collision approximation, namely, on the Landau collision integral. For slow particles, this approximation is not valid, and, hence, the conclusions drawn in that paper are not justified. Numerical simulations by the particle method based on *ab initio* principles prove the lack of equilibrium between cold ions and a group of low-energy electrons.

ACKNOWLEDGMENTS

This study was initiated by the presentation of paper [1] at the seminar chaired by A.A. Rukhadze. I am grateful to I.V. Sokolov and I.A. Kossyĭ, as well as to the seminar participants, for helpful discussions.

REFERENCES

1. I. V. Sokolov, Fiz. Plazmy **25**, 562 (1999) [Plasma Phys. Rep. **25**, 511 (1999)].
2. R. C. Elton, *X-ray Lasers* (Academic, Boston, 1990; Mir, Moscow, 1994).
3. R. Hockney and J. Eastwood, *Computer Simulation Using Particles* (McGraw-Hill, New York, 1984; Mir, Moscow, 1987).
4. S. A. Maĭorov, Kratk. Soobshch. Fiz., No. 1, 33 (1999).
5. S. T. Belyaev and D. I. Budker, Dokl. Akad. Nauk SSSR **107**, 807 (1956) [Sov. Phys. Dokl. **1**, 218 (1957)].
6. D. V. Sivukhin, in *Reviews of Plasma Physics*, Ed. by M. A. Leontovich (Atomizdat, Moscow, 1964; Consultants Bureau, New York, 1968), Vol. 4.
7. Ya. B. Zel'dovich and Yu. P. Raizer, *Physics of Shock Waves and High-Temperature Hydrodynamic Phenomena* (Nauka, Moscow, 1966; Academic, New York, 1966, 1967), Vols. 1, 2.
8. L. M. Biberman, V. S. Vorob'ev, and I. T. Yakubov, *Kinetics of Nonequilibrium Low-Temperature Plasmas* (Nauka, Moscow, 1982; Consultants Bureau, New York, 1987).

Translated by N.N. Ustinovskiĭ